広島大学学位請求論文

Development of Iridium Metallacycles with Arylated Dipyrido-annulated Carbenes

(アリール基で修飾されたジピリド縮環型カルベンによるイリジウム環状化合物の創生)

2023年

広島大学大学院
先進理工系科学研究科

中西一貴

A. TABLE OF CONTENTS

B. ACKNOWLEDGMENTS

The studies in this thesis have been carried out under the direction of Assit. Prof. Dr. Rong Shang in the Department of Chemistry, Graduate School of Advanced Science and Engineering of Hiroshima University.

I wishes to express my appreciation to Prof. Yohsuke Yamamoto for developing my foundation as a researcher when I was a butcher and a master's student. I would like to thank Prof. Hiroto Yoshida for my co-author in his work and providing his knowledge of organic chemistry from April 2020 to March 2022. I am also deeply grateful to Prof. Tsutomu Mizuta to give me comprehension of coordination chemistry and for helping my Ph.D work from April 2022 to September 2023 for his encouragement to me. Also, I would like to appriciate to the students who have belong to their laboratory for my student's life.

I am also grateful to Assoc. Prof. Dr. Shoko Kume for valuable discussion of CV, and Assoc. Prof. Dr. Kenji Komaguchi and Assoc. Prof. Dr. Masaaki Nakamoto for their kind supports of EPR study. In addition, I would like to thank to Prof. Dr. Sadafumi Nishihara and his student, Mr. Jun Manabe for the SQUID measurement. I would like to thank to Prof. Dr. Takeharu Haino, Prof. Dr. Katsuya Inoue and Asssit. Prof Dr. Goulven Cosquer for helpful discussions

I wish my appreciation to my collaborator out of Hiroshima University. I would like to thank to Prof. Dr. Seiji Yamazoe and Assit. Prof. Dr Soichi Kikkawa (Tokyo Metropolitan University) for XANAS study. I really appreciate to Assoc. Prof J. Oscar C. Jimenez-Halla and his student, Leonardo I. Lugo-Fuentes (University of Guanajuato) for DFT calculation, critical suggestions, and valuable discussion. Plus, Prof. Dr. Miquel Solà (Universitat de Girona) and Dr. Dariusz W. Szczepanik for evaluation of metallaaromaticity by theoretical calculation.

I would like to appreciate to staffs in Hiroshima University, especially many thanks to Ms. Naomi Kawata, Ms. Tomoko Amimoto, and Mr. Hitoshi Fujitaka in N-BARD of Hiroshima University for their help on the X-ray analysis, HRMS study, and NMR techniques, respectively. Additionally, I am grateful to the staffs in the Department of Chemistry, Graduate School of Advanced Science and Engineering of Hiroshima University, to help my chores and financial managements.

This study was partly supported by the research grant of JST SPRING, JPMJSP2132 in my research and personal life from October 2021 to March 2023.

Finally, I am strongly grateful to my family and for their constant assistance, affectionate encouragement, and providing a very comfortable environment to concentrate on research.

C. ABSTRACT of Ph.D Thesis

Development of Iridium Metallacycles with Arylated Dipyrido-annulated Carbenes

Chapter 1 discussed the carbene species, a divalent neutral carbene species, which had been considered an intermediate in the field of synthetic chemistry owing to its high reactivity. Since fully characterized *N*-heterocyclic carbenes (NHCs), in which the empty p orbital of carbene carbon was diminished by π-donating from adjacent nitrogen atoms was reported in the 1990s, NHCs became a bench-handling chemical in the 21st century. Carbenes and their metal complexes have been widely used from laboratory scales for fundamental science to the extremely large ones in the industry because of the carbene's structural diversity and facile tuning of electronic and steric parameters. Recently, the research direction of carbene chemistry has been orientated to design to enhance the strong s-donating and π-accepting ability of carbene carbons originating from neighboring atoms or functional groups. In contrast, the are few examples of carbenes with π-donation, and their application has not been explored. In this thesis, we focused on the dipyrido-annulated carbene (dpa-NHC), which extends the carbene backbone with two aromatic ring fusions. The dpa-NHC chemistry was reported by only a couple of groups including us. Although the investigation of catalytic activity and luminescent behavior of phosphine-anchored dpa-NHC complexes was reported, their potential exhibition based on a π-rich system of arylated dpa-NHC has remained and the research question of this thesis.

Chapter 2 discussed the establishment of a synthetic method for the cyclization of arylated dpa-NHC to iridium centers as LX_2-type pincer ligands. Meridional tridentate NHC-based pincer ligands contribute to a substantial growth in modern organometallic chemistry in both homogeneous catalysis and luminescence materials. Among all NHC-based pincer ligands, dianionic LX_2-type CCC-pincer ones constitute the smallest sub-category owing to the limited ligand frameworks suitable for complexation. This work reports a one-pot, high-yield synthesis of a homoleptic anionic all-carbon bis-pincer Ir(III) complex directly from a bis(aryl)-substituted dipyrido-annulated (dpa^{Ar2}) imidazolium salt and $[Ir(cod)Cl]_2$ via a cascade of deprotonation/C-H activation processes. Both experimental complexation chemistry and computational mechanistic investigation suggest that the large bite angle

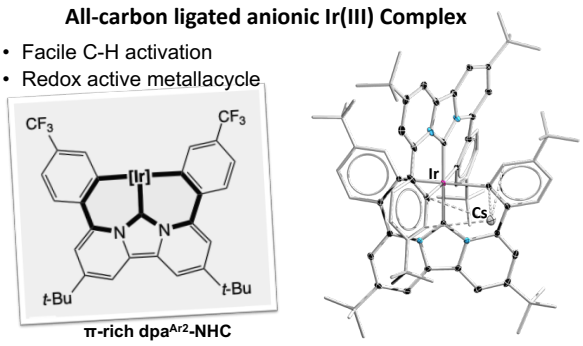

and π-rich character of the dpa^{Ar2}-NHC are responsible for its facile complexation as a dianionic LX_2-type CCC-pincer ligand precursor. The all-carbon ligated Ir(III) complex bearing a π-conjugated ligand scaffold showed remarkably low oxidation potentials, which allows future investigations in its redox chemistry and photophysical properties.

Chapter 3 discussed the oxidation behaviors of the newly synthesized anionic iridium complex with dpa-NHC based pincer ligands. Synthetic strategies to access high-valent iridium complexes usually requires use of π donating ligands bearing electronegative atoms (e.g. amide or oxide) or s donating electropositive atoms (e.g. boryl or hydride). Besides the h^5-(methyl)cyclopentadienyl derivatives, high-valent h^1 carbon-ligated iridium complexes are challenging to synthesize. To meet this challenge, this work reports the oxidation behavior of an all-carbon-ligated anionic bis(*CCC*-pincer) Ir^{III} complex. Being both s and π donating, the diaryl dipyrido-annulated *N*-heterocyclic carbene (dpa-NHC) Ir^{III} complex allowed a stepwise 4e$^-$ oxidation sequence. The first 2e$^-$ oxidation led to an oxidative coupling of two adjacent aryl groups, resulting in formation of a cationic chiral Ir^{III} complex bearing a *CCCC*-tetradentate ligand. A further 2e$^-$ oxidation allowed isolation of a high-valent tricationic complex with a ground triplet state. These results close a synthetic gap for carbon-ligated iridium complexes and demonstrate the electronic tuning potential of organic π ligands for unusual electronic properties.

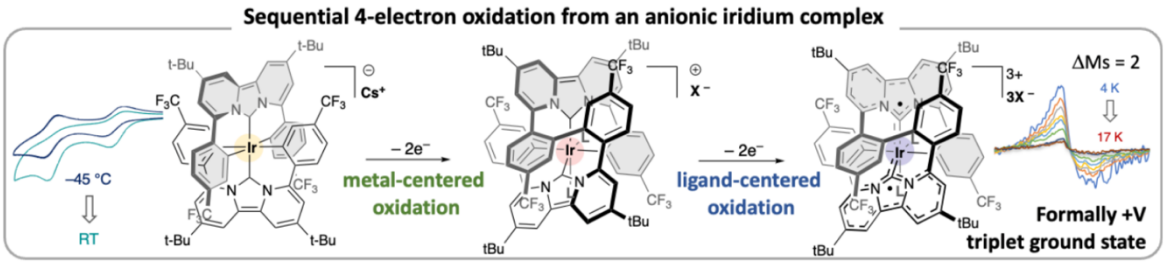

D. PUBLICATION LIST

Chapter 2

"Synthesis and Isolation of an Anionic Bis(dipyrido-annulated) N-Heterocyclic Carbene CCC-Pincer Iridium(III) Complex by Facile C-H Bond Activation"

Kazuki Nakanishi, J. Oscar. C. Jimenez-Halla, Seiji Yamazoe, Masaaki Nakamoto, Rong Shang, Yohsuke Yamamoto, *Inorg. Chem.,* **2021**, *60*, 9970-9976.

Chapter 3

"Redox Activity of Ir^{III} Complexes with Multidentate Ligands Based on Dipyrido-annulated N-Heterocyclic Carbenes: Access to High Valent and High Spin State with Carbon Donors"

Kazuki Nakanishi, Leonardo I. Lugo-Fuentes, Jun Manabe, Soichi Kikkawa, Seiji Yamazoe, Kenji Komaguchi, Shoko Kume, Dariusz W. Szczepanik, Miquel Solà, J. Oscar C. Jimenez-Halla, Sadafumi Nishihara, Kazuyuki Kubo, Masaaki Nakamoto, Yohsuke Yamamoto, Tsutomu Mizuta, Rong Shang, *Chem. -Eur. J,* **2023**, *Accepted, e202302303.*

E. LIST OF ABBREVIATIONS

Abbreviations	Definitions
AB	ammonia borane
acac	acetylacetonate
AFOE	anisotropic field oxidation enhancement
APCI	atmospheric pressure chemical ionization
Ar	aryl
ArF	3,5-bis(trifluoromethyl)phenyl
BIMe	*N,N*-dimethylbenzoimidazolylidene
BNC	*B,N*-heterocyclic carbene
Bpin	pinacolato boryl
BTPA	bis(diisopropylthiophosphoryl)amide
CAAC	cyclic alkyl amino carbene
CMA	carbene metal amide
cod	1,5-cyclooctadiene
COSY	correlation spectroscopy
Cp	cyclopentadienyl
Cp*	pentamethylcyclopentadienyl
CV	cyclic voltammetry
DFT	density functional theory
Dipp	diisopropylphenyl
DMAP	*N,N*-dimethylaminopyridine
DME	1,2-dimethoxyethane
DMF	*N,N*-dimethylformamide
DMSO	dimethyl sulfoxide
EDDB	electron density of delocalized bonds
EPR	electron paramagnetic resonance
ESI	electronic spray ionization
Et	ethyl
Fc	ferrocene
HMBC	heteronuclear multiple-bond correlation spectroscopy
HMDS	hexamethyldisilazamide
HMQC	heteronuclear multiple quantum correlation
HOMO	highest occupied molecular orbital
HRMS	high resolution mass spectroscopy
IAd	*N,N*-diadamantylimidazolidene
IBO	Intrinsic bond orbitals
IMes	*N,N*-dimesitylimidazolylidene
INT	intermediate
IPr	*N,N*-bis(diisopropylphenyl)imidazolylidene
I*t*Bu	*N,N*-di-tert-butylimidazolylidene
IXy	*N,N*-bis(2,6-dimethylphenyl)imidazolylidene
LUMO	lowest unoccupied molecular orbital
Me	methyl
Mes	mesityl
MO	molecular orbital
MR	membered ring

NBO	natural bond orbital
NHC	*N*-heterocyclic carbene
NICS	nucleus independent chemical shift
NIR	near infrared
NLMO	natural localized molecular orbital
NMR	nuclear magnetic resonance
NOESY	Nuclear Overhauser effect spectroscopy
NOHC	N-oxyl heterocyclic carbene
OAc	acatate
OLED	organic light-emitting diiode
OTf	triflate
PAH	polycyclic hydrocarbon
Ph	phenyl
pin	pinacolato
SCXRD	single crystal X-ray diffraction
SIMes	N,N-dimesity-4,5-dihydro-limidazolylidene
SIPr	N,N-bis(diisopropylphenyl)-4,5-dihydro-imidazolylidene
SOMO	single occupied molecular orbital
SQUID	superconducting quantum interference device
ST	singlet-triplet
t-Bu	tert-butyl
TADF	thermally activated delated fluorescence
TBA	tetra-*n*-butylammonium
TCNQ	tetracyanoquinodimethane
TD-DFT	Time dependent density functional theory
TEP	Tolman's electronic parameters
THF	tetrahydrofuran
THT	tetrahydrothiophene
TS	transition state
UV	ultraviolet
Vis	visible
VT	variable temperature
XANES	X-ray absorption near-edge stature
XPS	X-ray photoelectron spectroscopy

F. LIST OF COMPOUNDS

【Chapter 1】

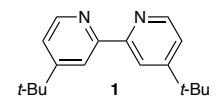

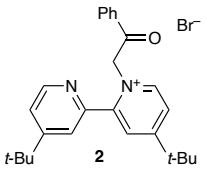

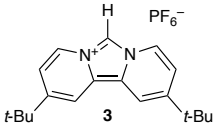

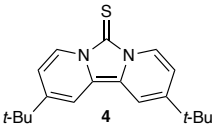

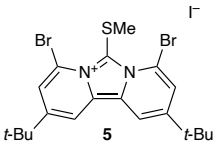

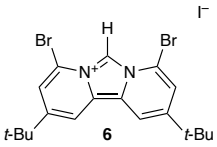

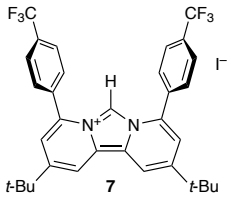

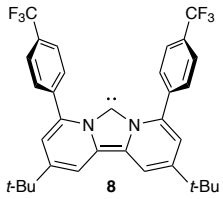

【Chapter 2】

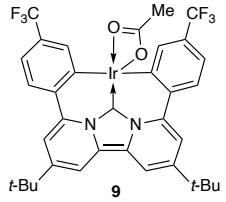

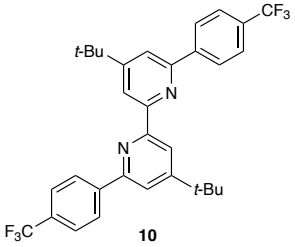

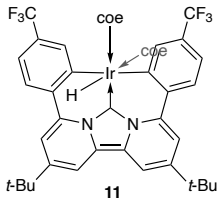

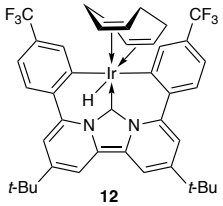

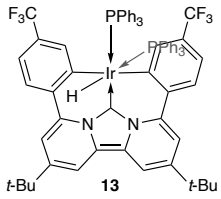

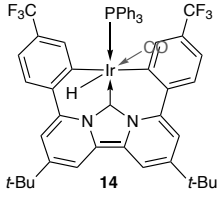

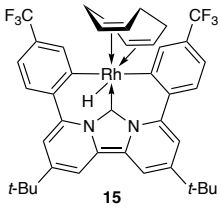

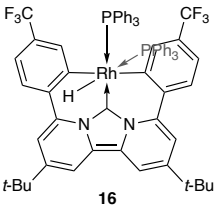

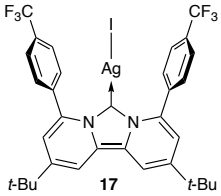

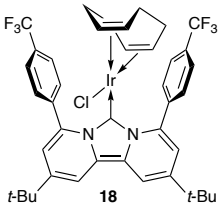

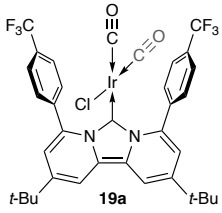

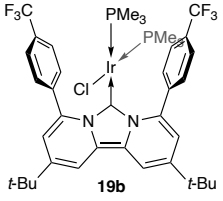

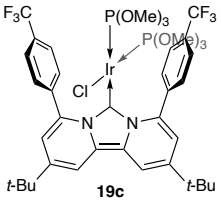

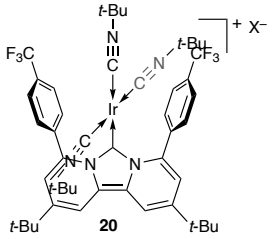

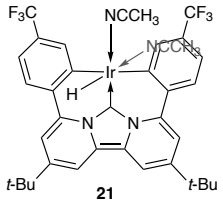

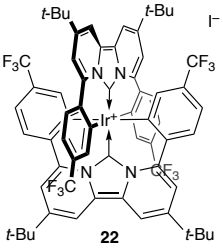

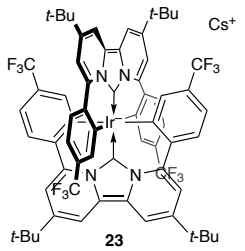

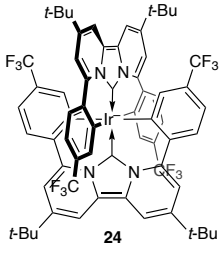

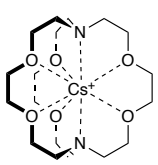

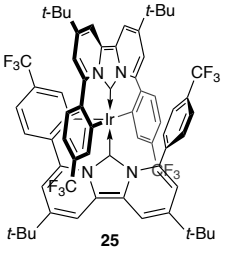

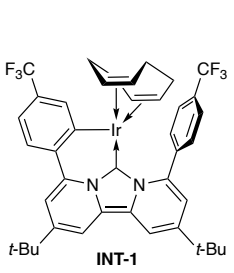

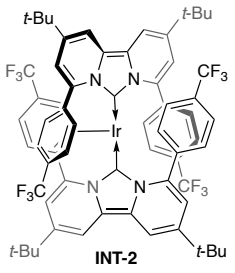

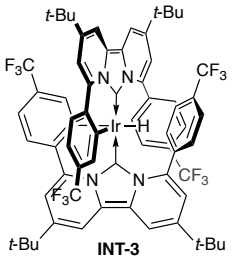

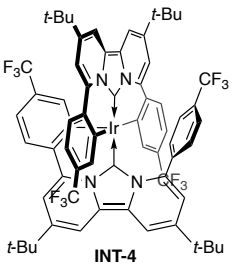

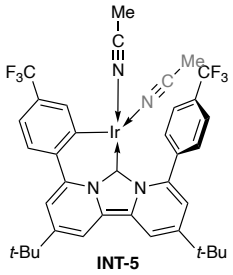

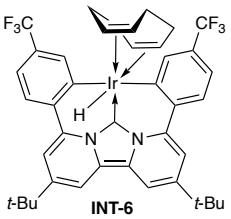

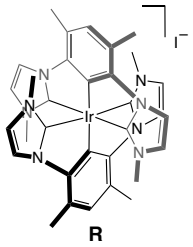

【Chapter 3】

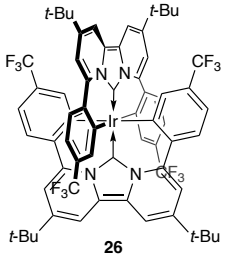

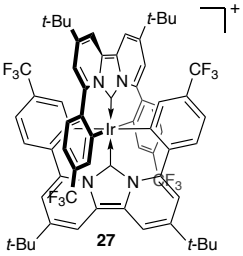

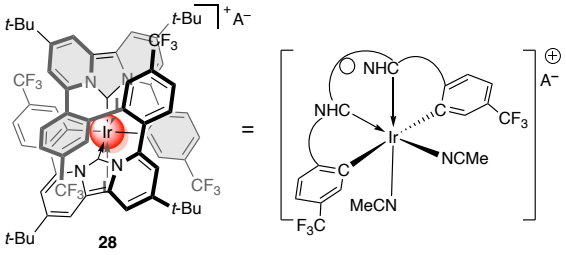

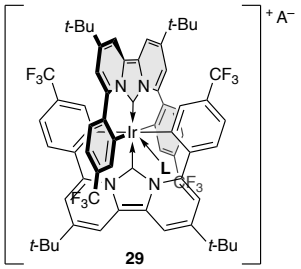

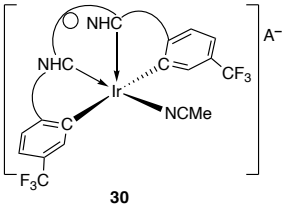

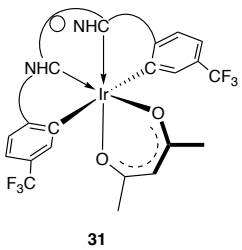

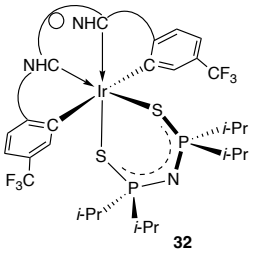

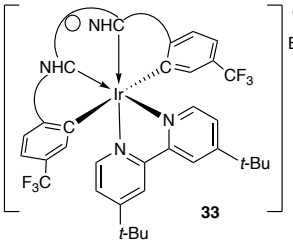

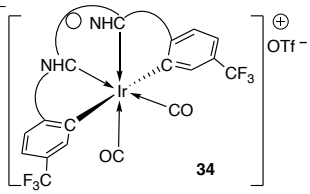

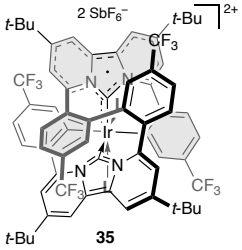

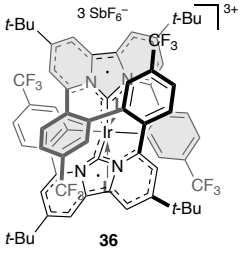

G. LIST OF TABLES

H. LIST OF FIGURES

I. LIST OF CHART

CHAPTER 1.
GENERAL INTRODUCTION

1.1. Carbenes and their complexes

The term 'carbene' refers to chemical species of neutral carbon(II) with six electrons, which is isolobal to neutral boranes. This makes them highly electron-deficient species and, therefore, highly reactive. Carbenes can adopt a single or a triplet state depending on how electrons occupy the orbitals. Singlet carbenes have occupied sp^2 and empty p orbitals because of the different energy levels between sp^2 and p orbitals. Whereas there are two half-filled p orbitals obeying Fund's rule for triplet carbenes[1]. On the other hand, A long history of continuous effect has been put in the synthesis and isolation of these species[2].

Carbenes are widely used as ligands in organometallic chemistry. Earlier studies by Fischer and Schrock led to the isolation and characterization of metal-stabilized carbenes corresponding to singlet and triplet states called "Fischer's carbene"[3] and "Schrock carbenes"[4], respectively. (Figure 1.1.) Fischer carbene complexes have been prepared by the electrophilic attack of carbon atoms in M–C≡E (E = O or N–R). late transition metal elements favor Fischer's carbenes owing to the high electronegativity and filled d-orbitals lower in energy., Because of the singlet carbene character, these Fischer carbenes work as both σ-donating and π-accepting ligands, and M–C bonds consist of the covalent bonds. Additionally, the lone pair of adjacent heteroatoms stabilize their carbene moieties. (Figure 1.1.A)

By contrast, deprotonation of α-elimination of alkyl groups on the earlier transition metal center has provided the Schrock carbene complexes. Alternatively, the diazomethane derivatives or dichrolomethylbenzene as carbene precursors are available[2] The M–C bonds are considered as covalent double bonds., Thus, carbene centers show nucleophilic natures as well as weak σ and strong π-acceptors. Schrock carbenes also refers to high-oxidation-state earlier transition metal alkylidene complexes, which often shows nucleophilic carbene reactivity (Figure 1.1.B)

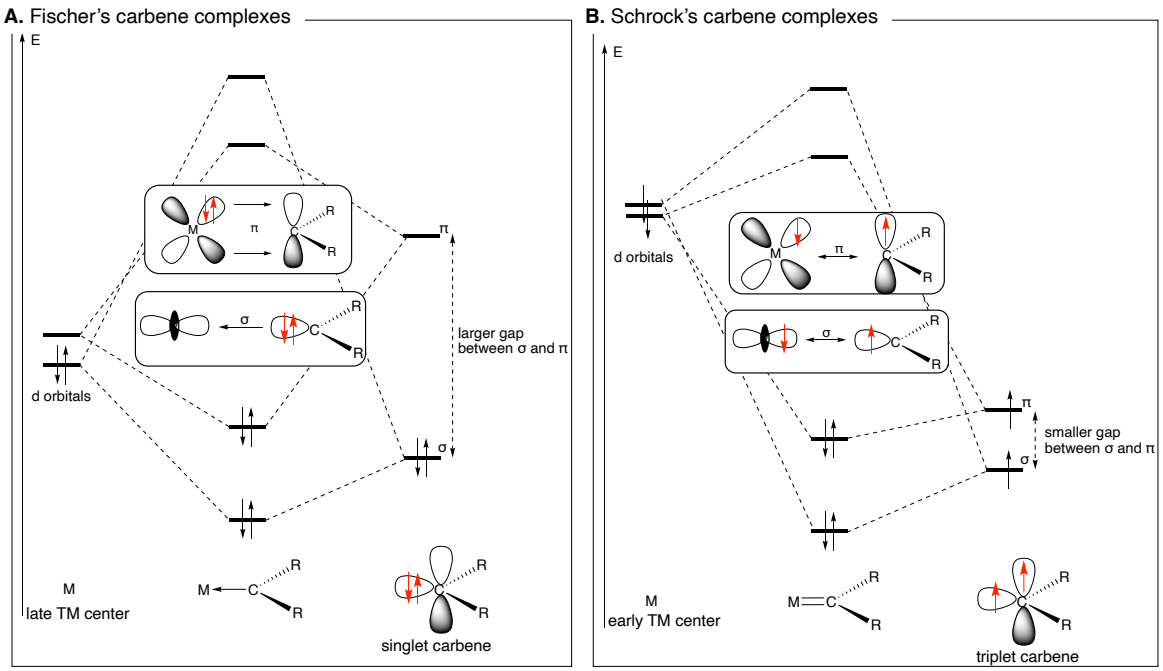

Figure 1.1. Bonding of Fischer and Schrock carbene complexes.[5]

1.2. N-Heterocyclic carbenes and their analogs

In 1988, Bertrand reported the first isolable free carbene that had silyl and phosphonyl bulky substituents[6] (Figure 1.2.A). Three years later, Arduengo successively isolated and fully characterized N-heterocyclic carbenes (NHCs, Figure 1.2.B and C)[7], which led to a rapid expansion in various fields of synthetic chemistry. The origin of stabilizing carbenes is a large contribution to the resonance structure of ylide. These breakthroughs provided an effective strategy, from which hundreds of thermally stable carbene were synthesized, isolated and fully structurally characterized. In the 1990s, for example, Arduengo also reported NHCs with saturated backbone, which demonstrated that aromatic stabilization was independent for isolable carbene[8]. In addition, Alder fully characterized the acyclic diamino carbenes[9], which expanded the designs of carbene significantly

In the 2000s, Bertrand reported that *N, C*-heterocyclic carbene (also called CAAC) was successively isolated, which has higher σ-donating and π-accepting properties than those of NHCs.[10] This is because of the replacement of nitrogen with more electropositive sp^3 carbon, is more σ-donating, and thus increases the σ-donating ability of the carbene carbon. Since only one π-donating amino group is left by the carbene center, the π-stabilization is reduced significantly, leaving the carbene center highly π-acidic. (Figure 1.2.D.) The push-pull style carbene could be prepared when the electropositive atoms were employed. For instance, Baceiredo reported the synthesis and isolation of a *B, P*-acyclic carbene[11]. The electron-deficient boron moiety serves as a π-acceptor to the carbene carbon in view of the donor-accepter interaction in the NBO analysis. Indeed, the precursor has a stronger interaction with adjacent nitrogen, reflecting the significantly shortened P–C bond distance (1.634(3) to 1.563(13), Figure 1.2.E.)

More recently, the structural diversity of carbene has developed rapidly in the last five years. Recent carbene chemistry revealed the introduction of transition metal atoms in the carbene frameworks. When the electron-rich late transition metal atoms such as Rh(I)[12] and Au(I)[13] were introduced to neighboring carbene carbon. The inclusion of a base metal fragment has been shown to increase the nucleophilicity of the carbene carbon enhanced owing to the electronic repulsion between lone pairs on carbene carbon and filled d-orbitals of the metal center, illustrated by NLMO and MOs compared with the H and Si substituted carbenes[13] (Figure 1.2.F).

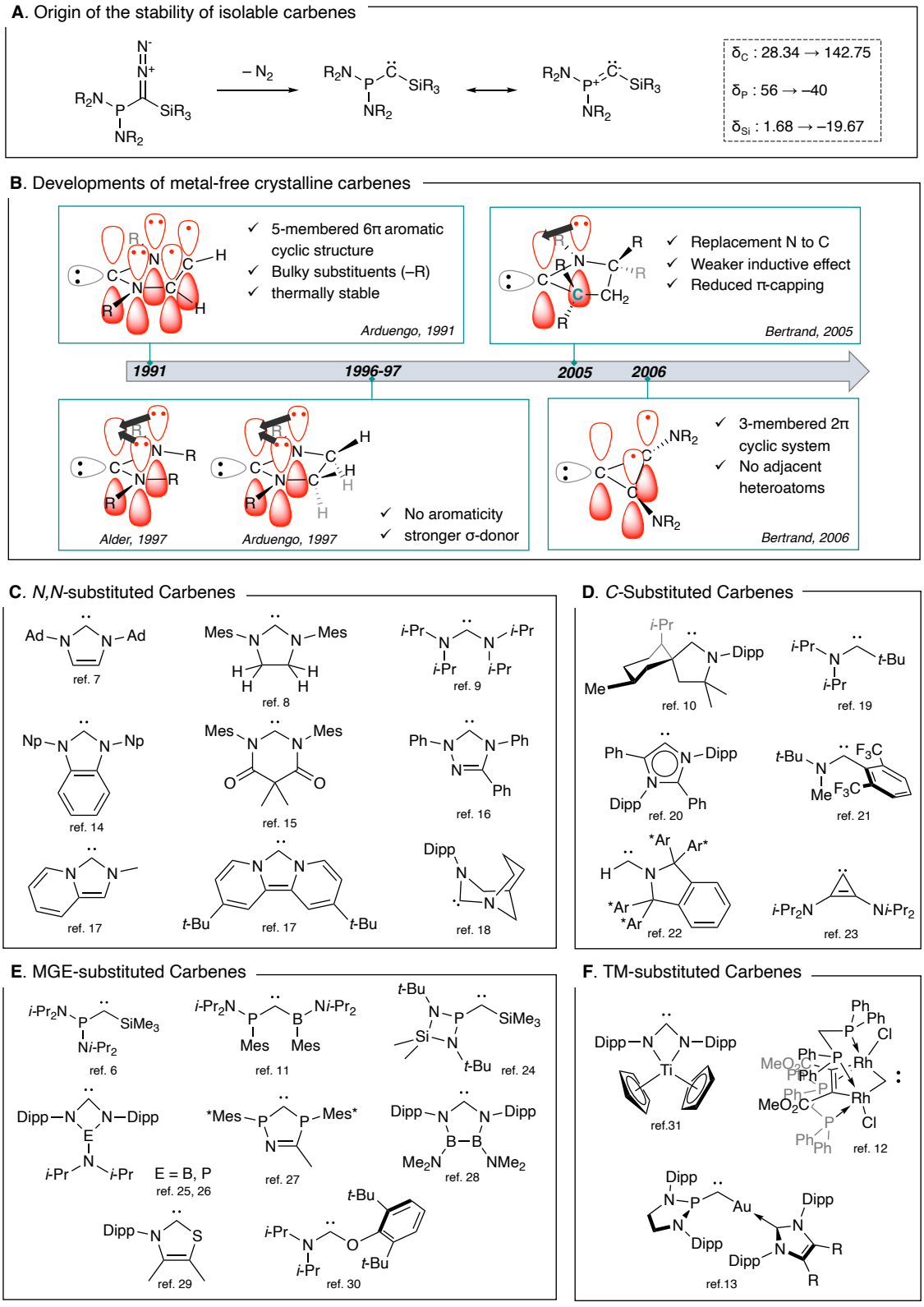

Figure 1.2. Selected examples of crystalline carbenes. [6,7,18–27,8,28–31,9,10,13–17]

1.3. Application of NHCs in synthetic chemistry

In comparison with the Fischer and Schrock carbene complexes, NHC takes advantage of using as a ligand. These varieties of carbenes made chemists strategize the designs of carbenes in view of the electronic and steric controls with the several factors of Backbone, ring size, neighboring atoms, and their substituents. (Figure 1.3 A). Taking the donating/accepting ability into account, atoms adjacent to carbene carbons are an important factor in determining both σ-donating and π-accepting ability based on the electronegativity of the atoms and (hyper)conjugation.

These electron properties were reflected in bond distances of both carbon-boron and boron-boron bonds in the solid-state structure of carbene-stabilized diboryne[32] (Figure 1.3.B). In the case of the IPr, The bond distance of both C–B and B–B bonds were 1.487(3)/1.495(3) Å and 1.449(3) Å, respectively. When the SIPr, which has a slightly strong π-accepting ability, was employed, the C–B bond was somewhat shortened (1.480(2)/1.482(2) Å), whereas the B–B bond elongated to 1.465(2) Å. Furthermore, the ^{Me}CAAC ligand made this length changes more remarkable. These experimental results imply that the π-accepting nature of the carbene carbon got enhanced the multiplicity of C–B bond and reduced that of B–B bond in diboryne species. In addition, their frameworks take control of electronic properties. For example, electron-withdrawing substituents such as cyano or chloro groups reduced σ-donating nature and enhanced π-accepting properties.

The steric factor is critical to the various selectivity in catalysis and the kinetic stabilization preventing dimerization. For instance, The steric parameter reflected the regioselectivity for copper-catalyzed borylation of terminal alkynes (Figure 1.3.C)[33]. When IMes was employed as a ligand for the copper complex, the trans-isomer was obtained as a major product, whereas when the Dipp substituted NHCs was used, the cis isomer was obtained as a major product. Other control of the steric parameters, such as a change to a 6-membered NHC improved yields and selectivity. One particular useful steric parameters is percent buried volume (V_{bur})[34], which can be estimated computationally.

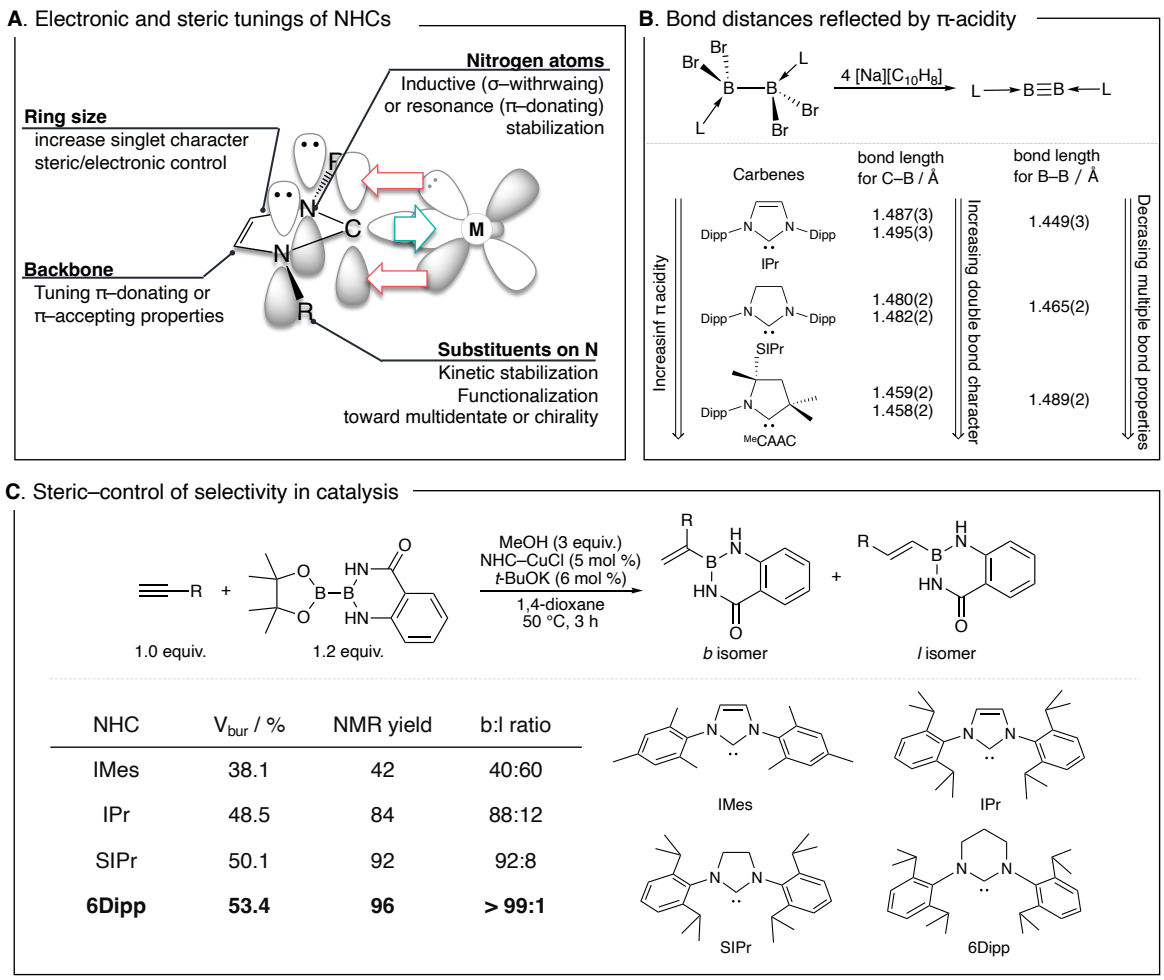

NHC	V_{bur} / %	NMR yield	b:l ratio
IMes	38.1	42	40:60
IPr	48.5	84	88:12
SIPr	50.1	92	92:8
6Dipp	**53.4**	**96**	**> 99:1**

Figure 1.3. steric and electronic control of carbene derivatives

The high tunability of carbene as ligands to metal complexes enabled their wide applications in various fields. (Figure1.4). In homogeneous catalysis, carbenes have stronger donating properties and steric bulkiness, which enhance the oxidative addition and reductive elimination process, respectively. Because of this, carbene complexes have been found to be highly efficient catalysts in various reactions such as cross-coupling reactions, olefin metathesis, C–H functionalization, cyclization, and polymerization. Recently, carbenes themselves have been shown to work as catalysts, used for the functionalization of aldehyde via (aza)benzoin condensation, Stetter reaction, azonium substitution, cycloaddition[1].

Besides wide applications in homogeneous catalysis, carbenes also have been used in luminescent materials for 20 years. Carbene's strong donation disfavored metal-centered transitions that are responsible for quenching the luminescent pathway. More recently, highly π-accepting carbenes such as CAACs, and amide-carbenes were able to work as electron-accepters in the carbene metal amide (CMA) complexes. The experimental and theoretical investigation of the luminescent mechanism of the CMA complexes revealed the thermally activated delay

fluorescence (TADF) process[35–39]. These short-lifetime luminescent materials are good candidates for organic light-emitting diodes (OLEDs)

In addition to organometallic molecular chemistry, carbenes are also used in nanoparticles and nano-cluster materials, a rapidly expanding field. The facile and fine control of electronic and steric factors allows systematical screening for suitable conditions for desired structures, functions, and stability in heterogeneous catalytic reactions.

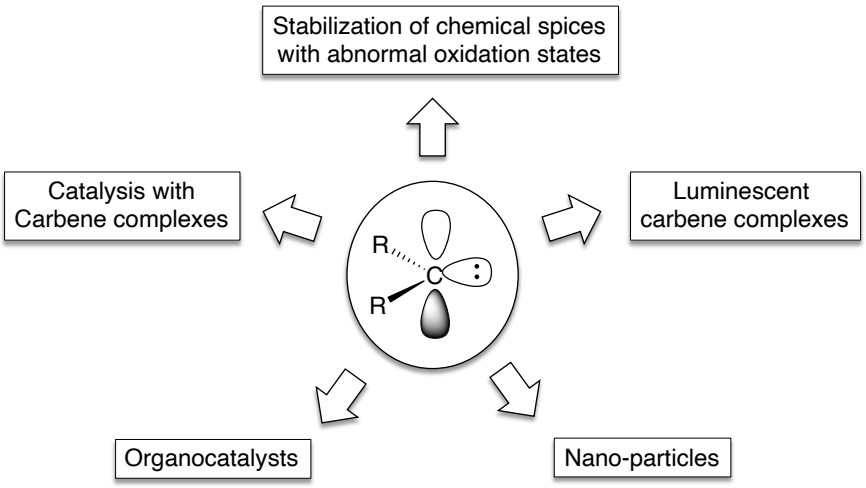

Figure 1.4. Application of carbene in synthetic chemistry

In the fundamental aspect of molecular structure and bonding, carbene played a crucial role in stabilization of chemical species of unusual oxidation state, particularly low-valent main-group element species[40,41]. The bonding between carbene and main-group elements can be considered as a donor-accepter type dative bond, firstly described by Frenking[42]. A typical example is Arduengo's NHC. In contrast, when strong π-acidic carbenes such as CAAC were used with lighter and high electropositive elements such as boron or beryllium, the carbene-element bonds are often found covalent in nature with multiple bond characters. (See Figure 1.5) Currently, the library of isolable and fully characterized main-group element species with formal low oxidation states of 0 or I are rapidly growing. This new class of compounds shows versatile reactivity towards small organic substrates, including H_2, CO, CO_2 N_2O, N_2, and O_2, which is a mimic of transition metal complexes[43].

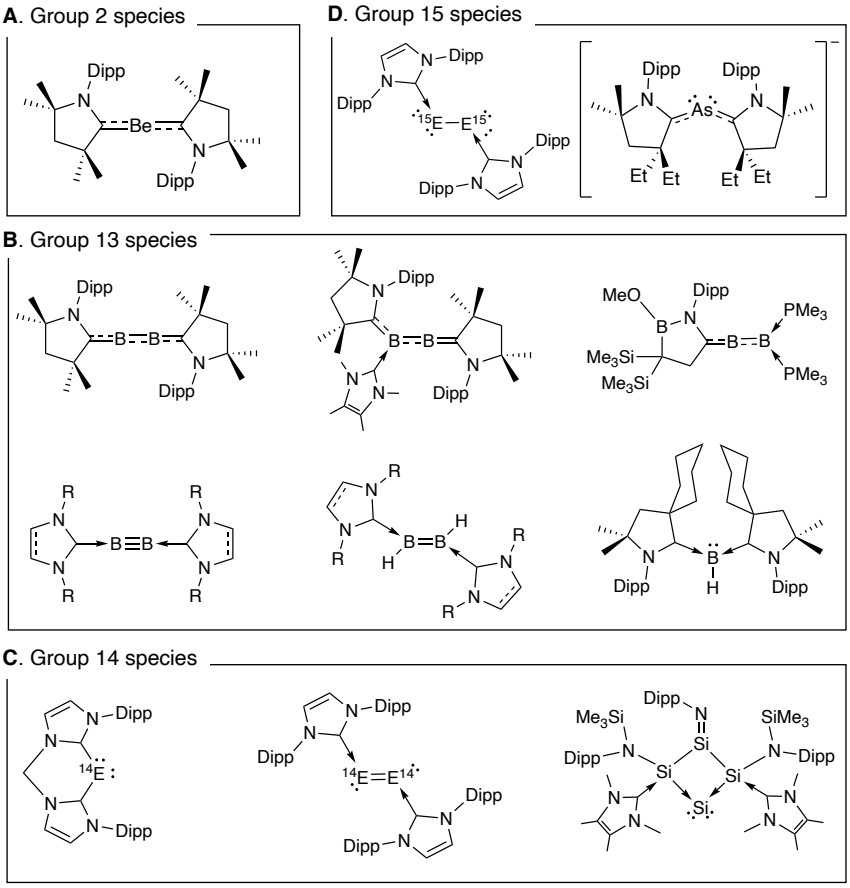

Figure 1.5. Selected examples of fully carbene-stabilized low-valent main-group element species that were selected in the ref. 41. All compounds were fully characterized.

In addition to stabilizing the low-valent species, carbene derivatives have been used to stabilize in the field of high-valent transition metal complexes because of the strong coordination toward the metal center and their availability of the designable multidentate ligands. In general, 3d-transition metal compounds are difficult to access the high valency because they have higher third and fourth ionization enthalpies in comparison with the corresponding 4d and 5d metals. In addition, smaller orbitals size caused Pauli repulsion between 3s/3p orbitals of metal elements and their ligands. To stabilize the 3d-metal complexes with a high oxidation state, electronegative atoms such as halogen, oxygen, and nitrogen were employed to form X-type bonds plus π interaction toward the metal center. The role of NHCs in this field is to support the multiple bonds, which is explained by theoretical calculation[44].

In the view of the electronic properties, the σ-orbitals in NHCs, as a HOMO, are stronger electron-donating ability and lie higher in energy than nitrogen or oxygen-based ligands. Additionally, the more diffused σ-orbitals are, the more effective the overlapping between the metal center and NHC fragments can be[44]. Indeed, the bidentate and tridentate NHC ligands allowed to access and isolate high valent 3d metal complexes (Figure 1.6 A)[45–49]. In contrast to

3d metal complexes, 4d and 5d transition metals are unfavored in high oxidation states, owing to the high electronegativity and unfavorable half-filled d-orbitals, especially late transition metal elements, the high valent complexes mostly have halide ligands (Figure 1.6 B[50,51] and C[52–54]).

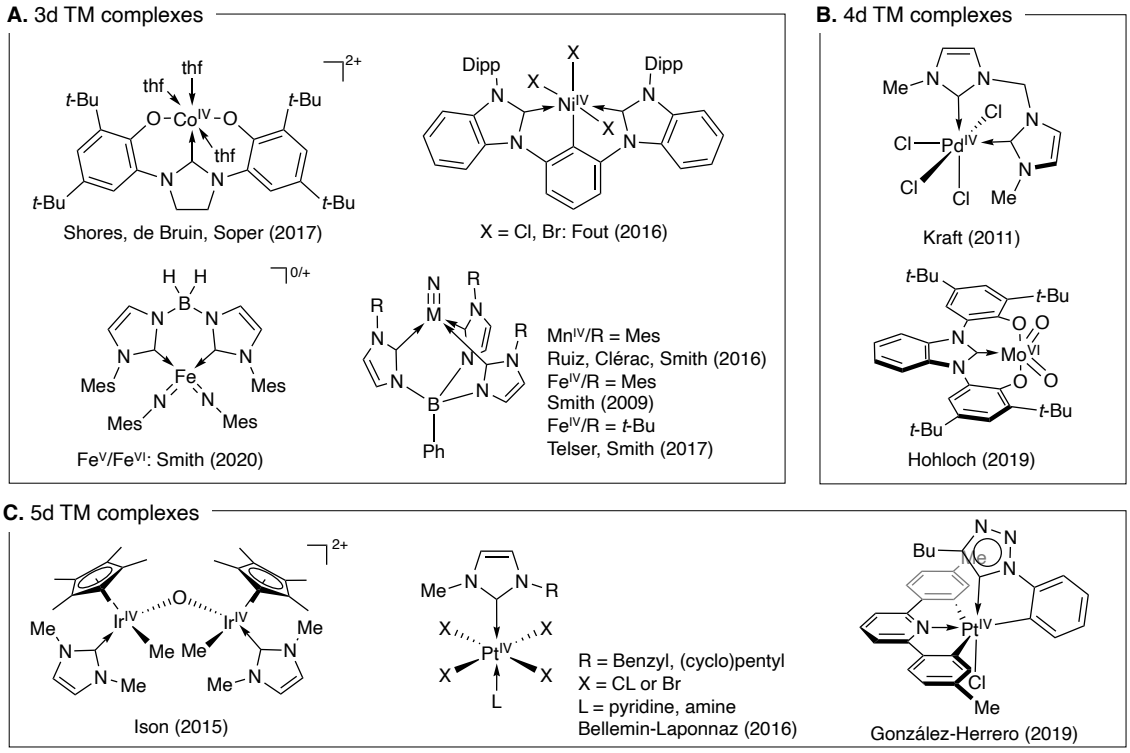

Figure 1.6. Selected examples of transition-metal NHC complexes with high oxidation states[45]

However, owing to the highly electron-deficient nature, the π-acidity of carbene affected the decomposing pathway[44]. For example, Figure 1.7.A illustrated Cl ligands in *cis* positions were able to interact with carbene's empty p-orbitals, which led to the dissociation of the NHC fragments from the metal centers. An example of this decomposition route can be found in Sack's copper(I) NHC complex. Upon chemically induced oxidation by SelectFluor, DFT studies showed the energetically favorable formation of the [Cu(III)FCl(NHC)(MeCN)]+ intermediate, which decomposes rapidly from the nucleophilic attack from the halide to the electrophilic carbene center to yield the experimentally observed halogenated imidazolium salts (Figure 1.7.B)[55].

Besides halogens, other electron-rich ligands can also insert between the carbene and metal fragments. Meyer systematically established the iron or cobalt azido complexes bearing tris- or bis NHC anchored amine ligands[56,57]. Their ligands effectively covered the M–N_3 fragments. Their theoretical calculation illustrated that SOMO of the terminal nitrido complex, which was generated by light-induced dinitrogen, had the interaction between lone pair of nitrido and carbene's p-orbital. This N-migratory insertion had a remarkably low activation barrier ($\Delta G^{\ddagger}$ = 1.2 kcal/mol), Interestingly, the C–H activation process, which is one of the most common decomposing pathways

for carbene complexes, had a higher activation energy (ca. 10 kcal/mol higher in energy) by comparison (Figure 1.7 C) .[56]

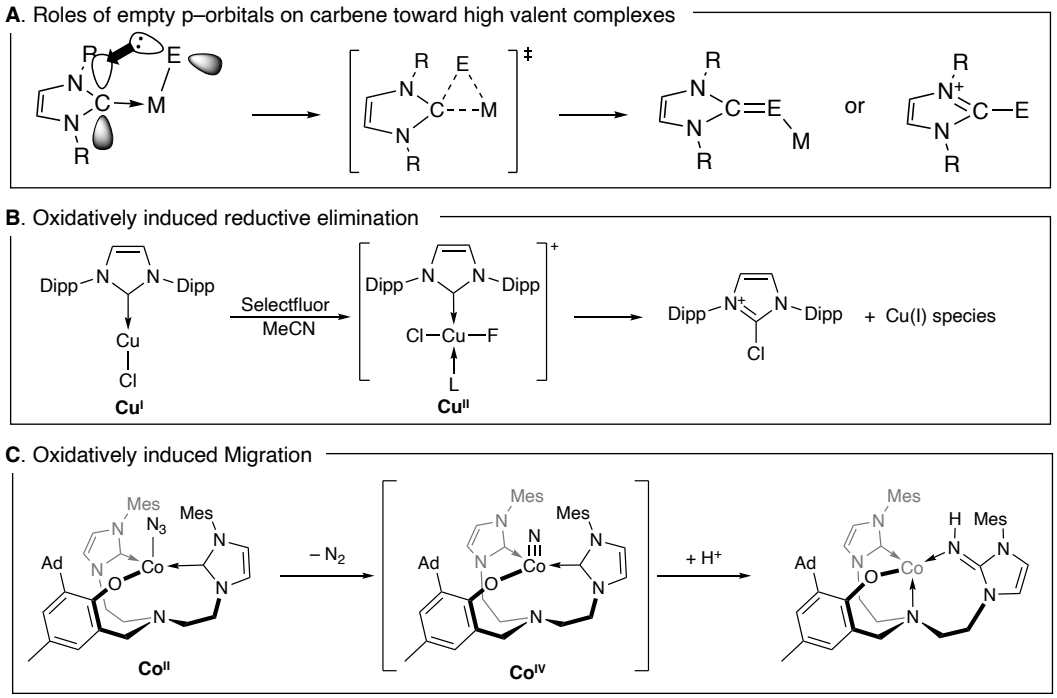

Figure 1.7 Disadvantages of carbenes toward stabilization of high valent transition metal complexes

1.4. π-Donating carbene ligands

Owing to the empty p orbital, singlet carbene as ligands are often evaluated as a π-acceptor. As mentioned above, the π-accepting ability of carbene is used to stabilize the low-valent main-group element species; however, it causes the decomposition of high-valent transition metal complexes. A fundamental question that is interesting to us is whether carbenes can be π rich. If so, what chemical and physical properties do these π-rich carbenes offer?

Currently, there are three strategies to increase the π-donation of NHCs. One is pushing the π-electrons from nitrogen atoms to the empty p orbitals of carbene carbons by neighboring atoms. Schreiner reported an example: substituents on the nitrogen of NHCs have an alcohol group (NOHCs). The lone pairs on oxygen pushed the π-donation, resulting in strong π-donation on carbene. These natures were confirmed by NMR spectroscopy with selenium adducts and gold complex as well as free NHCs. Note that NHC-selenium adducts having highly bulky substituents such as adamantyl and *tert*-butyl groups show large shifts to lower magnetic fields in ^{77}Se NMR spectroscopy owing to the non-classical hydrogen bonding with the selenium.[58] Considering that it could be said that NOHCs have stronger π-donation compared with Arduengo's NHCs (Figure 1.8).

A. Concept of the NOHCs

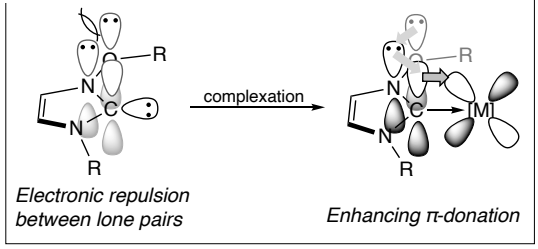

B. NMR chemical shift of the NHCs and NOHC

NHCs	δ_C (free NHC)	δ_{Se} (NHC=Se)	δ_C (NHC–AuCl)
IMes	219.7	27	173.4
IPr	220.6	90	175.1
IAd	211.4	197	166.3
^{Me}I*i*Pr	205.9	–18	168.4
^{Me}NOHC	203.9	201	165.8

Figure 1.8. Strong π-donation character of NOHCs and NMR spectroscopic data for the evaluation of π-donors[59].

The second example reported by our group is a 2-electron reduction of a *B, N*-heterocyclic carbene (BNC) at an Au(I) complex. Tri-*tert*-butyl-azadiboriridine was employed as a ligand precursor toward Au(I) centers. Complexation of Tri-*tert*-butyl-azadiboriridine yielded the three different products depending on the co-ligand on Au(I) precursors[60]. In the case of the phosphine-coordinated Au(I) complex with Tri-*tert*-butyl-azadiboriridine, the trivalent boron had Lewis acidity, which allowed the insertion of isocyanide between Au and B. This insertion provided the five-membered heterocyclic anionic BNC on Au(I) center. Looking at it from another perspective, neutral BNC coordinates to the Au(I) center, illustrating the remarkable low magnetic field shift of $^{13}C\{^1H\}$ NMR (δ_C = 251.3 ppm) By the reduction with elemental lithium in DME, the 2-electron reduction took place on BNC ligand. The solid-state structure of the reduced BNC complex revealed that the Au–C bond distance was dramatically shortened (2.064(3) Å to 2.017(3) Å). The NBO and IBO analysis illustrated that the lone pairs were on the two nitrogen atoms and one carbon atom. This BNBNC

five-membered ring showed 6π aromaticity, supported by NICS calculation. Owing to the localized lone pair on carbene carbon, the 6π-BNC ligand had strong π-donation, reflecting the shorting Au–C bond distance (Figure 1.9)[61].

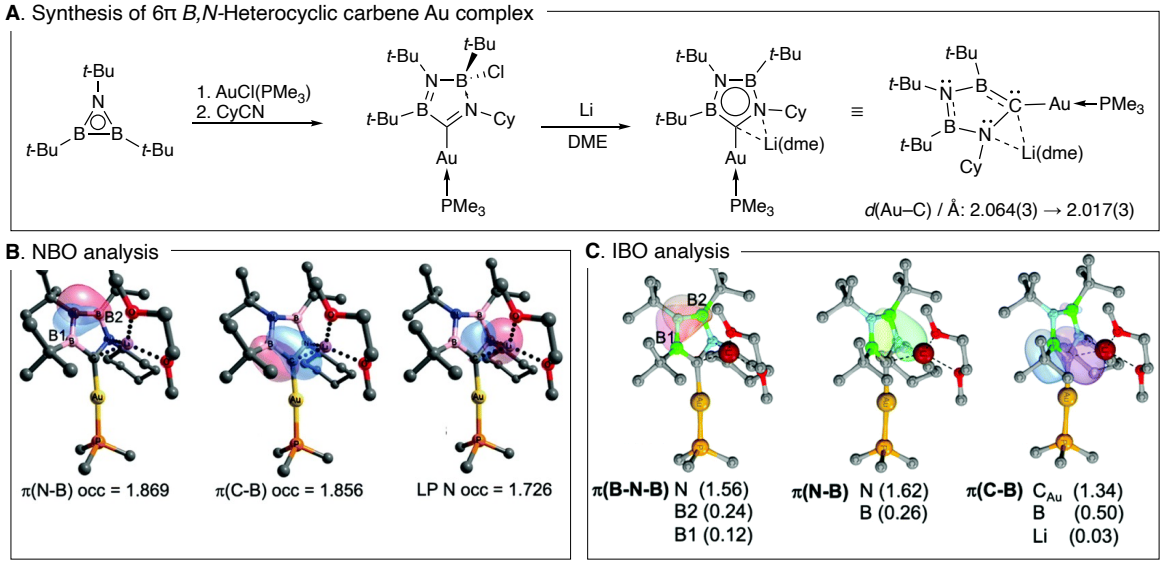

Figure 1.9. Synthesis and DFT-based bonding description of the *B, N*-heterocyclic carbene gold complex

The last strategy is the annulation of NHC rings, increasing the energy of π-orbitals via the expansion of conjugation. This nature was theoretically demonstrated that HOMO of dpa-NHC is a π orbital delocalized on the π orbitals over carbene carbon and its backbone, whereas the in-plane σ-orbitals corresponding to the lone pair of carbene constitutes s become HOMO–1 (Experimental investigation was conducted with Tolman's electronic parameters (TEP), *vide infra*). This is opposite to those observed on for a typical NHC (see Figure 1.11.) This is opposite to those observed on a typical NHC, suggesting π-donating character. According to Phukan's calculation results, the dpa-NHC theoretically suggested the highly carbone nature compared with the typical NHC derivatives[62]. The term "carbone" indicates the carbon(0) species bearing two dative bonds, such as phosphine and carbenes. For example, $^{13}C\{^{1}H\}$ NMR signal of carbene carbon was observed over 200 ppm in Arduengo's NHC, whereas much higher magnetic field shifted signals for carbone species were reported, such as a hexaphenylcarbodiphosphorane (δ_C = 13.4)[63] and carbodicarbene with two BIMe ligands (δ_C = 110.2 ppm)[64]. It is notable that dpa-NHC is working the same as Arduengo's NHCs, although they have the larger contribution of hidden carbone nature than those of NHCs.

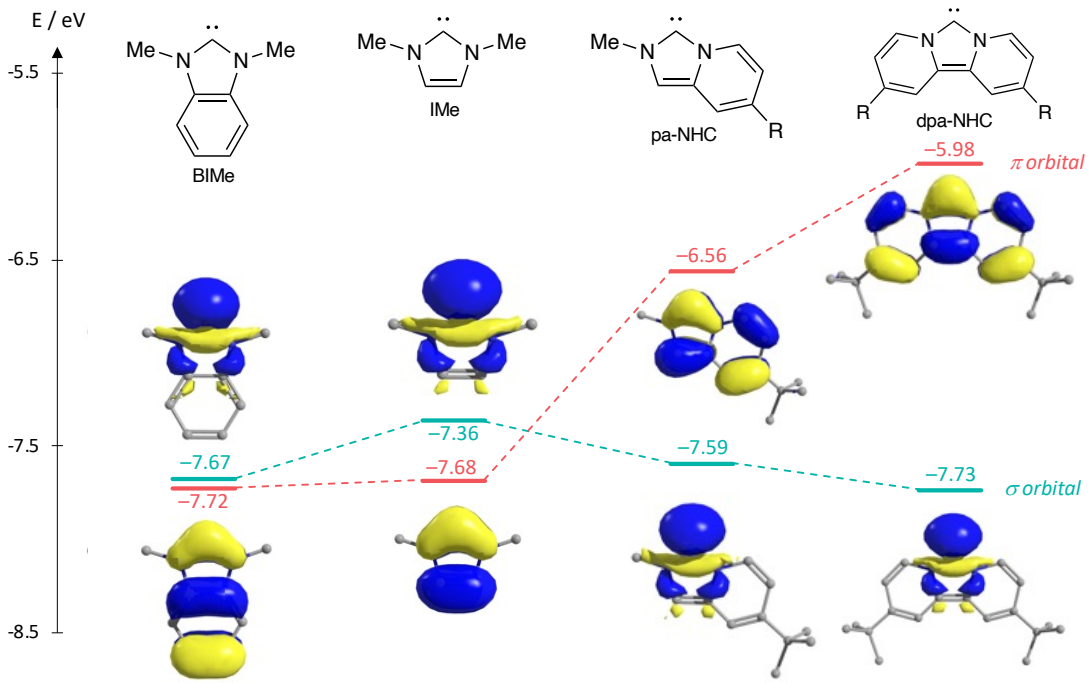

Figure 1.10. Molecular orbitals of free NHCs. These were calculated in the level of theory for M05-2X/6-311G(d,p).

The parent dpa-NHC was first reported by Weiss[65]. Their synthetic route was the cyclization of bipyridine using arsenic ylide with a release of triphenyl arsine. The imidazolium salt was deprotonated with *t*-BuOK at –30 °C *in situ* generations in which $^{13}C\{^{1}H\}$ NMR indicated a signal at δ = 196.41. The free carbene was trapped by selenium to yield C=Se species. This paper said that the dpa-NHC could work as both electron-acceptor and electron-donor moieties(Figure 1.11. C). The dpa-NHC chalcogen adducts were investigated by CV, indicating that the first oxidative waves were observed around 0.3 V (vs Fc/Fc^{+}). The SOMO of 1-electron oxidized the dpa-NHC sulfur adduct was delocalized in both π-orbital of dpa-NHC and p-orbital sulfur moieties, describing the resonance structures of 13π elections in Figure 1.11 C. However, the chemical oxidation of these species has not been achieved yet[66].

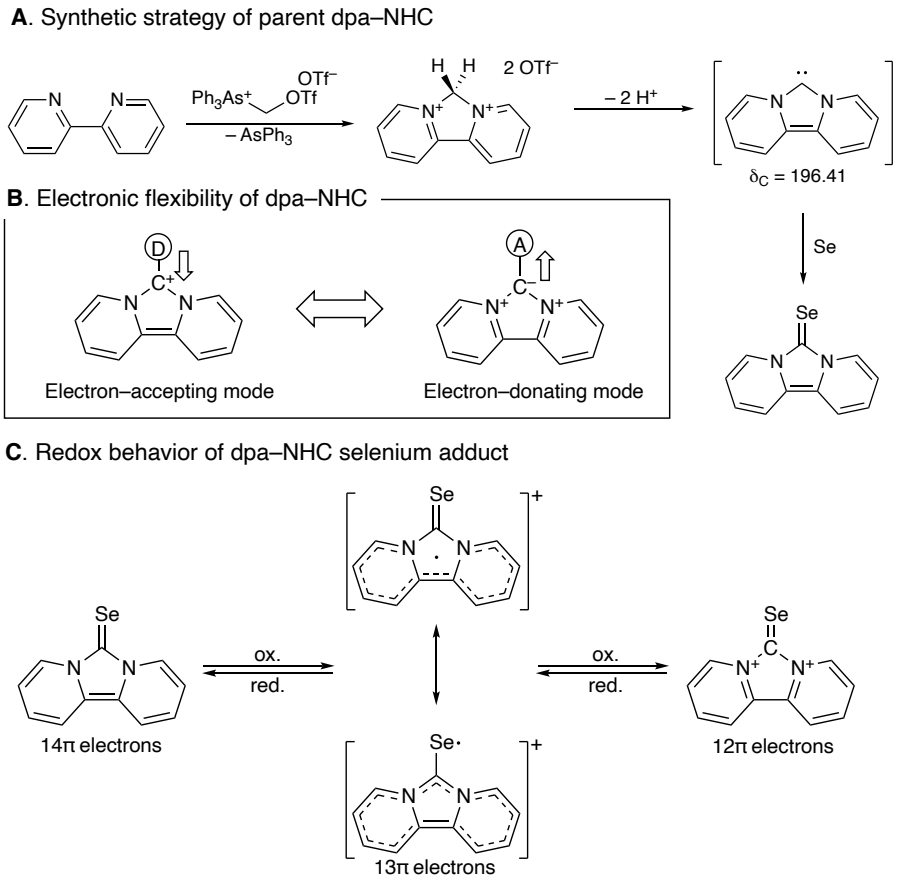

Figure 1.11. Synthesis and reactivity of the parent dpa-NHC reported by Weiss.

A couple of years later, Kunz reported the dpa-NHC as a ligand toward organometallic complexes[67]. She reported the complexation of parent and 2.10-di-*tert*-butyl dpa-NHCs to various transition metal fragments such as $M(CO)_5$, (M = Cr or W)[67], CuI[68], Rh(I)[68,69], and Pd(II)[70]. They established the following chemistry. 1) Facile synthesis and first full characterization of 2,10-di-*tert*-butyl dpa-NHC. Previous method was double S_N2 reaction from bipyridine to methylene iodide, which took 5 days and low yield. New method, describing in the next chapter in detail, was reported in similar yields (total 26% yield), however, it took only 3 day including workup steps[17]. Later, I improved the larger scale (×3.5) and higher yield (~85%). 2) The two complexation methodologies were developed, which one was the typical route of NHC complexation, and another was direct oxidative addition of brominated imidazolium salt toward Pd(0). 3) Evaluation of donor/accepter properties by TEP using $RhCl(CO)_2(NHC)$, $^{77}Se\{^1H\}$ NMR signal of selenium adduct, and molecular orbitals. They mentioned that the overall donating ability of dpa-NHC originated from π-donor rather than weak π-acceptor. The "built-in umpolung" of dpa-NHC suggested by Weiss could be shown by electrochemical study, and Kunz predicted to be able to stabilize the high oxidation state species with smaller number of ligands. [69].

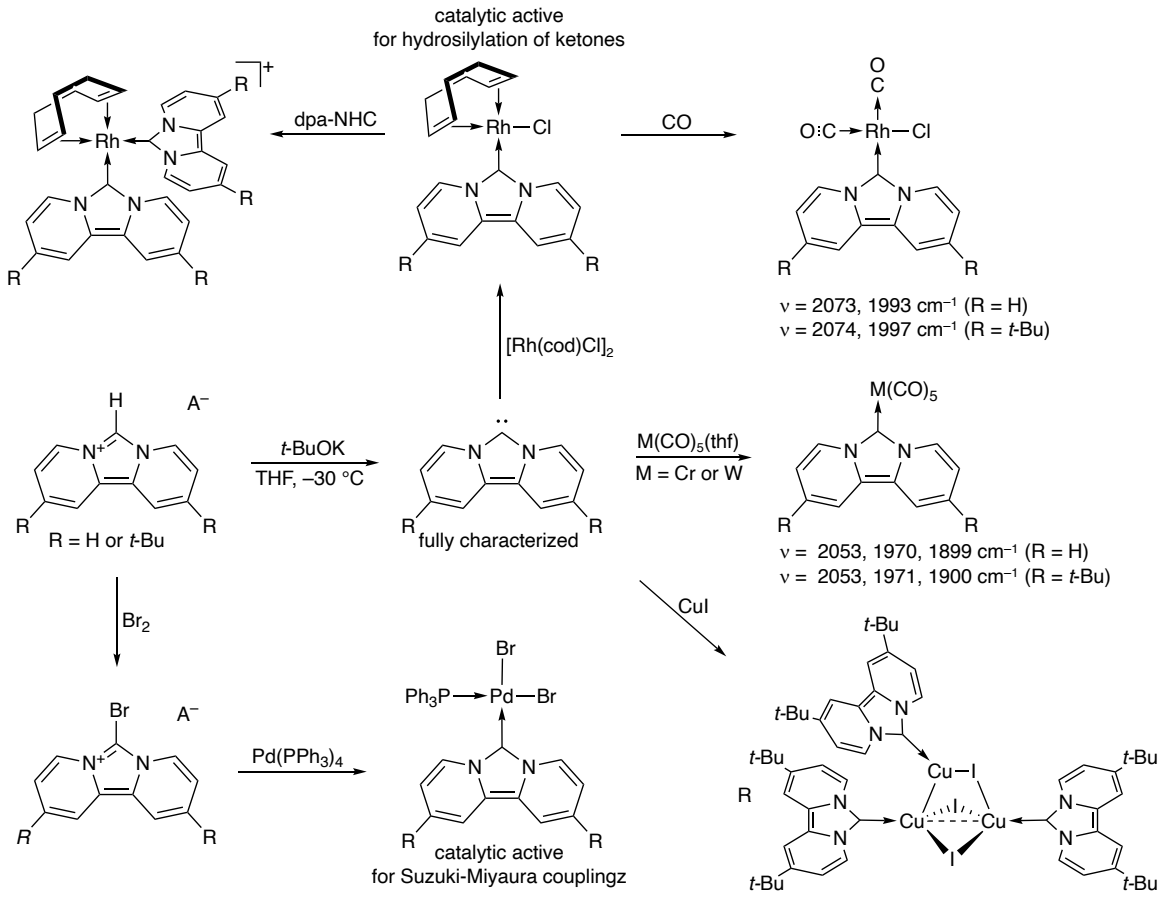

Figure 1.12 Summarized scheme of the dpa-NHC chemistry developed by Kunz

Recently, de Ruiter reported a successful synthesis of bis(diisopropylphosphino)dpa-NHC and complexation toward $FeCl_2$ provided a paramagnetic iron(II) complex. The two chloride ligands were replaced to hydride by $NaHBEt_3$ to yield the **Fe1** complex with the N_2 coordination[71]. The Fe(II) [(PCP)$FeCl_2$] could be reduced by KC_8 under the N_2 atmosphere, in which an Fe(0) complex was obtained. Treatment with $NaHBEt_3$ gave the Fe(0) hydride anion complexes (**Fe2**)[72]. In addition, (PCP)Fe(μ^2-N_2)$_2$ complex reacted with carbonyl arene species via oxidative addition. Interestingly, the functional group provided the different conformers. Activation of ketones showed the *cis-O* conformers toward the carbene carbon whereas those of ester and amide showed the *trans-O* conformer. These conformer differences were from the different bond-activation modes. After coordination of the O of carbonyl group, the ketone underwent to the η^3-(*C, C, O*) coordination. Then the C–H activation occurred to the product. In the cases of the ester and amide, η^3-(*C, C, O*) coordination mode was unfavored compared with the direct C–H activation process. Followed by carbonyl ligation provide the trans-conformer. This study demonstrated that the electron density on carbonyl group made a difference in the C–H activation process[73]. (Figure 1.14.A)

They also investigated that the catalytic activities of iron complexes. In particular, the **Fe1**

indicated unique catalysis. They found the **Fe1** in C_6D_6 showed slow exchange from H to D at the iron center. Applied that, the deuterium exchange from C_6D_6 to various (hetero)arene[71]. Furthermore, **Fe1** was available to the hydroboration of the terminal alkyne with HBpin, which regioselectivity depended on the temperature. Separately prepared (PCP)Fe(II)-HBpin adduct did not show the catalytic activity whereas absence of HBpin provided the alkyne dimerization. These studies indicated that alkyne ligation is the first step in the hydroboration[74]. Although **Fe1** did not have catalytic activity for olefin isomerization, Fe(0) complex **Fe2** was available to the olefin isomerization with a maximum of 160,000 turn-over number. This reactivity difference between **Fe1** and **Fe2** was the oxidation states and/or spin states for the active intermediates[72](Figure 1.14.B).

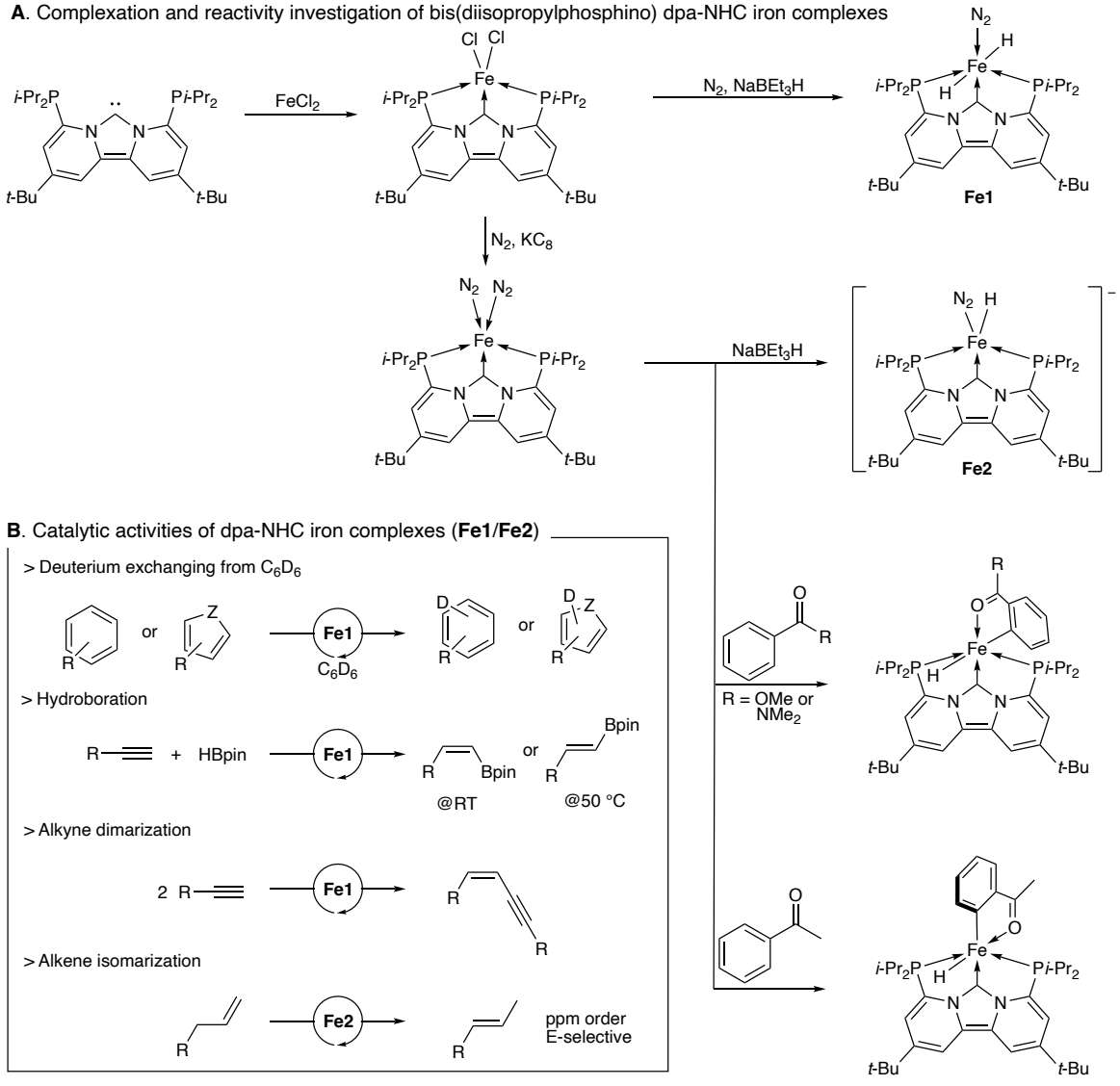

Figure 1.13 Summarized scheme of the dpa-NHC chemistry developed by de Ruiter.

With these dpa-NHCs, our groups reported the Cl, SPh, PPh_2 substituted dpa-NHCs were ligated to rhodium and made the pincer form as LCL type ligand (L = PPh_2[75], SPh[76], and Cl[76]). While the coordination to the Rh(I) center gave the same behavior of Arduengo's NHC, oxidation with I_2 allowed to form the pincer ligands in the case of L = Cl or SPh. PPh_2 derivatives had the different behavior that coordination to Rh(I) center formed the pincer ligand. The PCP–Rh(I) complex can be also oxidized to the Rh(III) by I_2[75,76]. Functionalization by electrophilic bromination followed by cross coupling reaction gave the arylated dpa-NHC, which was confirmed by the complexation with Au(I) centers[77]. (Figure 1.14.A)

In particular, the PPh_2 derivatives were applied for the coordination chemistry of multi-nuclear coinage complexes. One equivalent of the metal precursors gave the dimeric complexes. The gold bi-nuclear complexes were obtained with the stoichiometric dpa-NHC and Au precursors. Specially, an asymmetrical [(NHCAuCl)(NHCAuPAr$_3$)]Cl was prepared by use of the $AuClSMe_2$, whereas Au(tht)$_2$OTf, or halide abstraction from the [(NHCAuCl)(NHCAuPAr$_3$)]Cl yielded the symmetrical [(NHCAuPAr$_3$)$_2$](OTf)$_2$. Both dimeric complexes showed strong Au–Au interactions. Additionally, one more equivalent of a gold precursor, Au(tht)$_2$OTf, toward both symmetrical and asymmetrical Au dimeric complexes provided the tetra-nuclear complex with solvent (DMF) coordination[78]. In the case of Ag species, the symmetrical complexes of [(NHCAgPAr$_3$)$_2$](OTf)$_2$ could be characterized. As opposed to the Au complexes, [(NHCAgPAr$_3$)$_2$](OTf)$_2$ observed the dynamics for switching coordination sites with the dissociation process for its activation barrier of 25.3 kcal/mol. The dimeric complexes nuclear Cu complex was prepared in the same manner as those of Au or Ag complexes. However, the structure had asymmetrical bi-nuclear complexes with solvent coordination. Interestingly, one of the carbene carbon on the dpa-NHC coordinated with both Cu centers[79]. It is the reasonable structure that the dpa-NHC coordinated to one of two Cu centers as σ-coordination and unconventional π-coordination from dpa-NHC toward another Cu center. This would be the experimental evidence for the 'hidden carbone' nature[62].

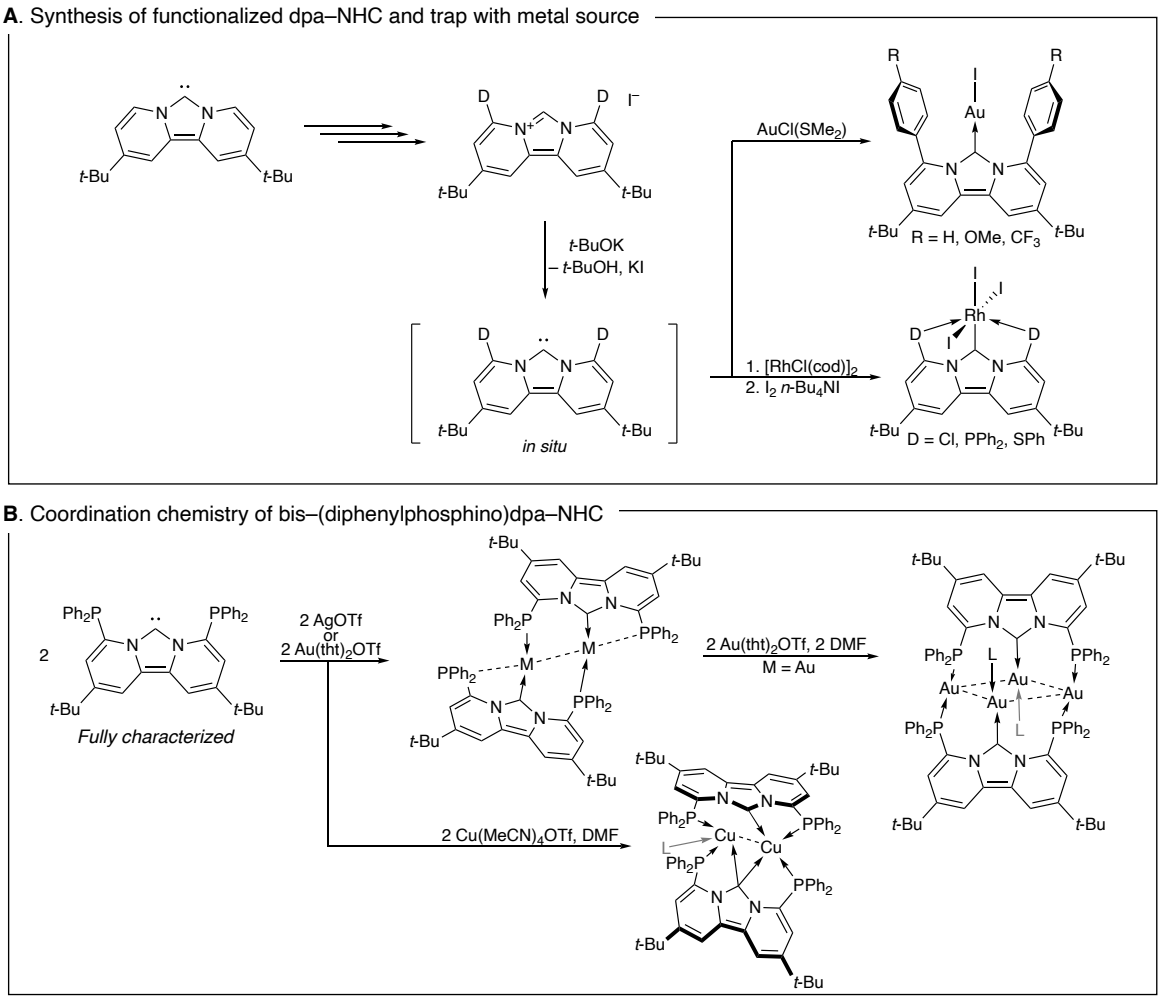

Figure 1.14. Synthesis and complexation of bis-functionalized dpa-NHC developed by our group.

1.5. Ligand synthesis

Scheme 1.1 described the synthesis of arylated dpa-NHC with the latest procedure. Original procedure was reported previously, but the overall yield was very low. To study for the suitable condition of formation of pincer ligand, large scale synthesis, facile workup, and high yield required.

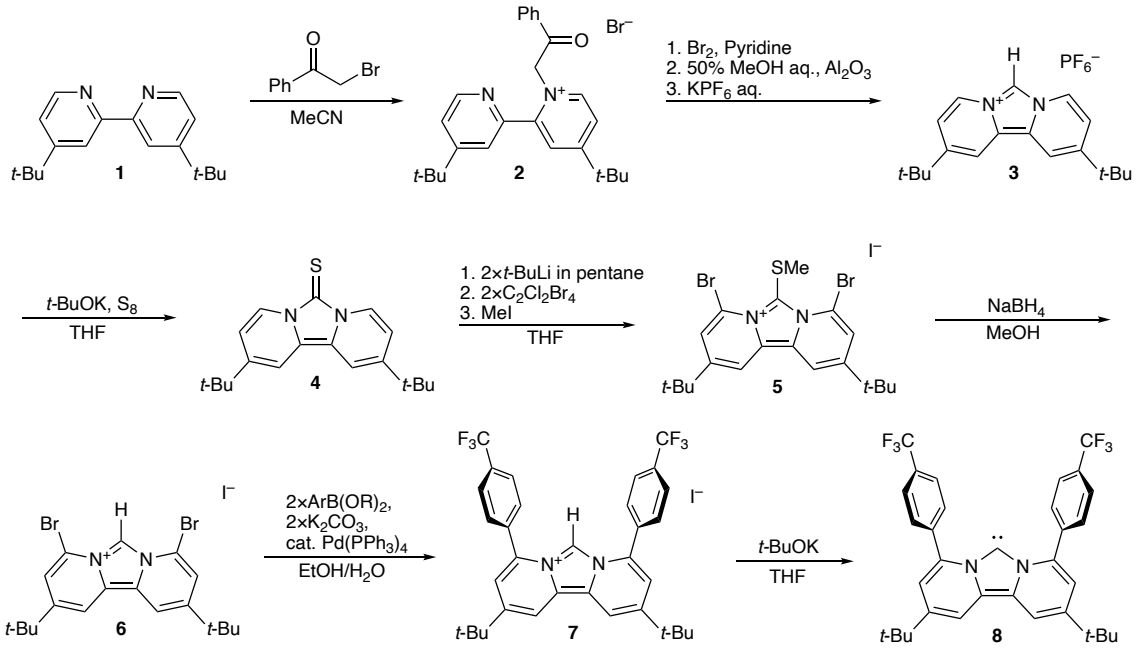

Scheme 1.1. Overall scheme for the synthesis of arylated dpa-NHC

This reaction shown in Scheme 1.2 is an S_N2 reaction in acetonitrile between **1** and phenacyl bromide where phenacyl bromide is in a slight excess. After removal of the solvent, the crude product became oily. However, this crude is available in the next step without further purification.

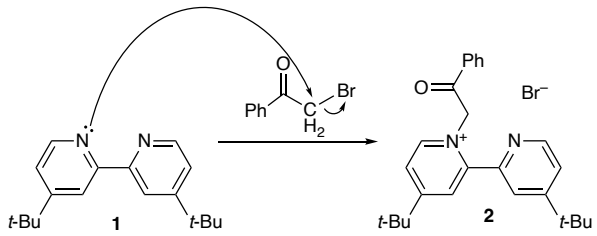

Scheme 1.2. First step as a S_N2 reaction of bipyridine to the alkyl bromide

To complete generation of the central 5-membered ring, compound **2** was dissolved in dry pyridine and the reaction with bromine was carried out at 60 °C (boiling point of Br_2). Note that Br_2 should be added as neat. When Br_2 dissolved in pyridine, the heat was generated and suddenly became black slily, likely over-reaction between Br_2 and pyridine. It takes five minutes to complete this cyclization. After the evaporation of pyridine, hydrolysis was conducted with MeOH/H_2O. The byproduct, benzenic acid, was removed by filtration with neutral aluminum oxide (provided by

Merck, other activated alumina was not available). If sonicate was used for hydrolysis, the amount of solvent could be reduced. The product must be dry enough to use the next reaction. Instated of evaporation of MeOH/H_2O, KPF_6 aq. was added to filtrate in order to decrease solubility toward water[68]. Note that the product was so moist, which required dryness as much as possible by washing with ether, followed by drying *in vacuo.*

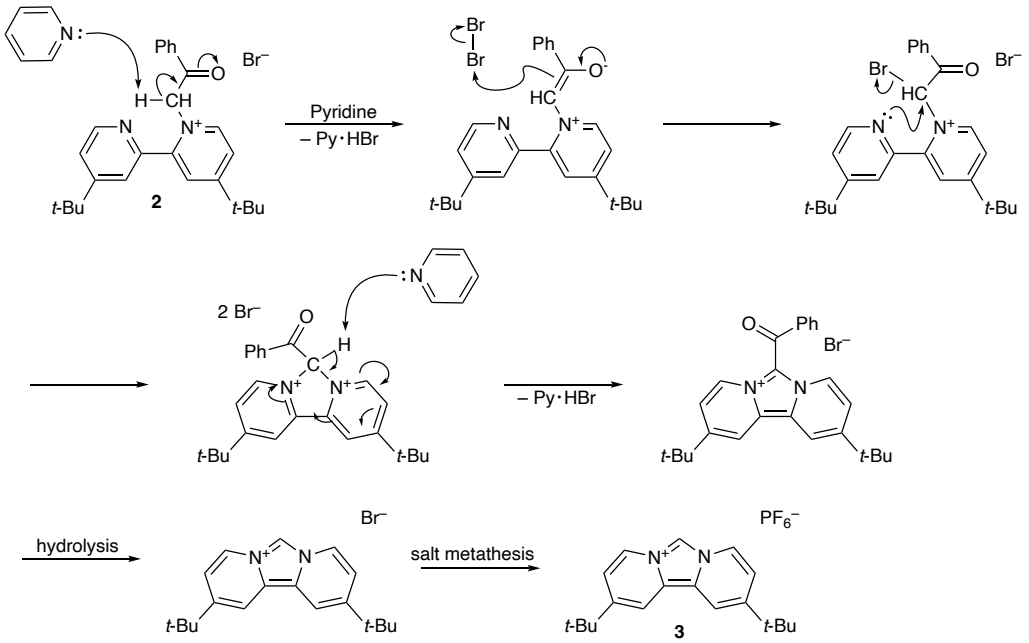

Scheme 1.3. Cyclization to form a dpa-NHC framework

The imidazolium salt **3** was treated by *t*-BuOK, resulting in free carbene being generated *in situ*, then trapping with elemental sulfur yielded the thiourea **4**. The efficiency or yield highly depended on the solubility of **3**. Compound **4** survives in silica gel and can be pre-purified with an eluent of THF/hexane (1:1). The next reaction required the pure **4** recrystallized from acetone. In the large-scale reaction, the solubility of *t*-BuOK would also be a problem. To overcome that, the additive for raising reactivity, such as 18-crown-6, or more organic bases, such as HMDA bases, may improve the yield and should be tested.

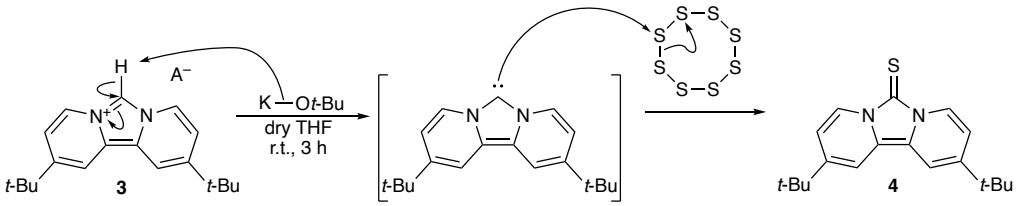

Scheme 1.4. Generation of free carbene and trapped by sulfur

Thiourea **4** was treated with over two equivalents of *t*-BuLi as a base, which generated dark yellow–green 4,8-lithiated intermediate. Due to the C=S moiety as a directing group, this reaction

was regioselective. Next, bromination took place with the addition of $C_2Cl_4Br_2$, giving a dark-red solution. This mechanism should be the E_2 elimination of $C_2Cl_4Br_2$, which lithiated carbon atom attacked to bromine atoms. Finally, the lone pair of sulfur attacks methyl iodide via S_N2 reaction at room temperature. It should turn dark orange. When the reaction mixture warmed up to room temperature before the addition of methyl iodide, The solution color changed to dark yellow. This was likely because the tetrachloroethylene worked as a nucleophile. Although this is a different process from the original scheme (scheme 1.4.), the same treatment, namely adding MeI into the freshly prepared THF solution or suspension followed by reduction by $NaBH_4$ in MeOH, can finally yield the desired product **6** (see below).

A suspension of **5** in MeOH was treated by adding $NaBH_4$ portion-wise, which produced the imidazolium salt **6**. $NaBH_4$ is a hygroscopic chemical, so it is better to weigh that in a vial. Note that $NaBH_4$ is gradually decomposed in MeOH. If $NaBH_4$ was added too fast, the reaction did not complete. In addition, when an excess amount of $NaBH_4$ was added into the reaction mixture, the dpa-NHC framework was decomposed to yield the bipyridine[80]. The next reaction required pure **6,** which can be obtained from recrystallization in acetone. Any NMR-silent byproduct or thiol derivatives may compromise the palladium catalysts.

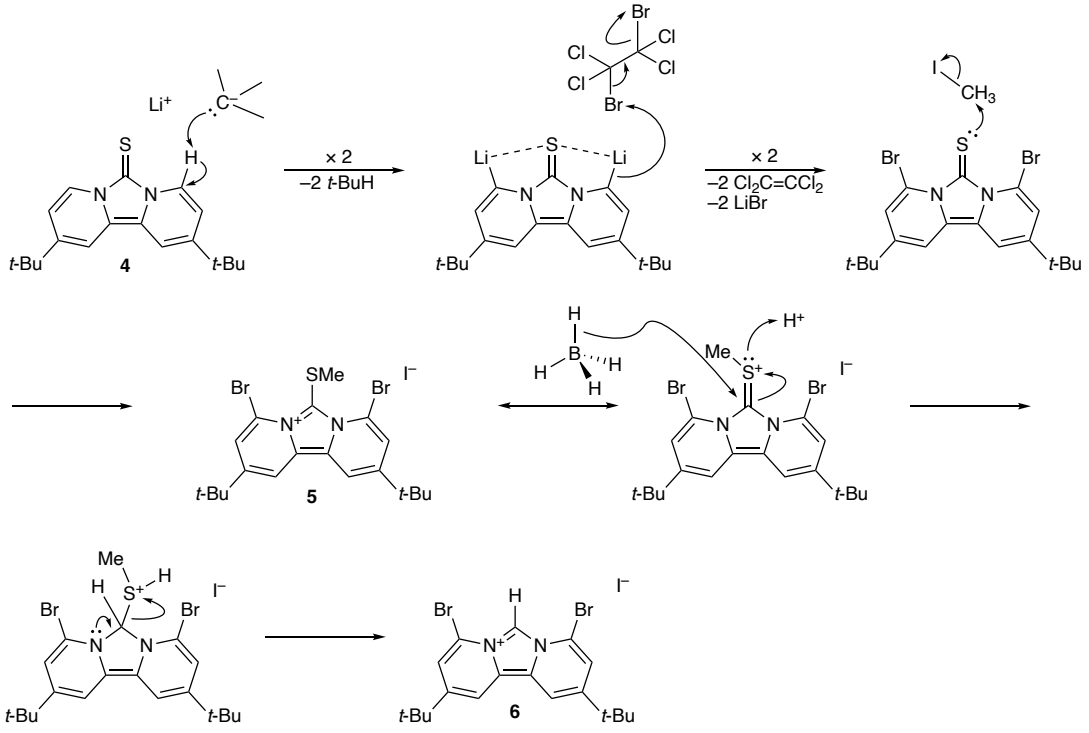

Scheme 1.5. Functionalization of dpa-NHC

Aryl moieties was introduced by Suzuki-Miyaura cross-coupling reaction. This could be processed in the general catalytic cycles in cross-coupling reactions. After the removal of the

inorganic salt, palladium waste must be removed. Previously, reprecipitation with THF/Et_2O was carried out for workup. However, the yield is moderate (~45%), which is not always reproducible purification. Sometimes the phosphine remained in the residue, or the decomposition products could not be removed completely. As a result of the various trials of purification, washing with fluorobenzene, followed by hexane is the best method to obtain the pure **7**. Once washed with fluorobenzene, the brown paste was obtained, which was solidified by hexane to provide the yellow solid of **7** in better yield (~60 %).

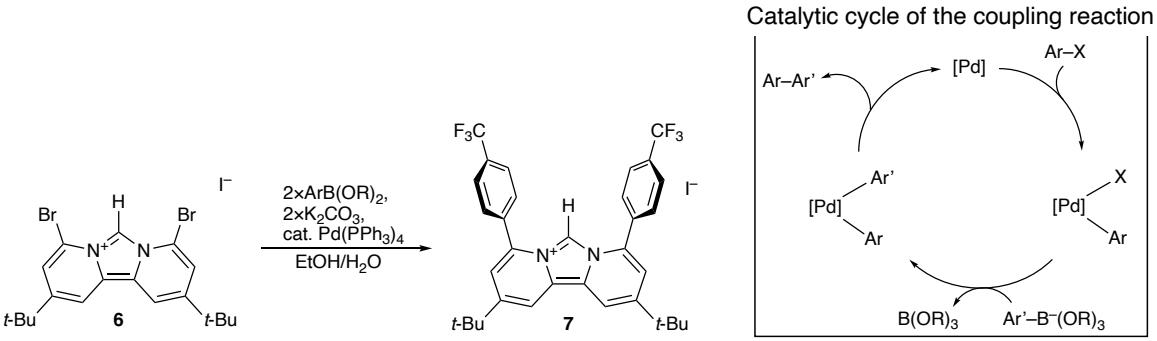

Scheme 1.6. Arylation of dpa-NHC through Suzuki-Miyaura coupling reaction

Generation of NHC, **8** was carried out in the same procedure of non-substituted dpa-NHCs.[67] The ^1H NMR resulted in the disappearance of a signal of C–H between two nitrogen atoms and $^{13}C\{^1H\}$ NMR indicated that a signal corresponding to carbene carbon was observed at 196 ppm, comparable to the dpa-NHC derivatives[67]. Compound **8** can be obtained in 64% yield from reactions at room temperature, which suggests good thermal stability of **8**. Filtration through dry Celite, glass wool, or glass-fiber paper can be used for the removal of salts after extraction with hexane. Recrystallization in toluene afforded a single crystal suitable for SCXRD. (see figure 2.8). The solid-state structure of **8** showed that the C1-N1 and C1-N2 distances of 1.374(2) Å and 1.376(2) Å and the N1-C1-N2 angle of 100.7(2)° are similar to those of the bisphosphine-substituted derivative (dpaP2-NHC: 1.368(2) Å, 1.378(2) Å and 100.2(2)°)27. The two aryl groups slightly rotate out of the plane of the dipyridyl backbone, likely due to the repulsion between the ortho-protons of the aryl- and the annulated phenyl moieties. Percent buried volume (V_{bur}), calculated by using the SambVca 2.1 server, based on the solid-state structure of our (**8**)AuI complex, is 67.2%, much larger than those found for aryl-substituted typical NHCs such as IMes and IPr (ca. 35-45%, IPr=1,3-bis(2,6-diisopropylphenyl)imidazole-2-ylidene). The proximity of aryl groups would permit a large bite angle at the ortho-phenyl position upon cyclometallation to form a pincer ligand.

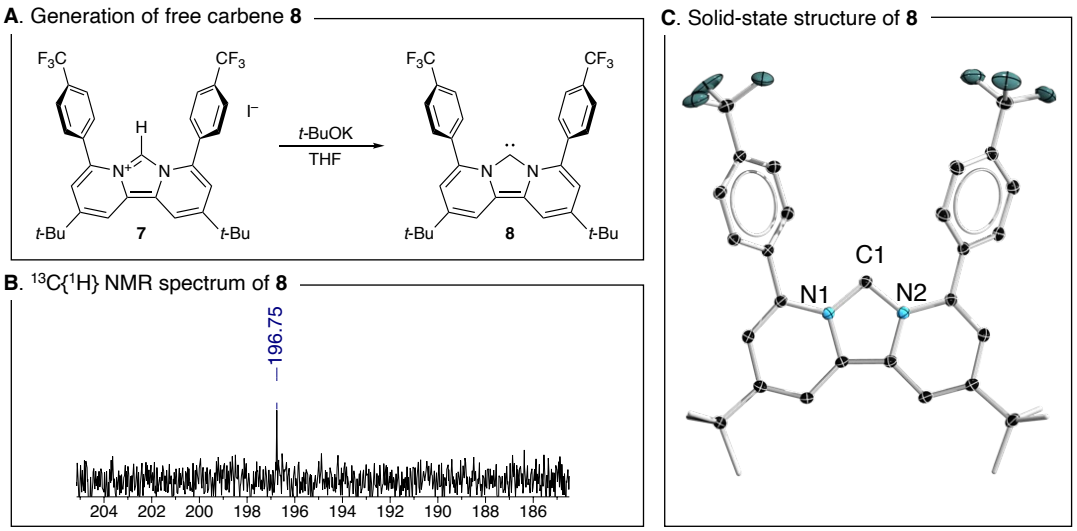

Figure 1.15.Synthesis and characterization of free dpa-NHC **8**

1.6. Aim and outline of this thesis.

This thesis explores the complexation methodology of the arylated dpa-NHC as a pincer ligand and applies that complex in redox chemistry. The pincer ligand – the term was coined by van Koten in 1989[81] – is a crucial design in the coordination chemistry of view, and various kinds of pincer complexes have been investigated since the first spectroscopic detection[82] and structural characterization[83] of pincer complexes in the late of 1970s. Along with their development, the design of the pincer ligand became varied. Indeed, Fill and Bourissou reported the electron-rich metal complexes tetra or tridentate ligands bearing σ-accepting borane centers (Z-type ligands), respectively[84,85]. After breaking through the synthesis stage, pincer complexes with Z-type ligands is getting powerful tools in catalysis with electron-rich metals such as gold and platinum[86]. The traditional 1-electron donor (X-type) and 2-electron donor (L-type) ligands also provide the different properties in the view of the charge and/or formal oxidation state in the various transition metal center. Therefore, the development of the complexation route is getting essential work. Our group has been investigating the synthesis and application of bis-functionalized dpa-NHC. While the sulfur or phosphine-substituted dpa-NHC could work as pincer ligands, arylated dpa-NHC had not been applied for a pincer ligand. In this thesis, we envisioned that the LX_2-type pincer based on dpa-NHC framework could be formed via cyclometallation. Cycloemtallated NHC complexes have been studied in the view of applications for catalysis[87–89] or luminescent materials[90–92]. We also imagined that such a dpa-NHC pincer complex would be available for applications such as homogeneous catalysis, luminescent materials, and electron-transfer transits.

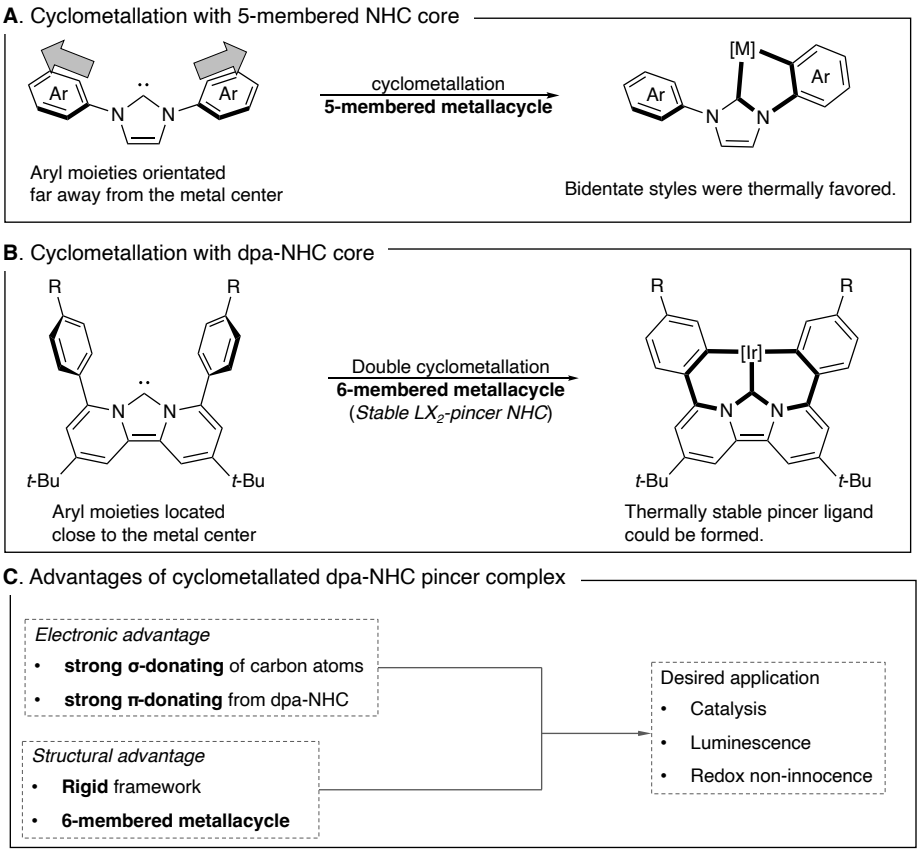

Chart 1.1. Ligand design and concept of iridium metallacyles with dpa-NHC

Chapter 2 discusses the synthetic routes for complexation to Ir and its cyclometallation. [dpa-NHC]Ir(I) complexes were obtained via transmetallation to Ag(I). Homoleptic complexes were obtained successfully whereas any attempt to synthesize heteroleptic (dpa-NHC)Ir(III) complexes were not successful. Homoleptic one was experimentally characterized as the anionic Ir(III) complex by SCXRD, trapping experiment, and XANES. This selectivity for cyclometallation was theoretically investigated. The electrochemical study suggested that the unprecedented oxidation behaviors.

Chapter 3 described the chemical oxidation of the new anionic iridium complex with bis-pincer ligand of dpa-NHC. Each 2-electron oxidized products were crystallographically characterized. The mechanistic study for the initial 2-electron oxidation was both spectroscopically and computationally investigated. The properties of final product by 4-electron oxidation were investigated by spectroscopic, magnetic, and computational measurements.

Chapter 4 summarized the work among chapter 1 to 3 and brought the outlook towards out future direction.

CHAPTER 2.

DEVELOPMENT OF COMPLEXATION STRATEGY FOR ARYLATED DIPYRIDO-ANNULATED NHC AS A DIANIONIC PINCER LIGAND TOWARD AN IRIDIUM CENTER

2.1. Introduction

Owing to the design flexibility in both electronic and steric properties, NHCs[93] based pincer ligands have been used widely across the fields of catalysts[94] as well as light-emitting materials[95]. The 2-electron L-type neutral carbon donor in the carbene is usually a stronger σ donor than the group 15 nitrogen and phosphorus donors, providing complementary reactivity and/or properties upon complexation to the metal center compared to pyridine and phosphine systems. Using Green's formalism[96], NHC-based pincers can be categorized into neutral (L_3), anionic (L_2X) or dianionic (LX_2) systems, allowing controllable access to different charges on metal complexes with different oxidation states.

L_3-type NHC pincer ligands were classified as mostly two systems: NHC-core and bis-NHC-anchor pincer ligands. While the library of L_3- or L_2X-type systems is expanding rapidly, examples of those bearing dianionic LX_2-type ligands remain sporadic due to limited metal-complexation strategies.[97] The most common design involves NHC core bearing group 15 and 16 anionic chelating moieties such as alkoxide, and amides[98] In most of these cases, the preparation procedure was the same as NHC-core L_3-type pincer ligands, and complexation was achieved through deprotonation.

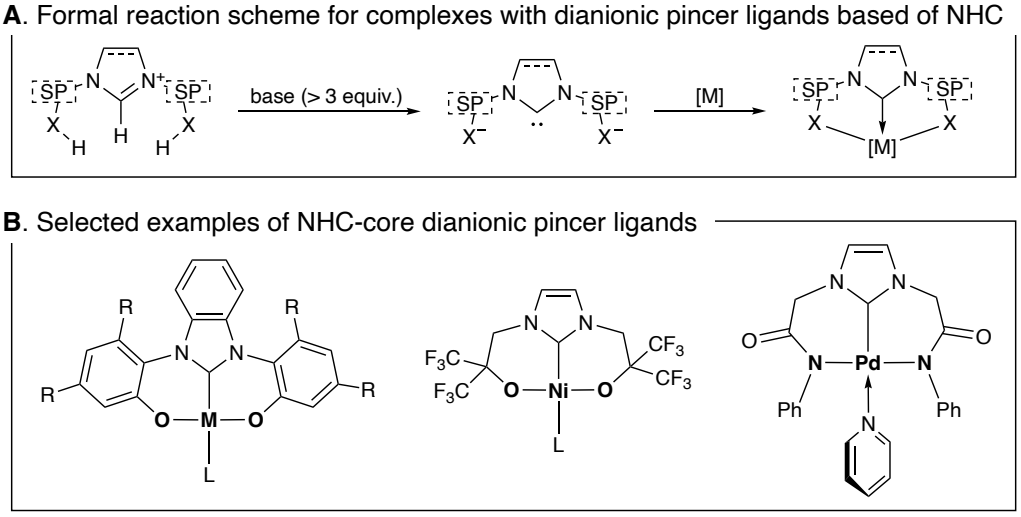

Figure 2.1 Complexation strategy of LX_2-type NHC pincer ligands

However, this strategy is less effective in synthesizing dianionic all-carbon (CCC-)pincers, whose complexation to the metal center mostly relies on cyclometallation through C-H bond activation processes. To date, there are very few ligand scaffolds and complexation strategies that allow access to LX_2-type CCC-pincer complexes (Figure 2.2). In the cases of cyclometallation via sp^3 C-H bond activation, almost all the examples were obtained from IMes-Ir(III) polyhydride complexes (**C1**).[99,100] A similar approach has been successfully applied to an anionic ruthenium complex, which was prepared from Ru(IXy)Cp*Cl (IXy=1,3-bis(2,6-dimethylphenyl)imidazole-2-ylidene) treated with $PhCH_2K$ stepwise (**C2**)[101]. An exception is Canac's phosphino-ylide CCC-pincer ligand bearing an NHC core, which complexed to palladium centers easily upon deprotonation (Figure 2.2, **C3**).[102]

In addition to the limited and highly reactive metal precursors typically required for double C-H bond activation in anionic CCC-pincers,[89,103,104] cyclometallation via sp^2 C-H bond activation also suffers from a less favoring (smaller) bite angle. Since the first report on a dianionic CCC-pincer of a hexaphenylcarbodiphosphorane system by Cavell (**C4**),[105] Esteruelas and Xia (**C5**)[106], Tu (**C6**)[107] and Danopoulos (**C7**)[108] reported the Rh, Os, Ir and Pd complexes bearing bis-aryl tethered NHC pincer ligands, respectively. Each features a strained 5-membered metallacycle, which makes them more susceptible to M–C bond cleavage, compromising stability, and thus hindering their applications in systematic reactivity and property investigations.

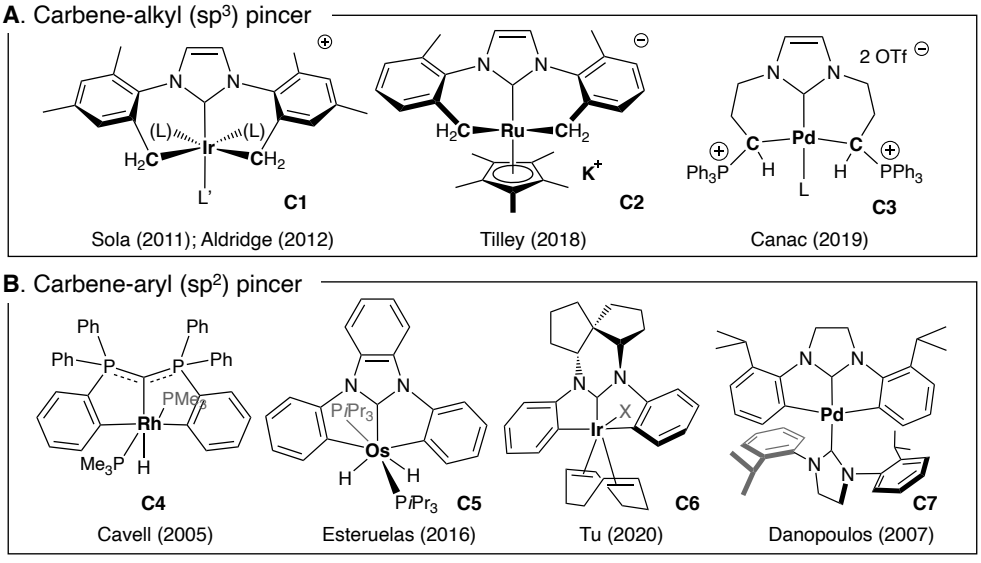

Figure 2.2 Selected examples of the late transition metal complexes bearing CCC-LX_2 NHC pincer ligands.

Due to these reasons, a new LX_2-type ligand system that allows easy complexation to afford stable complexes is highly desirable. As described in Chapter 1, arylated dpa-NHC **8** is one of the best candidates to form the LX_2-type pincer ligand. However, the recipe to prepare the pincer complex had not been developed. Thus, this chapter aims to establish the methodology to form the LX_2-type

dpa-NHC pincer ligand. Based on the literature, three proposals were suggested (Chart 2.1). Route A was suggested by Aldridge's examples, in which the free 6Mes ligand coordinated to the iridium center with C–H activation on an *ortho*-methyl group simultaneously[109]. This likely caused the facile approach toward the coordination space of the iridium center. This simulation might be close to our dpa-NHC **8**; thus, this strategy was employed. Besides that, two strategies were inspired by Peris' report[110]. Route B describes the stepwise reaction of complexation followed by cyclometallation. In this case, we can confirm each step and make it easy to trace the reaction. Although this system would give us a good understanding of the reaction mechanism, the overall yield could be low because one workup step is required in the complexation step. Route C provides the one-pod cyclometallation by using bases such as acetates, carbonates, amines, alkoxides, amides, hydroxides, or, sometimes Ag_2O. This direct synthesis would allow us to obtain the desired complex with a good yield. However, the reaction might take through undesired pathways, which usually require harsh conditions such as reflux of acetonitrile, toluene, and 2-ethoxyethanol in the presence of bases.

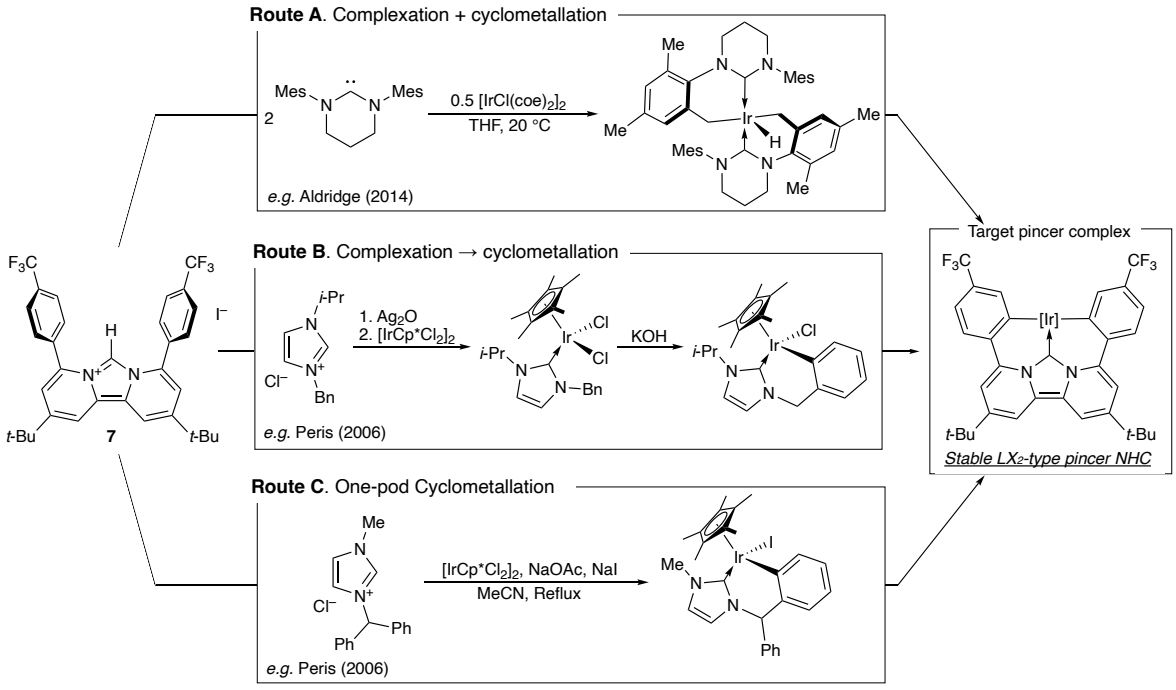

Chart 2.1 A strategy map to obtain the desired dpa-NHC-based LX_2 pincer iridium complex.

2.2. Initial attempts for complexation of dpa^{Ar2}-NHC toward iridium complexes as a pincer ligand

Cyclometallation is an intramolecular reaction of a metal complex, in which the C–H bonds on the ligand(s) cleaved and the C–M bonds were newly formed. The product has a cyclic structure containing the metal center. A general strategy is through oxidative addition of the C–H bond. Initially, the σ-coordination of the C–H bond occurred, followed by the C–H bond being cleaved. This process is favored by electron-rich metal centers, which have strong electron-donating ligands owing to the increase in the electron density on the metal center. To date, cyclometallation with strong L-type donors such as pyridines[111], NHCs[112], phosphines[113], and silylenes[114], was established. Whereas the single cyclometallation was readily undergoing, the double cyclometallation was highly challenging owing to the geometry limitation. In addition, harsh conditions were required because the double cyclometallated ligands provide pincer ligands, which are usually thermodynamically stable species[115]. The dpa-NHC has strong σ and π-donating nature as well as the aryl moieties are fixed around coordination space to the metal center. Thus, we developed the first strategy for cyclometallation by following these methods using the harsh conditions with iridium precursors.

The initial attempted condition for the complexation of carbene **8** as a pincer system was using $Ir(OAc)_3$ as a starting material. Generally, cyclometallation on the iridium center was performed with iridium chloride, however, that iridium source contained water as iridium chloride hydrate. Although several conditions were employed to obtain the desired iridium complex, the fragment of 1327.40979 (called complex **X**) was only observed as an iridium-containing species by HRMS. Any other species corresponding to iridium was not detected. In addition to this iridium species, a needle crystal was isolated by recrystallization with a toluene/hexane two-layer system. SCXRD illustrated the ring-opening byproduct **10**. This decomposition was readily assigned in both ^{1}H and ^{19}F NMR (δ_F = –62.20 ppm).

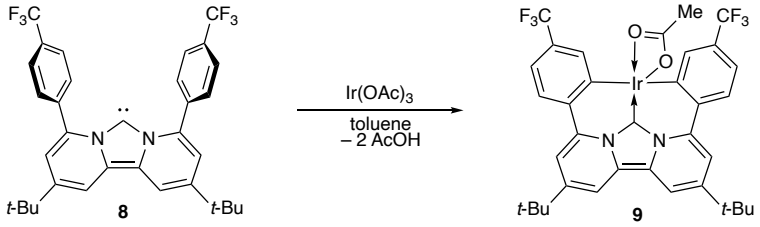

Scheme 2.1 Attempted cyclometallation of **8** with $Ir(OAc)_3$

We had suspected that acetic acid, which was generated in the reaction mixture, made carbene **8** decomposed to bipyridine. Therefore, Cs_2CO_3 was added to the reactant to quench the acid. However, the base seemed not to work. The yield of complex A was quite low (~ 15%) because of unmatched stoichiometry between Ir and carbene. Additional carbene **8** was added to accelerate the generation

of the detected complex. Although I tried different conditions of their stoichiometries of 1:1, 1:2, and 1:3 ratios respectively, the results were the same behaviors of the 1:1 reaction. The bottleneck of this reaction was the solubility of $Ir(OAc)_3$ toward organic solvent. There is an experimental fact that the starting material of $Ir(OAc)_3$ remained in the reaction form even though three equivalents of carbene **8** were used. Then, I changed starting materials, which are soluble in organic solvents.

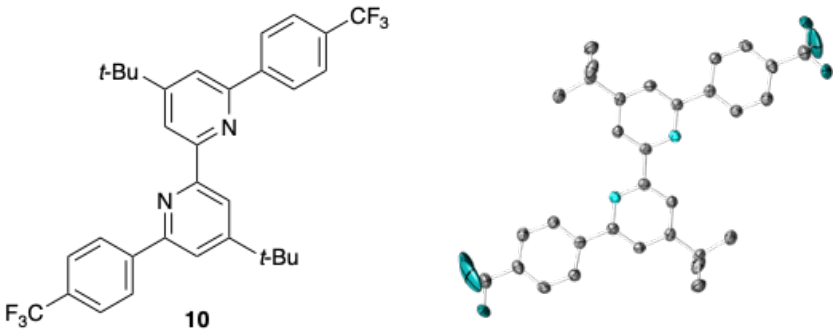

Figure 2.3 Solid-state stricture of **10**. Hydrogen atoms are omitted for clarity. The ellipsoid was set as 50% probability.

For the sake of preparing the desired pincer complexes, Ir(I) starting materials were employed as an alternative strategy. I employed four Ir(I) complexes, $[IrCl(olefine)_2]_2$, $IrCl(PPh_3)_2L$ (L = PPh_3 or CO), which were well-known that oxidative addition facially happens at Ir(I) center in the same condition as using $Ir(OAc)_3$ (Scheme 2.2).

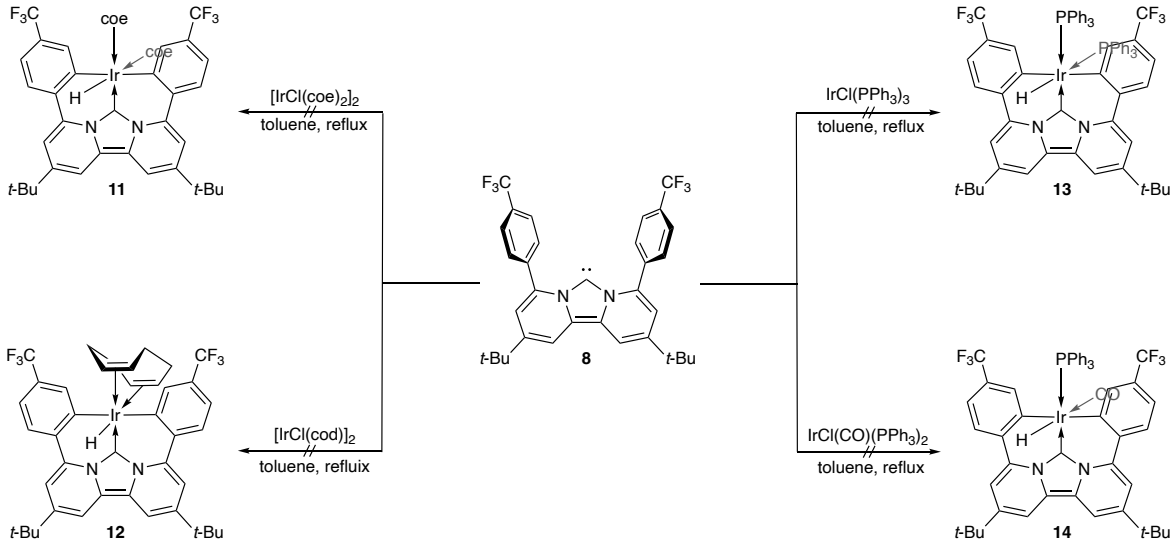

Scheme 2.2. Summary of attempted cyclometallation of dpa^{Ar2}-NHC from iridium(I)

$[IrCl(coe)_2]_2$ was employed as an iridium source and there were a lot of examples taking place C–H bond activation of aryl groups for cyclometallation. ^{19}F NMR spectra immediately changed

after mixing with carbene **8** at –30 °C. The initial step of this reaction was predicted to be the coordination of free carbene **8**, which yielded two possible intermediates (**11A** or **11B**). In comparison with the ^{1}H NMR spectrum of $[IrCl(coe)_2]_2$, the olefin signal was observed at 5.61 ppm, which could be assigned as free coe. Thus, **11B** might be generated as major species. After acceleration by reflux of toluene, a signal of –60.7 ppm disappeared. This signal could be considered intermediate likely complex **11C** or **11B**. A new signal at –61.96 ppm in ^{19}F NMR could be the thermodynamic product, which could be complex **A**, the second coordination of free carbene **8** might happen. However, any species was not isolated nor detected, thus this condition was not suitable (Figure 2.4).

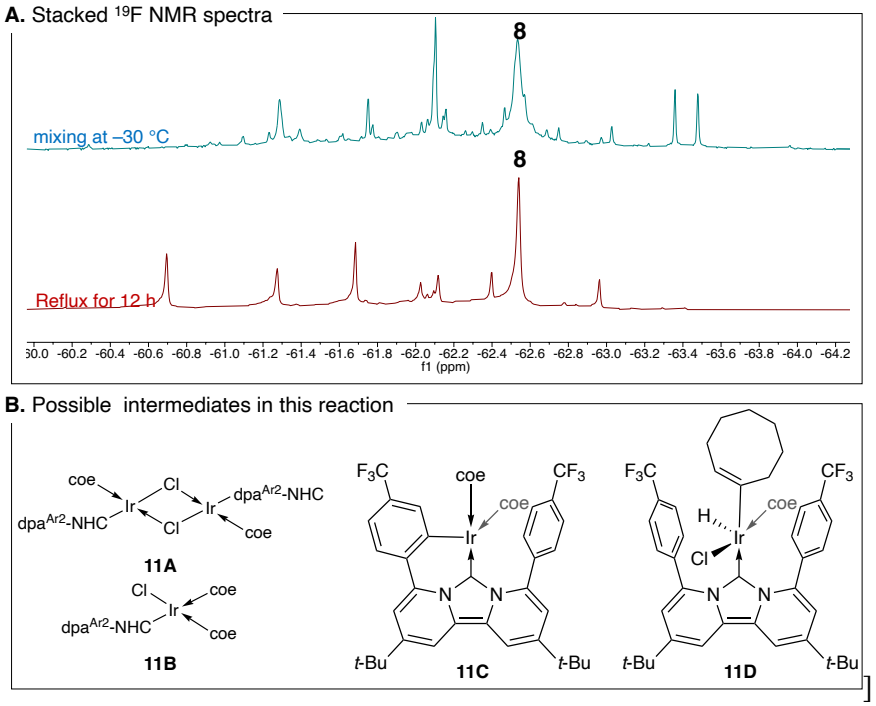

Figure 2.4 Attempted cyclometallation of **8** with $[IrCl(coe)_2]_2$ to complex **11**

We hypnotized two coordination styles, which were difficult to control the coordination either coe dissociation or monomerization, thus, $[IrCl(cod)]_2$ was employed owing to be sure for producing the IrCl(cod) fragment by preventing first dissociation of olefin ligand using bidentate cod ligands. Toluene reaction of **8** plus $[IrCl(cod)]_2$ was monitored by ^{19}F NMR by each 30 °C (Figure 2.5). Even though the reaction temperature raised to 80 °C, the reaction did not happen according to ^{19}F NMR. When the temperature reached to reflux, new two signals were grown. One of two signals was assignable to **10** based on the previous experiment. Another signal was not identified yet; however, compared to the $[IrCl(coe)_2]_2$ reaction, the reaction proceeding was clean. Unfortunately, the product was not isolated likely due to the similar solubility among **8**, **10**, and product, or the highly crystalline **10**.

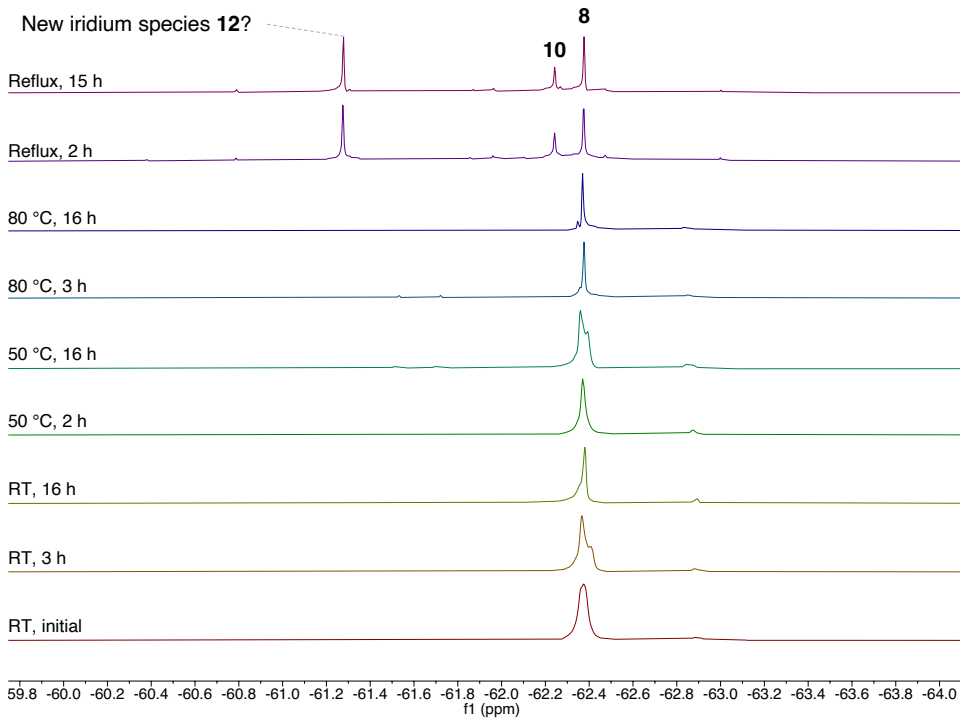

Figure 2.5. Stacked ^{19}F NMR spectra for monitoring reaction toward complex **12**

$IrCl(PPh_3)_3$, the iridium analog of a Wilkinson catalyst, is one of the iridium sources. This complex has doublet and triplet signals in $^{31}P\{^1H\}$ NMR spectroscopy corresponding to *trans* and *cis* PPh_3, respectively Thus, we can monitor the iridium species by $^{31}P\{^1H\}$ NMR spectroscopy. Firstly, the reaction was monitored at room temperature for 18 h, some reaction happened. Both ^{19}F and $^{31}P\{^1H\}$ NMR spectra indicated that the starting materials of **8** and $IrCl(PPh_3)_3$, respectively. After acceleration of the cyclometallation by heating at 60 °C for 6 h, initial iridium species were consumed completely, and a couple of doublet signals were observed. Two signals (or, one double doublet signal) around –90 ppm indicated the hypervalent phosphorus species, bearing a $^2J_{PP}$ coupling. On the other hand, the remaining signals appeared around 0 ppm, which is close to free PPh_3. However, all these signals have coupling, maybe with $^2J_{PP}$ coupling constants.

Focus on the ^{19}F NMR, free carbene **8** remained, although the reaction was carried out under the harsh condition of refluxed toluene. During the reaction, new species were generated (δ_F = –62.53 and –62.77). This situation could be considered in two matters: forming an iridium complex with asymmetrical bidentate from carbene **8** or two different species. Combined with $^{31}P\{^1H\}$ NMR, I suspected the latter idea of the existing two main species might be correct (Figure 2.6)

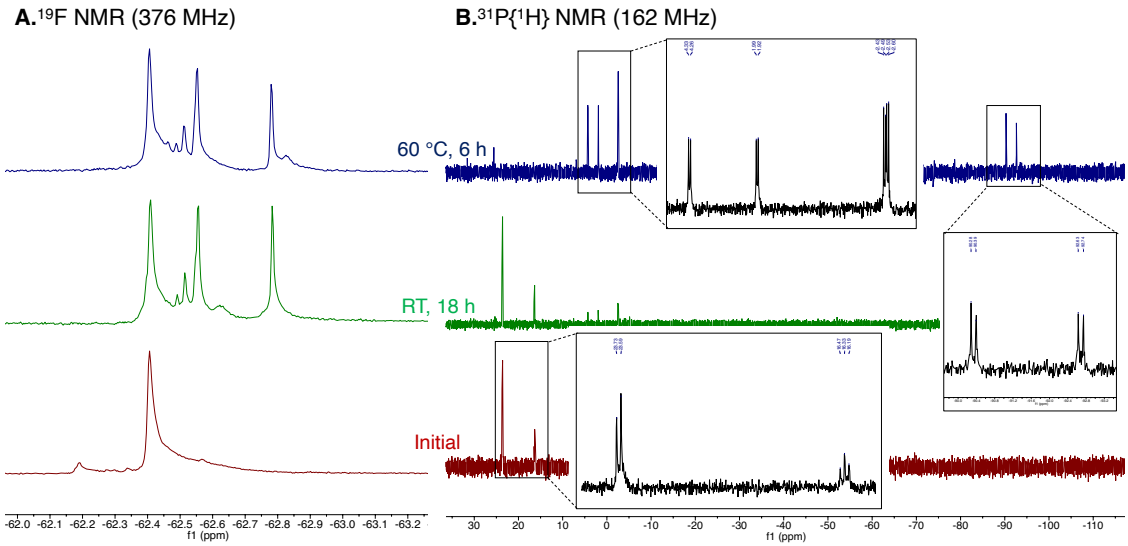

Figure 2.6 Attempted cyclometallation of **8** with $IrCl(PPh_3)_3$

Also, *trans*-$Ir(CO)Cl(PPh_3)_2$, Vaska's complex, was employed. This complex has only one signal on the ^{31}P NMR spectrum, so the reaction can be monitored more easily. Even though the reaction was performed under reflux conditions for 12 hours, the iridium starting material remained and a relative amount of free carbene **8** was decomposed to **10**. New signals in both ^{19}F and $^{31}P\{^1H\}$ NMR spectra suggest that the asymmetrical species might be generated. The $^{31}P\{^1H\}$ NMR spectra showed two large singlets, which suggests there were two major species, which are consistent with the ^{19}F NMR spectra. In any case, the products of iridium complexes have not been characterized yet (Figure 2.7).

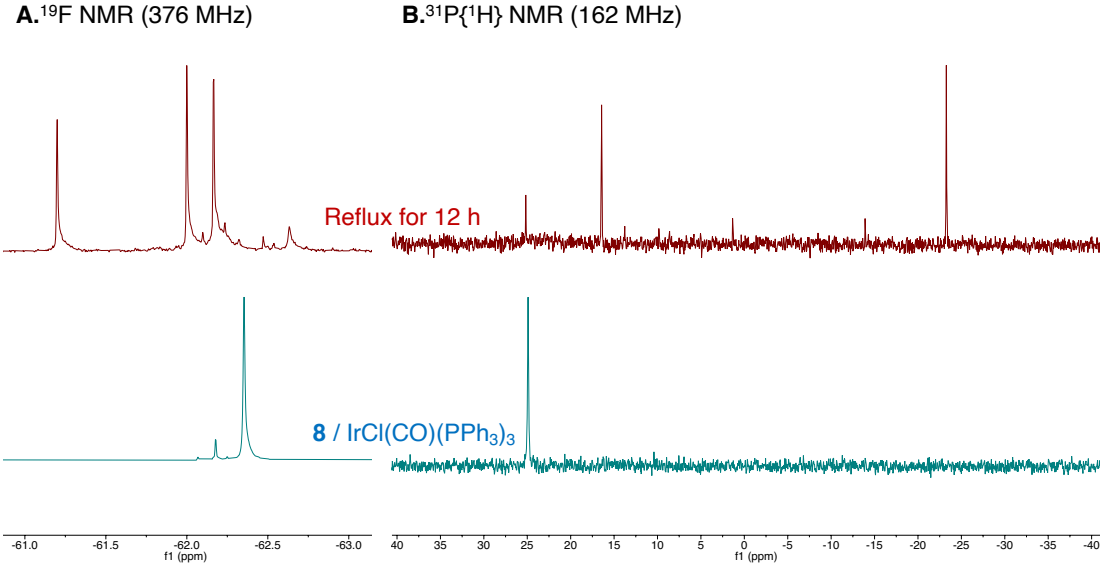

Figure 2.7 Attempted cyclometallation of **8** with $IrCl(CO)(PPh_3)_2$

Instead of the iridium centers, rhodium starting materials such as $[RhCl(cod)]_2$ or $Rh(PPh_3)_3Cl$ were employed because of the NMR-active Rh centers, providing the coupling with ^1H or ^{13}C nuclei. Although a similar condition for iridium starting materials was attempted, desired complexes **15** or **16** were obtained (Scheme 2.3).

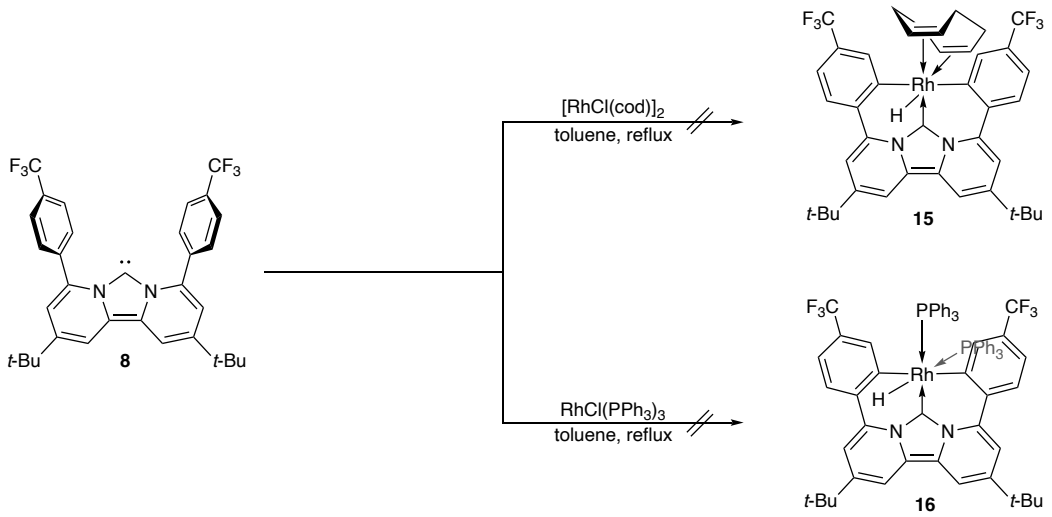

Scheme 2.3 Attempted complexation of dpa-NHC toward Rh centers.

In conclusion, cyclometallation from free carbene **8** was not clean reaction because of the thermal decomposition to provide bipyridine **10**. However, cyclometallated iridium dpa-NHC complexes might be detected like scheme 2.1. by MS. Therefore, there had still chances to obtain the desired cyclometallated iridium complexes. To overcome this problem, the stepwise reaction, which was a coordination of dpa-NHC followed by cyclometallation, was investigated. According to the screening, the $[Ir(cod)Cl]_2$ seems to be the best iridium source, therefore, $[Ir(cod)Cl]_2$ was selected as an iridium precursor.

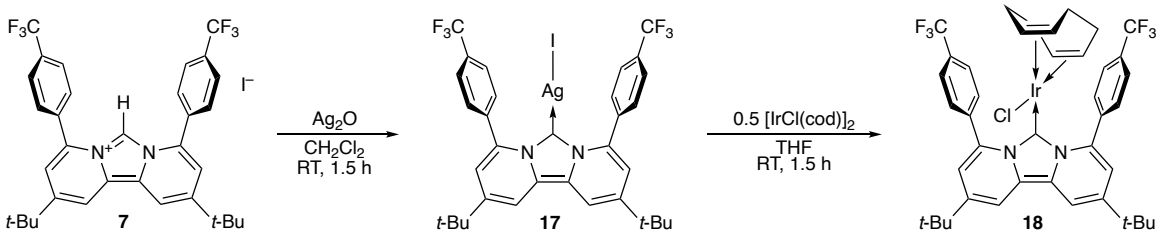

Scheme 2.4 complexation of dpa^{Ar2}-NHC with silver transmetallation.

The clean complexation was achieved by the reaction of imidazolium precursor **7** with Ag_2O followed by transmetallation to $[Ir(cod)Cl]_2$ which afforded [Ir(dpa-NHC)(cod)Cl] (**18**) as an orange solid in 81% yield. (Scheme 2.4). The silver intermediate was confirmed by NMR and HRMS. In ^1H

NMR spectra, the signals were in good agreement with the **8**-AuI complex. Chemical shifts of complex **17** shifted downfield due to the electronegativity (Ag:1.93, Au:2.54).

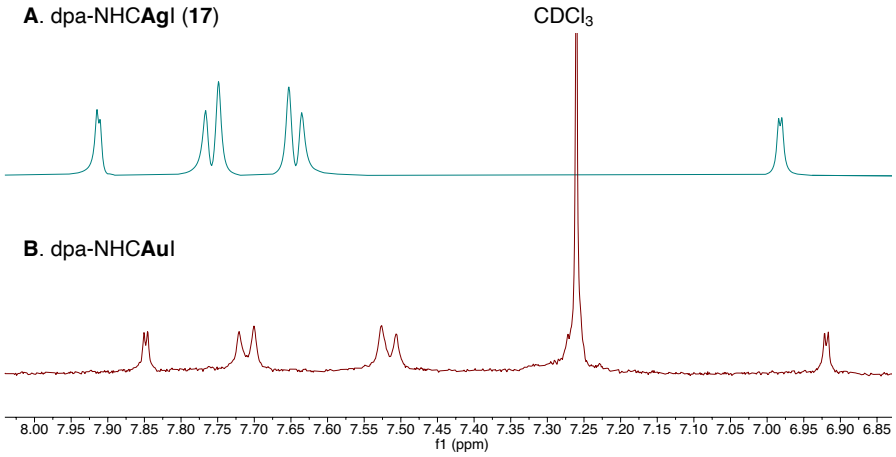

Figure 2.8 Stacked ^{1}H NMR spectra of complex **17** and its gold analog.

Single crystals of **18** were obtained from a CH_2Cl_2/n-hexane two-layer system. The solid-state structure of **18** from an X-ray crystallographic analysis shows an unremarkable Ir–$C_{carbene}$ distance of 2.064(2)/2.066(2) Å, falling in the typical range of those observed in Ir–NHC complexes. However, due to the bulky cyclooctadiene, the Ir(I) centre is forced out of the carbene backbone with an elongated Ir-Cl bond (2.3998(6)/2.4098(7) Å, Figure 2.9), comparable to that observed for the [Ir(IAd)(cod)Cl] complex (2.394(3) Å, Table 2.1).[116]

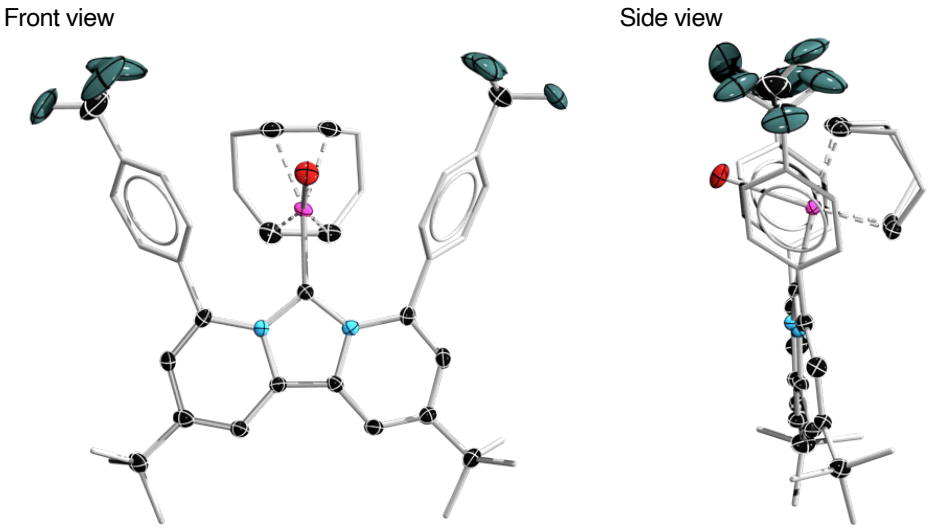

Figure 2.9 Solid-state structure of **18**. The ellipsoids were set at 30% probabilities. Periphery atoms on ligands and solvent molecules are omitted for clarity.

NHC	Ir–C^{car}	Ir–Cl	Ir–C$^{cis\text{-}cod}$	Ir–C$^{trans\text{-}cod}$
IAd	2.065(9)	2.394(3)	2.109(15)	2.1795(!4)
ICy	2.090(13)	2.357(3)	2.1015(18)	2.169(21)
IMes	2.055(5)	2.3527(14)	2.118(7)	2.1845(8)
IDipp	2.054(5)	2.3395(14)	2.125(7)	2.1845(8)
dpa^{Ar2}-NHC	2.064(3)	2.400(3)	2.095(1)	2.163(1)

Table 2.1 Bond length around iridium centers of IrCl(cod)(NHC) complexes

VT ^{1}H NMR experiments revealed that the four broad signals at room temperature, assignable to aryl groups, sharpened at –60 °C. The ^{19}F NMR spectrum shows a sharp singlet at –62.4 ppm with no changes at until dropping temperature to –60 °C (Figure 2.19). The ^{13}C{^{1}H} NMR spectrum of **18** in CD_2Cl_2 revealed a singlet at 161 ppm, assignable to the carbene carbon atom, upfield-shifted in comparison to the free carbene **8** (δ_C = 196 ppm in C_6D_6) and other dpa-NHC complexes in the literature[68–70,75,77–79,117].

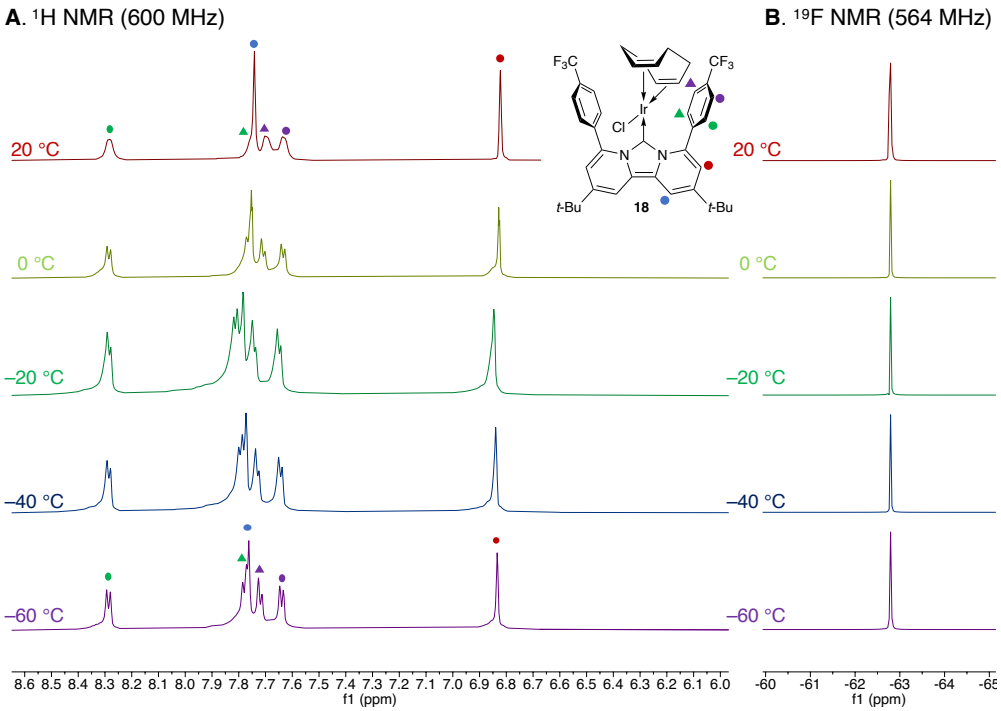

Figure 2.10 VT NMR of complex **18**

After obtaining the iridium complex, ligand substitution reactions were carried out for carbonyl(CO), phosphines, and phosphates (Scheme 2.5). In short, the carbonyl reaction has possibility to convert from cod to CO, but most of the reaction gave the recovery of starting materials. Carbonyl reaction should work in typical NHC complexes [IrCl(cod)(NHC)]; however,

ligand substitution to CO ligands on complex **18** did not work well. In CH_2Cl_2 solution, $Ir(NHC)Cl(CO)_2$ complex was readily decomposed to give the imidazolium salt with iridium counter-anion detected by X-ray crystallographic study. Although toluene was useful in providing ligand substitution, complex **19** was not fully characterized yet. Phosphine and phosphite were also used for ligand substitution as well as CO. However, neither phosphine nor phosphite was not providing clean products **19**.

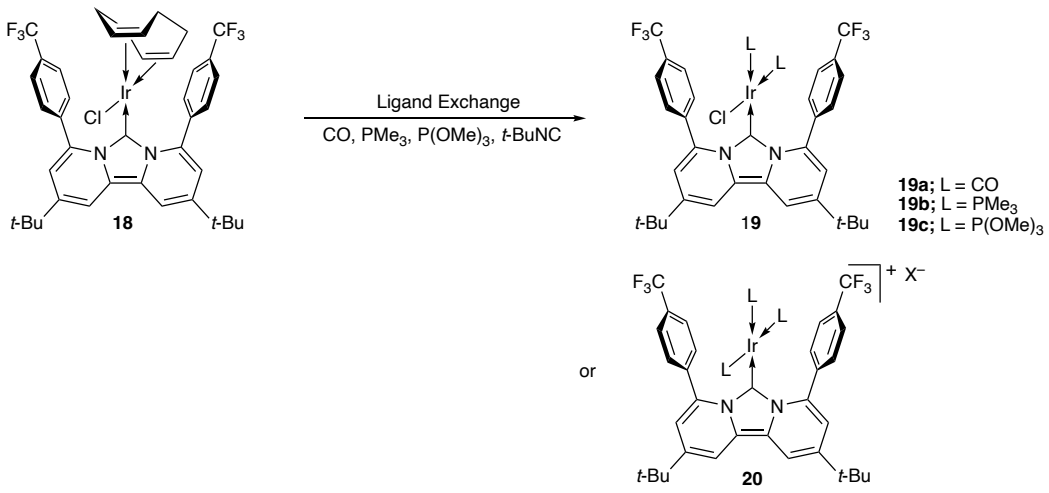

Scheme 2.5 Ligand substitution reaction from the cod ligand.

Ligand substitution seems to be hard because of sterically hindrance. Normal [Ir(NHC)Cl(cod)] complexes have vacant dz^2 orbitals without hindrance, which allows the first incoming ligand can be coordinated to the iridium center. Then, 18-electron trigonal bipyramidal geometry would be formed. After the original ligand was dissociated, the second incoming ligand was ligated. This "associative" process generally occurred. In the case of NHC with bulky substituents such as adamantyl (IAd), CO substitution was much slower than typical ones like IMes, IDr, and I*t*Bu[116] because of the satirical hindrance for metal dz^2 orbitals. For complex **18**, its dz^2 orbital was mostly covered by aryl groups. These prevent coordination toward the dz^2 orbital.

X-ray analysis on the red crystals of **20** in Figure 2.12 revealed a square planar geometry of the Ir(I) in the solid-state structure, residing in plane of the carbene backbone (Figure 4). The Ir-$C_{carbene}$ distance of 2.054(6) Å is similar to that in **3**. The Ir–C3 distance of 1.934(9) Å is slightly shorter than Ir–C2 and Ir–C4 (1.967(7) and 1.927(7) Å respectively), reflecting the structural trans effect of the dpa-NHC. The NMR spectra of **20** is unremarkable. The signal of carbene carbon was not observed in the $^{13}C\{^1H\}$ NMR spectrum.

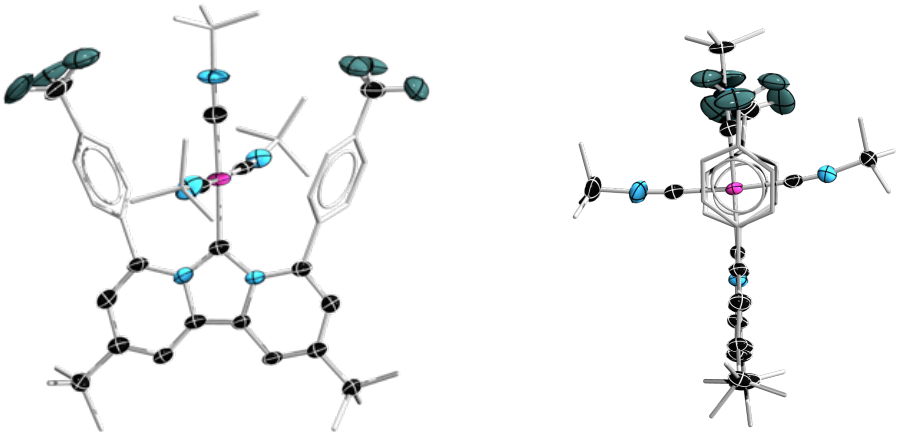

Figure 2.11 Solid-state structures of **20** The ellipsoids were set at 30% probabilities. Periphery atoms on ligands are omitted for clarity.

2.3. Cyclometallation of arylated dpa-NHC

Braunstein reported the detailed mechanistic investigation of the formation of iridium(III) complexes bearing *m*-phenylene-linked bis-NHC described in Scheme 2.6. This reaction mechanism was summarized in scheme 2.5. The initial step of this reaction was the complexation of NHC by base (Cs_2CO_3 or NEt_3), which isolated by brief refluxing in MeCN and fully characterized. Oxidative addition of the C–H bond between heterocyclic moieties took place accompanied by the ligand substitution from cod to two MeCN ligands. Afterward, deprotonation (or reductive elimination of HX) yielded the iridium(I) species bearing the mono-cyclometallated NHC ligand. Finally, the oxidative addition of the C–H bond between nitrogen atoms on the imidazolium ring provided the desired pincer complex. The hydride on iridium was confirmed by the deuterium experiment[103].

What is noticeable for the pincer complex is coordinated MeCN ligands. One MeCN readily replaced by iodide, which was from the carbene precursor. When weakly coordinated counter-anions such as BF_4 or PF_6, ligand exchange did not occur. If bulky substituents such as *t*-butyl or adamantyl, coordinatively unsaturated iridium(III) complexes were obtained with the open coordination space trans to the aryl group[89], or mixed NHC/abnormal NHC pincer ligands were synthesized[118].

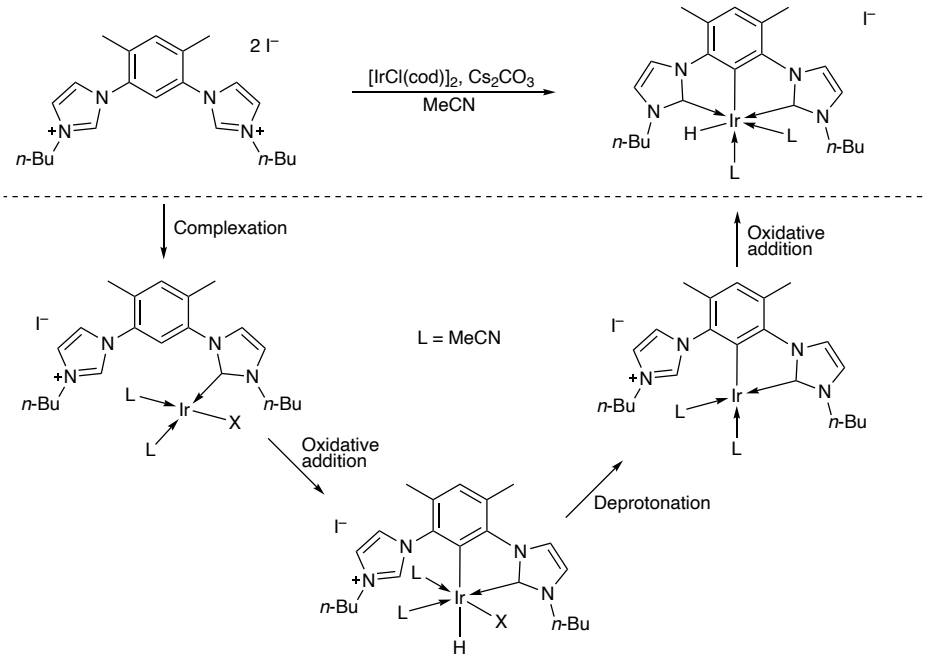

Scheme 2.6 Proposed reaction mechanism of pincer NHC complex by Braunstein[103]

For the NHC-core pincer ligands with aryl anchors, Tu investigated with DFT calculation (Scheme 2.7).[107] After NHC complexation toward $[IrCl(cod)]_2$, the first metallation took place. In the case of η^4-cod coordination, these activation barriers were no lower than 30 kcal/mol, which were inconsistent with their experimental condition of room temperature (298 K). In particular, base-promoted metalation required much high energy barriers (85.2 kcal/mol) likely owing to the steric

repulsion between the base of HMDS and NHC substituents. Alternatively, it provided a reasonable energy barrier (23.0 kcal/mol) to change the coordination mode of cod from η^4 to η^2. Afterward, oxidative addition of C–H activation at the opened coordination space. Noticeably, such a C–H activation process was favored in their NHC with spiro-bicycles. In the case of 5 or 6-membered NHC with phenyl substituents on nitrogen, higher activation energy is required than that of a spiro-bicycles system. Elimination of HCl, which was quenched by HMDS, and spontaneous re-coordination of free olefin moiety of cod gave a bidentate-NHC iridium(I) complex. This intermediate was almost the same as Braunstein's, which yielded the pincer complex through the second C–H activation with oxidative addition.

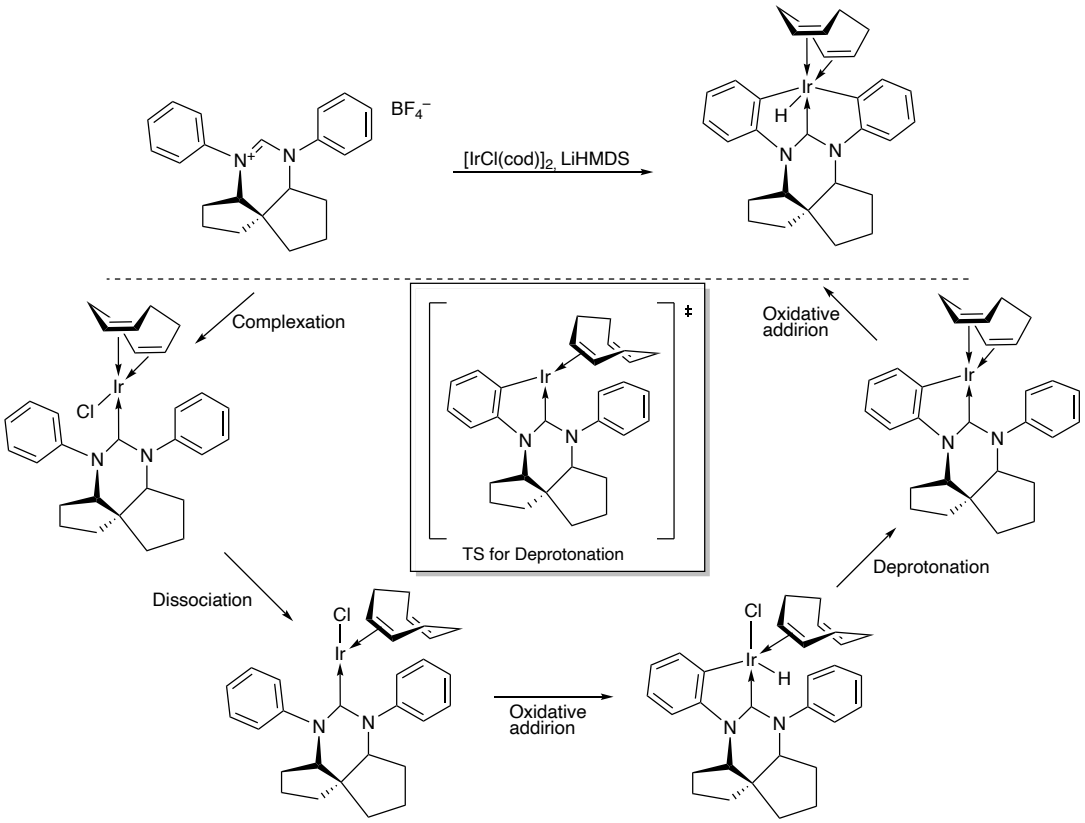

Scheme 2.7 Proposed reaction mechanism of pincer NHC complex by Tu

In short, the formation of NHC-pincer iridium complexes consisted of first C–H activation, deprotonation of Ir–H, and second C–H activation. Based on the reported mechanism for cyclometallation, we hypothesized that complex **18** would undergo cyclometallation. Oxidative addition of C–H bond at ortho position on aryl moieties provided the one-side cyclometalled Ir(III) complex. Afterward, deprotonation by a base such as Cs_2CO_3, followed by the second oxidative addition might yield the desired iridium pincer complex (Scheme 2.8).

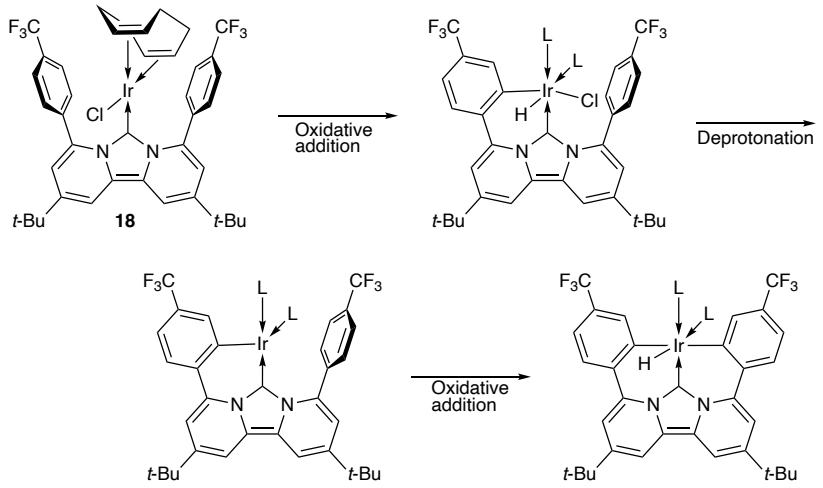

Scheme 2.8 First expected reaction mechanism for cyclometallation of **18**

To promote C–H bond activation for synthesis and isolation of any Ir(III) complex, reaction mixture of complex **18** in toluene or acetonitrile were refluxed overnight in the presence of the base (Cs_2CO_3). All attempts led to mixtures of unidentified products, which was an inseparable mixture. All attempts to obtain heteroleptic pincer complexes told us that this method could not be suitable. In view of the DFT calculation, the first oxidative addition of the C–H bond was unfavored in the Gibbs energy (ΔG^0_R = 14.6 kcal/mol). In addition, cyclometallation from complex **20** was attempted upon reflux in MeCN in the presence of Cs_2CO_3. ^1H and ^{19}F NMR spectra suggested no reaction. This is due to the electron-deficient metal center by π-withdrawing isocyanide ligands.

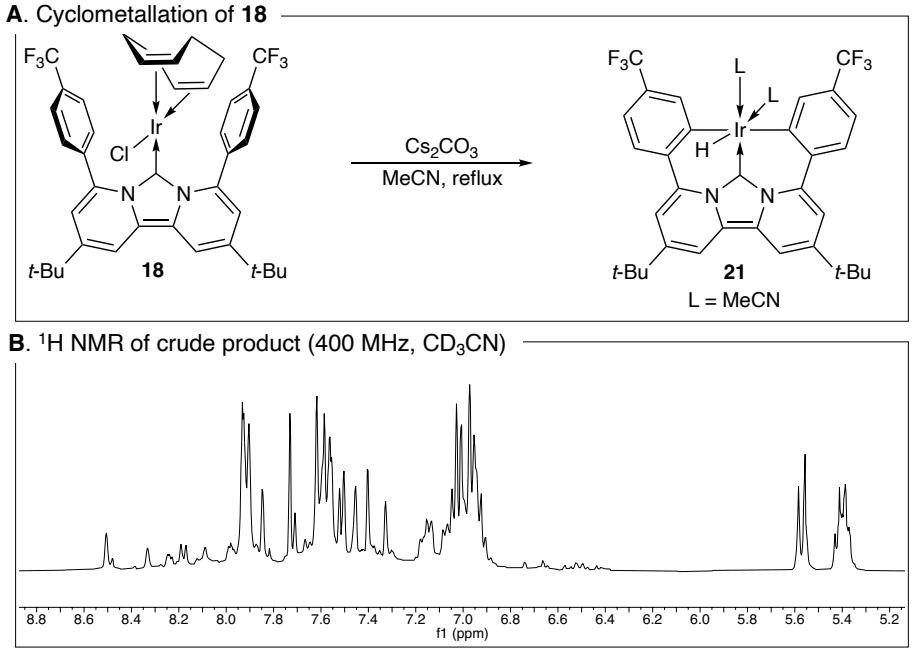

Figure 2.12 Attempted cyclometallation from **18**

However, a one-pot reaction of **7** and over quarter equivalents of $[Ir(cod)Cl]_2$ at the reflux of acetonitrile in the presence of Cs_2CO_3 afforded a major product isolated as a wine-red solid (Scheme 2.9). Note that Cs_2CO_3 was hygroscopic, which made a decomposition during the reaction. Therefore, this base must be dry prior to use. (We can dry it up *in vacuo* overnight.) ^{19}F NMR spectrum of the product in CD_3CN showed a sharp singlet at –62.9 ppm corresponding to the four chemically equivalent $–CF_3$ groups. ^1H NMR indicated the formation of the pincer ligand based on dpa-NHC framework. Various 1D and 2D techniques were used for the assignment of all the observed signals. In the $^{13}C\{^1H\}$ NMR spectrum, a singlet at 151 ppm was assigned to the carbene carbon atom, which is more up-field shifted than that of the Ir(I) complex **18**. The iridium-bound sp^2 carbon atoms are assigned to the most down-field singlet at 159.78 ppm.

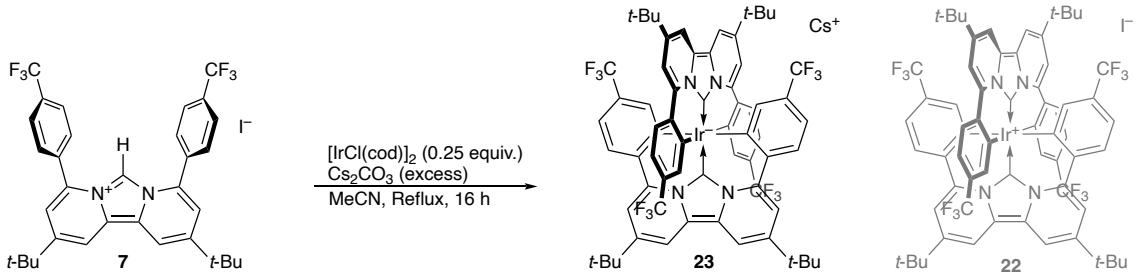

Scheme 2.9 Optimized cyclometallation reaction from the NHC precursor **7**

Single crystals of this product were obtained from the slow diffusion of *n*-pentane into a saturated THF solution. Its solid-state structure in Figure 2.14 A showed an octahedral bis(CCC-pincer) iridium structure with S_4 symmetry, bearing six σ Ir–C bonds with the carbene moieties trans to each other (Figure 2.13 A). The axial $Ir–C_{carbene}$ distance of 1.990(5) Å is shorter than the equatorial iridium-aryl distances (2.109(4) Å and 2.092(3) Å), similar to those observed in octahedral Ir(III) complexes with all η^1-carbon ligands[103,119]. Owing to the formation of 6-membered metallacycles, the CCC-(dpa^{Ar2}-NHC) bite angle (∠C2-Ir1-C3) was 175.73(5)°. This is closer to an ideal meridional pincer bite angle of 180° than those observed in previously reported dianionic carbene-aryl pincer ligands (144.92(15)°-155.27(15)° for C5-C7). In addition, the CCC-pincer backbone is not completely planar, but with C2-C-C-N2 and C3-C-C-N1 torsion angles of 3.8(2)° and 18.4(2)°, respectively, owing to the steric or electronic repulsion of C–H moieties between dpa-NHC framework and aryl moieties.

With this iridium moieties, counter-ion was obtained. According to the numbers of electrons for $I^–$ and Cs^+, the solid-state structure could not characterize the product completely, which means complex **22** $[(CCC\text{-}dpa^{Ar2}\text{-}NHC)_2Ir]^+[I]^–$ or complex **23** $[Cs]^+[(CCC\text{-}dpa^{Ar2}\text{-}NHC)_2Ir]^–$. To identify the counter-ion, the salt metathesis of iodide was attempted. Taking into consideration the counter-anion source from imidazolium salt **7**, this cyclometallation was carried out using **7** with $PF_6^–$. The product and single crystal were obtained in the same manner; however, the SCXRD analysis showed

the same structure in the case of **7** with iodide. On the other hand, the Cs^+ ion was confirmed by trapping with cryptand (Scheme 2.10). In the presence of a cryptand, **24** can be recrystallized with ion separation (Figure 2.13 B). The dissociation of the cesium cation did not change the bonding features of the anionic iridium complex. In the crystal lattice of **24**, the counter ion Cs^+ bridges two adjacent molecules through π-coordination to aryl moieties, forming a chain structure in the crystal lattice (Figure 2.13 C). The Cs–C distances range between 3.420(2) Å to 3.750(2) Å.

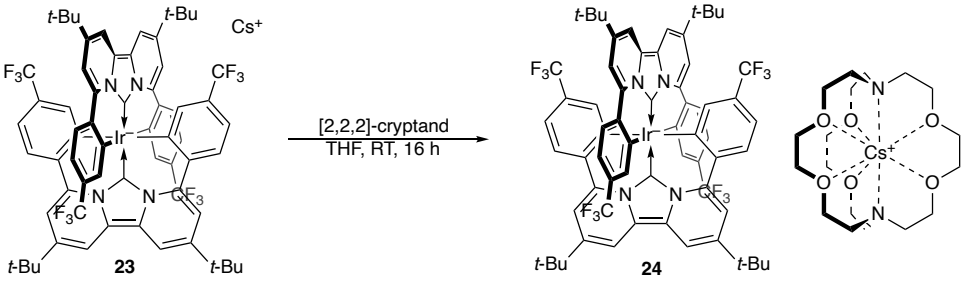

Scheme 2.10 A Cs^+ trapping experiment

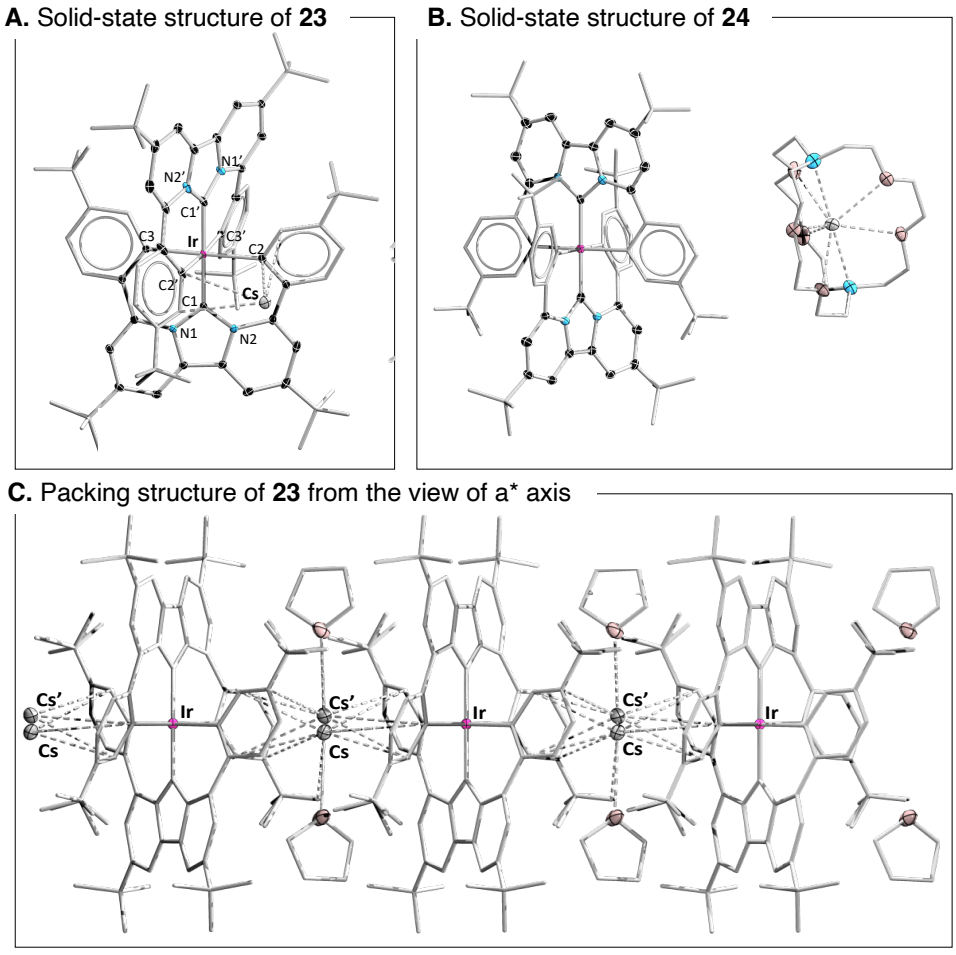

Figure 2.13. Solid-state structures of **23** and **24**. The ellipsoids were set at 30% probabilities. Periphery atoms on ligands are omitted for clarity. The cesium ion for **23** has an occupancy of 0.5, disordered from its special position.

To understand the reaction mechanism, this reaction has been monitored by ^{1}H and ^{19}F NMR spectroscopy in J. Young's tube (See Figure 2.14 and 15). After mixing chemicals, the spectra revealed the reaction did not occur immediately. For 40 hours at room temperature, the complexation of imidazolium **7** to **18** slowly took place. Warming up until reflux accelerated this reaction. ^{19}F NMR spectroscopic monitoring suggested the couple of intermediates was generated and then consumed, which finally served the product **23** and unreacted **7**. However, any intermediate was not observed as a single product, which suggested that the rate-determination step seemed to be in the early stage.

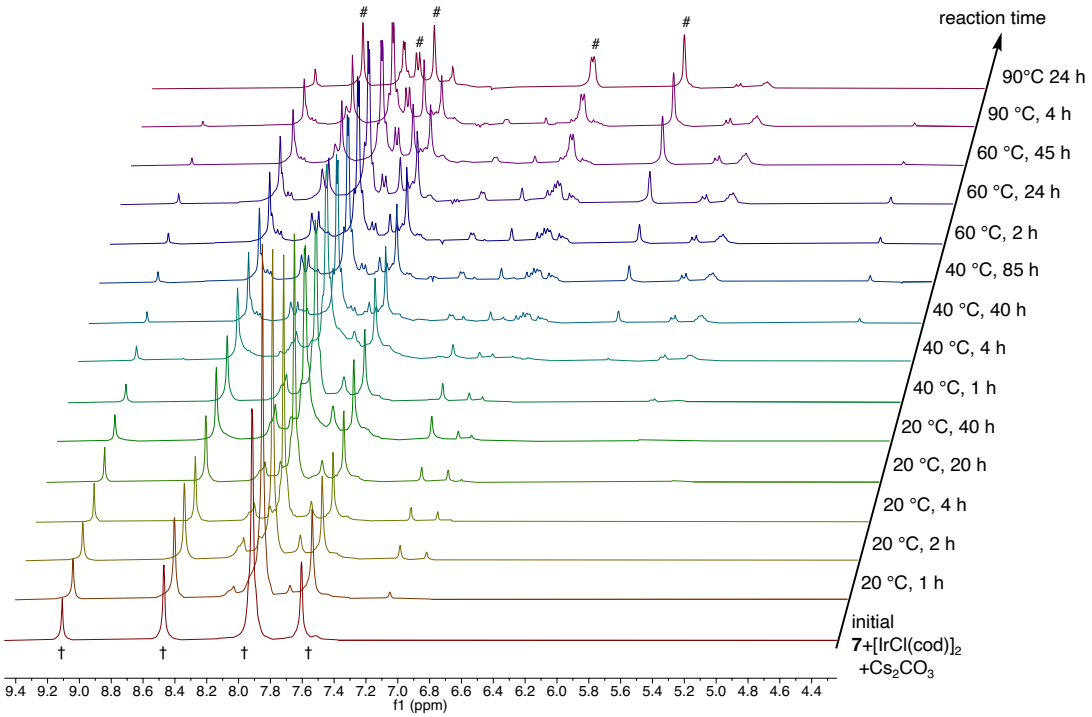

Figure 2.14 Stacked ^{1}H NMR (400 MHz) spectra for cyclometallation from **7**(†) to **23**(#)

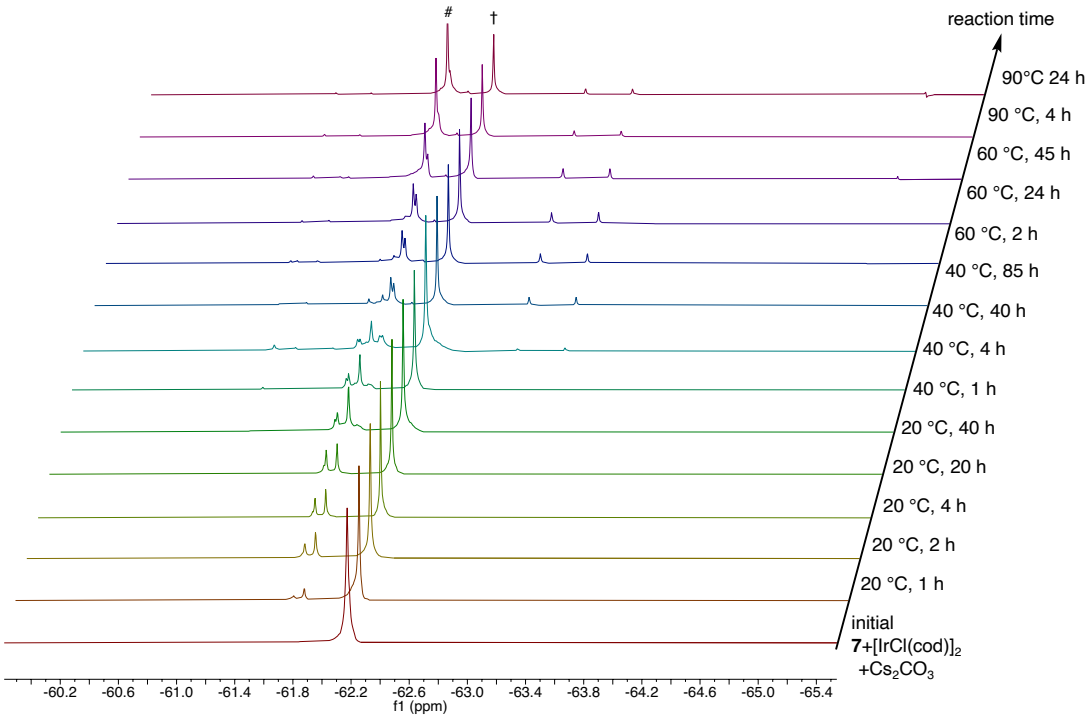

Figure 2.15 Stacked ^{19}F NMR (376 MHz) spectra for cyclometallation from**7**(†) to **23**(#)

To obtain the heteroleptic pincer complex, co-ligands were added to the condition for cyclometallation. Braunstein reported the synthesis of the CF_3-substituted m-phenylene bis-NHC pincer iridium complex[120]. PhCN was added as a co-ligand in this synthesis, and Ir–NCPh complex was obtained. Inspired by this report, PhCN, DMAP, and t-BuNC were employed as additives. For *t*-BuNC, which is strong π-withdrawing, provided complex **20**, assigned by ^{1}H NMR. After complexation, *t*-BuNC was coordinated to the Ir center, probably exchanged to chloride first. Then, owing to the electron-deficient metal center, further ligand replacement rather than C–H activation proceeded. For PhCN or DMAP additive, complex **22** was generated as a sole product. (Due to the mistake for stoichiometry in the NMR scale, imidazolium **7** remained.) The second coordination of dpa-NHC was much favored compared to nitrile and pyridine derivatives.

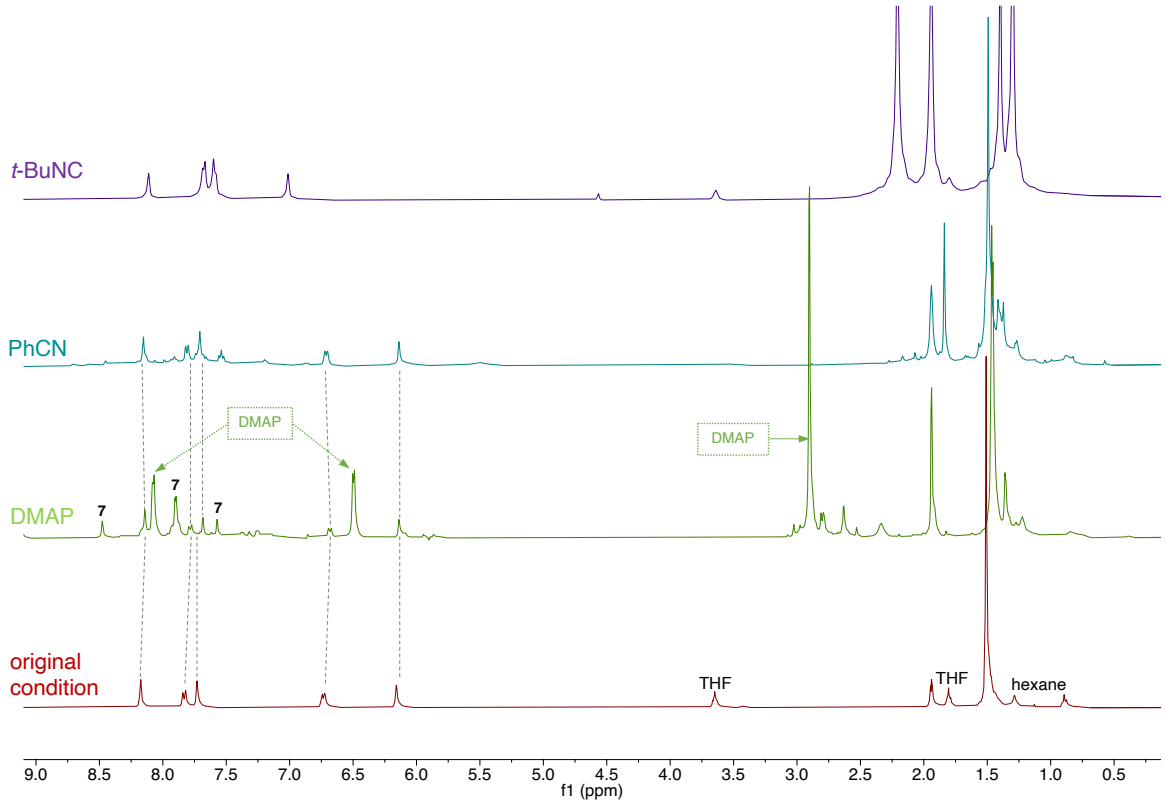

Figure 2.16 ^{1}H NMR spectra comparison of trials to cyclometalation with no additive, PhCN, DMAP, and *t*-BuNC.

The selection of base was also important for this reaction. When K_2CO_3 was employed instead of Cs_2CO_3, complex **23** with potassium cation was not obtained according to the ^{1}H NMR spectra of the crude product. On the other hand, by addition the same equivalent of 18-crown-6 or [2,2,2]-cryptand to K_2CO_3 to increase its solubility of K_2CO_3 such as 18-crown-6 or [2,2,2]-cryptand helped the formation of complex **23** with probably additive-potassium counter-cation fragments. In addition, using Cs_2CO_3 with their additives, complex **23** with cesium adducts (crown ether or cryptand) were obtained with the same efficiency as the original condition. According to these experiments, we could suggest that counter-cation did not affect the reaction mechanism, and the solubility of carbonate was important. Compared with the potassium cation, the cesium cation is larger so that a larger number of solvent molecules were able to interact with the cation. The crown ether and cryptand increase the solubility of byproduct salt, making isolating the desired product difficult. Thus, the most practical method to synthesize complex **23** was to employ Cs_2CO_3 only (Figure 2.17).

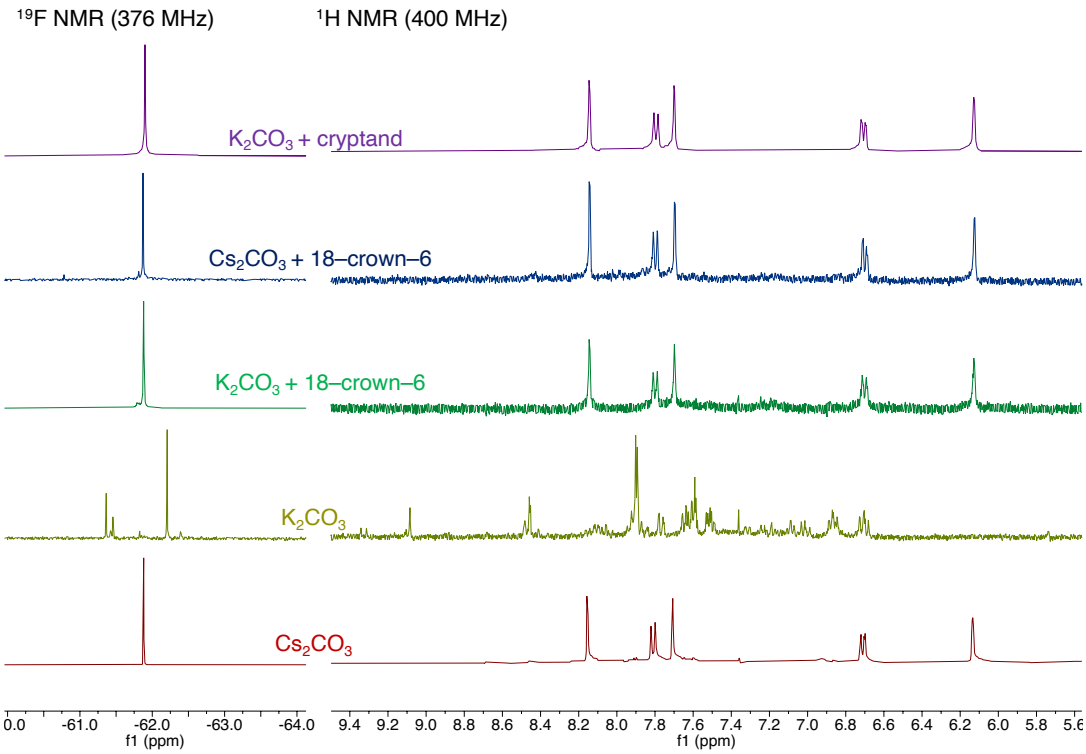

Figure 2.17 Stacked NMR spectra (in CD_3CN) of crude products toward **23** with various bases.

Additionally, the mechanism of the formation of **23** was investigated by DFT theoretical calculations. (Figure 2.18) According to our best mechanistic proposal, the reaction starts from **7** and Cs_2CO_3, which produces cesium iodide and cesium carbonate through $\mathbf{TS_{1(H)I}}$ ($\Delta G_1^{\ddagger}$ = 19.3 kcal/mol). The free carbene complexes to the monomeric [IrCl(cod)] exothermically (ΔG_{R1} = –34.8 kcal/mol) to form **18** (See Figure 2.19 A. for the equilibrium between monomer and dimer). From here, a second Cs_2CO_3 assists in the first C-H bond activation: cesium chloride is first obtained, and via $\mathbf{TS_{18\rightarrow INT\text{-}1}}$ ($\Delta G_2^{\ddagger}$ = 26.4 kcal/mol), $CsHCO_3$ and **INT-1** are produced (ΔG_{R2} = –25.7 kcal/mol)[121,122]. Interestingly, generated $CsHCO_3$ reduced the decomposition barrier of H_2CO_3 (Figure 2.19. B–D). A third cesium carbonate molecule repeats this process downhill deprotonating one more **7** [$\mathbf{TS_{INT\text{-}1\rightarrow INT\text{-}2}}$: $\Delta G_3^{\ddagger}$ = 23.4 kcal/mol], releasing the cod ligand, CsI, $CsHCO_3$ and coordinating the second carbene in **INT-2** (ΔG_{R3} = –22.4 kcal/mol). At this point, the oxidation state of the metal center remained the same. However, given the proximity of the ancillary phenyl rings, an oxidative addition activates one C-H bond from the second coordinated carbene ligand [$\mathbf{TS_{INT\text{-}2\rightarrow INT\text{-}3}}$: $\Delta G_4^{\ddagger}$ = 22.6 kcal/mol] to form an Ir(III) center. The Ir(III) hydride complex **INT-3** is only –4.3 kcal/mol (ΔG_{R4}) below **INT-2.** Still, it triggers a third C-H bond activation mediated by the Ir center [$\mathbf{TS_{INT\text{-}3\rightarrow INT\text{-}4}}$: $\Delta G_5^{\ddagger}$ = 24.0 kcal/mol], eliminating H_2 to yield **INT-4** as an intermediate. This neutral species undergoes its fourth C-H bond activation mediated by Cs_2CO_3 [$\mathbf{TS_{INT\text{-}4\rightarrow 23}}$: $\Delta G_6^{\ddagger}$ = 10.1 kcal/mol] to get one more cesium bicarbonate and the anionic Ir(III) complex **18** (with Cs^+ as counterion). This

reaction is highly exergonic. Although some energy barriers are somewhat high, the reaction can be achieved under the reflux conditions described above. Because of its cascade nature, each early reaction step releases enough kinetic energy to prevent slowing down the next one until completing the whole process.

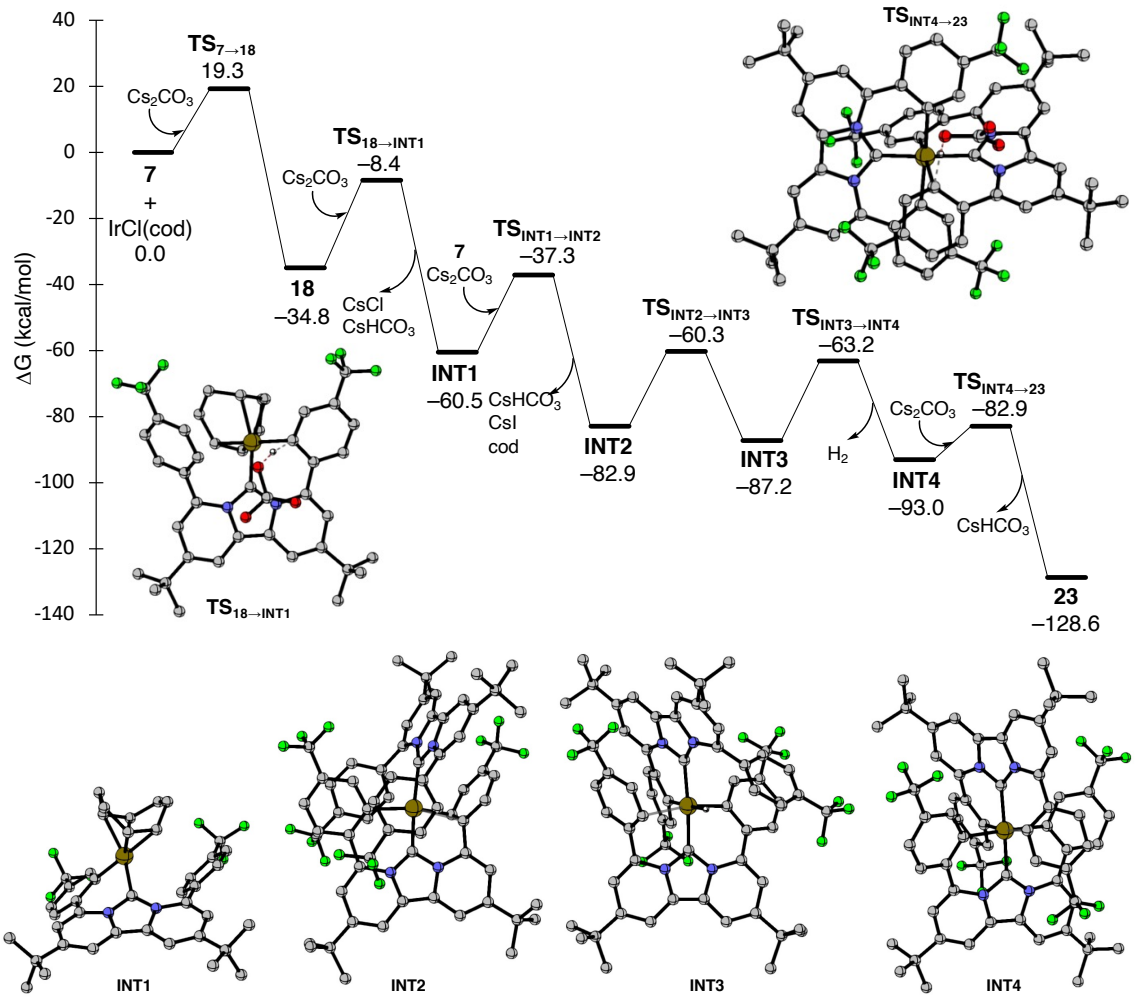

Figure 2.18 Calculated mechanism of the formation of **23** from **7** calculated at the (SMD:acetonitrile)ONIOM[ω-B97XD/(6-31G(d), mod- LANL2DZ):PM6] level.

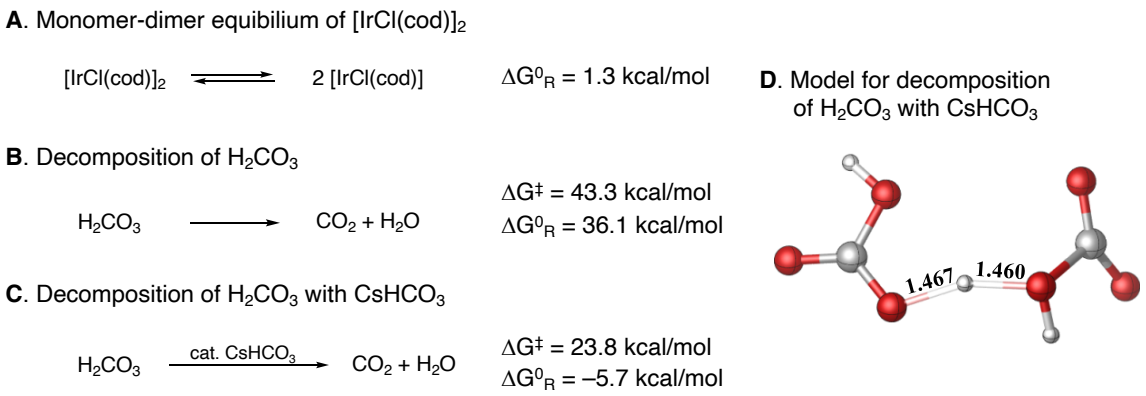

Figure 2.19 Predicted mechanism of side reaction during the formation of **23** form **7**. calculated at the (SMD:acetonitrile)ONIOM[ω-B97XD/(6-31G(d), mod- LANL2DZ):PM6] level.

As described in Scheme 2.6. and 2.7, other reaction mechanisms could be considered. First, C–H activation should occur through a concerted metallation deprotonation process. If our cyclometallation occurred according to Braunstein's mechanism, the cod ligand should have replaced acetonitrile from the **INT-1**. However, Our DFT results implied that this exchange toward **INT-5** is thermally unfavored (ΔG^0_R = 25.4 kcal/mol, see Scheme 2.11.A.). In addition, the HOMO of complex **18** was delocalized on π-orbitals of cod moieties. Based on those, the C–H activation of cod ligand could happen simultaneously[123].

With respect to Tu's mechanism, one of two olefin moieties was dissociated to make coordination space for C–H σ-coordination. We did not calculate that pathway. However, the last intermediate was the same as **INT-1;** therefore, the last process is important in mechanisms. The oxidative addition from **INT-1** was estimated in the higher-lying Gibbs energy as 11.7 kcal/mol with the typical transition state of oxidative addition of 31.0 kcal/mol toward generation of **INT-6**. Compared with the most favored pathway (from **INT-1** to **INT-2**, $\Delta G^‡$ = 23.2 kcal/mol), their Gibbs energy for both the transition state and the product were unfavored (See Scheme 2.11 B).

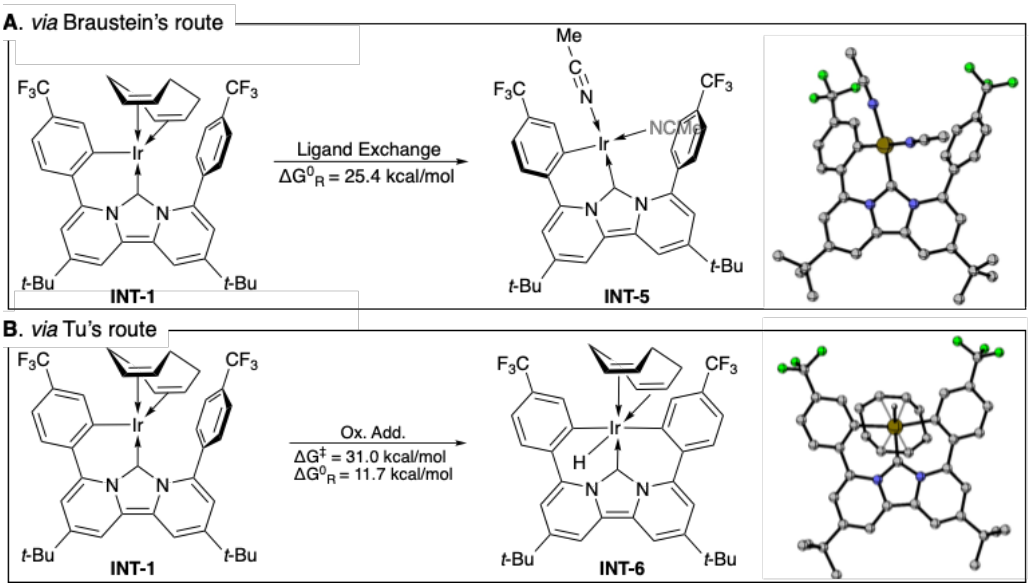

Scheme 2.11. DFT studies for the different reaction pathways suggested by other groups.

The last deprotonation/metalation step of the calculated mechanism was verified experimentally. The protonation of **23** in acetonitrile by equimolar of Et_3N•HCl (Scheme 2.12) led to a relatively clean formation of a neutral Ir(III) complex **25** (**INT-4** in Figure 2.18), from which reddish brown single crystals were obtained (NMR yield ca. 80%). The solid-state structure of **25** revealed that one aryl group was protonated concurrently with an Ir-C bond cleavage (shown in Scheme 2.10), leaving the Ir(III) with a square pyramidal coordination geometry. The closest distances between iridium and the protonated aryl group, Ir-C3 (2.713(5) Å) and Ir-H3 (2.6613 Å) are significantly longer than those of (η^2-CC)-Ir coordination in **18** (2.091(2)-2.165(2) Å). The ^{1}H NMR spectrum of **25** showed two sets of doublets for the protonated aryl group, suggesting no strong localized coordination between the metal and aryl groups in solution at room temperature. In figure 2.14. a signal at 4.5 ppm appeared once and disappeared at the end of the monitoring. According to the ^{1}H 1D and ^{1}H-^{1}H COSY 2D NMR spectra of **25**, the generation of **INT-4** was observed during our monitoring.

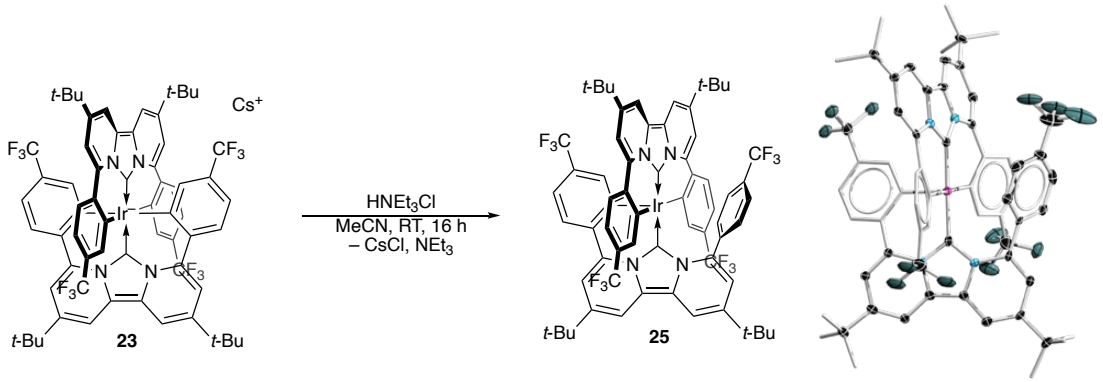

Scheme 2.12 Protonation of **23**

2.4. Electronic properties of 23

The oxidation state of Ir(III) was confirmed by X-ray absorption near edge structure (XANES) measurements. Figure 2.22 shows the Ir L_3-edge XANES spectra. The strong peak appearing at the absorption edge was assigned to the 2p → 5d electronic transition and the oxidation state of Ir can be determined by the peak intensity. The peak intensity of **23** was similar to that of **R** which is an Ir(III) reference compound. Both absorptions are lower than that of Ir(IV)O_2, suggesting the oxidation state of **23** is close to Ir(III).

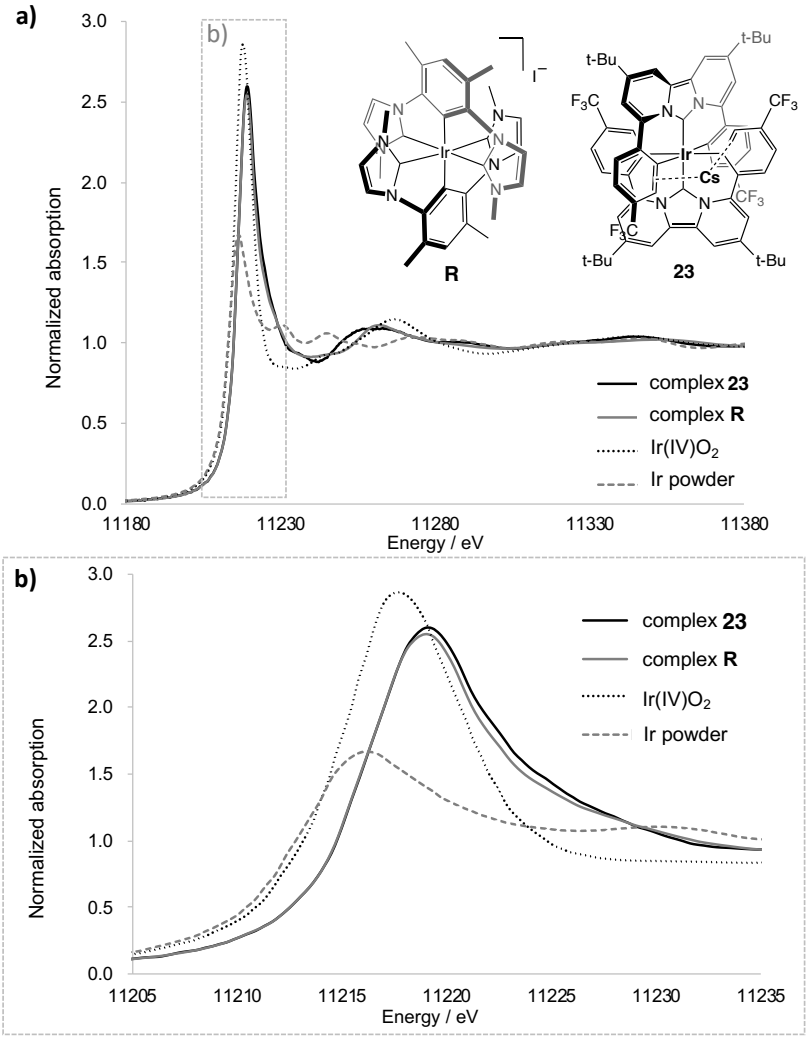

Figure 2.20. Normalized Ir-L3 edge XANES spectra for complex **23** (black solid line), reference compounds **R** (grey solid line), IrO_2 (black dotted line) and Ir(0) powder (grey dashed line). An expansion of a) is shown in b).

Both NMR and UV-Vis spectra of **24** in acetonitrile are almost identical to those of **23**, which suggests a facile dissociation of the ion pair in the solution (Figure 2.23). The UV-vis spectra of **23** and **24** showed a broad absorption with a maximum of 450 nm and 452 nm, respectively. Unfortunately, both **23** and **24** are non-emissive in solution and solid-state. Although the

spectroscopic comparison reviled the almost the same, **23** has a half-life of about 3 days in acetonitrile in air, significantly longer than that of **24**, which is about 3 hours.

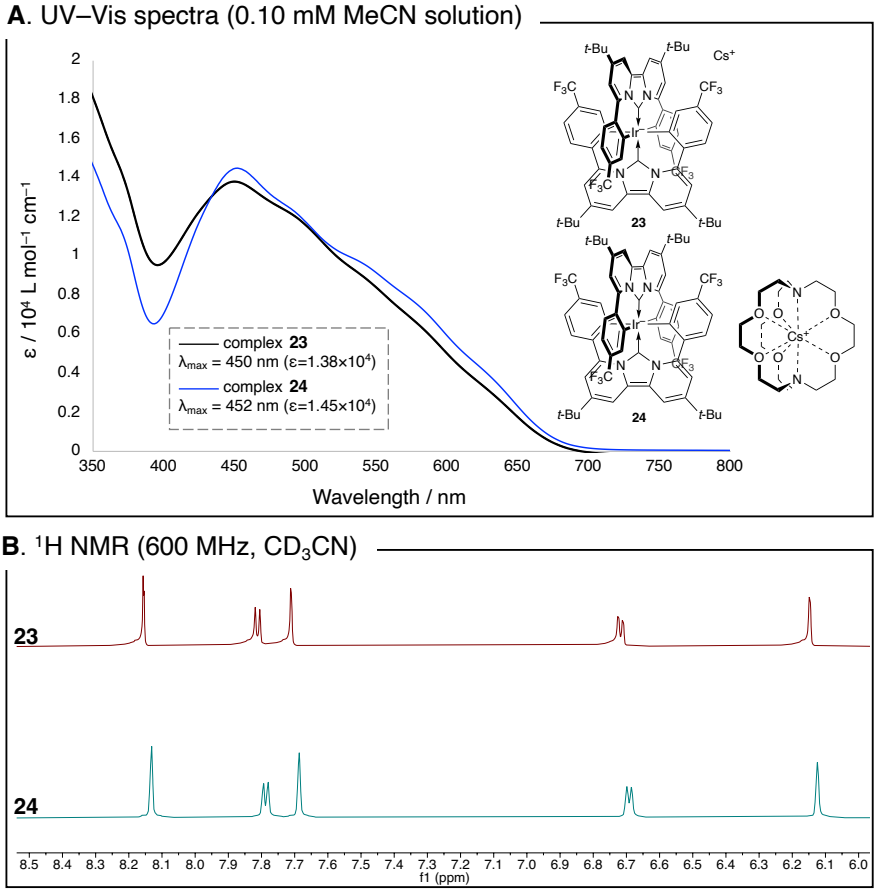

Figure 2.21 Spectroscopic comparison between **23** and **24**

Cyclic voltammetry (CV) measurement of **23** from the open-circuit voltage in acetonitrile showed four redox events (Figure 2.22). The first redox step at $\Delta E_{1/2}$ = –0.51 V (vs Fc/Fc^+) was reversible in a separate experiment, while the second redox event was found irreversible. The $\Delta E_{1/2}$ of the first redox step is much lower than those observed in typical Ir(III) complexes. It is, however, comparable to Rohde's dialkyldiarylguanidinato Ir(III) complexes ([Ir{ArNC(NR_2)NAr}$_3$], $\Delta E_{1/2}$ = –0.27 - –0.41 V vs Fc/Fc^+)[124] and Crabtree's mononuclear pyridine-alkoxide Ir(III) system ($\Delta E_{1/2}$ = –0.18 - –0.69 V vs Fc/Fc^+)[125–127], both of which could be oxidized to afford isolable Ir(IV) and/or Ir(V) complexes. The facile oxidation of **23** is likely due to the extended conjugation between the metal d orbitals with the π-rich CCC-dpa^{Ar2}-NHC pincer ligand.

On the other hand, the second redox event corresponding to Ir(IV/V) couple was found to be irreversible at room temperature. However, when measured at –45°C, the voltammogram showed three reversible waves. These results suggest that while the oxidation from Ir(III) to Ir(V) may be possible at low temperatures, the Ir(V) species generated after $2e^-$-oxidation undergoes an

irreversible chemical reaction rapidly in solution at room temperature (See Chart 2.2). This CV also suggested the third signal close to 0.35 V was observed at –45 °C. This could be assigned as the ligand-based redox wave. CV measurements of both compound **7** and **8** were conducted. While **8** was decomposed during measurement, two redox waves were observed in compound **7**. Thus, this wave could be ligand-based redox behaviors.

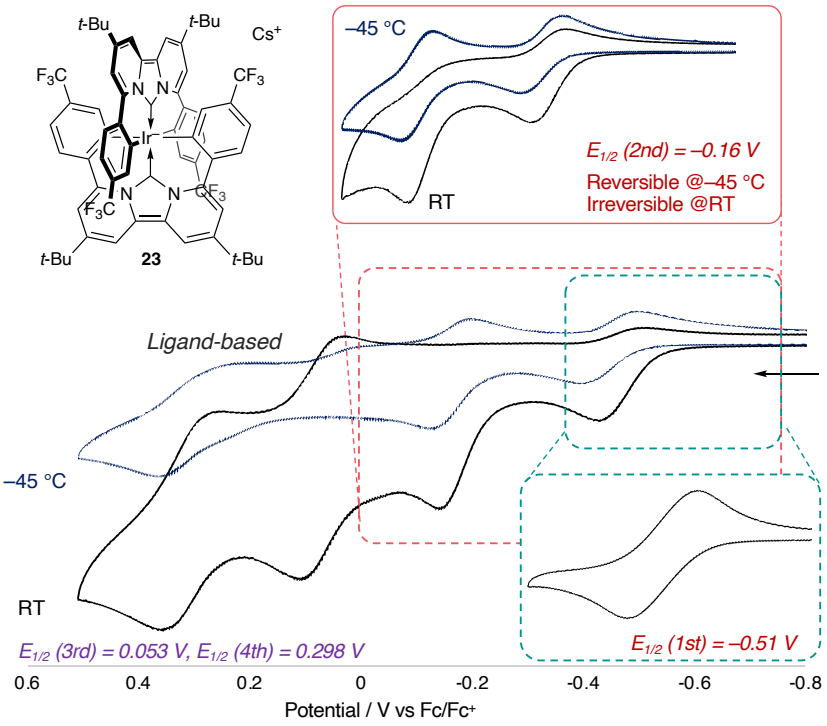

Figure 2.22. CV of complex **23** in MeCN solution with 0.1 M $TBAPF_6$. Scan rate : 100 mV/sec.

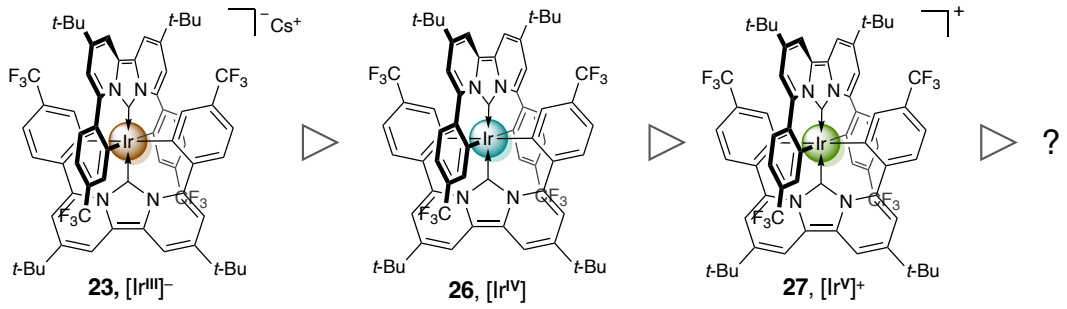

Chart 2.2 Expected oxidation behaviour from complex **23**

2.5. Conclusion

This capture discusses the search of suitable reaction conditions to obtain the arylated dpa-NHC pincer complex. Three general strategies were investigated, including 1) heating free arylated dpa-NHC to promote the cyclometallation (intramolecular C–H activation), 2) stepwise formation via simple complexation of dpa-NHC, and 3) the one-pot synthesis from dpa-NHC precursors. While the first trial did not afford desired results due to the thermal stability of carbene, the complexation of dpa-NHC with silver oxide provided the Ir(I)–NHC complex. Using that complex, the cyclometallation was attempted in the presence of the base. This cyclometallation made the product afforded a complex mixture. In order to tune the reactivity, the co-ligand was added to the cyclometallation condition. Strong donating co-ligands did not improve the selectivity, whereas the isocyanide could give the ligand exchange of both cod and halide ligands on iridium, which did not allow cyclometallation even at elevated temperatures. Lastly, the one-pot synthesis from dpa-NHC precursor gave the cyclometallated product with dpa-NHC-based pincer ligand. The charge and oxidation state of the new iridium complex were confirmed by trapping with cryptand and XANES study, respectively. NMR monitoring of this reaction suggested that the rate determination step could be in the early stage and any intermediate could not be identified. Based on DFT study, the reaction mechanism could be considered as the first cyclometallation that occurred after complexation, which was the rate determination step. Afterward, the second complexation, followed by the sequential cyclometallation, yielded the product.

CHAPTER 3.
TRACING OXIDATION BEHAVIOUR FROM AN ANIONIC IRIDIUM COMPLEX TO A TRI-CATIONIC IRIDIUM COMPLEX BEARING DYPIRIDO-ANNULATED NHC-BASED MULTIDENTATE LIGANDS

3.1. Introduction

Since Zhou, Schrobilgen, and Riedel achieved the detection and characterization of the formal oxidation state of IX on the iridium center[128], iridium became to have the largest number of its formal oxidation states in the periodic table[129]. In contrast to the readily available, well-studied Ir(III) complexes, those with high-oxidation states such as Ir(IV) and Ir(V) are fundamentally interesting chemical species[130] in view of the rapidly growing oxidation catalysis field[88,131,132] as well as their role as intermediates in the direct C-H activation in various homogeneous catalytic processes[133–137] Readily available access to iridium's higher oxidation states and larger metal coordination space are thought to provide opportunities for alternative reactivities in catalytic cycles that are previously inaccessible[2], such as C–H, H_2O[131] and H_2[138] oxidation.

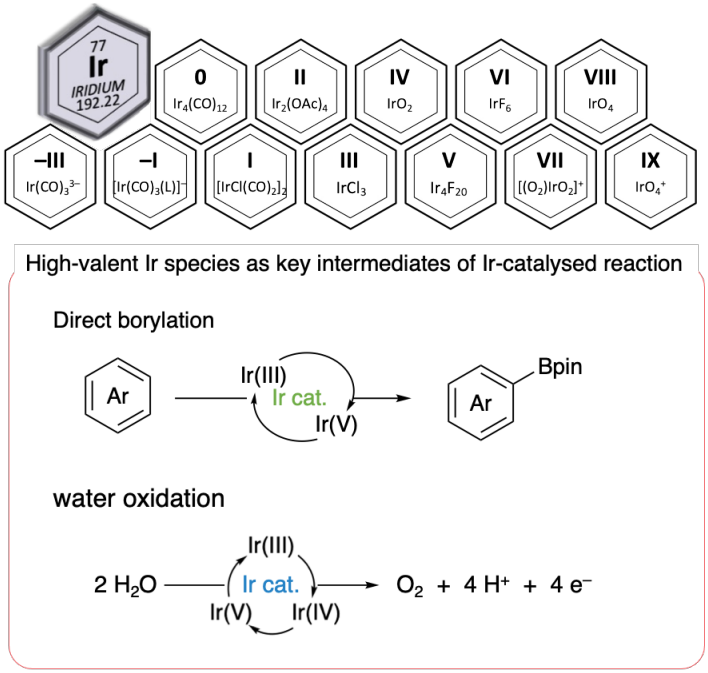

Figure 3.1. Various oxidation states on iridium centers and the crucial role for high oxidation state iridium species in catalysis

One strategy to isolate their high-valent species is employing electropositive elements as donor sites. Electron density increased due to a partial anionic charge on an iridium center. In the last

decade, seven-coordinated Ir(V) polyhydride complexes bearing strong s-donors such as Al[139], Si[140–144], and Ga[145] were fully characterized. Note that Don Tilley's silyl complex was an exception of the six-coordinated iridium complex with highly distorted octahedral geometry[142]. Another strategy is using π-donating ligands, which enable metal-centered oxidation. Cp* has a much strong donating ability and gives thermal stability to high valent iridium species.

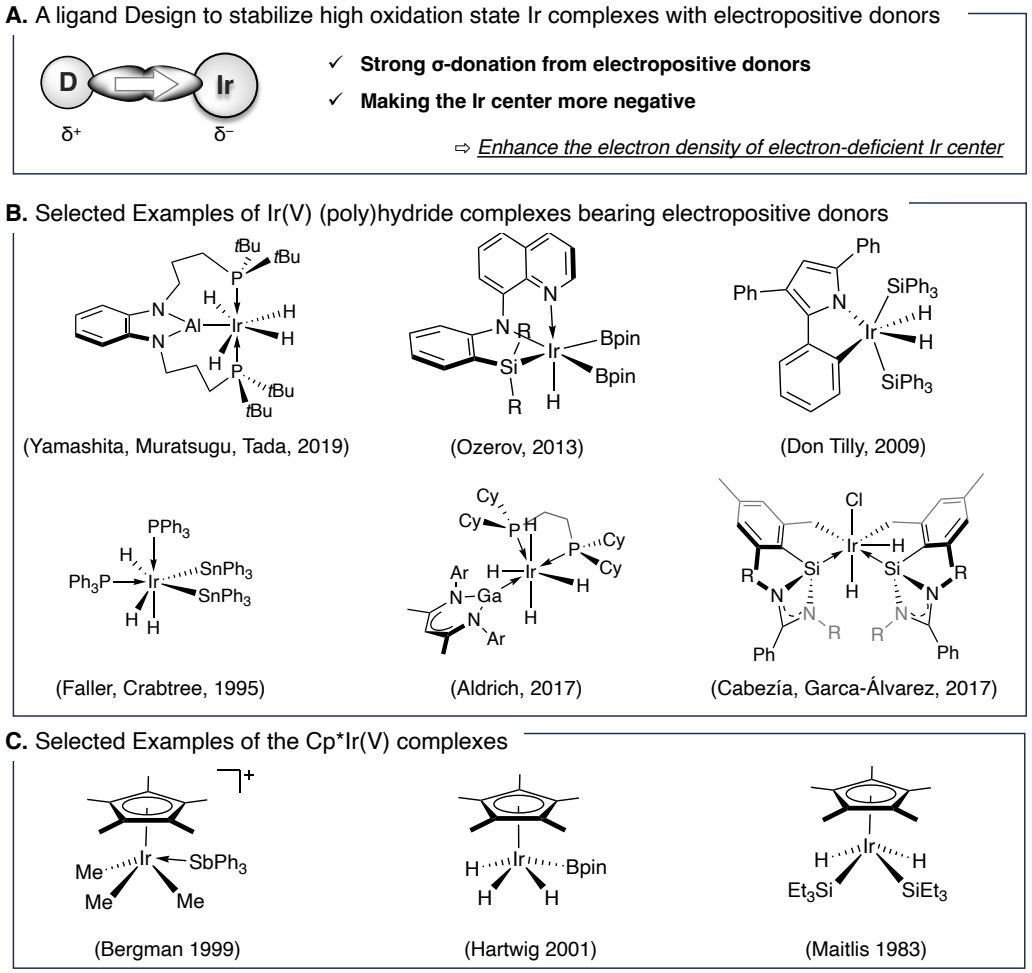

Chart 3.1. First strategy to stabilize Ir(V) complex by electropositive donors

Alternative strategy is using π-donating ligand to stabilize the high valent Ir(IV) and/or Ir(V) complexes. An early work by Levason in 1980s was the systematic investigation of *cis*- and *trans*-L_2IrX_4 (X = Cl or Br) using pnictogen and chalcogen donors, suggesting that electronic properties of ligands were key factors to stabilize electron-poor Ir(IV) species rather than kinetic stabilization[146,147] After the structural characterization of formally Ir(IV)Cl_4 species bearing 1,10-phenanthroline **A** in 1988[147], π-donating (π-rich) ligands have been employed to access the high oxidation states of iridium complexes (Chart 1). Eisenstein and Crabtree investigated the redox behaviour of their cyclometallated Ir(III) biphenyl complexes **B**[148], which π-orbital on biphenyl made complex **B** oxidized readily. Cp* (pentamethylcyclopentadienyl) iridium complexes **C**[149] and **D**[138] also showed their redox activities in low potentials compared with cyclometallated Ir(III)

complexes. Using strong π-donating donors such as phenoxide (**E**)[150], amide (**F**)[151] guanidinato (**G**)[124] or alkoxide (**H**)[125,152] ligands, their potential indicated remarkably lower than the reference of ferrocene/ferrocenium (Fc/Fc^+) couple. Especially, the pyridine-alkoxide ligand could stabilize with the Ir(V) complexes[126,153,154]). Through the metal-ligand secondary π interactions, the usually low-lying filled 5*d* orbitals are destabilized (a phenomenon known as anisotropic field oxidation enhancement, AFOE)[155], which allows further oxidization. In addition to the selected examples in chart 3.1 or 3.2, various ligand designs such as bis-phosphino amide pincer ligands[156–159], salen tetradentate ligand[160], and Kläui tripodal ligand[161] were available to access the iridium complexes with high oxidation states

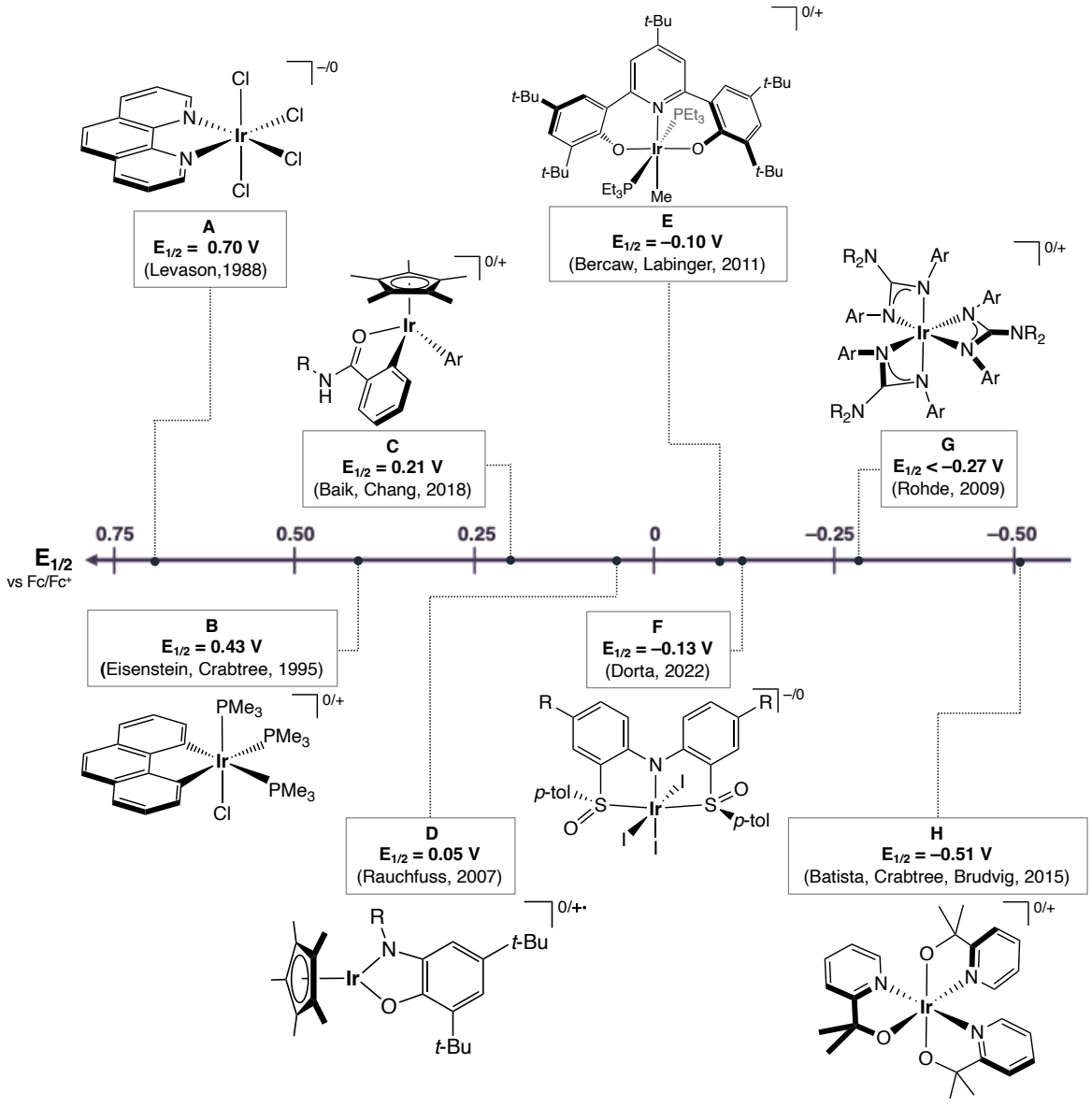

Chart 3.2. Potential chart for Ir(III/IV) redox couple referenced on Fc/Fc^+

Recently the polycyclic aromatic hydrocarbons could be oxidized with the typical oxidants such as $SbCl_5$ or magic blue[162], even though benzene oxidized in abnormally harsh conditions, or unique

special substituents were required. With this concept, the iridacycles could be oxidized as well as showing the reactivity for aromatic compounds[163]. In 1991, Bleeke demonstrated the chemical reactivity of the iridabenzene with various chemicals. Reaction with iodine yielded the diiodide iridabenzene with the dissociation of phosphines, which was said metal-centered oxidation[164]. The unique behavior for only metallabenzene was isomerization. For example, Angelici investigated the redox behavior of the η^4-thiophene iridium complex. Oxidation of the thiophene complex made a product of iridathiabenzene in good yield. Treatment of iridathiabenzene by a base such as triethylamine or basic alumina got the η^4-thiophene complex reversibly[165].

While the insertion of the metal fragment into the benzine ring made a big difference, the polycyclic aromatic hydrocarbon with the metal fragment was rarely studied. To the best of ours knowledge, Yin, and Liu prepared iridium-containing PAHs that have various ring functionality. Their study suggested that the HOMO should have the contribution of iridium's d-orbitals, supported by both red-shift of the tail in UV-Vis absorption and theoretical calculation. The electronic properties, however, showed a reversible redox wave with potentials over 0.8 V, which indicated that their iridium complexes could hardly be oxidized. Considering these results, a new ligand design for facile oxidation of iridium complexes was proposed: a π-rich conjugated system that allows effective interactions between ligand's extended π-orbital and metal d-orbitals.

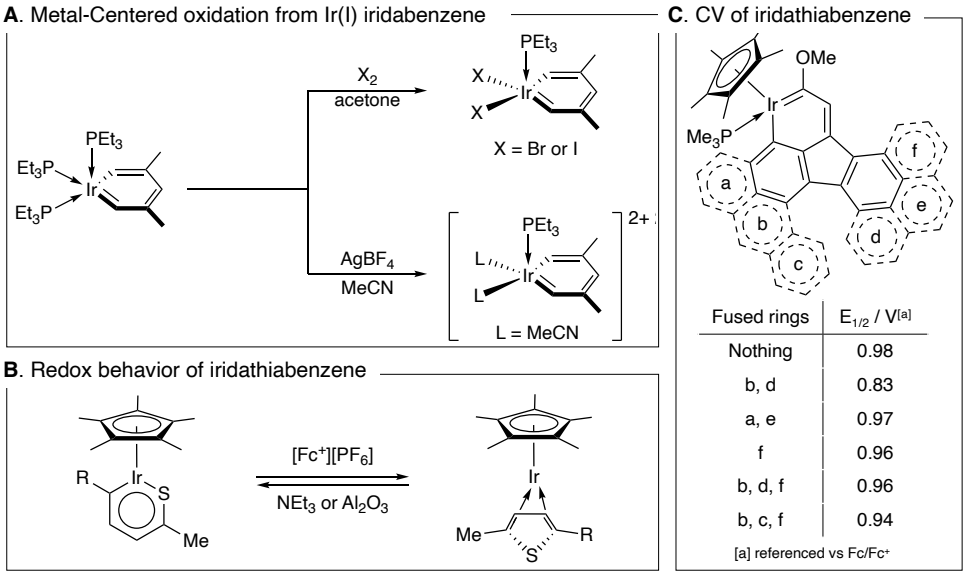

Fused rings	$E_{1/2}$ / V[a]
Nothing	0.98
b, d	0.83
a, e	0.97
f	0.96
b, d, f	0.96
b, c, f	0.94

[a] referenced vs Fc/Fc^+

Chart 3.3. Redox chemistry of iridabenzene derivatives

Previously we established the synthesis of the homoleptic iridium(III) anionic complex **1** bearing the aryl-anchored dipyrido-annulated *N*-heterocyclic carbene (dpa-NHC). The first redox potential of **1** showed –0.51 V, which is remarkably lower than those observed from typical carbon-ligated iridium(III) complexes[166]. The 6-membered metallacycles with dpa^{Ar2}-NHC pincer ligands prevented its decomposition by ligand dissociation. Additionally, dpa-NHC's π-richness reduced the

nature of empty p-orbital in carbenes[65,66,69], which is expected to prevent from migration of ligands to the carbene center at the metal complexes with high oxidation states[44]. Herein, we report the total four-electron chemical oxidation of homoleptic anionic Ir(III) complex **1** bearing bis-pincer ligands. The first two-electron oxidation provided the seven-coordinated Ir(V) intermediate at low temperature, which warming to allow the oxidative coupling of C–C bonds. On the other hand, later two-electron oxidation accessed the high-spin state of the iridium complex.

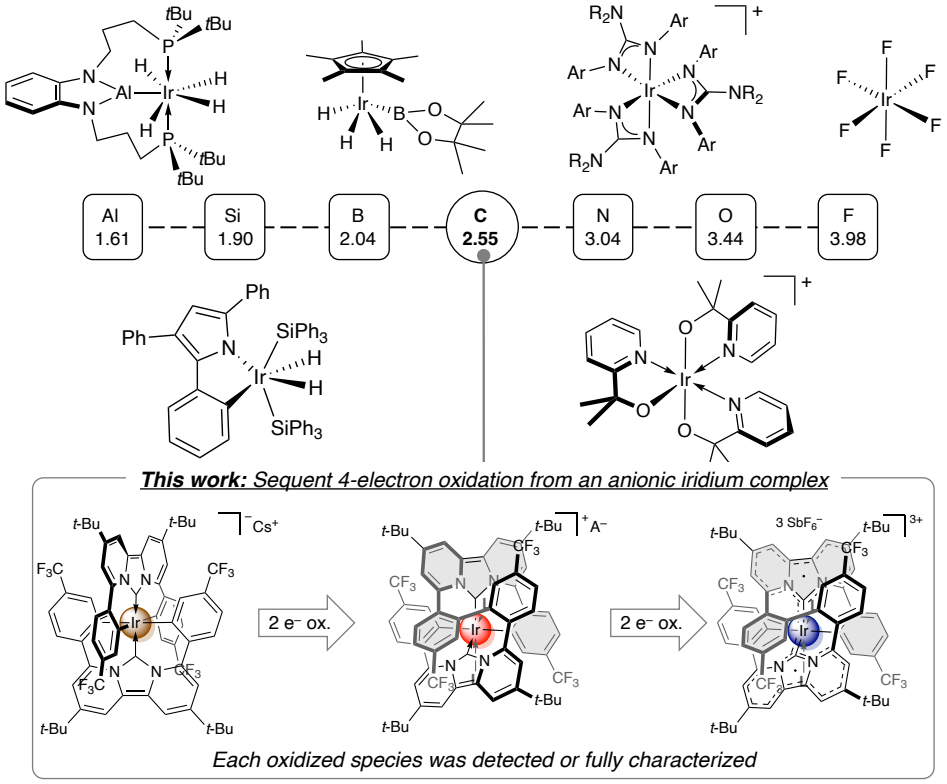

Figure 3.2 A strategy map in chapter 3

3.2. 2-Electron oxidation of the anionic bis-pincer complex 23

The irreversible second oxidation suggests that a chemical reaction occurs after a 2-electron oxidation. This potential was –0.16 V in the MeCN solution, so the oxidants having potential around 0 V such as trityl (–0.11 V), ferrocenium (0 V), and Ag^+ (0.04 V) were employed. The $2e^-$-chemical oxidation of complex **23** was optimized as using 2 equivalents of AgOTf in MeCN at room temperature, yielded a reddish black solution with precipitation of elemental Ag, from which dark red crystals of complex **28** were obtained in 83% yield (Scheme 3.1).

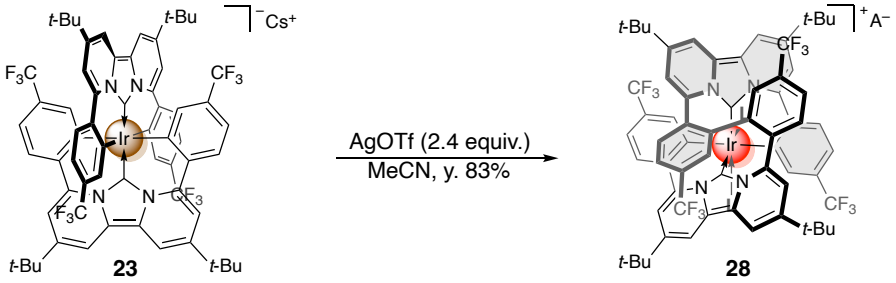

Scheme 3.1. 2-electron oxidation of **23**

In order to obtain the solid-state structure for single crystals for X-ray analysis, counter-anion of cationic complex **28** was exchanged from triflate to BAr^F_4 (Ar^F = 3,5-bis(trifluoromethyl)phenyl). Then, a single crystal was obtained from slowly evaporating a mixture of CH_2Cl_2/*n*-hexane at room temperature. X-ray crystallographic studies of its single crystals revealed a spiro-Ir(III) cationic complex resulting from an oxidative C-C bond coupling of two adjacent aryl groups of the originally separate dpa-NHC units Its solid-state structure also suggested an octahedral anionic CCCC-tetradentate iridium structure (Figure 3.3). This complex had coordinated acetonitrile, which came from solvent. The equatorial Ir–C_{car} distances of 1.977(6) Å and 1.972(6) Å are shorter than the axial Ir–C_{Ar} distances of 2.091(5) Å and 2.087(6) Å. Compared with the starting material **23**, bond distances show no change, whereas the bond angle of C_{car}–Ir–C_{car} was dramatically changed from 180° to 102.4(2)°. Two acetonitrile molecules were confirmed as ligands on the iridium center. Ir–N distances are 2.062(5) Å and 2.080(5) Å, which were in good agreement with Ir–NCMe distances of trans-NHC (~ 2.07(1)) Å.

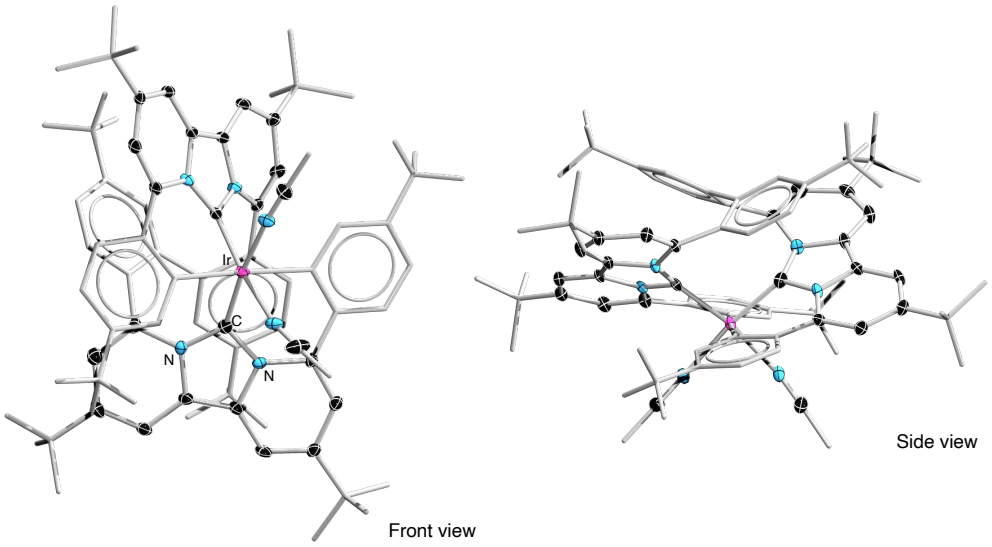

Figure 3.3. Solid-state structures of **28** The ellipsoids were set at 30% probabilities. Periphery atoms on ligands and counter anion of $[BAr^{F}_{4}]^{-}$ are omitted for clarity.

The ^{1}H and $^{13}C\{^{1}H\}$ NMR spectra of **28** showed twice as many signals as those of **23**, indicating that the previously 4-fold symmetry of chemically equivalent protons of **23** in solution had reduced to 2-fold (figure 3.4). Systematic studies by ^{1}H-^{1}H and ^{1}H-^{13}C 2D coupling experiments allowed the assignment of a small singlet at 153.8 ppm to be the Ir-bound aryl carbon atoms, slightly up-field shifted than that in **23** (161.4 ppm). Another small singlet at 161.4 ppm was assigned to the carbene carbon atom, which is about 10 ppm down-filed shifted than that of **23** (153.8 ppm, See Figure). This oxidative coupling reaction at room temperature is consistent with the irreversible 2nd redox event observed in the CV at room temperature.

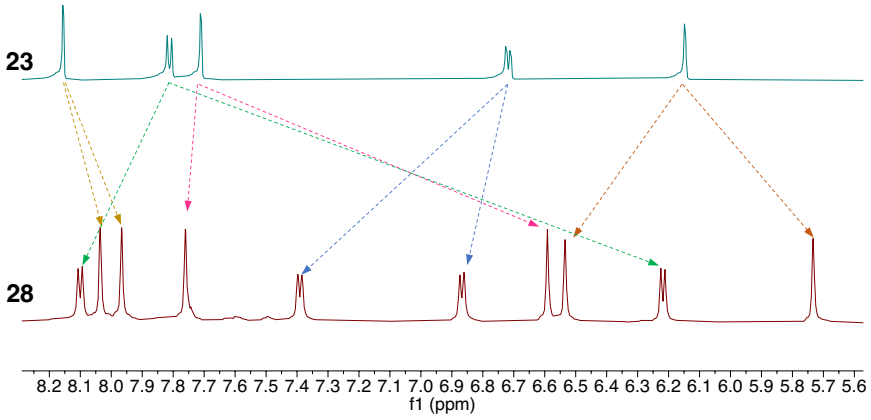

Figure 3.4. ^{1}H NMR spectra of complex **23** and **28**.

While the ferrocenium cation also provided the same product (because of the facile workup, Ag^{+} was employed as the best oxidant to obtain complex **28**, the trityl cation gave the complex mixture, including product **28**. Based on the ^{19}F NMR spectroscopy, the side product could be similar structure of Ir–C bond cleaved product **25**. This is likely due to the close redox potentials between

the trityl cation and the second wave of complex **28**, therefore the trityl cation worked as not only an oxidant but also an electrophile (Figure 3.5 A).

Interestingly, the purplish black solution was obtained when the $SbCl_6$ anion was employed as a counter-anion of trityl. The single crystal was prepared by a two-layer system of CH_2Cl_2/hexane. The X-ray analysis indicated the analog of complex **28**, bearing two Cl^- ligands on the iridium center instead of MeCN. In addition, the counter-anion could be the $SbCl_4$ with seesaw geometry (Figure 3.5 B). Owing to the bad data quality and no reproducibility, publishable data could not be obtained. The UV-Vis-NIR absorption spectroscopy illustrated the NIR absorption with a very wide half-width (over 300 nm) observed as well as an onset of 1000 nm for the UV-Vis absorption band (Figure 3.5 C).

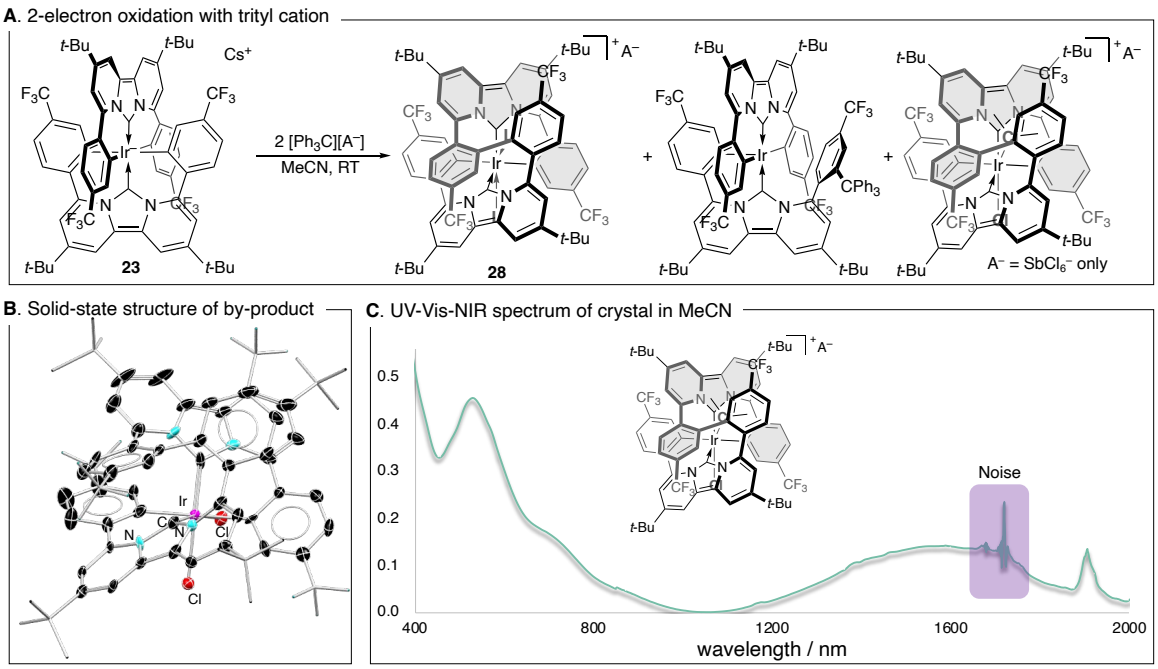

Figure 3.5 oxidation of **28** by trityl cation

3.3. Mechanistic study

In order to observe and identify the intermediate for this ligand-transformation reaction, one-electron oxidation was attempted. To target the oxidation protentional of only the first redox wave (> –0.2 V), $B(C_6F_5)$, $B(OPh_3)$, $(CAAC^{Me})B(C_6F_5)_3$, TCNQ, C_2Cl_6, I_2, O_2 and $[Cp^*_2Fe]^+$ were employed. In the cases of all organic radicals except $(CAAC^{Me})B(C_6F_5)$, the reagents did not work as oxidants, but electrophiles, which is the same as a side product of trityl oxidation (Figure 3.6 A) The oxidation with $(CAAC^{Me})B(C_6F_5)_3$ showed no reaction, probably this was not strong enough to oxidize the iridium complex, or too bulky for carbene to get close to each other. Oxidation reactions by I_2, or O_2 afforded an orange-colored solution, which was NMR silent. However, the UV-Vis-NIR absorption spectra did not show any red to NIR absorption, a characteristic band for Ir(IV) species (Figure 3.6 B and C).

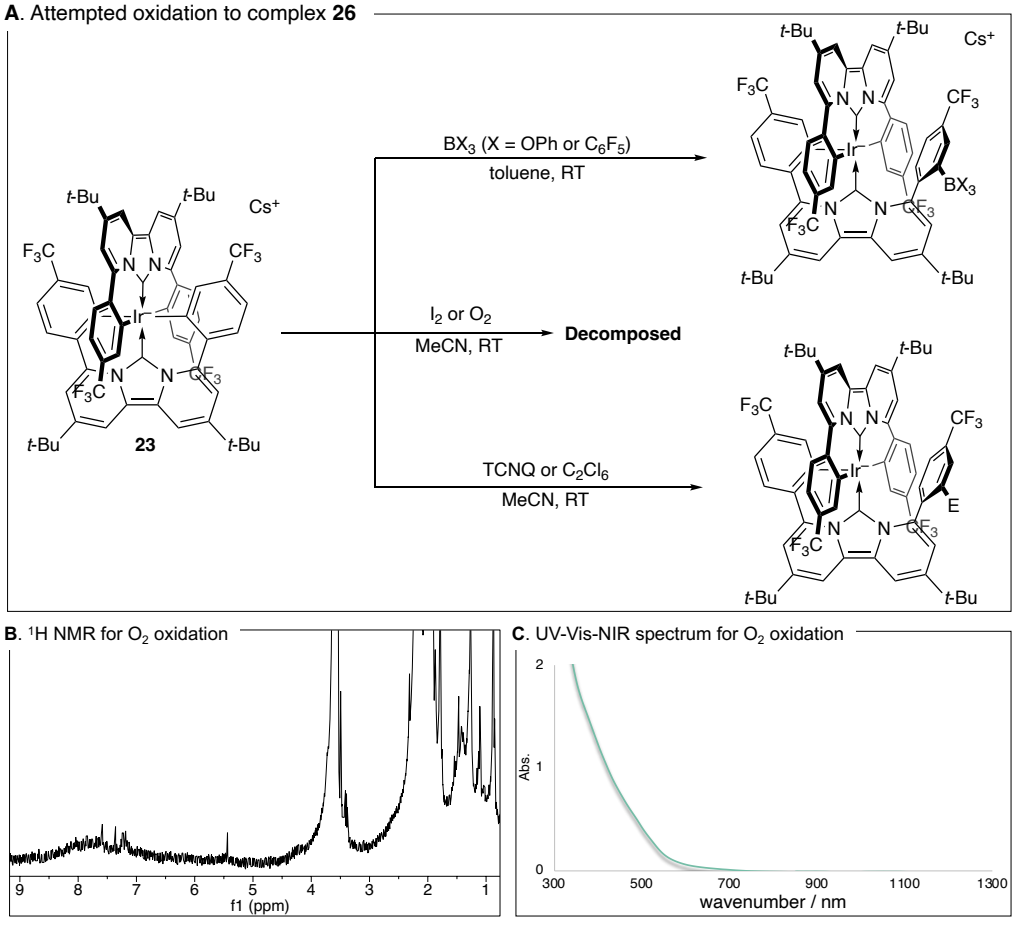

Figure 3.6 Attempted detection of complex **26**.

The reactions of **23** with less than one equivalent of $[FeCp^*_2][OTf]$ ($E_{1/2}$ = –0.49 V, Cp* = C_5Me_5)[167] in acetonitrile-d_3 led to a generation of transient paramagnetic species **26** (Scheme 3.2). This was evident by a significant broadening of the reaction mixture's ^1H and ^{19}F NMR signals,

indicating the paramagnetic species' generation. The signal at –40 ppm in ^{1}H NMR was consistent with the [FeCp*$_2$][OTf] even though less than one equivalent was added, which implied the reaction was slow. [FeCp*$_2$][OTf] does not have electrophilicity different from organic oxidants. Only oxidation occurred regardless of the same potential of **23** for the first redox wave (Figure 3.7).

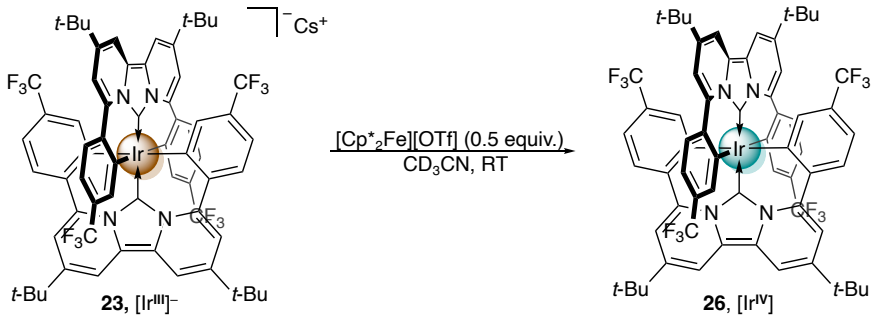

Scheme 3.2 one electron oxidation of complex **23**

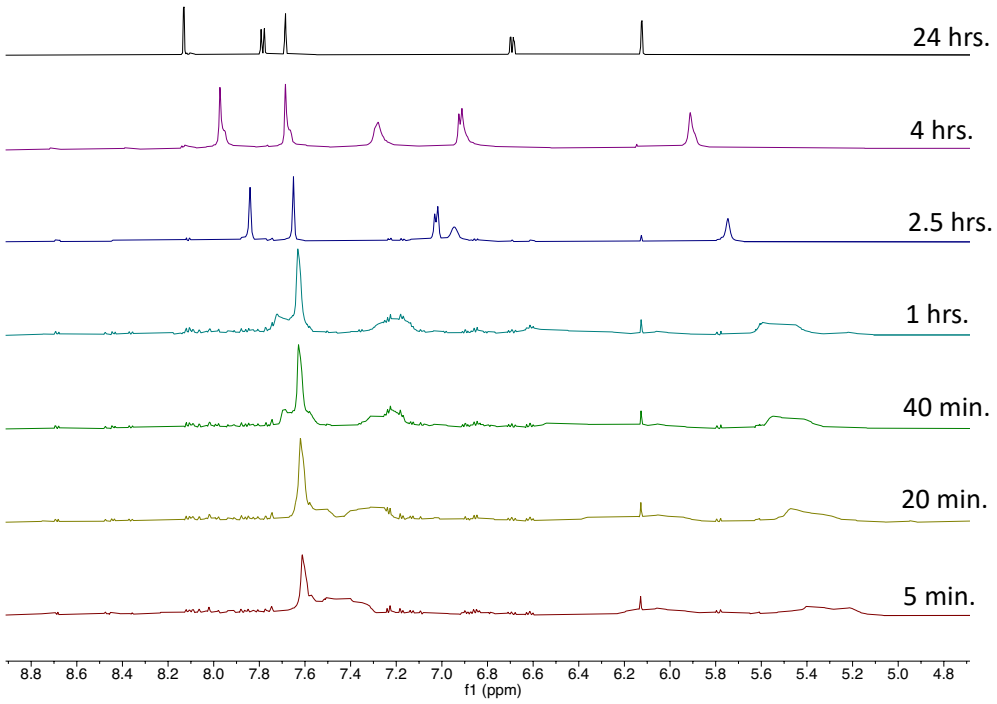

Figure 3.7 ^{1}H NMR screening for oxidation of **23** by 0.5 equivalent of [FeCp*$_2$][OTf].

Based on the NMR study, [FeCp*$_2$][OTf] was employed for detection and isolation of Ir(IV) intermediate **26**. In an *in situ* reaction of **23** with 0.5 equivalent of the [FeCp*$_2$]OTf, a weak signal assignable to Ir(IV) species was detected by X-band electron paramagnetic resonance (EPR) spectroscopy at 4.2 K. The difference spectrum between those of the reaction mixture and the [FeCp*$_2$]OTf provided rhombic signals (g_{xx}= 2.091, g_{yy}= 1.920, and g_{zz}= 1.817, Figure 3.8 A). These relatively small g anisotropies indicated that unpaired electron was delocalized in both the

ligand and the Ir center. A calculated spin-density plot of **26** indicates the radical is metal-based, with some degree of delocalization at one dpa-NHC moiety, reflecting the small g anisotropy or averaged isotropic g value of 1.943(Figure 3.8 A).

Theoretical calculation supported the EPR result. The spin density plot in Figure 3.8 B illustrated the largest contribution from the iridium center (32.9 %) This value is close to the Dorta's Ir(IV) complex (33%)[151]. Interestingly, the next largest contributions were from the C=C π orbital on the 5-membered ring of dpa-NHC. (ca. 8%) Weiss's calculation suggested that SOMO for analogs of compound **4** demonstrated the large contribution of the π-orbitals on the ortho- and para-positions, which is constated with our theoretical results[66]. In addition, IBO analysis showed that the electron-occupied d-orbitals were found as two full and one half-filled 5d orbitals (Figure 3.8 C). Especially, the half-filled one had a strong interaction with one carbene's p-orbitals for the β-electrons. This suggested half-filled d-orbital was interacted with π-orbital of dpa-NHC efficiently, which could reflect the anisotropy of g value in complex **26**.

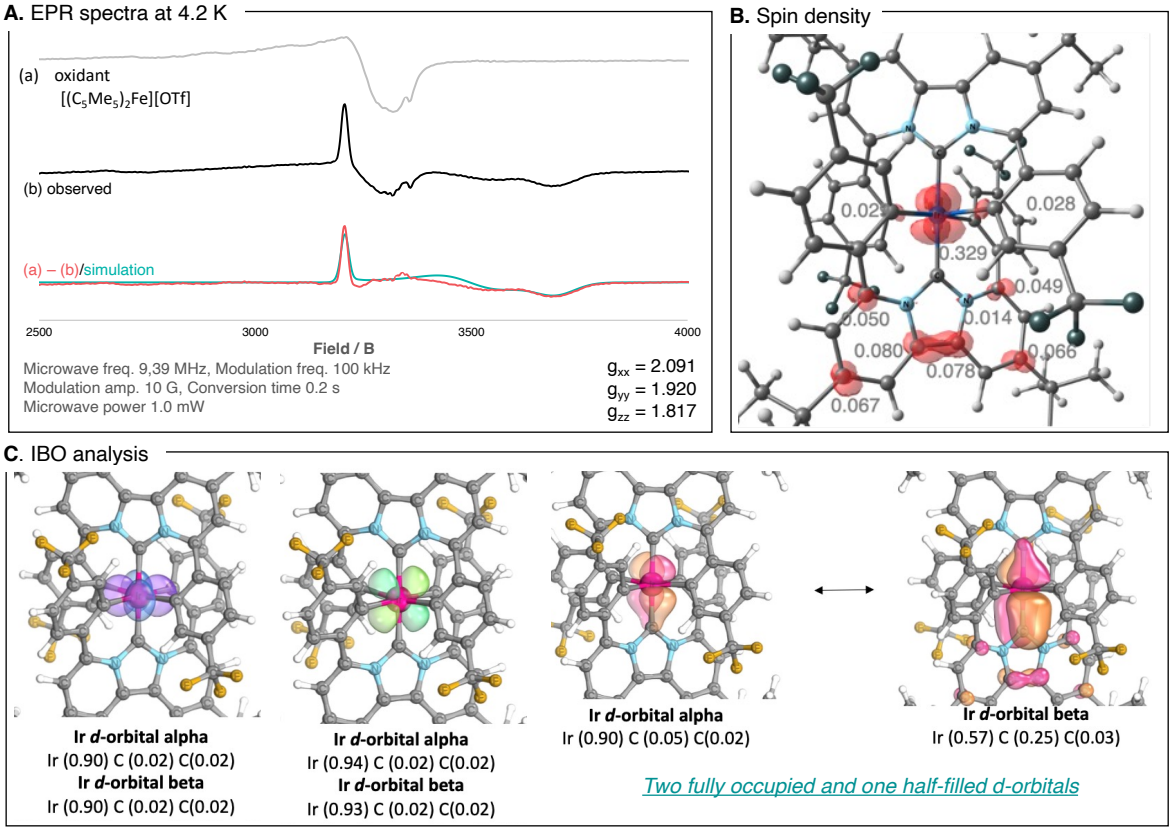

Figure 3.8. Detection and DFT study of Ir(IV) complex **26**

The EPR studies were carried out with stronger oxidants such as Ag^+ and $[thianthrene]^+$. As described, the oxidation of **23** with Ag^+ provided the complex **28**, therefore, the intermediates must contain **26**. The *in-situ* EPR measurement was conducted by use of 0.5 equiv. of AgOTf at –40 °C.

The spectrum was taken at 77 K (liq, N_2), which was likely assignable by red stars in Figure XX. Owing to the too strong potential and/or highly reactive species the additional signals corresponding to likely complex **27** were probably observed. (Figure 3.9)

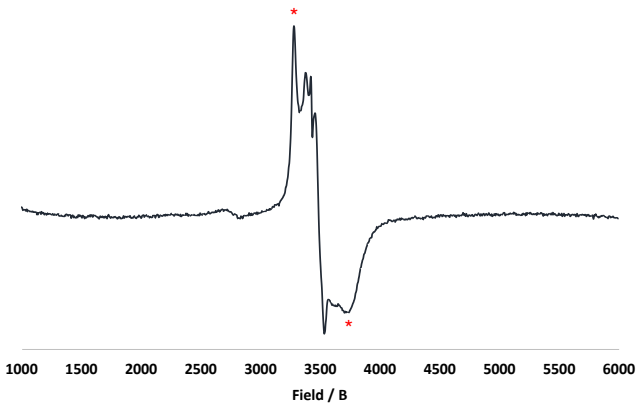

Figure 3.9. X-band EPR spectra of *in situ* oxidation of **23** by AgOTf in MeCN measured at 77 K.

Complex **23** was treated with the cationic thianthrene radical, and the oxidation was monitored by VT-EPR measurements. Although a small amount (0.2 equiv.) of thianthrene radical cation was used, the signal corresponding to this oxidant was observed (Figure 3.10 A). In a similar manner, the oxidation by using $[Cp^*_2Fe][OTf]$ also showed residue signals of the Fe(III) oxidant, the subtracted spectrum was compared with that of$[Cp^*_2Fe][OTf]$. The sharp signal appeared in a different region, whereas a broad signal was obtained in the same field, which is highlighted by a gray box in Figure 3.10. However, NMR monitoring suggested a different product from complex **26**. The spin density was attributed to the reaction mechanism, in which the π orbital of C=C on the 5-membered ring was reacted with thianthrene. ^{19}F NMR spectra implied that the up-filed shifted from starting material, likely addition of thianthrene[168] toward complex **26** (Scheme 3.2).

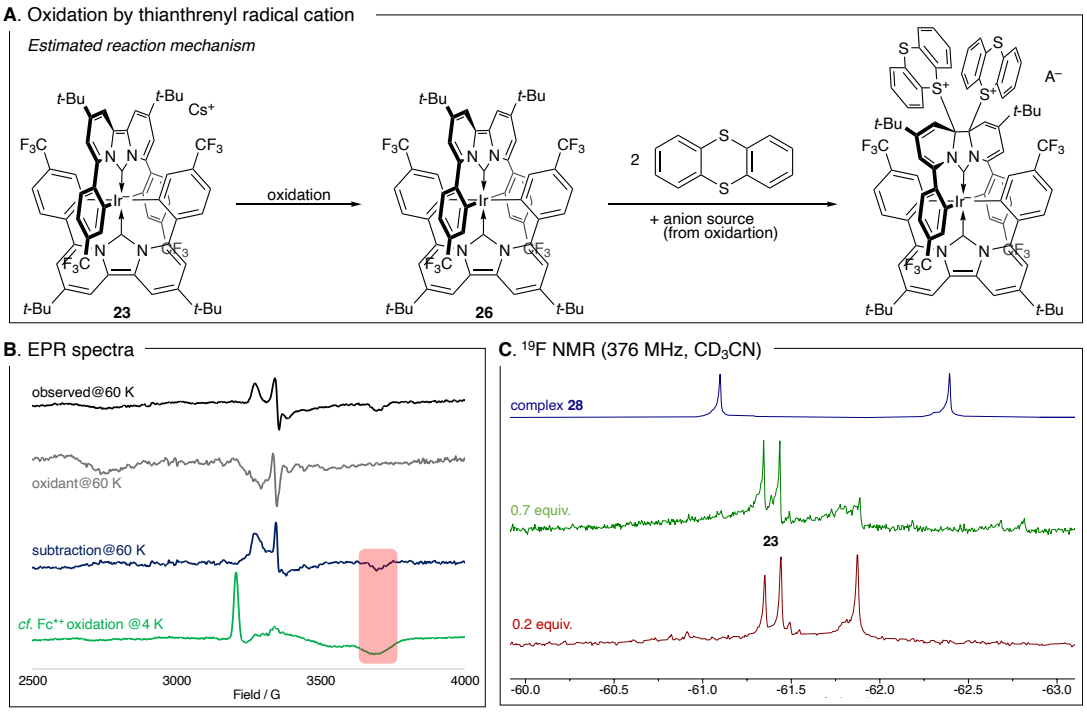

Figure 3.10 Spec oxidation of **23** by thianthrenyl radical cation

Although the oxidizing potential, as well as the stoichiometry of [Cp*$_2$Fe][OTf] (0.9 equiv.) used in the reaction, should not be enough for 2e$^-$ oxidization of **23,** the cationic Ir(III) **28** was observed together with regeneration of **23** by ^{1}H NMR spectroscopy after 2-3 days at room temperature. This suggests the neural Ir(IV) can readily disproportionate to form an Ir(V)/Ir(III) ion pair, from which the cationic Ir(V) undergoes reductive elimination to generate complex **26**.

While increasing the equivalency of [Cp$^*_2$Fe][OTf] made the reaction rate faster, less than 0.5 equivalent of oxidant led to recovery of the starting material **23** after the generation of the paramagnetic species **26**. NMR screening revealed a slow consumption of the [Cp$^*_2$Fe][OTf] and generation of Cp$^*_2$Fe. Taking the use of the J. Young tube into account, the transient paramagnetic complex **26** could be light-sensitive (Figure 3.11 and 3.12).

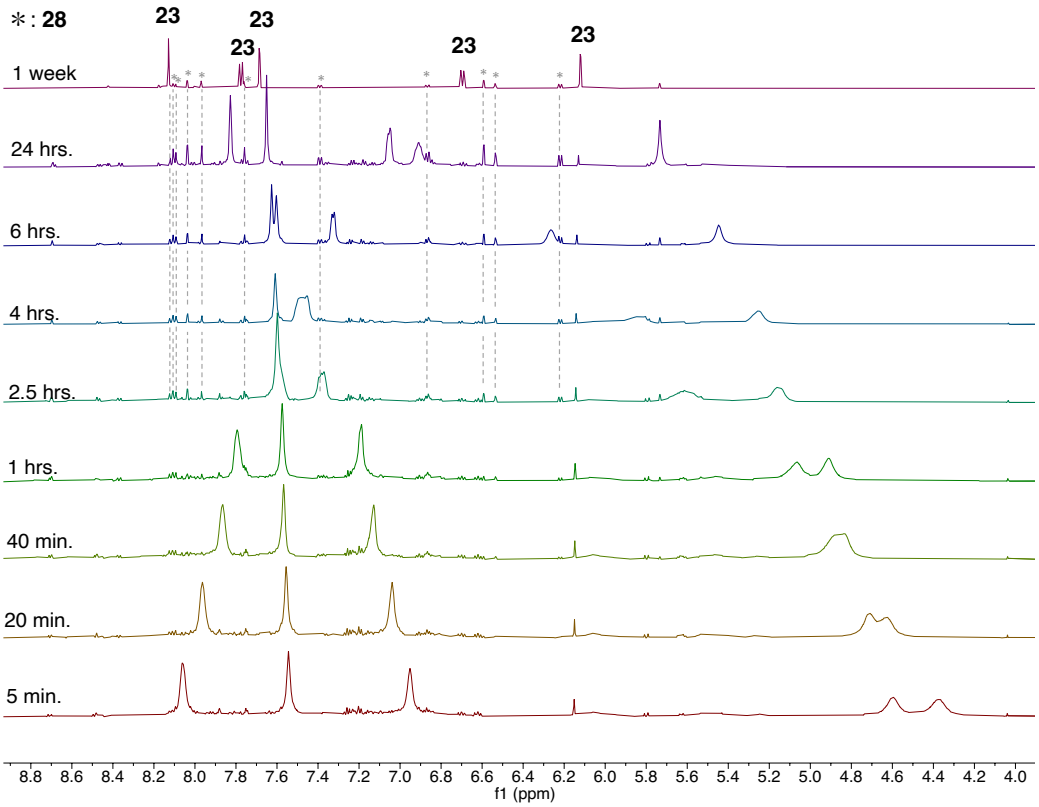

Figure 3.11. ^{1}H NMR monitoring of [Cp$^{*}_{2}$Fe][OTf] oxidation in CD_3CN

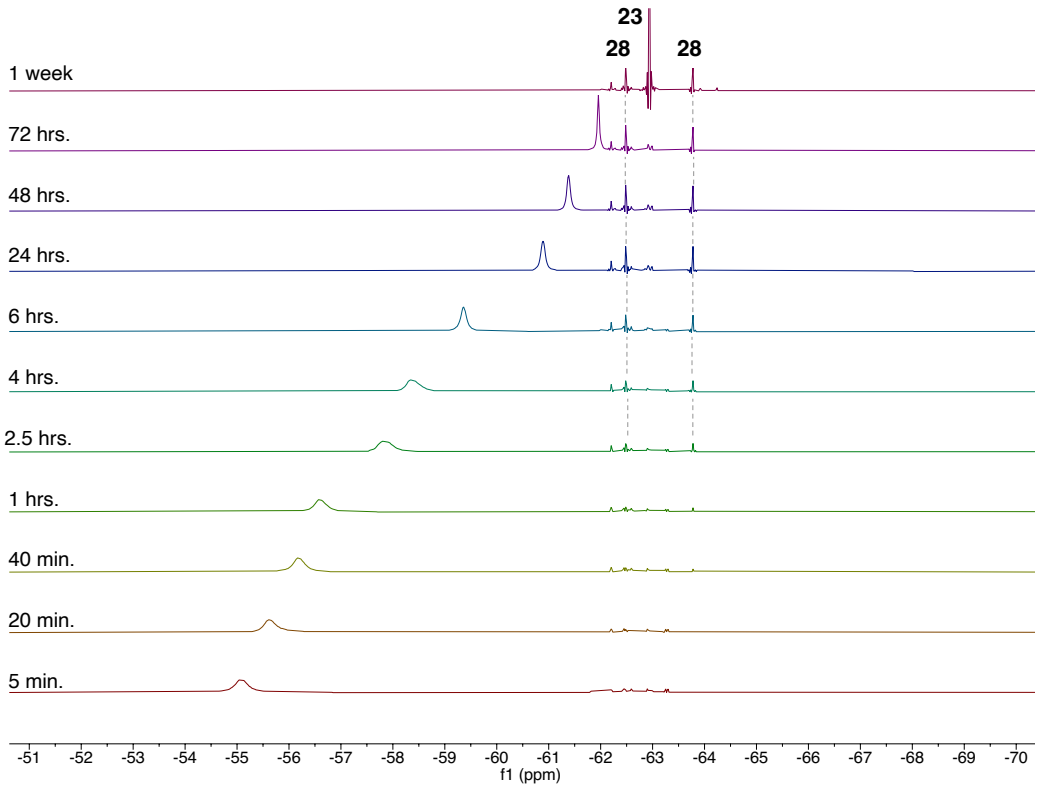

Figure 3.12 ^{19}F NMR monitoring of [Cp*$_2$Fe][OTf] oxidation in CD_3CN

UV-Vis absorption spectroscopic measurements of **23** with 0 ~ 2.0 equivalent of AgOTf did not show clear isosbestic points in the overlaid spectra, suggesting the reaction was not strictly stepwise (Figure 3.13). Likely more than two species were present simultaneously over the course of oxidation. This was in good agreement with the NMR studies, corroborating a disproportionation behavior of the neutral Ir(IV) species **26**.

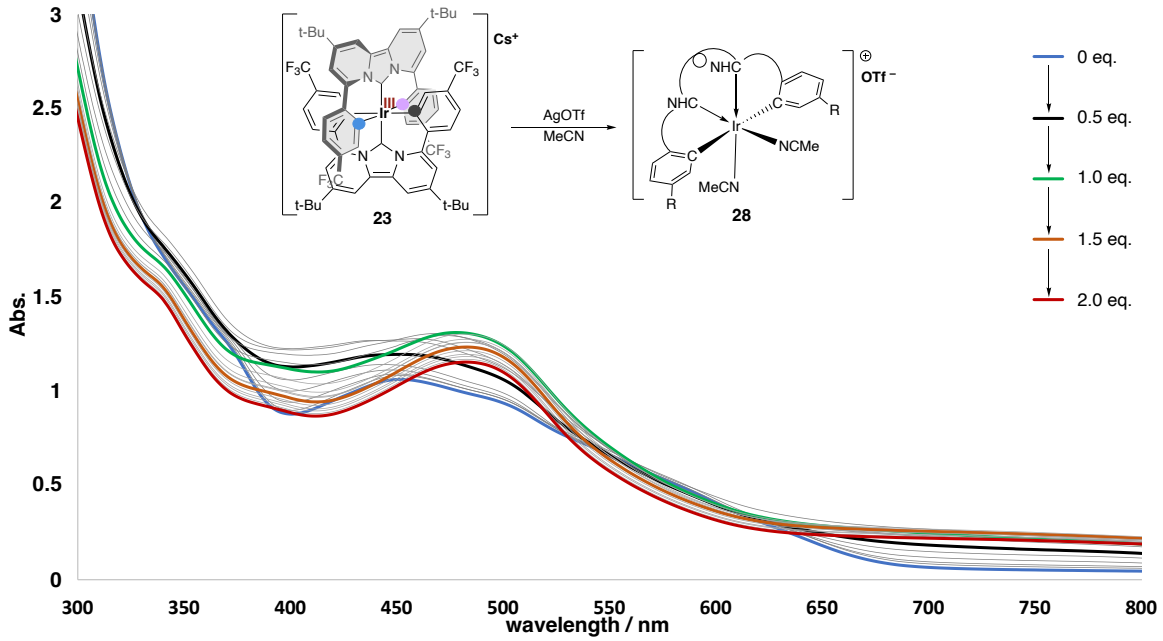

Figure 3.13 stacked UV-Vis spectra for tracing oxidation of **23**

An *in situ* NMR experiment involving **23** with 2 equivalents of AgOTf at –40 °C in acetonitrile-d_3 revealed a clean generation of a diamagnetic species (not **27**, but **29**, Scheme3.3). Its ^{1}H NMR spectrum revealed a complete loss of chemical equivalency in the structure, which led us to propose a pentagonal bipyramidal Ir(V) structure with coordination of acetonitrile as a ligand (Figure 3B, **3**). At temperatures above 0 °C, Complex **29** readily converts to the oxidative coupling product **28** quantitatively, presumably via reductive elimination. When the CV was taken at 0 °C, the voltammogram illustrated the same as that at room temperature, which had the second irreversible oxidation wave. This result supported reductive elimination from complex **29** around 0 °C (Figure 3.14).

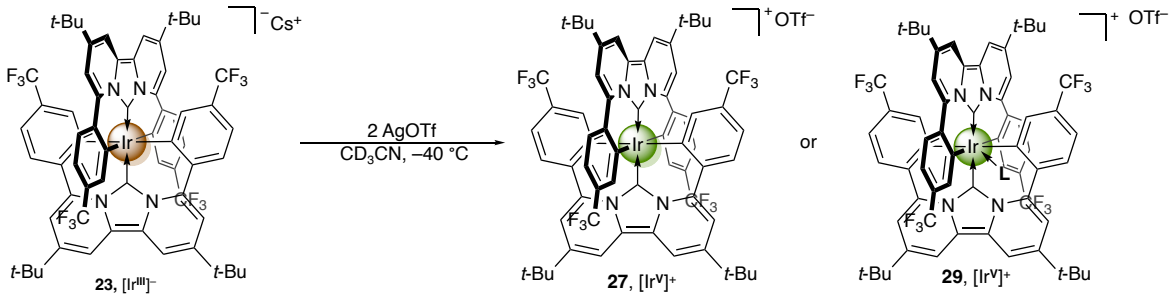

Scheme 3.3 Detection of Ir(V) intermediates

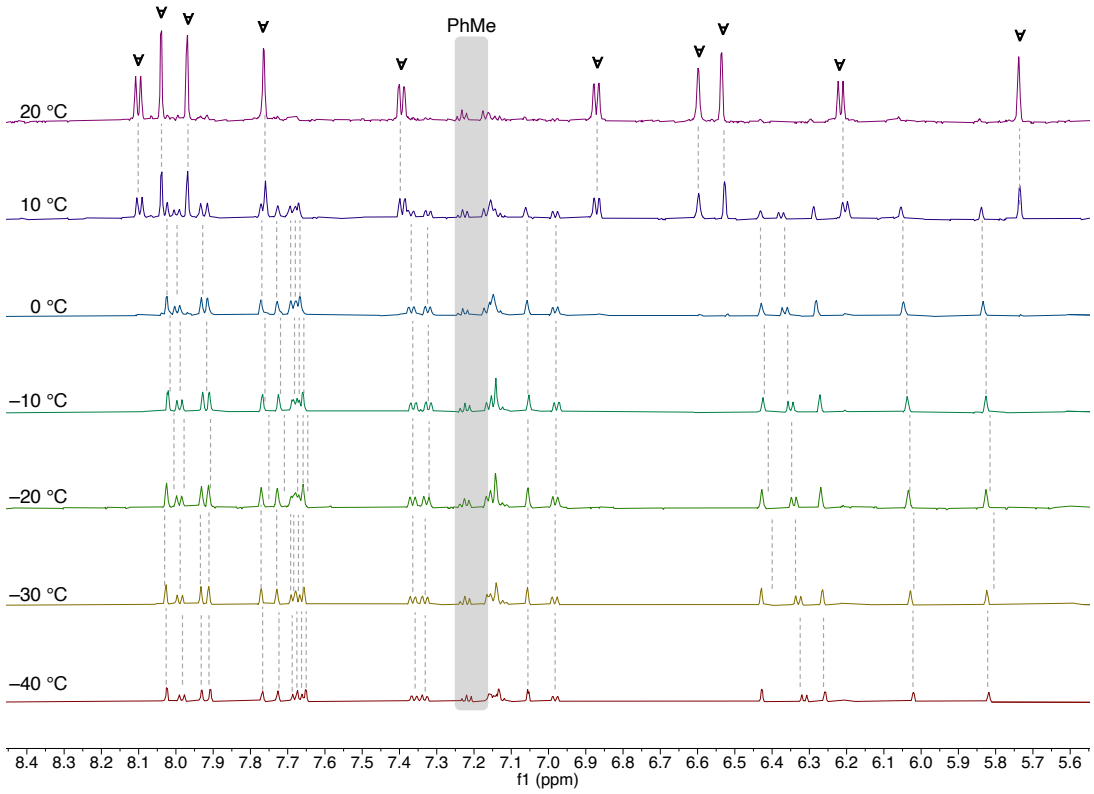

Figure 3.14 VT-^{1}H NMR spectra of *in situ* generation of **29** toward **23**

The possible structure of intermediate **29** was investigated by theoretical calculations using DFT methods (Figure 3.15). Both the hypothesized acetonitrile-coordinated pentagonal bipyramidal Ir(V) structure (**29**) and the octahedral structure without the addition of nitrile (**27**) were optimized. The 7-coordinated structure **29** has been predicted to be the thermodynamically more stable isomer (by 22.1 kcal/mol), which then undergoes reductive elimination by C-C coupling of the two adjacent aryl groups with a small energy barrier (8.4 kcal/more), followed by coordination of an additional acetonitrile to generate **28**. For oxidative coupling, the acetonitrile is also important. When this reaction was carried out in THF, the analog of complex **29** was not obtained.

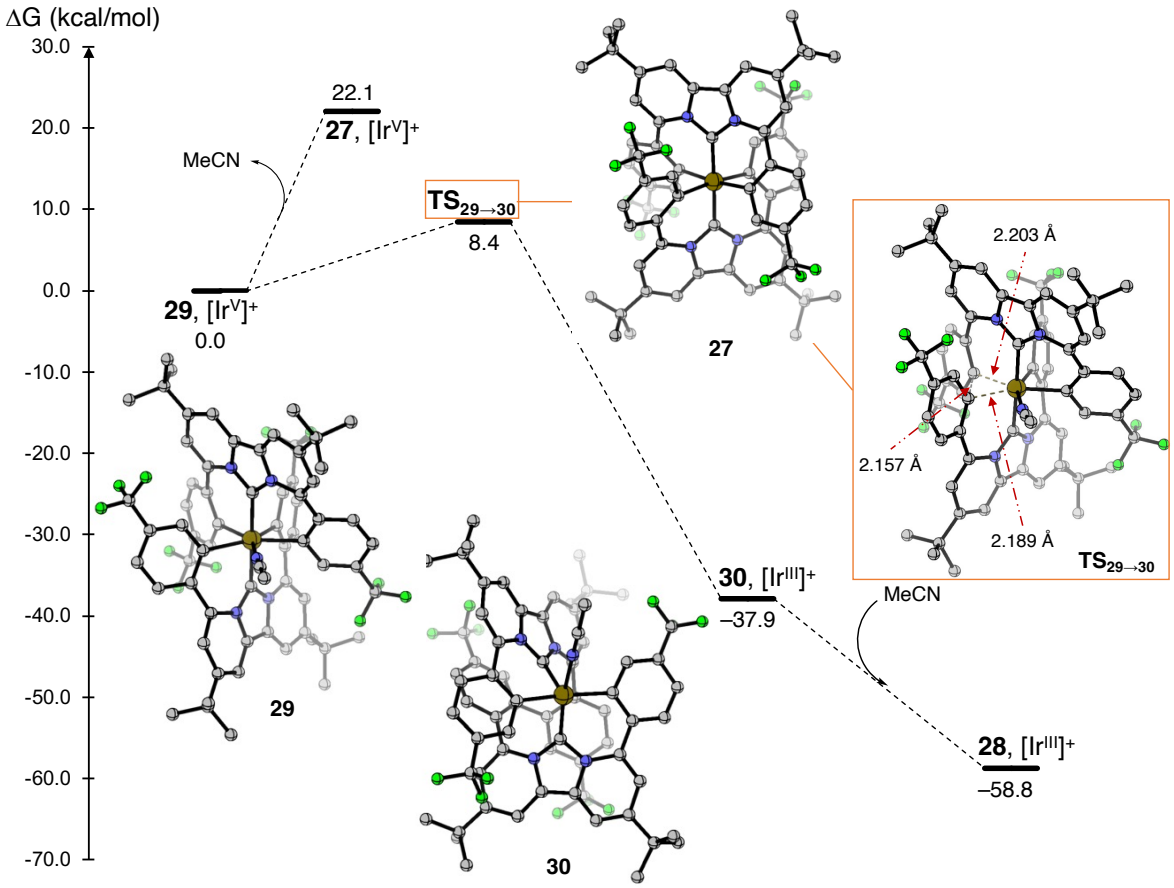

Figure 3.15 Computated reaction mechanism from 2-electron oxidized iridium complex **23** (= **29)** to the tetradentate iridium complex **28**

To obtain information about electronic states, the IBO analysis was carried out. Focus on the 5d orbitals of the iridium center. Only two occupied d-orbitals were predicted, suggesting the oxidation state of V on the iridium center of complex **29**. On the other hand, π-orbitals seemed to remain those of dpa-NHC (Figure 3.16 A, see also Figure 1.10). These IBO results provided that the good explanation toward d-orbital spitting of the pentagonal bipyramidal geometry, in which two lowest lying energy levels were only occupied (Figure 3.16 B). Based on the experimental and theoretical investigation, The transient intermediate complex **29** was characterized as the seven-coordinated Ir(V)complex with pentagonal bipyramidal geometry triggered by MeCN-coordination.

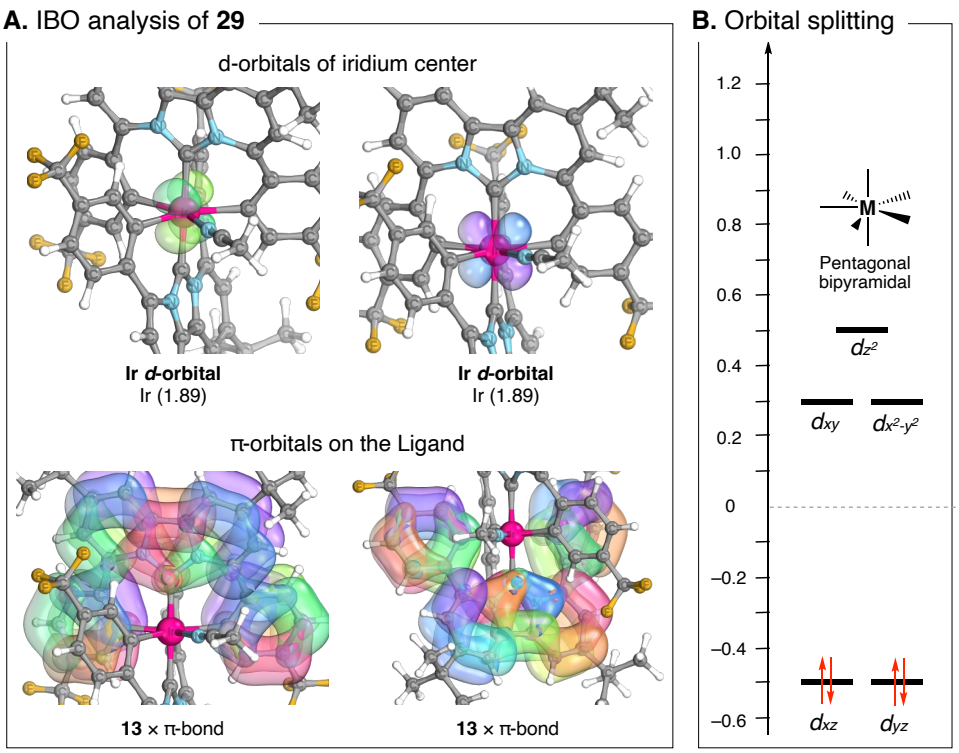

Figure 3.16 Description of **29** based oon DFT study.

To summarize the mechanistic study in scheme 3.4, 1-electron oxidation of **23** was conducted at metal-centered to yield the EPR-active transient Ir(IV) species **26**. Further 1-electron oxidation provided the Ir(V) complex **29** with the additional coordination of an acetonitrile ligand at low temperature. These high-valent iridium species have d_5 octahedral and d_4 pentagonal bipyramidal geometry, predicted by DFT calculation. During warming up to room temperature, it completes the formation of **28** that reductive elimination and subsequent second acetonitrile coordination. The calculated low activation barrier of 8.4 kcal/mol supported the thermal instability of complex **29**, observed by the VT-NMR study. When the oxidant was smaller equivalent than two, once complex Ir(IV) species **26** was generated. Then, disproportionation underwent to the ion pair of [Ir(V)][Ir(III)] species, followed by salt metathesis with Cs salt giving the complex **23** and **29**.

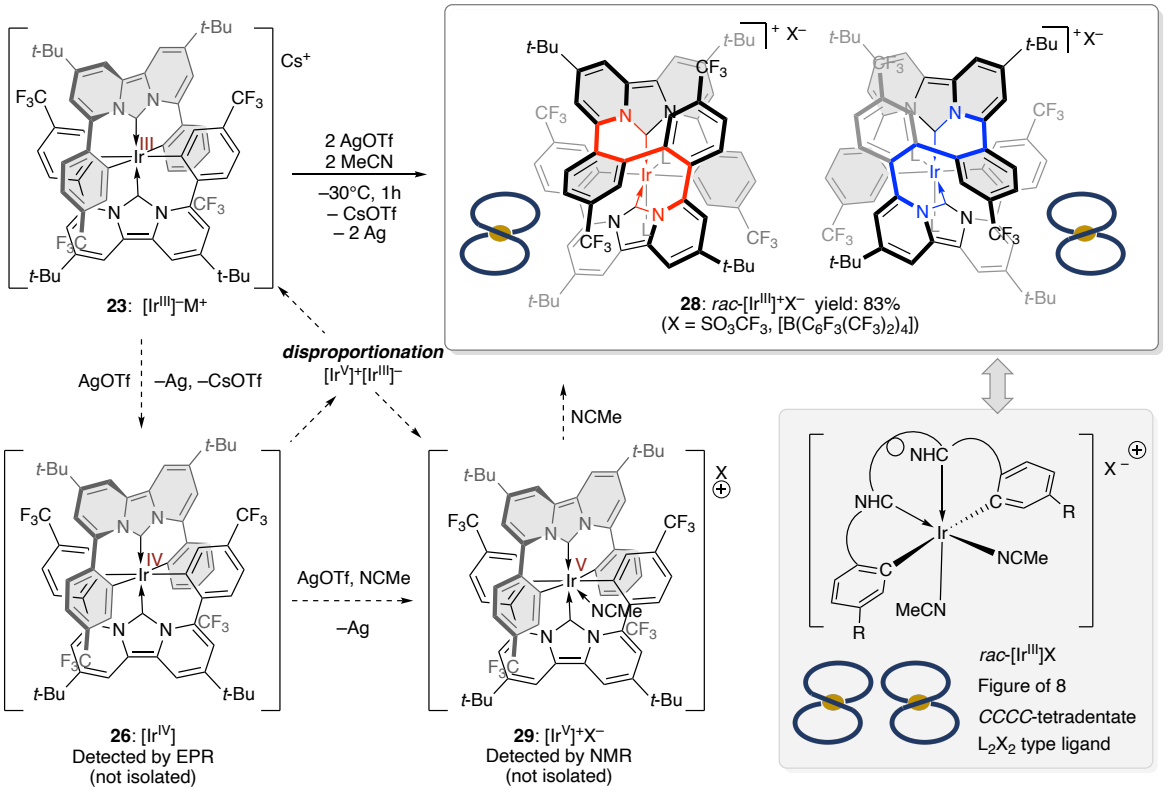

Scheme 3.4 Reaction mechanism of oxidatively induced ligand transformation reaction.

3.4. Reactivity study of 28

A neutral acac sprio-Ir(III) complex **31** was obtained in 80% yield by a simple ligand exchange using a stoichiometric amount of **28** and Lithium acetylacetonate (Scheme 3.5). X-ray crystallographic studies of single crystals of **31** revealed an octahedral structure similar to that of **28** (Figure 3.17). The $^{13}C\{^{1}H\}$ NMR spectrum of **31** showed a down-field shift for the metal-bound aryl and carbene carbon atoms (167.2 ppm and 171.5 ppm, respectively) compared to those observed in **28**.

The isoelectronic BTPA ligand (bis-diisopropylthiophosphoryl amide) was also employed, and the exchange was conducted in the same manner as the synthesis of the acac complex. Although the yield was lower than that of acac complex due to the solubility difference of the ligand source, the BTPA complex was fully characterized. The $^{31}P\{^{1}H\}$ spectra indicated the slightly down-field shift from 63.1 ppm to 61.4 ppm, likely the coordination of phenyl-substituted BTPA ligands toward Ir(III) centers. ^{19}F NMR spectrum remained the two signals close to those of acac complex, indicating the electronic properties were so similar. The single crystal was obtained from the concentrated acetonitrile solution. The solid-state structure of BTPA complexes revealed similar bond distances and angles in acac or MeCN complexes.

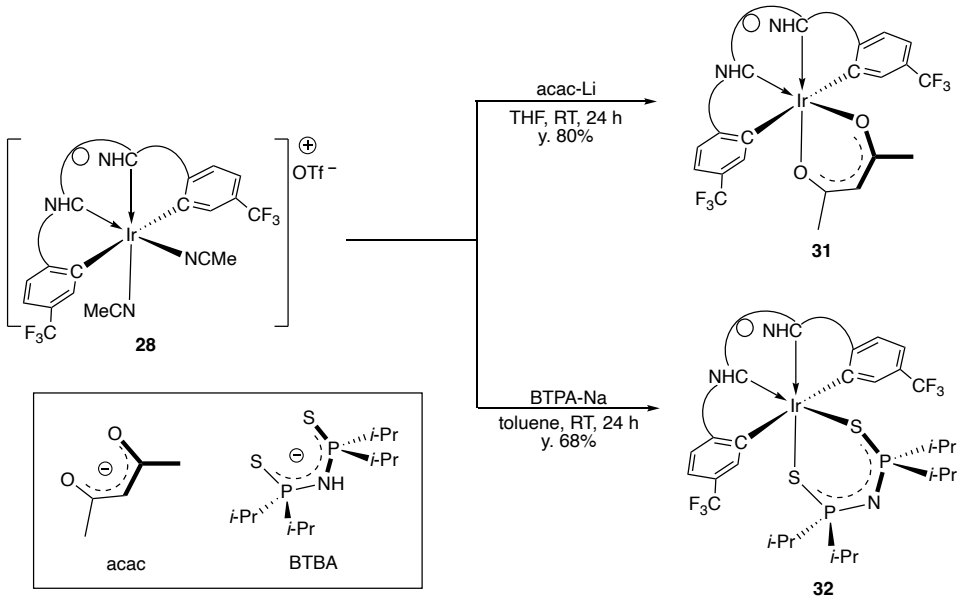

Scheme 3.5. Ligand exchange from MeCN to LX-type bidentate ligands

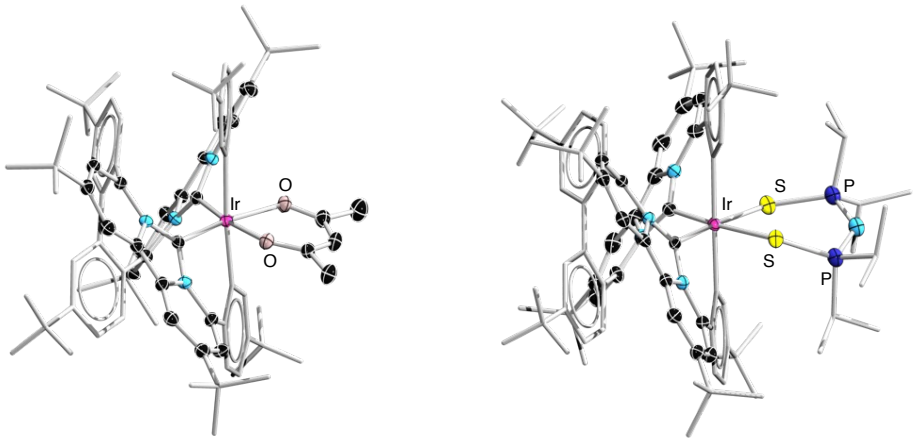

Figure 3.17 solid-state structures of the neutral iridium complex with the *CCCC*-tetradentate bis(dpa-NHC) ligand **31** and **32**. The ellipsoids were set at 30% probabilities. Periphery atoms on ligands and solvent molecules are omitted for clarity

The L-type ligands were also employed for ligand exchange reactions. The *t*bubpy was a famous bidentate L_2-type ligand, and ligand and counter-anion exchange were carried out in DCM simultaneously. The *t*-bubpy complex **33** was obtained in good yield (89%). Owing to the facile evaporation of Et_2O from the crystal lattice as well as the solution, the data quality of crystallographic analysis was not good. The $^{13}C\{^1H\}$ NMR illustrated the signal of the carbene carbon slight down-field shift from 161.4 ppm in the MeCN complex (from OTf complex; $BAr^F{}_4$ complex showed overlapping with the signal of the *ipso* carbon of $BAr^F{}_4$ anion to the 163.01 ppm).

The coordinated acetonitrile was slowly exchanged to the CO ligands in the DCM under the CO atmosphere toward **33** (Figure 3.18). The reaction was monitored by ^{1} H NMR, which initial spectra after just purged CO gas show a broad and messy spectrum. Twenty-four hours later, however, the clean conversation to CO complex was confirmed by a color change to orange as well as ^{1}H NMR, which signals of dpa-NHC framework were obviously down-field shifted whereas those of aryl moieties remained (Figure 3.18 C). Although the clean conversion was observed, the single crystal was not obtained in the ambient atmosphere. This is likely recrystallization in the CO atmosphere required. When this CO complex dissolved in MeCN, the MeCN was coordinated immediately.

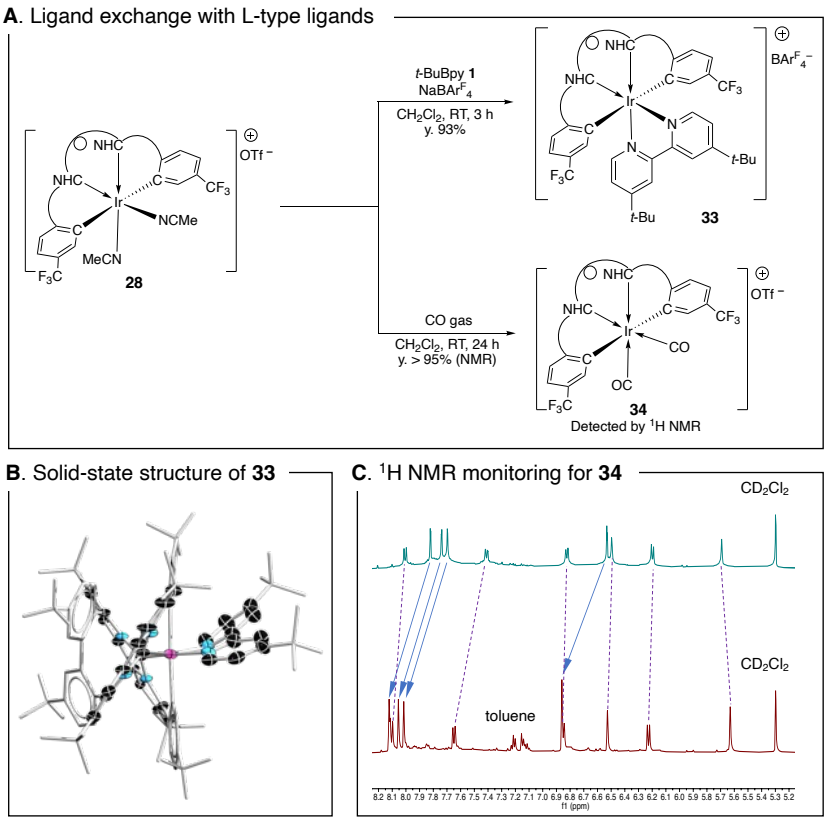

Figure 3.18 Ligand exchange from MeCN to L-type ligands

UV-Vis absorption spectra were taken in MeCN for complex **28**, **31**, **32**, and, **33**. The spectra of all complex were similar, and there are trends between cationic complex (**28** and **33**) and neutral complex (**31** and **32**) . Cationic complexes have red-shifted and larger absorption maxima, whereas the neutral complex showed *vice versa*. These trends might be the co-ligand effects through π-donation toward iridium centers.

TD-DFT calculation of **28** was conducted. These characteristic absorptions were assigned as HOMO to LUMO+1, +2, and +3 at 495, 479, and 469 nm, respectively. Compared with the typical iridium(III) complexes, the contribution of iridium's orbital toward HOMO was smaller, which was brought by the conjugated π-orbital of dpa-NHC frameworks. This small contribution made complex 28 its low redox potential saying later. (Figure 3.19)..

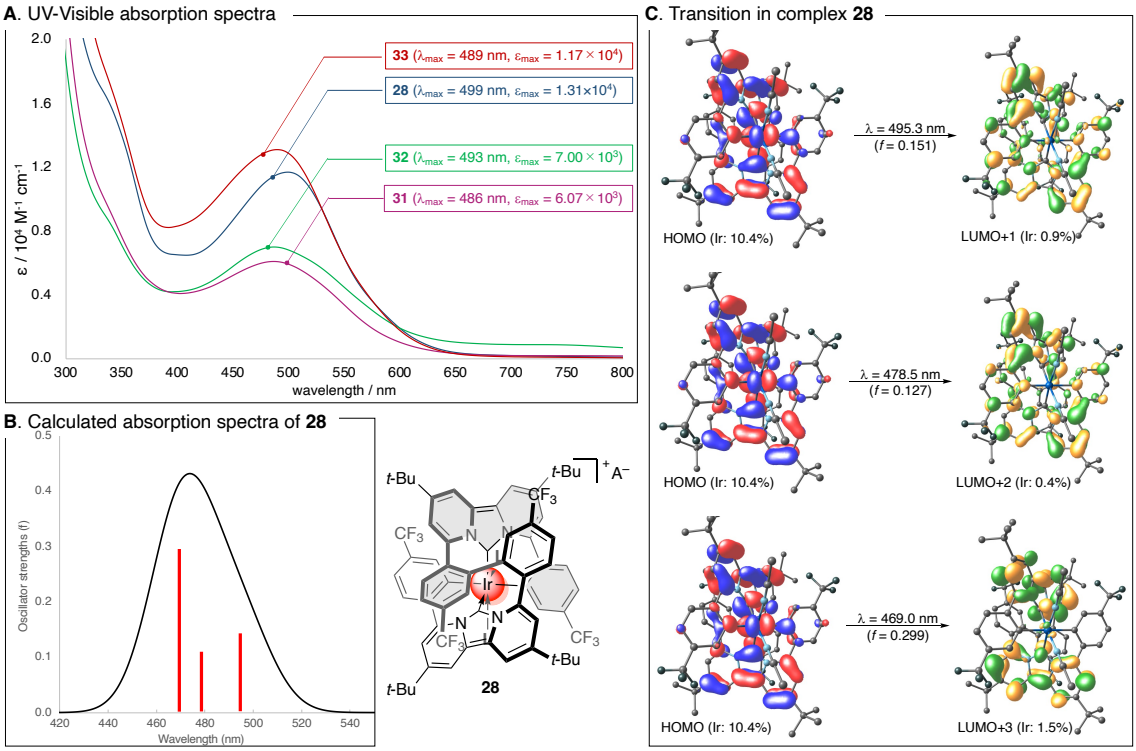

Figure 3.19 UV-Vis absorption spectra of Ir(III) complexes with spiral tetradentate ligands and TD-DFT study of **28**

Catalytic activity was investigated for alkane or ammonia borane dehydrogenation. Whereas dehydrogenation of cyclooctane catalyzed by MeCN complex was not proceeded until heated up to 40 °C, that of ammonia borane gave the H_2, detected by ^{1}H NMR. ^{11}B NMR screening experiment suggested that the signal of ammonia borane (quartet, $^1J_{BH}$ = 96 Hz) was reduced while that of borazine derivatives (doublet, $^1J_{BH}$ = 141 Hz) was enhanced. Other signals were too small to estimate their coupling constant, likely too strong borate anion and/or ammonia borane. Based on the chemical shift, three intermediates could be predicted (Figure 3.20).

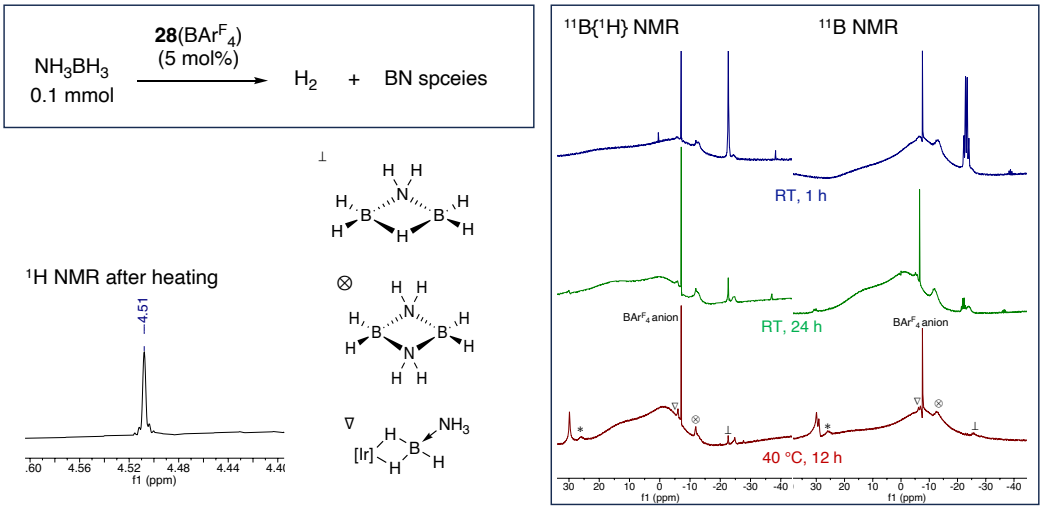

Figure 3.20 Catalytic dehydrogeneration of ammonia borane

3.5. 2-Electron oxidation of MeCN complex 28

Three complex **28**, **31,** and **33** showed two reversible waves in their CV measurement at room temperature in MeCN or C_6H_5F for **28** only (Figure 3.21 and 3.22, respectively). The two redox events of the cationic Ir(III) complex **28** with $\Delta E_{1/2}$ at –0.05 V and 0.28 V (vs Fc/Fc^+) were slightly more positive than the corresponding potentials observed for the neutral complex **31** at –0.24 V and 0.110 V vs Fc/Fc^+ as expected. All of these are significantly lower than those observed for most Ir(III)-NHC complexes[119,169] The spiro tetradentate iridium complexes also consist of two dpa-NHC moieties, which have both strong σ and π donors. This nature could work to stabilize electron-poor iridium spices implying the possible access to the high-valent Ir(IV) and/or Ir(V) spices. It is notable that complex **28** was a rare example of the cationic iridium(III) complex with remarkably low redox potentials, which allowed to be oxidized chemically. (See also Chart 3.4).

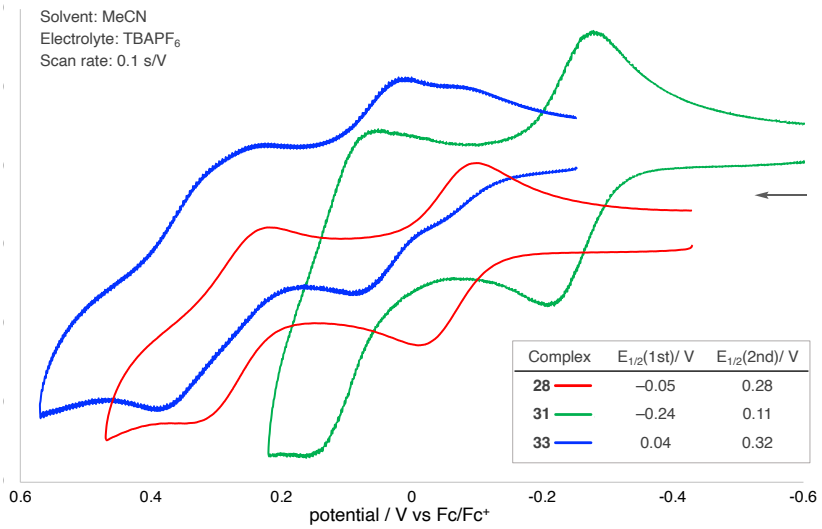

Figure 3.21 CV of *CCCC*-tetradentate spiro-Ir(III) complexes in MeCN

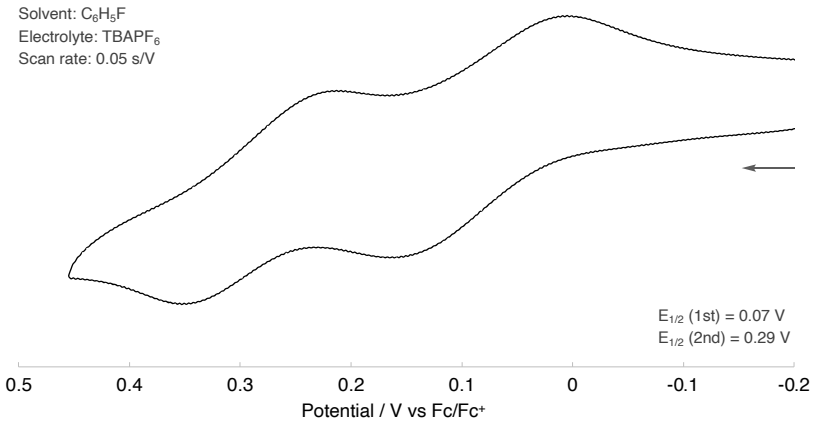

Figure 3.22 CV of complex **28** in fluorobenzene

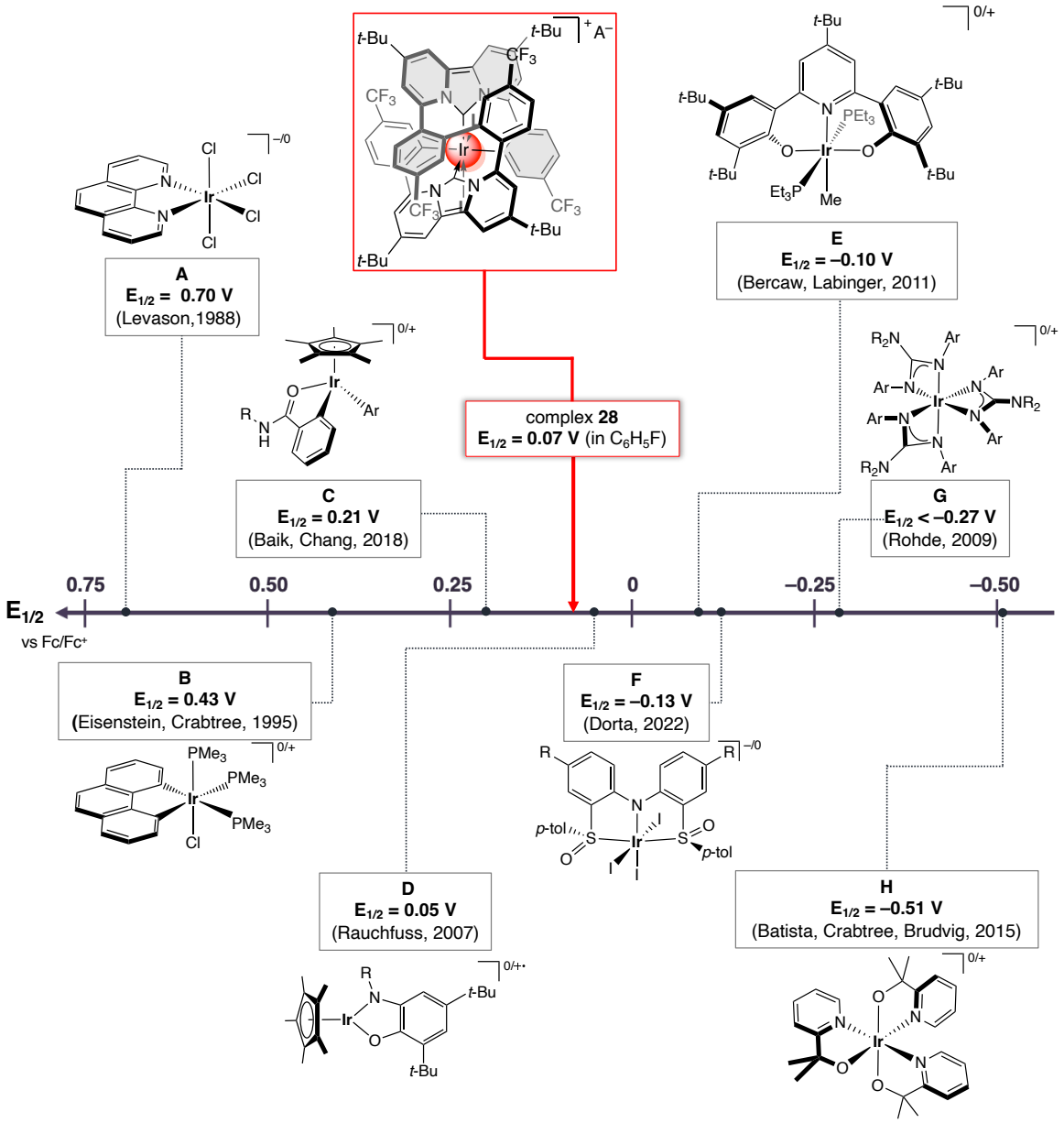

Chart 3.4 Redox potential chart of iridium(III) complexes including complex **28.**

Encouraged by the low reversible redox couples observed for **28**, chemical oxidation using $AgSbF_6$ was carried out in fluorobenzene at room temperature (Scheme 3.6). The dicationic complex **35** from $1e^-$ oxidation could not be isolated. However, when a large excess (5 equivalent) of $AgSbF_6$, the reaction mixture gradually turned from dark red to purplish black, from which a black solid was isolated. The product **36** could be detected by ESI-HRMS as (m/z = 469.14854, z = 3), which tends to contain dicationic species **35** (m/z = 703.72367, z = 2)) as an impurity (Figure 3.23).

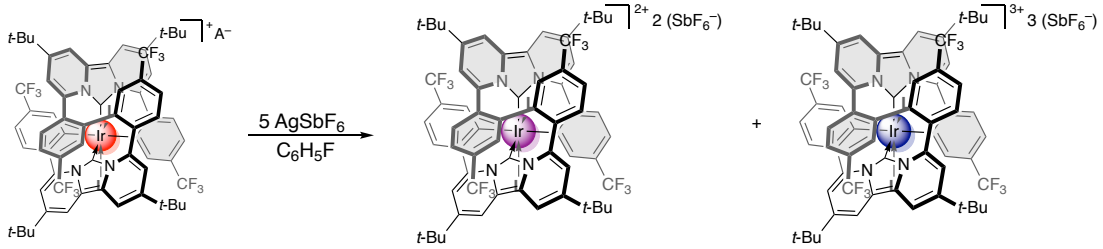

Scheme 3.6 oxidation of **28**

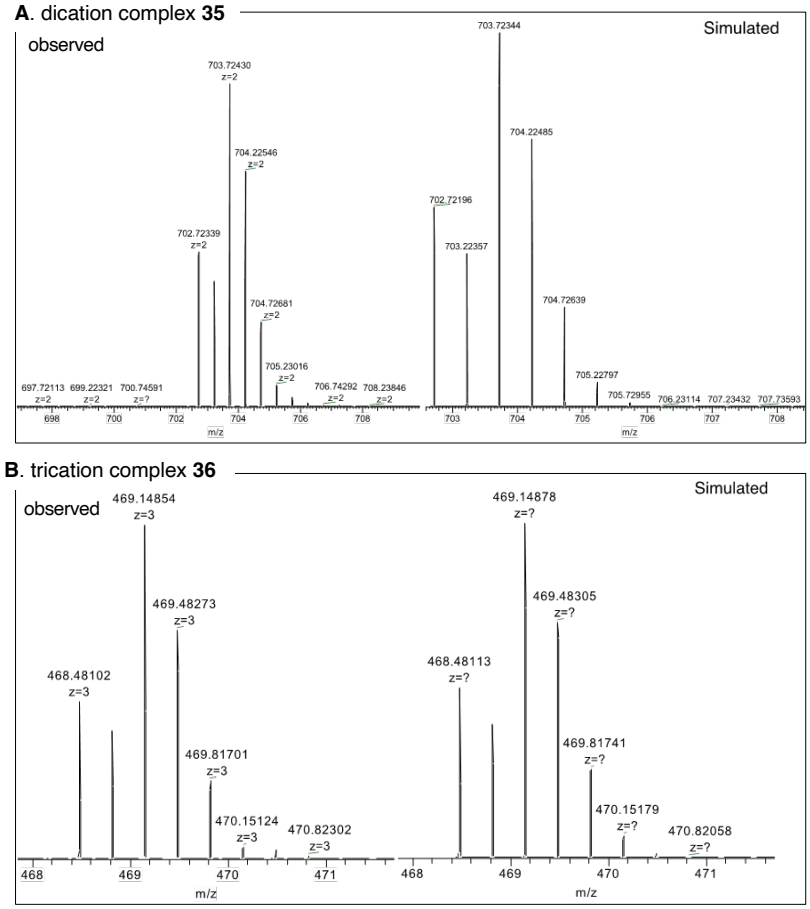

Figure 3.23 ESI-HRMS of complex **35** and **36**

Oxidation was monitored by UV-Vis-NIR spectroscopy in fluorobenzene in Figure 3.24. The 1 equivalent of $AgSbF_6$ was added to the complex **28** provided the dark brown suspension, and the spectrum was dramatically changed. Over 2 equivalents made the sample colour purple gradually. Interestingly, the NIR absorption band was generated when two electron was undergone. This band signal became saturated by use of 5 equivalents of $AgSbF_6$, which was employed as the reaction condition of the oxidation of **28**

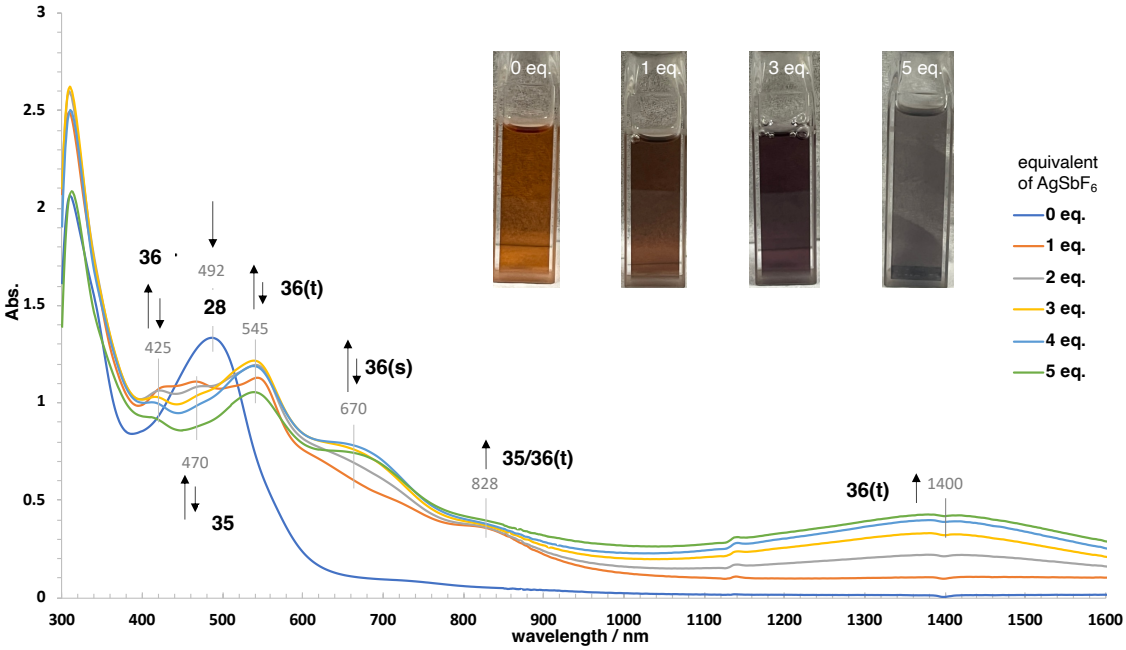

Figure 3.24 UV-Vis-NIR absorption spectra to trace oxidation behaviour of complex **28** in fluorobenzene.

Recrystallization in fluorobenzene at room temperature yielded purplish-black single crystals (**36**). X-ray analysis revealed that the solid-state structure of **36** consists of a tricationic iridium complex with three hexafluoroantimonate anions (Figure 3.25). The bond angles around the Ir centre in **36** are similar to those observed in the cationic (**28, 33**) and neutral (**31 32**) complexes, despite of the changes in overall charges (Table 3.1). Remarkably, the Ir–C_{NHC} bond distances in **36** were significantly shorter than those observed in **28** (1.974(6)/1.977(5) Å) and **31** (1.926(6)/1.929(6) Å), showing an increased multiple bond character after oxidation. In addition, the central imidazole ring in *dpa*-NHC showed a reversed single-double bond alternation in **36** compared with those in **28** (Table 3.1), suggesting significantly different electronic structures in these complexes after oxidation. Computational analysis at the ωB97X-D/[6-31G(d), LANL2DZ] was performed to compare the calculated bond distance with experimental data. In the case of the complex **28**, although the Ir–C_{NHC} distances were estimated slightly longer, the other parameters were good agreement with the experimental data. For complex **36**, two-electron oxidation could give the triple open-shell species such as Schneider's iridium PNP pincer complexes with nitrile[158] or oxo ligands[159]. Thus, DFT calculations were conducted for both the singlet state and the triplet state of complex **36**. The experimental distance seemed to be good agreement with the **36-S**, however, it is noted that the contribution from the triplet state could not be ignored because of the not irrelevant value.

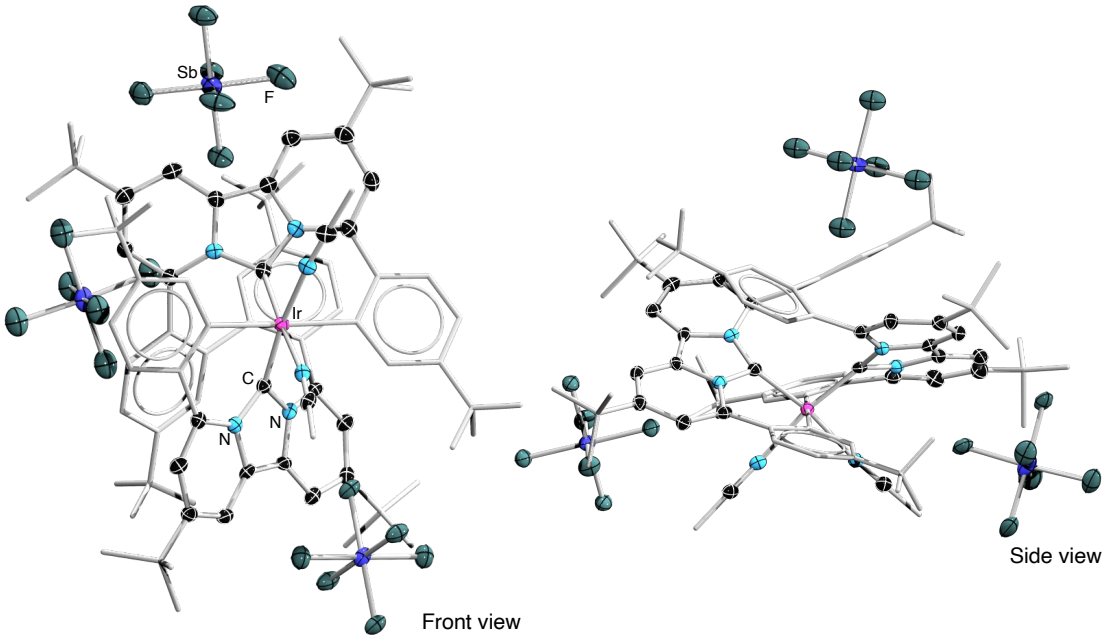

Figure 3.25 solid-state structure of **36**. The ellipsoids were set at 30% probabilities. Periphery atoms on ligands and solvent molecules are omitted for clarity

Table 3.1 Experimental and calculated bond distances of complex **28** and **36**

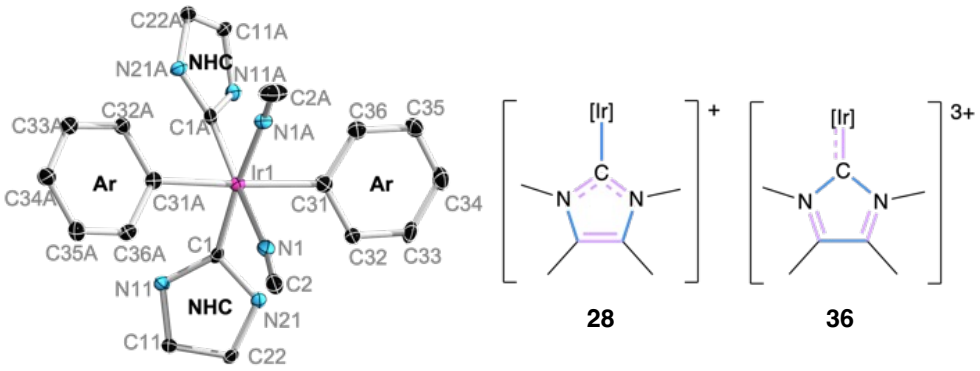

Complexes	**28** (exp)	**28** (cal)	**36** (exp)	**36-S** (cal)	**36-T** (cal)
C_{Ar}–Ir–C_{Ar}	176.2(2)	178.2	175.9(2)	177.2	176.3
C_{NHC}–IrC_{NHC}	102.4(2)	104.0	102.9(3)	104.4	103.6
N–Ir–N	85.42(19)	88.1	85.1(2)	81.1	83.9
Ir–C_{NHC}	1.974(6), 1.977(5)	2.018, 2.018	1.926(6), 1.929(6)	1.926, 1.925	1.977, 1.976
Ir–C_{Ar}	2.092(5), 2.087(5)	2.099, 2.099	2.105(7), 2.109(6)	2.111, 2.111	2.013, 2.013
Ir–NCMe	2.061(5), 2.081(5)	2.092, 2.092	2.096(6), 2.089(6)	2.142, 2.142	2.119, 2.117
C1–N11	1.376(6), 1.378(6)	1.371, 1.371	1.418(8), 1.418(8)	1.409, 1.409	1.400, 1.400
C1–N21	1.379(6), 1.376(6)	1.370, 1.370	1.424(8), 1.410(8)	1.416, 1.416	1.395, 1.395
N11–C11	1.413(6), 1.404(6)	1.397, 1.397	1.378(9), 1.374(8)	1.378, 1.378	1.381, 1.381
N21–C22	1.411(6), 1.397(6)	1.395, 1.395	1.387(9), 1.375(8)	1.378, 1.378	1.425, 1.425
C11–C22	1.382(7), 1.375(7)	1.382, 1.382	1.414(9), 1.418(9)	1.431, 1.431	1.378, 1.378

To figure out the origin of reversed single-double bond alternation, the electron density of the metal center was investigated by XANES. The spectra obtained from a solid sample of **36** at room temperature showed lower white line intensity than those of **23** and **28** due to the electron sufficiency of iridium species, suggesting the oxidation state of the iridium center in **36** is close to those in **23** and **28** (Figure 3.26).

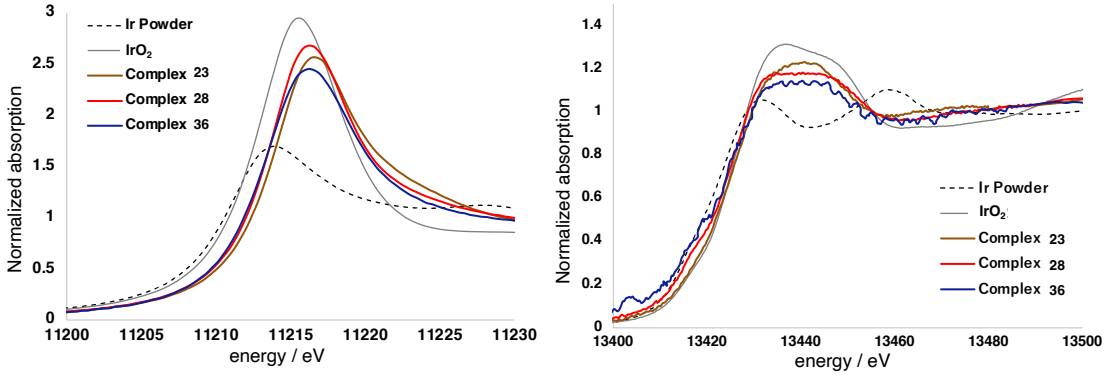

Figure 3.26 Ir L_3 (left) and L_1 (right) edge XANES spectra.

Additional investigation was carried out to support the XANES spectra results. The IBO analysis of complex **23**, **28**, and, **36**. As described in Chapter 2, the XANES spectrum of **23** was so close to the known Ir(III) complex **R**. IBO results of **23** illustrated the three occupied d-orbitals. Owing to the ideal bite angle of the dpa-NHC-based pincer ligands, two of three d-orbitals have π-interaction with carbon atoms (Figure 3.27 A). The same applies to complex **28**, which was the typical Ir(III) cationic complex (Figure 3.27 B) of complex **36** indicated that the three occupied d-orbitals as well as complex **23** and **28**, which implied the oxidation state of **36** was similar to those of **23** and **28**. It is noticeable that one of the three d-orbital in complex **36-S** has a relatively strong interaction between carbene's p-orbitals compared with that of **36-T**. This could be the root of the remarkable shortening Ir–C_{NHC} distances (Figure 3.27 C and D).

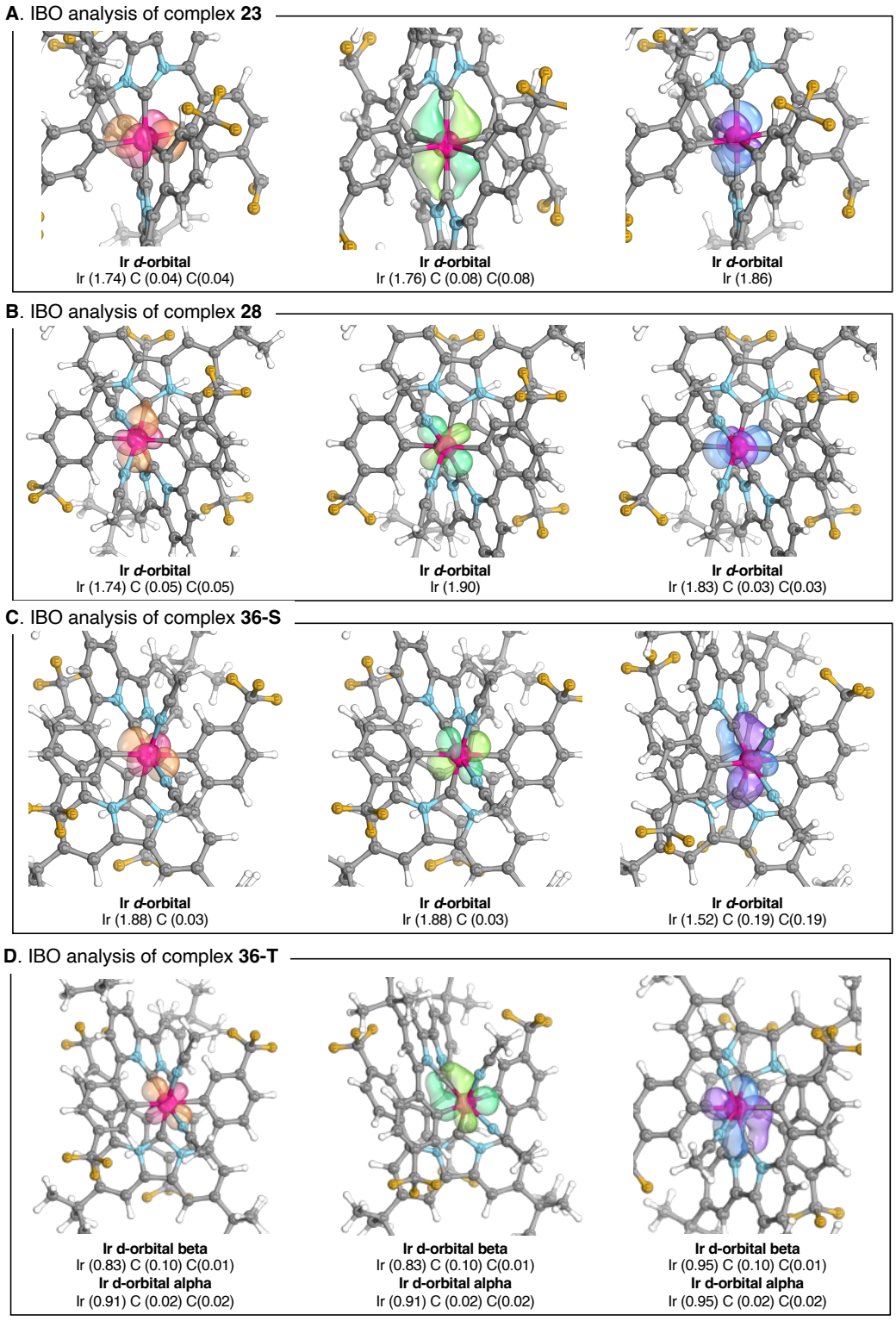

Figure 3.27 IBO analysis of Ir centers of **23**, **28** and **36**

In addition to the bond distance calculation and IBO analysis, we estimated NBO charge By increasing the total charge of the complex, only NBO charge on the *CCCC*-tetradentate ligand increased dramatically, whereas the iridium center and coordinated MeCN remained compared

with the mono-cationic complex. These NBO charge differences were good agreement with the IBO analysis and experimental XANES spectra. The single-triplet energy gaps of mono and tri-cationic complexes were estimated. That ST-gap for complex **28** showed –34.3 kcal/mol, which is the singlet ground state with the large gap. This is in good agreement with the typical Ir(III) complex. On the other hand, tri-cationic complex **36** estimated the ST-gap of +1.3 kcal/mol, predicting the triplet ground state (Table 3.2) .

Table 3.2 Computated ST gap and NBO charge among **28**, **35**, **36**

		Summary of NBO charges per fragment				
Complexes	ST gap	Ligand	Ir	MeCN	MeCN	Total Charge
28 $[Ir]^{+}$	–34.3 kcal/mol	–0.017	+0.637	+0.190	+0.190	+1.000
35 $[Ir]^{2+}$	——	+0.910	+0.682	+0.207	+0.201	+2.000
36 $[Ir]^{3+}$	+1.3 kcal/mol	+1.878	+0.683	+0.219	+0.220	+3.000

For the purpose of the experimental confirmation of the triplet ground state in complex **36**, VT-EPR measurements of **36** in 1,2-difluorobenzene were carried out between 4.2 and 16.7 K. A signal with both $|\Delta Ms| = 1$ and 2, characteristic of a triplet state was observed at 4.2 K, which decreased as the temperature increased. Above 55K, the signal at both regions weakened significantly, with little changes to further temperature rise. The intensity of this signal at both regions increased again when the sample was cooled again, supporting a triplet ground state.

It is known that the absorption area of the EPR signal is proportional to the magnetic susceptibility, which shows temperature dependence following the Bleaney–Bowers equation[170]. A plot of the AT v.s.1/T allowed a good fitting ($R^2 = 0.9747$, Figure), yielding an $\Delta E_{S\text{-}T}^{exp}$ of 0.12 ± 0.02 kcal/mol (Figure 3.28).

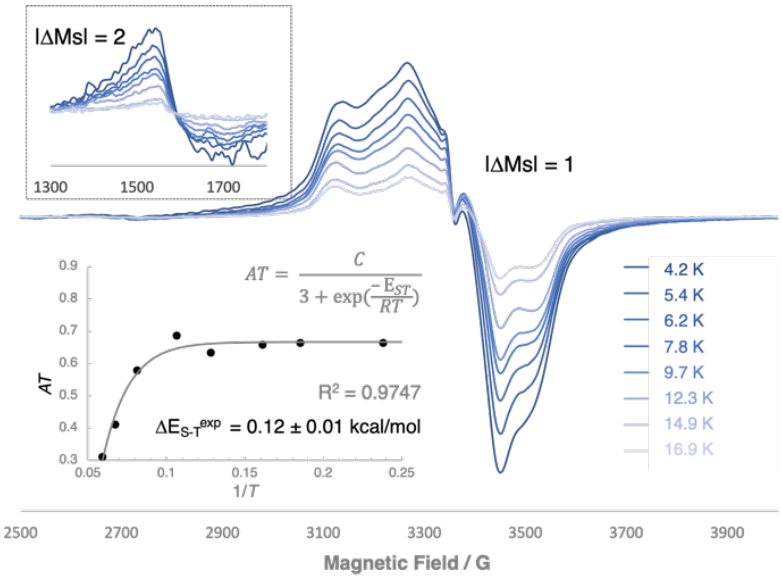

Figure 3.28 VT-EPR of complex **36** between 4.2 K and 16.9 K including Bleaney–Bowers plot, where *A* is the EPR signal intensity, *T* is the absolute temperature, *C* is the constant, R (cal/mol K) is the gas constant, and $\Delta E_{S\text{-}T}^{exp}$ (cal/mol) is the energy gap between singlet and triplet states**.**

Magnetic properties were moreover investigated with SQUID methodology (Figure 3.29). The χT value of **36** reduced with decreasing temperature. Note that solid state of **36** undergoes slow decomposition in air, making quantitative evaluation challenging. The χT value of **36** decreases with decreasing temperature, resembling the magnetic behavior reported for pincer-type Ir(III) complex that exhibit large zero-field splitting.[158,159], or presence of the temperature-independent paramagnetism. Upon further lowering the temperature, a magnetic anomaly (an increase in χT value) was observed around 55 K, which suggests the presence of a triplet state.

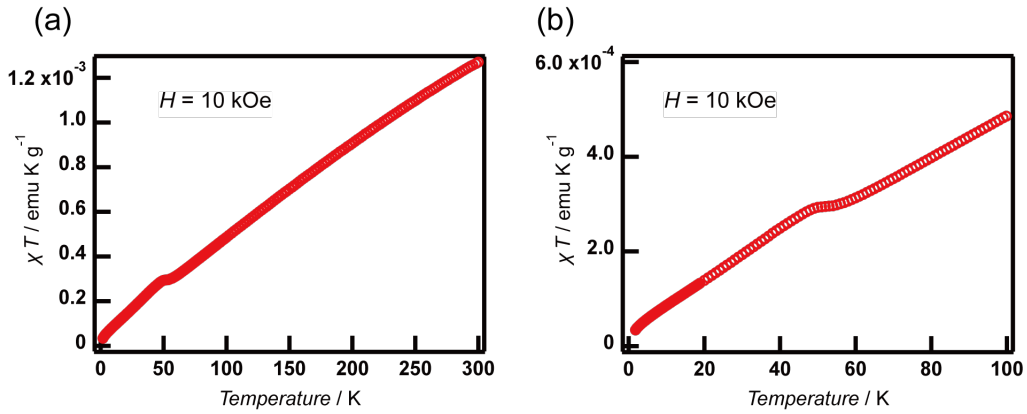

Figure 3.29 Plot of χT versus temperature for complex **36** in the temperature range of (a) 2 to 300 K and (b) below 100 K.

VT-NMR of complex **36** showed the similar behavior. ^{1}H and ^{19}F NMR in THF-d_8 illustrated the broad signals between 60 °C and –80 °C. Moreover, the signal became broader when the temperature decreased, implying the open-shell nature of **36**. In 2017, Harris demonstrated that

the chemical shift of VT ^{19}F NMR for paramagnetic transition metal complex is utilized as the thermometers for spin-crossover in Fe(II) complexes[171]. Figure 3.30 B illustrated the T or 1000/T vs $\Delta\delta_F$ plots referenced fluorobenzene as 0 ppm. Note that owing to the further spitting signals at 60 °C, the plot at 60 °C was not taken These plots suggested the paramagnetic species are more prominent over the entire temperature range. Negative coefficients of the fitting line indicated the Curie behavior, which indicated the presence of open-shell species over –80 °C. New signals appeared at 20 °C and increased the signal intensity at higher temperature. These new signals could be the other spin state(s) of complex **36**, likely one of the reasons reflecting the increase in χT value over 150 K.

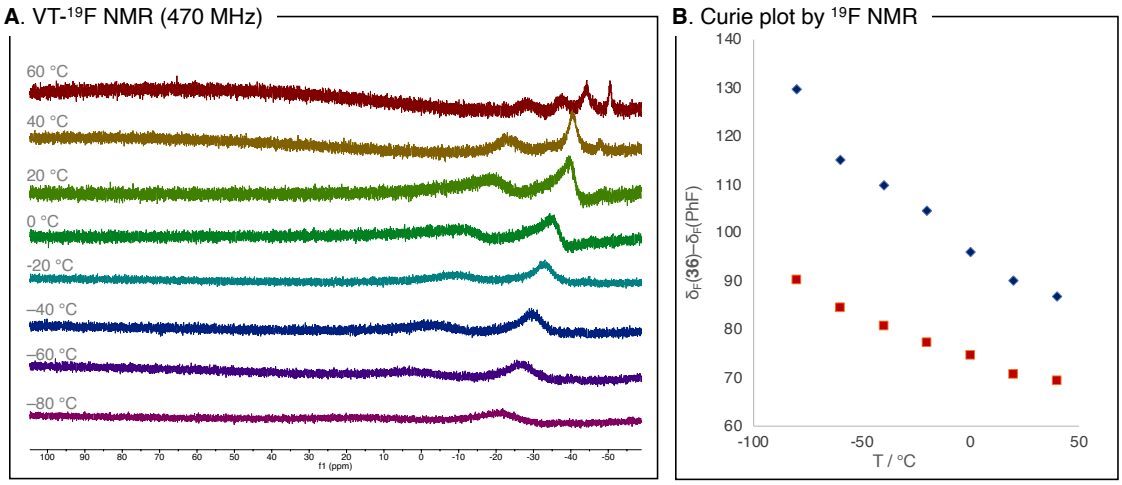

Figure 3.30 NMR study of complex **36**

DFT calculation was conducted to understand where each radical was located. Table 3.4 summarizes the NBO charge difference between complex **28** and **36**, and spin density plot of **36**. (Table 3.3) Both calculation results suggested that each radical was delocalized on each dpa-NHC fragment and the iridium center. NBO charge differences from complex **36** to **28** provided over 0.1 at C13 and C23, connected to the *t*-Bu groups, and C1, C11, C15, C21, and C25 have 0.05 to 0.06 differences. Note that the iridium center has a close value of 0.046. Focus on the spin density. the value tendency followed the NBO charge difference except for C1, namely carbene carbon. This large spin density could be derived from the orbital coefficient of C1, which was demonstrated by Weiss's calculation of dpa-NHC chalcogen adducts. Interestingly, the spin density of the iridium center was larger than those of C13 and C23, unmatched by the NBO charge difference. This is likely that the iridium center is able to interact with both dpa-NHC fragments.

Table 3.3 NBO charge deffeirence between **28** and **36**, and spin density of **36**.

Atom Name	NBO charge (**36**)–(**28**)		Spin density		Atom Name	NBO charge (**36**)–(**28**)		Spin density	
Ir	0.046		0.187						
C1	**0.060**	0.074	0.325	0.326	C31	0.001	0.001	0.032	0.032
N1	0.007	0.007	–0.030	–0.030	C32	0.009	0.009	N.D.	N.D.
N2	0.007	0.007	–0.031	–0.031	C33	0.034	0.021	N.D.	N.D.
C11	**0.054**	**0.054**	0.068	0.068	C34	0.015	0.015	N.D.	N.D.
C12	0.023	0.023	N.D.	N.D.	C35	0.021	0.021	N.D.	N.D.
C13	**0.104**	**0.104**	0.110	0.109	C36	0.020	0.020	N.D.	N.D.
C14	0.021	0.020	–0.042	–0.042	C41	0.003	0.003	N.D.	N.D.
C15	**0.060**	**0.060**	0.107	0.107	C42	0.005	0.005	N.D.	N.D.
C21	**0.064**	**0.064**	0.082	0.083	C43	0.019	0.019	N.D.	N.D.
C22	0.016	0.016	N.D.	N.D.	C44	0.004	0.004	N.D.	N.D.
C23	**0.109**	**0.109**	0.122	0.122	C45	0.008	0.008	N.D.	N.D.
C24	0.002	0.002	–0.049	–0.049	C46	0.027	0.027	N.D.	N.D.
C25	**0.060**	**0.061**	0.110	0.110					

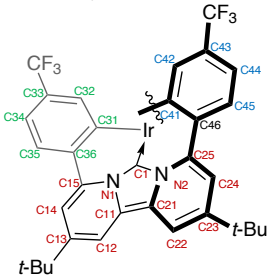

Spin density plot of **36**

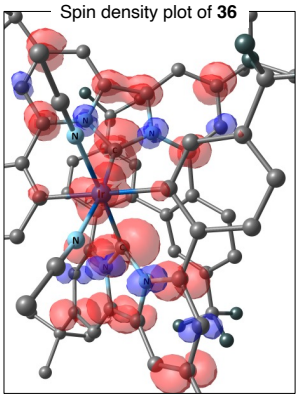

IBO analysis of complex **36** was furthermore carried out for the π-orbital of arylated dpa-NHC fragments. In the case of **36-T**, π-electron on dpa-NHC moieties, including aryl rings, illustrated the typical π-orbitals for dpa-NHC for (a) and (c) in Figure 3.31 A. On the other hand, IBO result of (b) and (d) provided that the delocalization of π-electron was likely the bipyridine-like π-orbitals, which could increase the nature of carbons species stabilized by bipyridine ligands. This bipyridne-like character appeared in IBO results of **36-S** (Figure3.31 B (e) and (f)). What is notable to mention is the one of the π bonds illustrated the spreading through two dpa-NHC moieties. This suggested the **36-S** could be lying the open shell singlet species (Figure 3.31 B (g)).

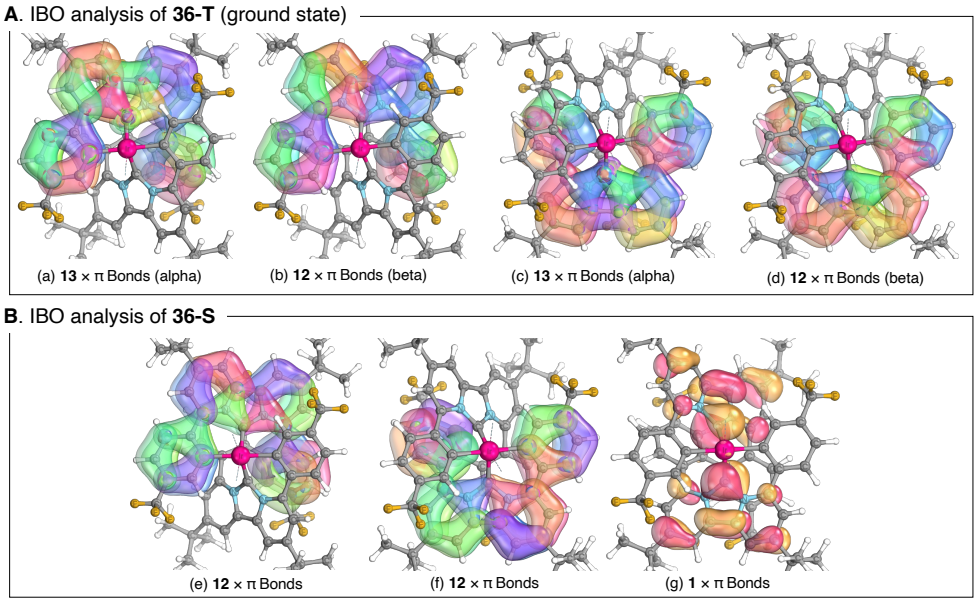

Figure 3.31 IBO analysis of **36**

Finally, to understand the stability of the oxidation process from **28** to **36**, we analyzed possible aromatic stabilization in the complex **28** using the electron density of delocalized bonds (EDDB)[172,173]. The $EDDB_G(r)$ function isocontours from three different views are shown in Figure 3.27. We analyzed the effectiveness of cyclic delocalization of electrons in two (planar) 6-membered rings (the 6-MR containing $IrC_{NHC}NCCC_{Ar}$) and one (twisted) 11-membered circuit containing among others $C_{NHC}IrC_{NHC}$ (Figure 3.31). The calculated EDDB-based population of cyclically delocalized electrons in both the six- and eleventh-membered cycles is 0.3 e^-, which is close to zero and far from the population of delocalized electrons in the archetypical aromatic ring of benzene (5.3 e^-)[174]. Therefore, despite the extensive electron π-delocalization in the ligands, the 5d orbitals of the Ir atom are not involved in aromatic stabilization. This notwithstanding, the $EDDB_G(r)$ function clearly show the extended delocalization over ligands and much more effective conjugation of the Ir–C bonds compared to the coordinative covalent bonds Ir–N (Figure 3.32).

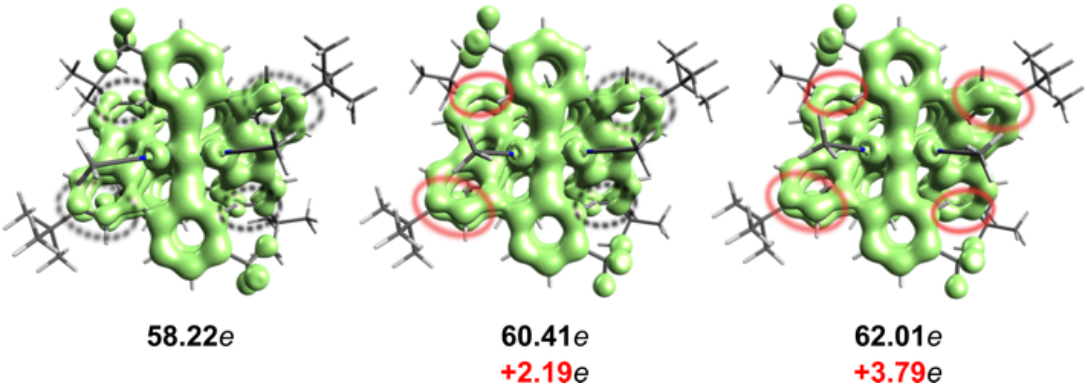

Figure 3.32. The isovalue contours (τ = 0.02) of the global electron density of delocalized bonds ($EDDB_G$) and the corresponding EDDB-electron populations in complexes **28**, **35**, and **36-T** (red numbers refer to the corresponding relative change of the global EDDB-population due to oxidation).

In conclusion, complex **36** could be described as an iridium(III) tri-cationic complex with *CCCC*-tetradentate ligand, which is open-shell, and triplet ground state di-radical species delocalized on each dpa-NHC fragment. The singlet-triple gap is estimated as 0.12 ± 0.02 kcal/mol. Because of the delocalization of radicals through dpa-NHC fragments and the iridium center, the bond distance related to these moieties dramatically changed in comparison with the starting material complex **28**. Especially the remarkably shortening Ir–C_{NHC} distance originated from the reduced repulsion between Ir center and carbene carbon. A similar phenomenon was reported by England and Ye, describing that the carbodicabene (CDC) iron complex, shows the remarkable C–Fe shortening distance versus the remaining Fe–N bond after oxidation on the CDC ligand[175,176]. In addition to their iron complex, including cobalt and chromium center, there are few examples of the complexes bearing open shell diradical on ligands (Figure 3.33)[175–180]. Most of the example complexes have anti-parallel spins on ligands, whereas, complex **36** was the ground state of parallel spins (triplet) on dpa-NHC ligand, which is rarely reported even though the organic diradicals.

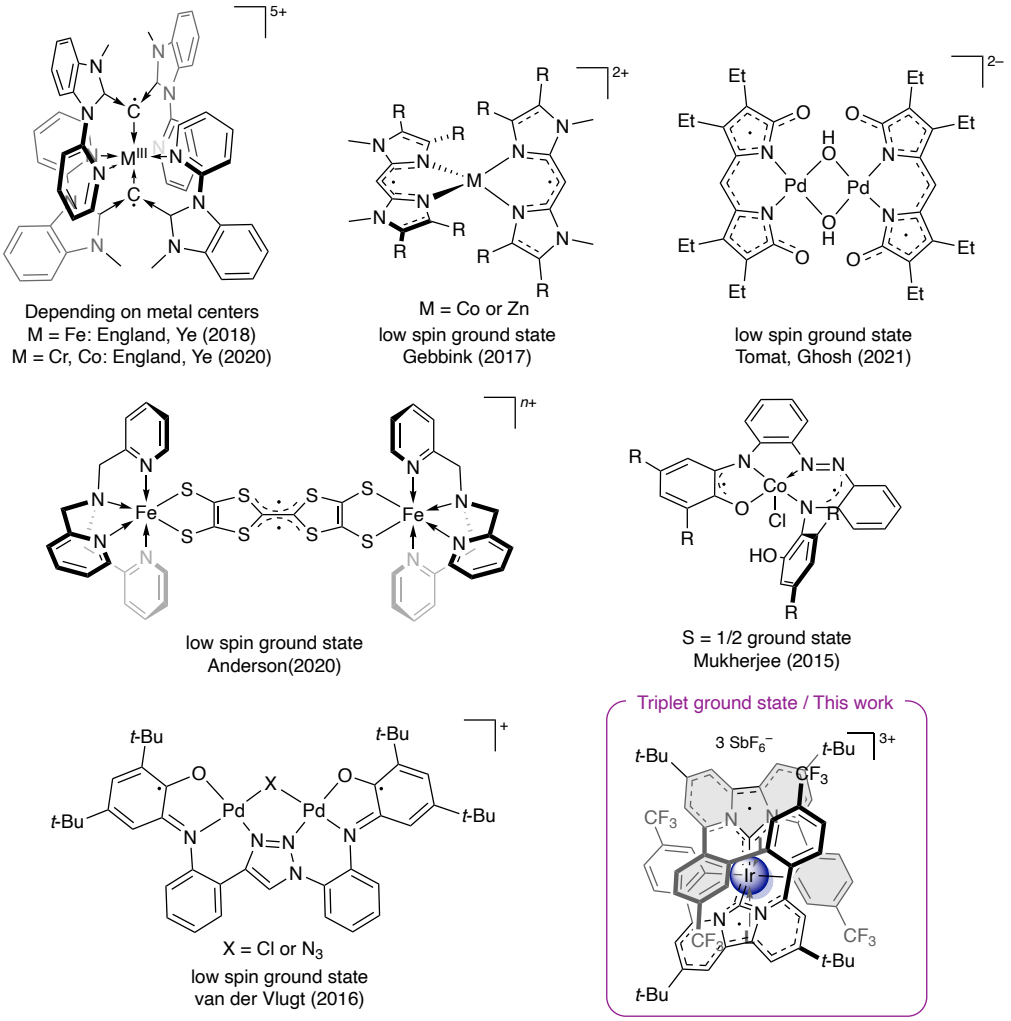

Figure 3.33 Selected examples of the TM complexes bearing open shell diradical on ligands.

We carried out TD-DFT calculation to follow the oxidation as well as understand the absorption spectra (Figure 3.34). Interestingly, **36-S** has a remarkably distinctive absorption band in the NIR region. TD-DFT suggested this band corresponded to the HOMO-LUMO transition (a). In consideration of the IBO results, This transition could be assigned as an intraligand charge transfer (ILCT) because of the transition between dpa-NHC moieties linked by biaryl fragment. Despite the unique properties of **36-S**, that of **36-T** has these bands below 600 nm. For example, transition (c) seemed to be like the lowest-energy transition of **28**. Probably, owing to the low-lying energy of α-LUMO by tri-cationic character or half-filled orbital, the required transition energy got lower. It is notable that any transition does not have a spin-flip system.

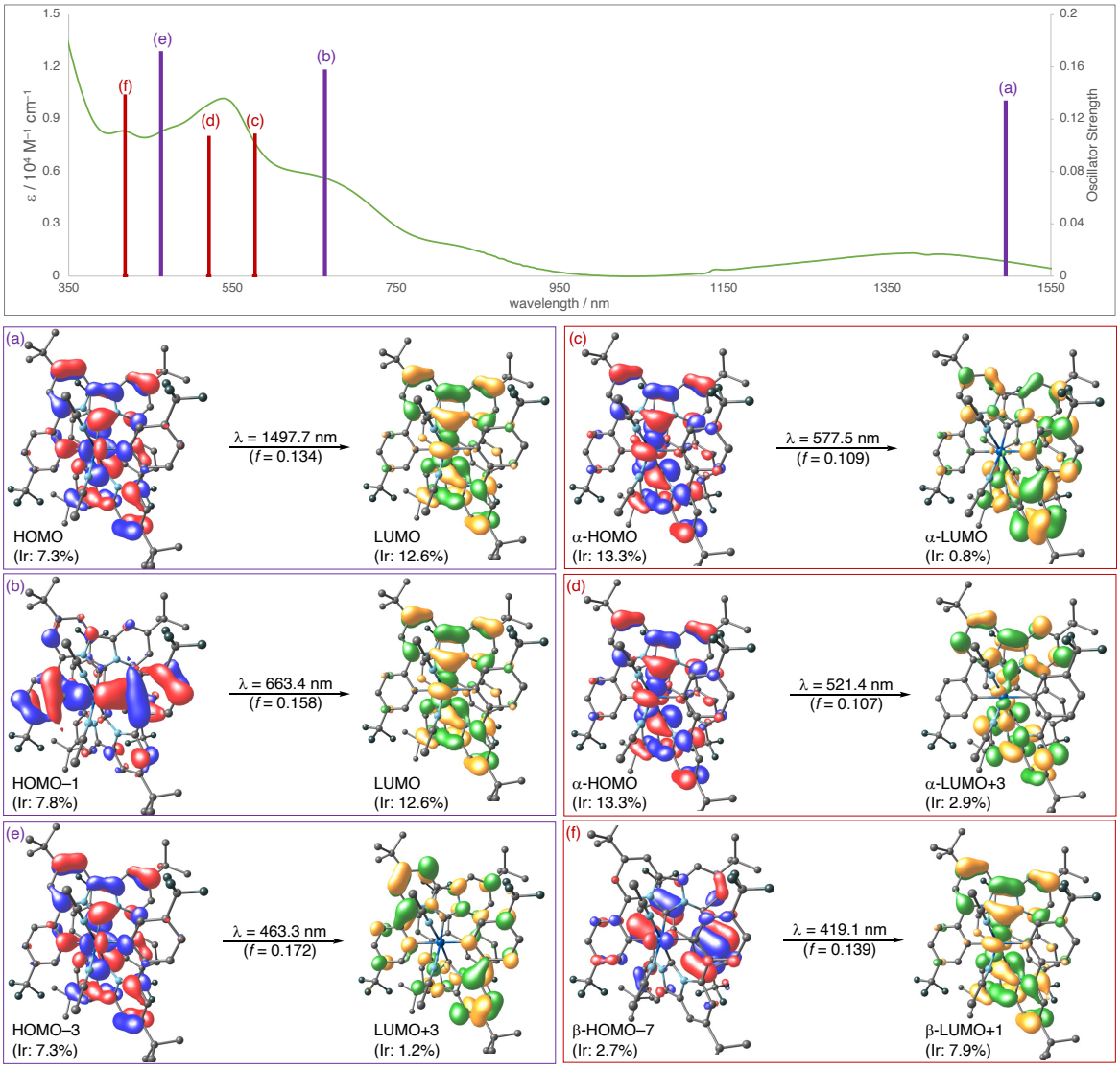

Figure 3.34 TD-DFT calculation of **36** and corresponding transition description

According to the tracing reaction in Figure 3.23, complex **35** should be generated. Thus, its detection was attempted (Scheme 3.7). Although an oxidant of silver cation lightly less than stoichiometry afforded the brown suspension of the reaction mixture, complex **35** could not be isolated, likely due to the almost same solubility of **28**. the EPR spectrum of the crude product of complex **35** was taken even though considering the no effect of EPR-silent species of closed shell complex **28** (Figure 3.35). The signal was observed between 3000 and 3700 G, implying that ligand-center oxidation could happen. A couple of iridium(III) complexes bearing radicals on redox non-innocent ligands showed a similar region.[138,181,182] The calculated spin density illustrated that the radical were delocalized on one of two dpa-NHC and the Ir center (14.6%) Compared with that of Thompson's iridium(III) and platinum semiquinolinate complexes (~5 %)[181], the value of **35** was larger. However, the anisotropy seemed to be small, probably due to the measurement at higher temperature.

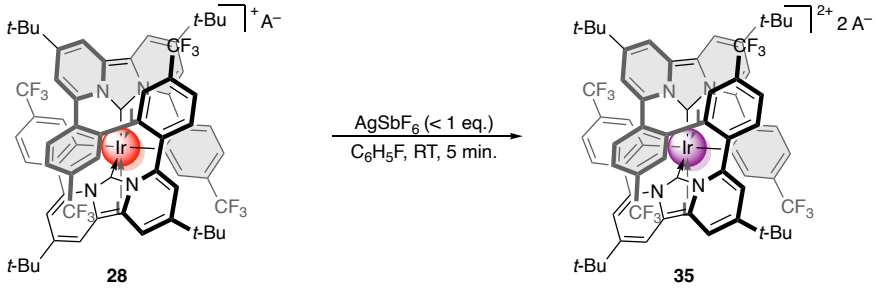

Scheme 3.7 Generation of complex **35**

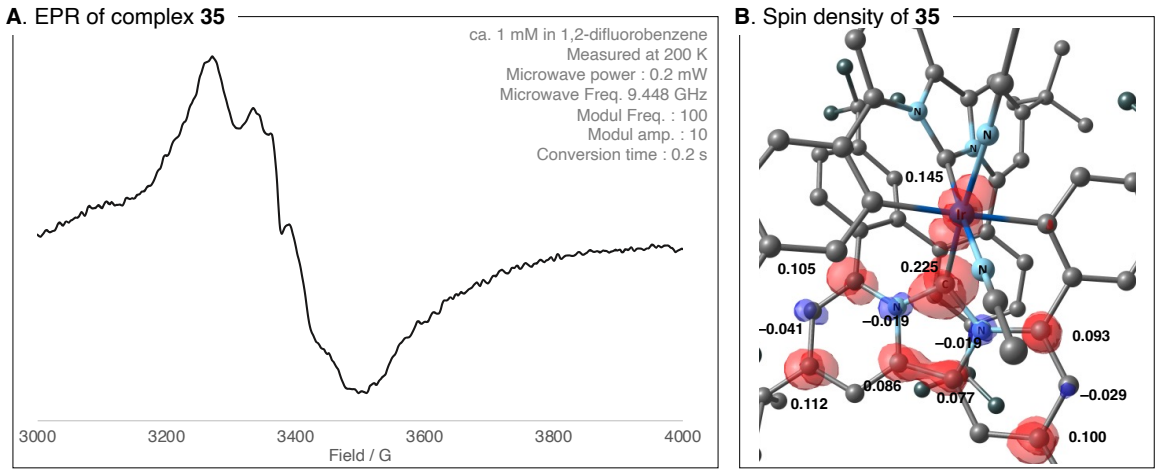

Figure 3.35 Detection of complex **35**

IBO analysis of complex **36**, indicated the d-orbitals of iridium and π-orbitals of dpa-NHC tetradentate ligand trended the that of complex **36**, namely three occupied d-orbitals and α dpa-NHC style π-orbital plus another β bipyridine-type π-orbitals. These results supported the ligand-center oxidation from **28** at one dpa-NHC fragment, followed by another framework (Figure 3.36).

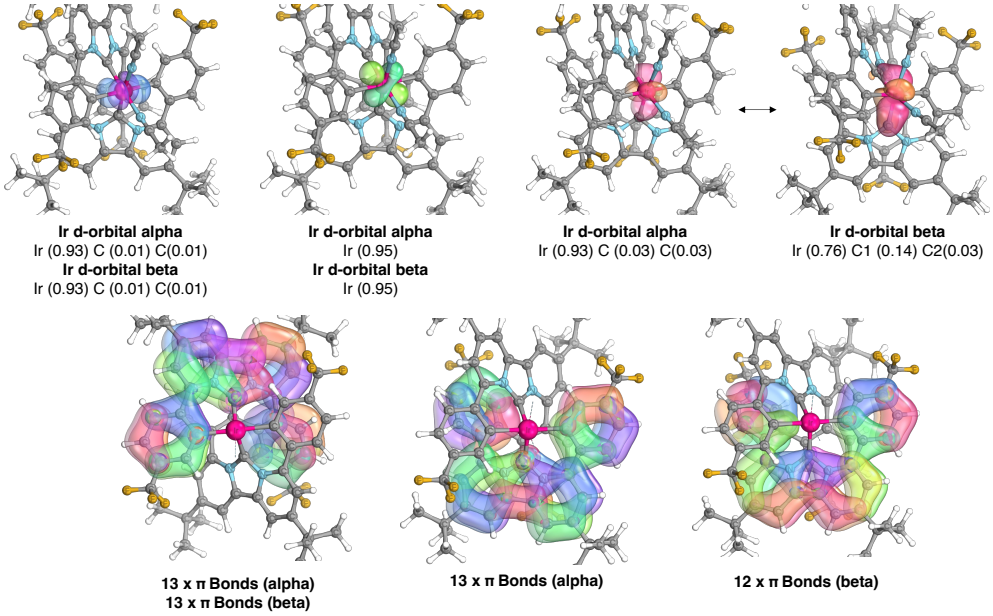

Figure 3.36 IBO analysis of complex **35**

TD-DFT calculation was conducted in order to follow the monitoring oxidation. Figure 3.37 illustrated the UV-Vis-NIR spectra of in situ generated **35** in fluorobenzene and TD-DFT results, which was in good agreement with the experimental spectrum. One of the most characteristic ones was the absorption at 605.3 nm (transition (a)) from β-HOMO–4 to β-LUMO. This absorption seemed to be close to Thompson's iridium(III) semiquinoline complex[183]. This cause likely because of the energy level reduction of β-LUMO by oxidation (Originally, β-electron was fulfilled in HOMO in complex **28**. That is why the absorption wavelength became red-shifted although the donor orbital is lying lower in energy (β-HOMO–4). Other large oscillator strength looked similar transition compared with those of complex **28**.

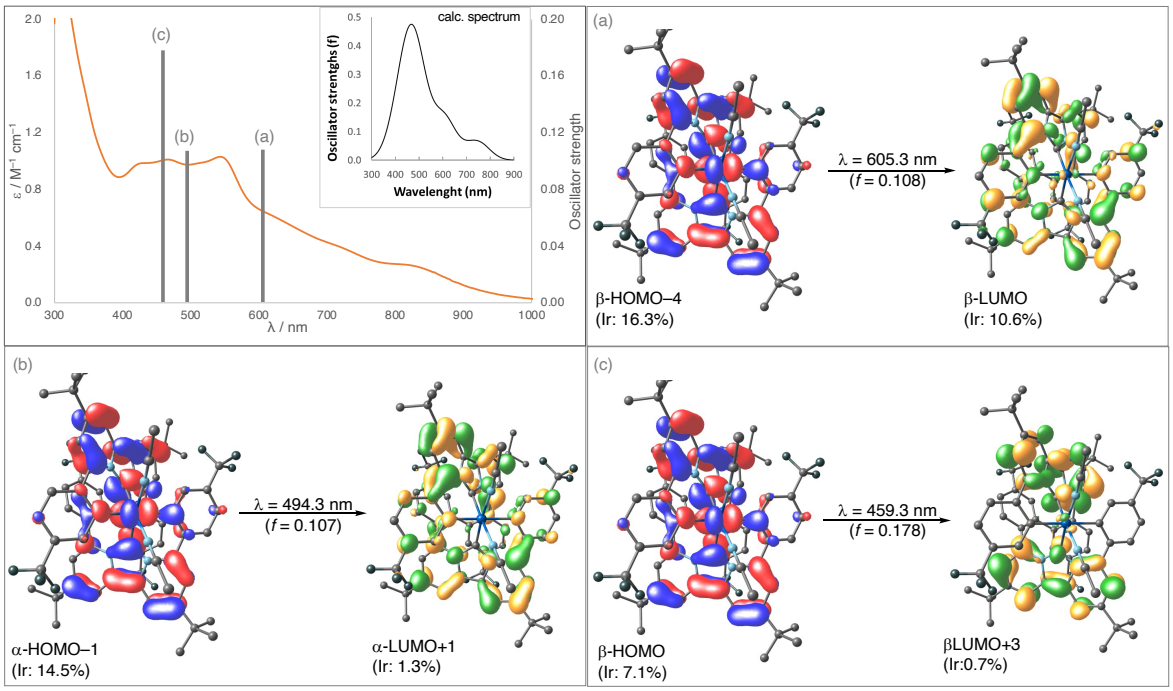

Figure 3.37 UV-Vis-NIR spectrum of complex **35** in fluorobenzene with the results of TD-DFT calculation. Transitions (a) to (c) correspond to the described MOs. TD-DFT study was performed at the level of (SMD:fluorobenzene)M06/def2svpp//oniom(wB97X-D/[6-31G(d),LANL2DZ]:pm6).

3.6. Reactivity investigation for 36

Finally, the reactivity of complex **36** was investigated. Rauchfuss reported the Cp*Ir(III) complex bearing redox non-innocent *ortho*-aminophenol oxidized H_2 and Et_3Si–H to proton trapped by 2,6-di-*tert*-butylpyridine[138]. Following that, the oxidation of H_2, Et_3Si–H, and pinB–H were attempted using $AgSbF_6$ and complex **36** as a catalyst (2.5 mol%) In the case of hydrogen, the reaction mixture turned from blacky purple to deep red, implying that complex **36** was reduced the complex **28**. Although the reduction was confirmed by NMR as well as the color change, the protonation of 2,6-di-*tert*-butylpyridine was not observed. Even though the color change was observed, the precipitation of elemental silver was not generated, which suggested likely complex **28** was reduced by hydrogen gas. (Scheme 3.8)

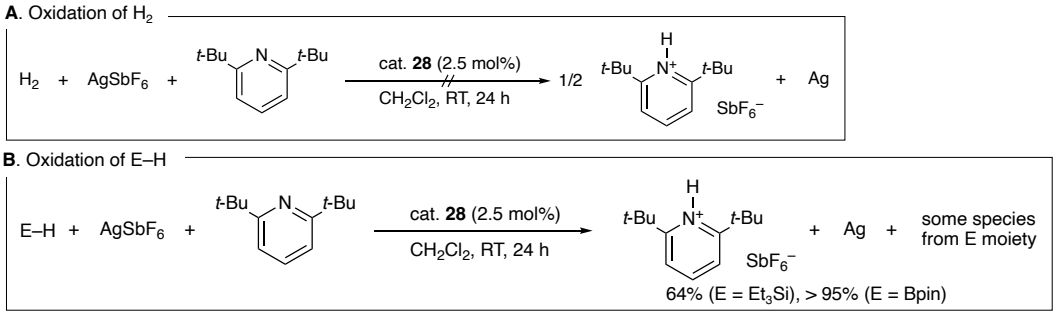

Scheme 3.8 Oxidation of E–H (E = H or BR_2 or SiR_3) catalyzed by complex **36**

On the other hand, Et_3SiH, and HBpin were oxidized through the iridium catalyst **36**. (64% and > 95% NMR yield respectively) whereas the non-poler H–H bond, the H moieties in E–H bonds have partial negative charges according to the electronegativity. In addition, HBpin has oxygen atoms that can coordinate toward the metal center. Taking the enhancement of Lewis acidity by tri-cation complex **36** into account, the *O*-coordination of HBpin accelerated the oxidation process, reflecting the yield compared with that of $HSiEt_3$.(Figure 3.38)

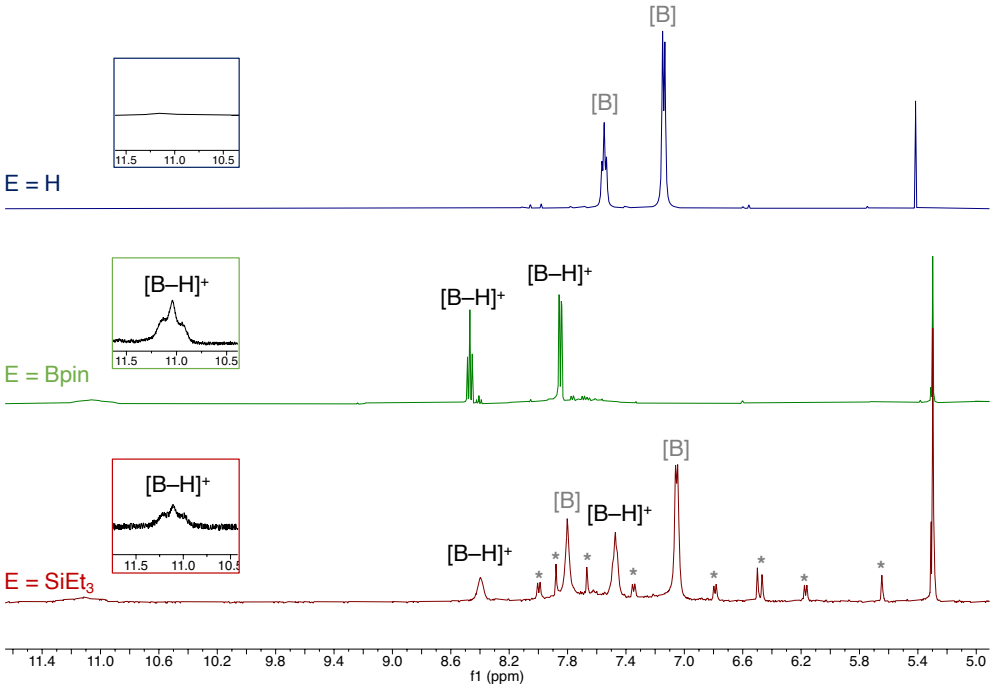

Note [B]: 2,6-di-*tert*-butylpyridine, $[B–H]^+$: 2,6-di-*tert*-butylpyridinium salt, *: complex **28**

Figure 3.38 NMR spectra of the crude products for E–H oxidation

With respect to the E moieties after oxidation, the product was predicted using the $^{11}B\{^1H\}$ NMR. Two signals at 21.5 and 19.7 ppm were observed, which could be assignable as pinB–O–Bpin, and pinB–OH, respectively. (Proton-coupled ^{11}B NMR got no coupling with H, providing the consumption of HBpin, See Figure 3.39). When sampling, a wet CD_2Cl_2 was used. Thus, the water was contaminated in the sample, which could be from the Bpin radicals. Applying this prediction to the $SiEt_3H$ oxidation, $Et_3Si–O–SiEt_3$, and/or $Et_3Si–OH$ were observed; however, these species were not observed yet. Using these potentials, the oxidative borylation/silylation of the organic molecules such as olefine are planning to the next stage as an application of catalysis for complex **36**.

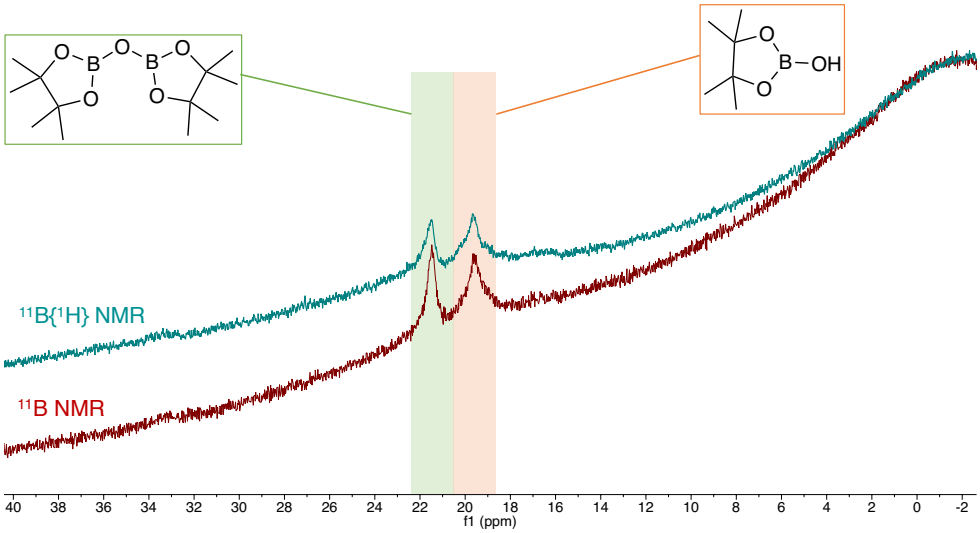

Figure 3.39 Stacked ^{11}B and $^{11}B\{^{1}H\}$ NMR spectra of the crude product for H–Bpin oxidation

3.7. Conclusion

By using the diaryl-substituted dpa-NHC as a LX_2 ligand for a rigid and stable iridium metallacycle, the strong s and π donating properties allowed versatile redox behavior from the anionic bis(*CCC*-pincer)iridium complex **23**. The first $2e^-$ oxidation led to oxidative coupling of the adjacent aryl groups, resulting in a racemic mixture of chiral cationic Ir^{III} complex (**28**) bearing a figure of 8 tetradentate L_2X_2 type *CCCC*-ligand. Although the intermediate Ir^{IV} (**26**) and Ir^{V} (**29**) complexes could not be isolated, they were long-lived enough for characterization by CV, EPR and NMR experiments. Shown by a reversible CV voltammogram, a further $2e^-$ oxidation from complex **28** was possible. A chemical oxidation by excess $AgSbF_6$ afforded a tricationic high-valent iridium complex **36**. Although **36** was expected to have a +V oxidation state formally, iridium L_3-edge energies measured from XANES suggested a physical oxidation state lower than +III. Computational studies suggested a triplet ground state for **36**, with a small singlet-triplet energy difference of 1.3 kcal/mol. Spin-density population suggested a major spin contribution from the dpa-NHC ligands (16.4% from each carbene center) and a significant contribution from the metal (9.3%). The ground triplet state was confirmed by low-temperature detection of a characteristic half-field signal by VT-EPR as well as magnetic properties measured by SQUID, which afforded an experimentally estimated singlet-triplet energy difference of 0.12+0.02 kcal/mol.

The carbon-ligated metallacycles of iridium reported in this study closed the electronegativity gap in the synthetic strategies for high-valent iridium. The present case of the tricationic complex **36** demonstrated that despite a seemingly high-valency (with a formal oxidation state of +V), the physical oxidation state of the metal centre may be very different (~ +III). In the oxidation steps from **28** to **36**, the *CCCC*-tetradentate ligand worked as a redox-non-innocent ligand, aromatically stabilizing the triplet state as the overall charge increased, demonstrating the electronic tuning potential of π-conjugated carbon ligands.

CHAPTER 4.
SUMMARY AND OUTLOOK

The chemical species of 'carbene' has been known in the 120 years ago, which was postulated as an intermediate of cyclopropanation Since the breakthrough report for the first isolation of the NHC by Arduengo in 1991, the carbene chemistry rapidly exploded in recent three decades. The trend of carbene in the 21st century was toward an increase in the π-acidic properties such as CAACs, boron-substituted carbene, and acyclic carbenes. These carbenes were easily tunable in the view of the electronic and steric characters, which make their transition metal complexes applied in various fields of catalysts and luminescent materials. Additionally, the carbenes were widely used in main-group chemistry, especially low-valent boron, and silicon chemistry, which work to cap the empty p-orbitals.

Whereas the large application of carbenes in low-valent species, the high-valent transition metal complexes with carbenes remain sporadic owing to the empty p-orbitals. Generally, the 3d transition metal complexes with formally high oxidation states require electronegative ligands such as halogen, nitrogen, and oxygen. Lone-pairs on these ligands (X) easily interacted to the carbene's p-orbitals, which resulted in the insertion of X into the metal-carbon bond, or dissociation with the carbene-X adduct. Focus in the 4d and 5d transition metal complexes, the high-valent organometallic complexes were rarely reported because of their nature of large gap for each d-orbitals. Even though the formal oxidation state was higher in the metal center, the physical oxidation state of the metal centers could be assigned as lower oxidation states by inverted ligand field theory.

To overcome the undesired decomposition or reduce the barrier for high oxidation states, we engaged in the π-rich carbene. Alkoxide substitution on the nitrogen of NHC brought about pushing electrons toward the NHC ring. And the highly π-acidic carbenoid complexes of antiaromatic nature could be reduced to the 6π-carbene system, in which π-electron was localized on carbene carbon, predicted by theoretical calculations. While these carbene systems seem to be difficult to utilize the multidentate ligands, the ring-expanded NHC (dipyrido-annulated NHC, dpa-NHC) have been studied by a couple of groups. Dpa-NHC took advantage of the high-lying π-orbitals in energy, which could work as a strong π-donor, compared with Arduengo's NHCs in both experimental and theoretical points of view. Even though the dpa-NHC has a stronger carbone (carbon(0) species) character, Weiss, Kunz, de Ruiter, and we demonstrated working as carbene based on NMR studies of their own and complexes.

The parent and 2,10-di-*t*-butyl substituted (para-position from pyridio ring) dpa-NHCs were reported by Weiss and Kunz, respectively. In addition, our group established how to introduce the

functional groups at ortho positions. The phosphine-functionalized dpa-NHCs were well-studied in the field of coordination chemistry in coinage metal or iron complexes applied in homogeneous catalysis. On the other hand, arylated dpa-NHC was developed in synthesis; however, the application as pincer ligands had been elusive.

With this carbene, we envision a new LX_2 pincer ligand based on the dpa-NHC framework. In addition to the electronic advantage, the topological analysis according to the percent varied volume showed 67.2%. This value was significantly larger than other arylated NHCs, which provided spherical 6-membered metallacycles with an ideal bite angle. However, reported LX_2-type metallacycles have a poor library owing to the facile cleavage of M–C bonds from the highly strained rings containing metal centers. Due to these reasons, a new LX_2-type ligand system that allows easy complexation to afford stable complexes is highly desirable.

We made three complexation strategies to obtain desired metallacycles, direct double cyclometallation from **8**, stepwise synthesis, and cascade formation from the imidazolium salt **7**. In the first method, toluene-reflux with **8**, spontaneously reacting any iridium precursor (*Route A*) gave a decomposition **10**. According to ^{19}F NMR studies and HRMS results, $Ir(OAc)_3$ brought about the double coordination of **8** with a couple of C–H bond activation. Remarkably, $[Ir(cod)Cl]_2$ resulted in a relatively reduced amount of decomposition and one (or two) products.

In the manner of $[Ir(cod)Cl]_2$ as an iridium source, stepwise synthesis was attempted (*Route B*). The early stage of the desired complex was the successful synthesis of IrCl(cod)(dpa-NHC) **19** via transmetallation by use of Ag. With this complex, the base-promoting C–H activation was attempted, which resulted in an unassignable complex mixture. Although any supporting ligands were added in this process, desired C–H activation was not obtained.

Interestingly, the one-pod reaction of **7** and $[Ir(cod)Cl]_2$ in the presence of Cs_2CO_3 provided the desired but doubly dpa-NHC pincer-coordinated iridium complex (*Route C*). The counter-ion and its oxidation state were confirmed by trapping with [2,2,2]-cryptand and XANES study respectively. The number of dpa-NHC pincer could not be controlled by stoichiometry, which the rate-determining step was the first cyclometallation from **19** by theoretical calculation. After that, the energy profile illustrated the downhill process reflecting the experimental result. In addition, the retro-reaction of cyclometallation with the weak acid produced the Ir–C bond cleavage complex **25**, which was predicted as the last intermediate by DFT calculation (Scheme 4.1).

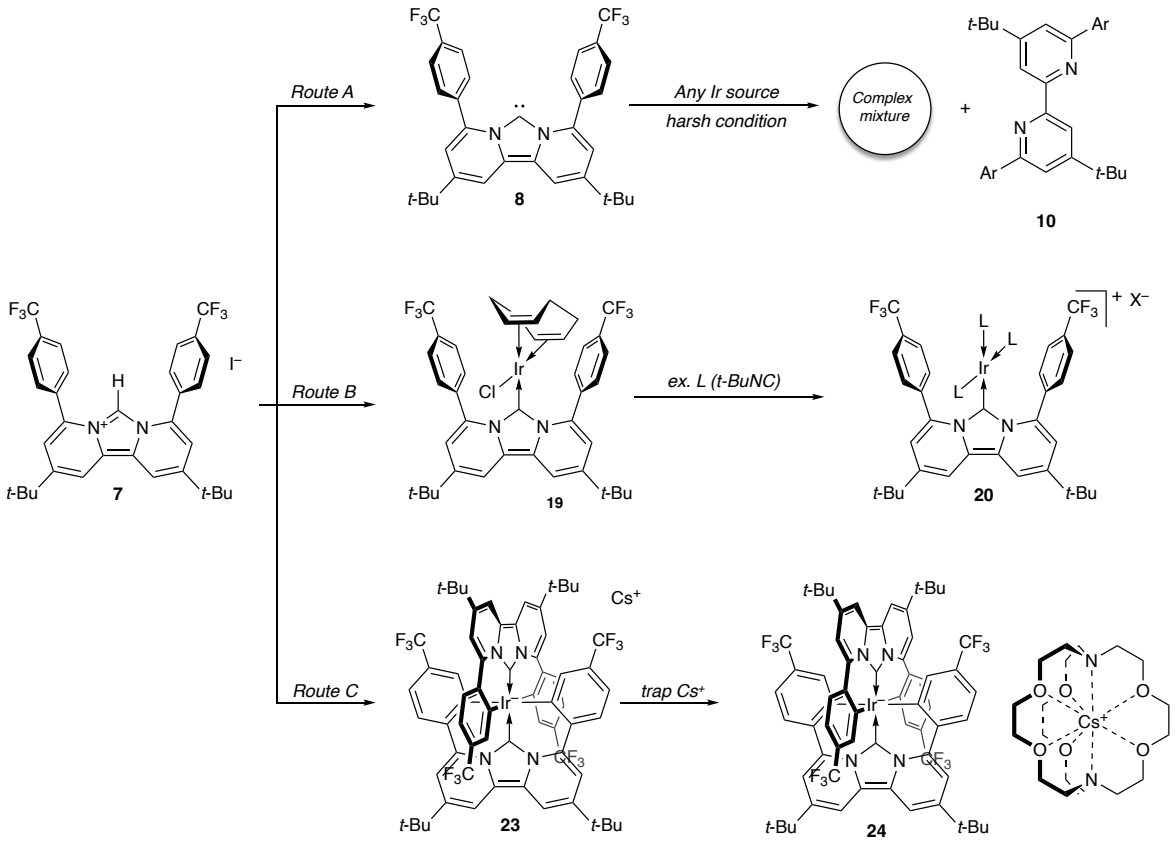

Scheme 4.1. Cyclometallation of arylated dpa-NHC toward iridium centers.

A unique property of complex **23** is oxidation behavior. According to CV, four oxidation wave was observed, and which second one was irreversible. Low-temperature CV measurement became reversible on the second wave. Chemical two-electron oxidation formed a spiro Ir cationic complex through an oxidative C-C bond coupling of two adjacent aryl groups of the originally separate dpa-NHC units. This transformation reaction took a metal-centered oxidation, which detected the one-electron and two-electron oxidized intermediates by extremely low-temperature EPR and low-temperature NMR studies, respectively. The key process was the MeCN coordination in high-valent Ir intermediate, supported by DFT calculation. The low-lying activation barrier for reductive elimination implied the generation of the thermally unstable Ir(V) complex (Scheme 4.2).

Several ligands facilely replaced coordinated acetonitrile ligands such as two L-type, L–L bidentate, and L–X bidentate ligands. These supporting ligands made electronic properties slightly changed. For example, the redox potentials became only little shifts, likely depending on the π-donating/withdrawing abilities of supporting ligands. Although the electronic properties had differences, the structural parameters remained slimier. Unfortunately, the catalytic abilities of the complex were not able to be found including the alkane dehydrogenation and direct C–H borylation on aromatic compounds.

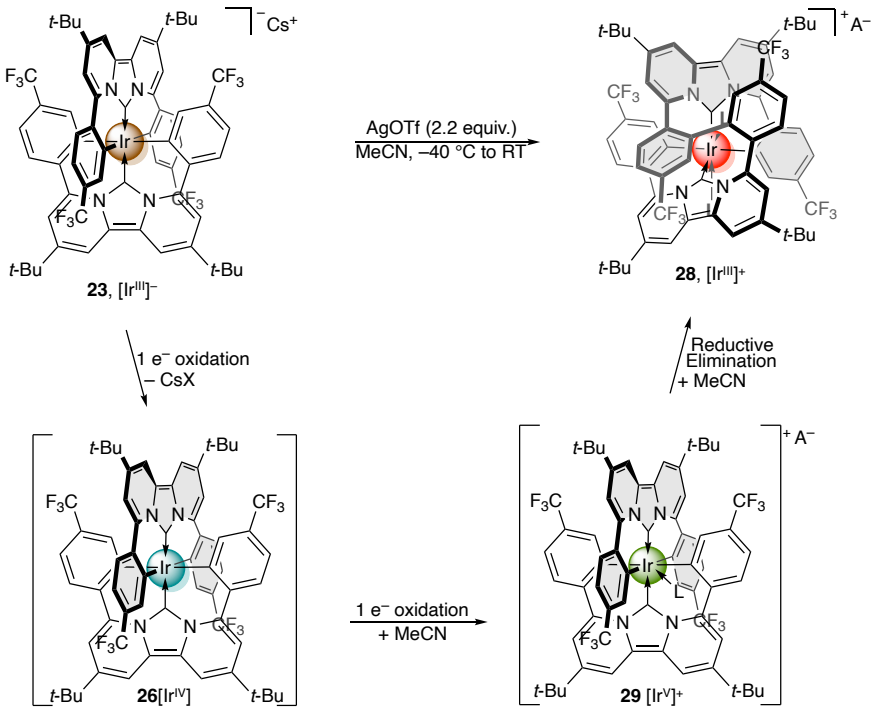

Scheme 4.2. Oxidatively induced ligand transformation from the anionic iridium complex **23**

The CV showed the two reversible redox waves, which had the similar potential for the third and fourth ones of complex **23**. Encouraged by the low reversible redox couples observed for **4**, chemical oxidation using excess $AgSbF_6$ was carried out in fluorobenzene at room temperature. This led to the isostructural iridium complex with the three counter-anion of the SbF_6^-. While the bond angles remained the same, this oxidation resulted in dramatic changes in the bond distance, exhibiting the bond alternation on dpa-NHC framework. By specific investigation of both experimental and theoretical insights, the oxidation mainly took place on each dpa-NHC framework favorable triplet ground state. The oxidation state was predicted using XANES and IBO analysis, suggesting the equal or smaller than +III. The singlet-triplet energy gap of 0.12 kcal/mol was estimated using EPR and SQUID measurements. Compared with the reported open-shell transition metal complex with redox non-innocent ligand(s), the contribution from the iridium center was larger, reflecting the slight anisotropic g value and small spin density population. This tri-cationic complex can oxidize negatively polarized hydride species such as borane and silane. This trace exhibited that the dpa-NHC allowed to access high-valent transition metal complexes as well as to demonstrate working as a redox non-innocent ligand (Figure 4.1).

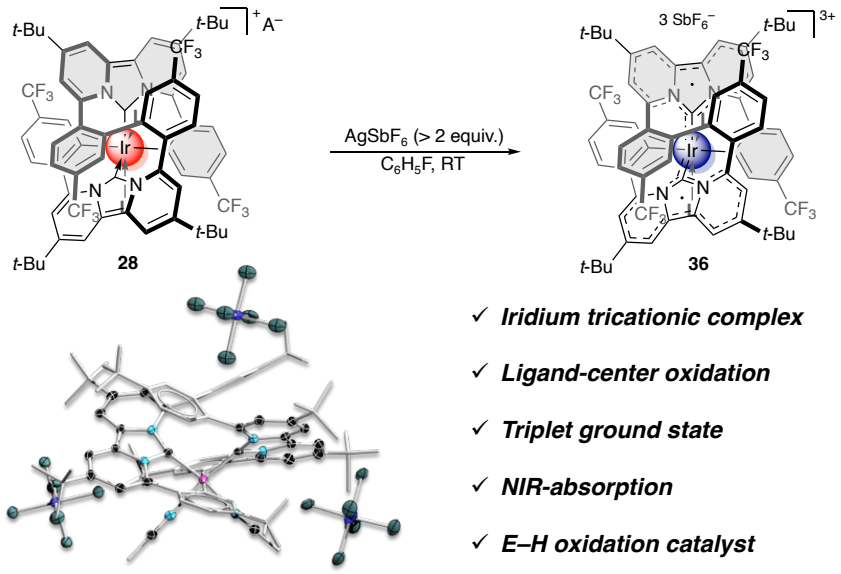

Figure 4.1 Oxidation of complex **28**

Our establishment of base-promoted cyclometallation of arylated dpa-NHC could apply to other transition metal centers. Avoiding the direct C–H activation took advantage in the cyclometallation for remaining oxidation states or unfavored metal center for C–H activation such as coinage metals. This aspect made organometallic chemistry developed the new methodology and enchaining the candidate for application toward luminescent materials.

We could also give our prospects through only-one property of CCCC-tetradentate iridium complexes; the oxidative coupling provided the racemic products, which could be separated enantiomers by use of the chiral counter-anion of borate or phosphate. Through this assumption, we can turn over the chiral nature and its application such as circular polarization or catalysis of asymmetrical functionalization via nucleophilic attack to E^+ generated with the oxidation by enantio-pure tri-cationic iridium complex.

CHAPTER 5.
EXPERIMENTAL SECTION

5.1. General remarks

All manipulations involving the air- and moisture-sensitive compounds were carried out under an argon atmosphere using the standard Schlenk and workups were carried out on the bench unless mentioned. Inert gases (both N_2 and Ar) were passed through a dry column of P_2O_5. All glassware was dried in 80 °C ovens. Acetonitrile (acetonitrile-d_3) and dichloromethane (dichloromethane-d_2) were pre-dried with $CaCl_2$, then distilled with CaH_2 under N_2. THF, hexane, Et_2O, and toluene were dried by distillation with Na and stored over molecular sieves prior to use. Benzene-d_6 was purified by use of potassium mirror and stored in molecular sieves 4A.

^1H (500 MHz), $^{13}C\{^1H\}$ (125 MHz), ^{19}F (480 MHz), NOESY and COSY were recorded using a JEOL ECA-500 spectrometer. ^1H (600 MHz), $^{13}C\{^1H\}$ (150 MHz) ^{19}F (564 MHz) and any 2D NMR (^1H-^1H COSY, NOESY, ^1H-^{13}C HMQC and ^1H-^{13}C HMBC) were recorded using a JEOL ECA-600 spectrometer. The chemical shifts (δ) were referenced to C_6D_6 (^1H: δ = 7.16 ppm, ^{13}C: δ = 128.26 ppm), CD_2Cl_2 (^1H: δ = 5.32 ppm, ^{13}C: δ = 53.84 ppm) and CD_3CN (^1H: δ = 1.93 ppm, ^{13}C: δ = 118.62 ppm) as external standard and from internal $CFCl_3$ for ^{19}F (δ= 0.00 ppm). High-resolution mass spectra (HRMS) were recorded with a Thermo Fischer Scientific samples. UV/Vis absorption spectra of 0.10 mM sample in acetonitrile was recorded on UV-1650 PC (SHIMADZU) in ambient atmosphere at room temperature. Cyclic voltametric measurement was performed by using ALS/CHI610E potentiostat/galvanostat in 0.1 M $[nBu_4N][PF_6]$ solution with argon atmosphere. Working, counter and reference electrode were employed as glassy carbon, platinum wire and saturated calomel electrodes, respectively. Internal referenced was employed as the redox couple of ferrocene and ferrocenium as 0 V. The EPR spectra were taken by using a Bruker ELEXSYS E500 spectrometer and simulated by WinSimphonia. The internal reference of ferrocene was used. The XPS spectra was collected using a monochromatic 1486.7 eV Al Kα X-ray source of ESCA-3400 HSE X-ray photoelectron spectrometer with 0.5 eV system resolution. The energy scale was calibrated using C 1s (285 eV) on the carbon tape.

Crystals suitable for the X-ray structural determination were mounted on a Bruker SMART APEXII CCD diffractometer and irradiated with graphite monochromated Mo Kα radiation (λ = 0.71073 Å) for data collection. Or crystals suitable for the X-ray structural determination were mounted on a Rigaku XtaLAB Synergy DW system and irradiated with graphite monochromated Mo Kα radiation (λ = 0.71073 Å) for data collection. The data were processed using the CrysAlisPro suite.

All structures were solved by an intrinsic phasing method using the SHELXT program (ver. 2014/4–2014/5)[184]. Refinement on F^2 was carried out using full-matrix least-squares with the SHELXL[185] and expanded using Fourier techniques. All nonhydrogen atoms, except those of disordered solvents, were refined using anisotropic thermal parameters. Hydrogen atoms were assigned to idealized geometric positions and included in structure factor calculations. The SHELX was interfaced with SHELXLE GUI for most of the refinement steps[186]. All the pictures of the molecules were prepared using Pov-Ray 3.6.[187]

5.2. Synthetic procedures

Chapter 1

- *Synthesis of **2***

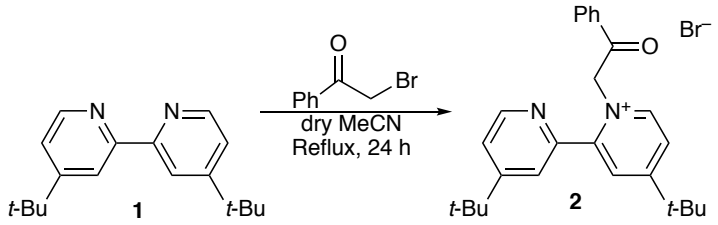

A colorless suspension of 4,4'-di-*tert*-butyl-2,2'-bipyridyl (5.40 g, 20.1 mmol) and α-bromoacatophenone (4.20 g, 21.1 mmol) in acetonitrile (70 mL) was refluxed until the color changed to reddish. The solution was evaporated as much as possible. Bubbly orange solid was used for next reaction without further purification was not carried out.

^{1}H NMR (400 MHz, $CDCl_3$)

δ 1.32 (s, 9H), 1.50 (s, 9H), 6.99 (s, 2H), 7.39 (dd, ^3J = 5 Hz, ^4J = 2 Hz, 1H), 7.47 (t, ^3J = 8 Hz, 2H), 7.60 (s,1H), 7.62 (t, ^3J = 8 Hz, 1H), 7.84 (d, ^4J = 2 Hz, 1H), 8.00 (dd, ^3J = 8 Hz, ^4J = 1 Hz, 2H), 8.06 (dd, ^3J = 7 Hz, ^4J = 2 Hz, 1H), 8.34 (d, ^3J = 5 Hz, 1H), 9.86 (d, ^3J = 7 Hz, 1H) *Unable to find the coupling partner of the dot-lined proton which possesses the Coupling Const. ^4J = 1 Hz.

- *Synthesis of **3***

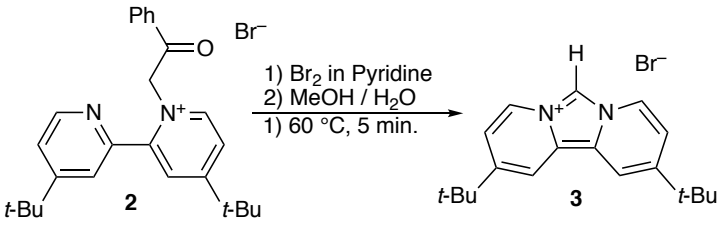

A reddish solution of crude **1** (ca. 9.5 g) in pyridine was heated up to 60 °C, then Br_2 (1.2 mL, 23.4 mmol) was added and stirred at the same temperature for 5 min. (Note that pyridine reacted with Br_2 to afford black sticky solid, thus Br_2 must be added as neat) The solution was evaporated and MeOH and water (both 250 mL) were added for hydrolysis. the yellow precipitation was filtered off with Aluminum oxide 90. KPF_6 (4.00 g, 21.7 mmol) was added to the filtrate, which yielded brown precipitation. MeOH was evaporated as much as possible and then collected by filtration with a Kiriyama funnel. Brown solid was dried *in vacuo*. This brown crude was used for the next reaction without further purification.

^{1}H NMR (400 MHz, $CDCl_3$)

δ = 1.42 (s, 18H), 7.44 (dd, ^3J = 7 Hz, ^4J = 2 Hz, 2H), 7.93 (d, ^4J = 1 Hz, 2H), 9.14 (dd,^3J = 7 Hz, ^4J = 1 Hz, 2H),11.6 (s, 1H) *Unable to find the coupling partner of the dot-lined proton which possesses the Coupling Const. ^4J = 2 Hz.

- *Synthesis of **4***

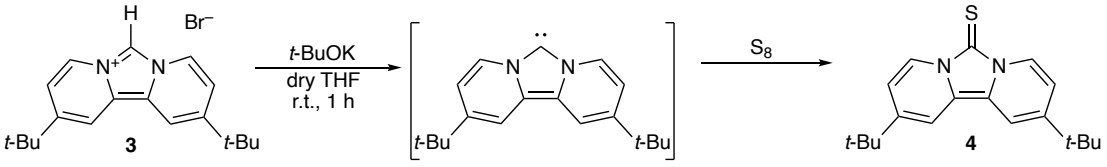

A brown suspension of crude **2** (ca. 11 g) and element sulfur (664 mg, 2.59 mmol) in dry THF was stirred under inert gas atmosphere at room temperature. *t*-BuOK (2.56 g, 22.8 mmol) was added into the suspension, resulting dark red solution and stirred for 1 h. Byproduct salts were filtered off from reaction mixture with Celite. The filtrate was evaporated, and crude product was washed with hexane and crystallized in acetone at –20 °C gave **4** as reddish orange solid in 78% yield from 4,4'-di-*tert*-butyl-2,2'-bipyridyl **1**.

^{1}H NMR (400 MHz, DMSO-d_6)

δ = 1.38 (s, 18H), 7.30 (dd, ^3J = 8 Hz, ^4J = 2 Hz, 2H), 8.20 (s, 2H), 8.43 (d, ^3J = 8 Hz, 2H) *Unable to find the coupling partner of the dot-lined proton which possesses the Coupling Const. ^4J = 2 Hz.

- *Synthesis of **5***

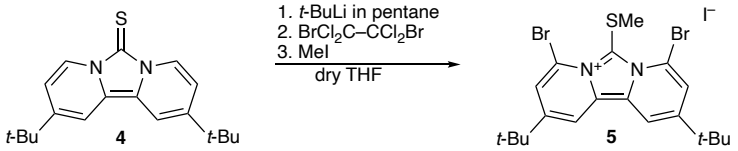

A solution of dry **4** (1.00 g, 3.20 mmol) in dry THF was cooled to –78 °C. *t*-BuLi in pentane solution (1.62 M, 4.8 ml, 7.77 mmol) was added dropwise with additional funnel and stirred for 1.5 h. 1,2-Dibromotetrachloroethane (3.42 g, 8.00 mmol)was added with solid-insertion tube under inert gas atmosphere then, stirred further 2 h. Iodomethane was added into reaction solution by use of syringe at –78 °C. The reaction mixture was warmed to room temperature and stirred additional 1 h. THF was removed from reaction solution, then extracted with CH_2Cl_2 and wash with water, then dried over with Na_2SO_4. The salt was removed by filtration then, filtrate was also removed overnight. Addition/removal cycles with acetone following hexane was carried out, which gave **5** as dark-brown solid. Note that product contained **6** as well as **5** based on ^{1}H NMR spectra.

^{1}H NMR (400 MHz, $CDCl_3$)

δ = 1.56 (s, 18 H), 1.96 (s, 3 H), 8.05 (s, 2 H), 8.70 (s, 2 H).

- *Synthesis of* ***6***

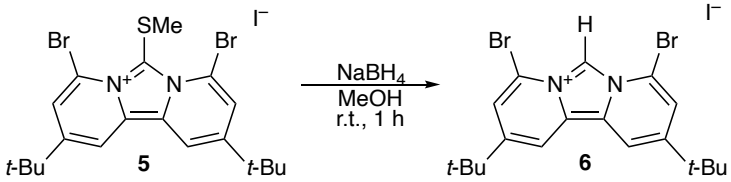

A suspension of crude **5** in MeOH (50 mL) was stirred under air. $NaBH_4$ was added (296 mg, 7.68 mmol, as portion-wise with generation of small amount of bubble. After addition of $NaBH_4$, this mixture was stirred for 1 h. Remained $NaBH_4$ was quenched with small amount of NH_4I, then MeOH was removed. The residue was extracted with CH_2Cl_2 and wash with water, then dried over with Na_2SO_4. The salt was removed by filtration then, the filtrate was also removed. The residue was washed with hexane and Et_2O followed by recrystallization with acetone yielded **6** as brown solid (1.10 g, 1.95) in 61% yield (from **4**).

^{1}H NMR (400 MHz, $CDCl_3$)

δ = 1.52 (s, 18 H), 7.84 (s, 2 H), 9.01 (s, 2 H), 9.75 (s, 1 H).

- *Synthesis of 7*

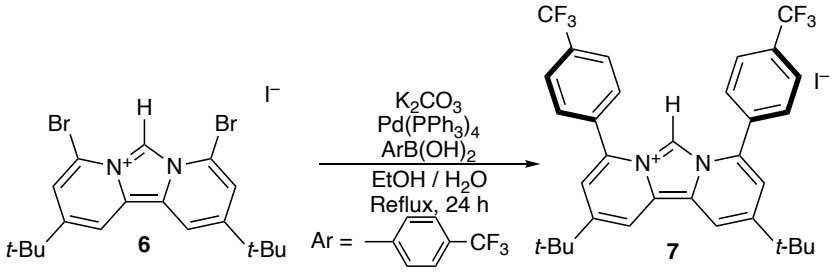

Method A

A solution of **6** (1.15 g, 2.03 mmol p-(trifluoromethyl)phenylboronic acid (949 mg, 5.00 mmol) and $Pd(PPh_3)_4$ (353 mg, 0.30 mmol, 15 mol%) in degassed EtOH (44 mL) was prepared. Degassed K_2CO_3 (680 mg, 4.92 mmol) aq. (8 mL) was added. The reaction mixture was heated up until reflux behavior was observed and continued that temperature for 18 h. After cooled to r.t., the reaction solution was allowed to be evaporated. Extraction with CH_2Cl_2 followed by wash with water and dry over Na_2SO_4. The filtrate was evaporated and wash with hexane to remove CH_2Cl_2. The residue was purified in precipitation with THF/Et_2O (1:400 ratio) yielded imidazolium salts **7** as yellow powder (600 mg, 0.861 mmol) in 42% yield.

Method B

A solution of **6** (800 mg, 1.42mmol), *p*-(pinacolboryl)benztrifluoride (756 mg, 2.85 mmol) and $Pd(PPh_3)_4$ (245 mg, 0.212 mmol, 15 mol%) in degassed EtOH (32 mL) was prepared. Degassed K_2CO_3 (390 mg, 2.85 mmol) aq. (8 mL) was added. The reaction mixture was heated up until reflux

behavior was observed and continued that temperature for 18 h. After cooled to r.t., the reaction solution was allowed to be evaporated. Extraction with CH_2Cl_2 followed by wash with water and dry over Na_2SO_4. The filtrate was evaporated and wash with hexane to remove CH_2Cl_2. The residue was purified in crystallizing acetone/Et_2O yielded imidazolium salts **7** (614 mg, 0.882 mmol) as yellow solid in 63% yield.

^{1}H NMR ($CDCl_3$, 400 MHz)

δ = 1.49 (s, 18 H), 7.38 (s, 2 H), 7.87 (d, $^3J_{HH}$ = 8 Hz, 4 H), 8.20 (s, 2 H), 8.27 (d, $^3J_{HH}$ = 8 Hz, 4 H), 8.95 (s, 1 H).

^{13}C{^{1}H} NMR ($CDCl_3$, 100 MHz)

δ = 30.58, 35.61, 110.44 (q, $^3J_{CF}$ = 2 Hz), 112.70, 120.89 (q, $^1J_{CF}$ = 276 Hz)121.80, 124.31, 125.01, 127.11 (q, $^2J_{CF}$ = 4 Hz), 130.20, 133.02, 133.32, 135.07, 147.80.

^{19}F NMR ($CDCl_3$, 376 MHz)

δ = –63.45 (s, 6F)

- *Synthesis of **8***

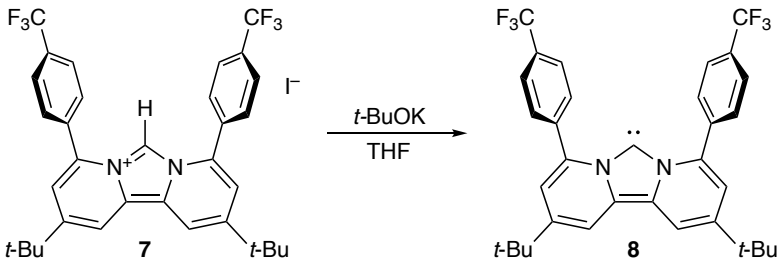

To a stirred yellow suspension of **7** (203 mg, 291 μmol) in THF (25 mL), *t*-BuOK (35.0 mg, 312 μmol) was added at room temperature. The solution changed to orange immediately and was stirred for 20 min. After evaporation of volatiles, the residue was extracted with hexane. Filtration of the hexane extract followed by evaporation *in vacuo* afforded 1 (105 mg, 185μmol) as an orange solid in 64% yield. Single crystals of **8** were prepared by recrystallization from a toluene/pentane two-layer system at –30 °C in glovebox.

^{1}H NMR (600 MHz, C_6D_6)

δ = 1.17 (s, 18H, *t*-Bu), 6.75 (d, 2H, $^4J_{HH}$ = 2 Hz, H_a), 7.29 (d, 4H, $^3J_{HH}$ = 8 Hz, H_c), 7.56 (d, 2H, $^4J_{HH}$ = 2 Hz, H_b), 7.90 (d, 4H, $^3J_{HH}$ = 8 Hz, H_d)

^{13}C{^{1}H} NMR (150 MHz, C_6D_6)

δ = 30.01 (C($\underline{C}H_3)_3$), 34.25 ($\underline{C}(CH_3)_3$), 111.20 (C3), 115.89 (C5), 124.51 (q, $^1J_{CF}$ = 225 Hz, C11), 124.67 (C2), 130.27 (q, $^2J_{CF}$ = 34 Hz, C10), 130.60 (C9), 133.91 (q, $^3J_{CF}$ = 6 Hz, C8), 138.86 (C7), 139.66 (C6), 140.74 (C4), 196.37 (C1)

^{19}F NMR (564 MHz, C_6D_6)

δ = –62.40 (s, 6F)

- *Synthesis of **18***

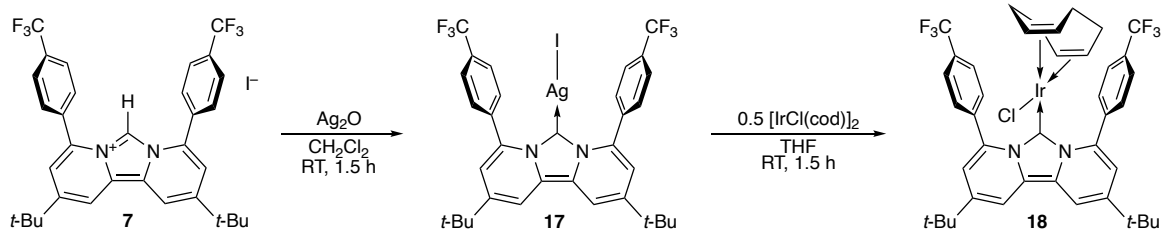

A yellow suspension of **7** (142 mg, 204 μmol) and Ag_2O (55.0 mg, 238 μmol) in CH_2Cl_2 (10 mL) was stirred for 2 h in the dark. The reaction mixture was filtered, and the filtrate was freed of volatiles *in vacuo* to afford silver intermediate **17** a yellow solid. Then, a THF (10 mL) solution of $[IrCl(cod)]_2$ (70.0 mg, 104 μmol) was added to the reaction vessel of **17**. After stirring of the reaction mixture for 2 h, the inorganic salts were filtered off. Evaporation of the filtrate *in vacuo* followed by washing with hexane and Et_2O provided complex **18** as an orange solid (150 mg, 166 μmol) in 81% yield. Single crystals suitable for X-ray diffraction were obtained from a DCM/hexane two-layer system at –20 °C.

*NMR Data of silver intermediate **17***

^{1}H NMR (500 MHz, CD_2Cl_2)

δ = 1.43 (s, 18H, *t*-Bu). 6.98 (d, 2H, $^4J_{HH}$ = 2 Hz), 7.65 (d, 4H, $^3J_{HH}$ = 8 Hz), 7.76 (d, 4H, $^3J_{HH}$ = 8 Hz) 7.91 (d, 2H, $^4J_{HH}$ = 2 Hz)

^{13}C{^{1}H} NMR (125 MHz, CD_2Cl_2)

δ = 30.04, 34.84, 111.65, 119.26, 124.51 (q, $^1J_{CF}$ = 225 Hz, CF_3), 124.55, 126.94 (q, $^3J_{CF}$ = 6 Hz), 129.86, 132.27 (q, $^2J_{CF}$ = 34 Hz), 136.59, 137.98, 143.70

A signal of the carbene carbon cannot be found because of the coupling of NMR-active nuclear of silver ($^{107/109}$Ag)

^{19}F NMR (470 MHz, CD_2Cl_2)

δ = –62.69 (s, 6F)

*Spectra data of complex **18***

^{1}H NMR (600 MHz, CD_2Cl_2)

δ = 0.69–0.73 (br, 2H H_j), 0.94–0.99 (br, 2H H_h), 1.23–1.29 (br, 2H, H_i), 1.38 (s, 18H, *t*-Bu), 1.60–1.68 (br, 2H, H_k) 1.96–2.00 (m, 2H, H_l), 3.53 (m, 2H, H_g), 6.84 (d, 2H, $^4J_{HH}$ = 2 Hz, H_b), 7.60–7.68 (br, 2H, H_f), 7.64–7.73 (br, 2H, H_d) 7.75–7.81 (br 2H, H_c, overlapping with H_a) 7.76 (d, 2H, $^4J_{HH}$ = 2 Hz, H_a) 8.28–8.34 (br, 2H, H_e)

*Peaks of H_c, H_d, H_e and H_f became doublet ($^3J_{HH}$ = 8 Hz) at –40 °C.

^{13}C{^{1}H} NMR (150 MHz, CD_2Cl_2)

δ = 27.51 (C15), 29.95 (C(*C*H$_3$)), 32.09 (C14), 34.40 (*C*(CH$_3$)), 49.06 (C13), 81.70 (C16), 111.47 (C3), 121.52 (C5), 124.51 (q, $^1J_{CF}$ = 225 Hz, *C*F$_3$), 124.02–124.28 (br, overlapped with 2 peaks, C9/C11), 129.57 (C8), 130.12 (q, $^2J_{CF}$ = 28.5 Hz C10), 134.78 (C12), 137.82 (C7), 139.76 (C6), 141.20 (C4), 160.94 (C1)

^{19}F NMR (564 MHz)

δ = –62.36 (s, 6F)

ESI-HRMS (positive)

[$C_{41}H_{42}N_2F_6IrCl$] Calc. for 869.28814 as [M–Cl]$^+$, found for 869.28693 as [M–Cl]$^+$

- *Synthesis of complex **20**.*

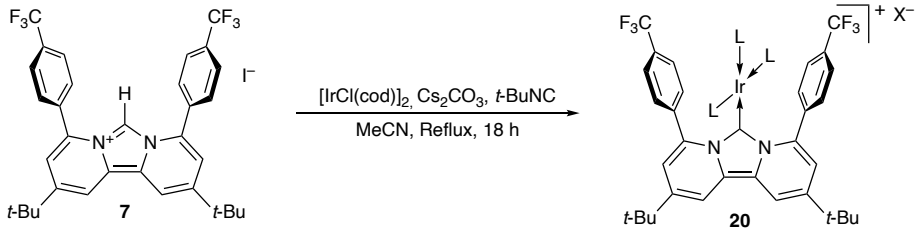

An orange suspension of NHC precursor **7** (71.1 mg, 102 μmol), dry Cs_2CO_3 (43.0 mg, 132 μmol), *t*-BuNC (35.3 mg, 424 μmol) and [IrCl(cod)]$_2$ (36.4 mg, 54.1 μmol) in MeCN (5 mL) was refluxed for 16 h. After cooling to room temperature, the reaction mixture was filtered to remove any insoluble salts and the collected filtrate was evaporated in vacuo. The resulting residue was washed with hexane to afford the desired product **20** as reddish solid (80 .3 mg, 79.6 μmol) in 78 % yield. Single crystals suitable for X-ray diffraction were prepared by DCM/hexane at –20 °C.

^{1}H NMR (600 MHz, CD_2Cl_2)

δ = 1.321 (s, 9H, *trans*-*t*-BuNC), 1.327 (s, 18H, *cis*-*t*-BuNC), 1.42 (s, 18H, *t*-Bu on dpa-NHC). 6.94 (d, 2H, $^4J_{HH}$ = 2 Hz, H$_b$), 7.55 (d, 4H, $^3J_{HH}$ = 8z Hz, H$_d$), 7.59 (d, 4H, $^3J_{HH}$ = 8 Hz, H$_c$) 7.94, (d, 2H, $^4J_{HH}$ = 2 Hz, H$_a$)

^{13}C{^{1}H} NMR (150 MHz, CD_2Cl_2)

δ = 30.04 (*C*H$_3$ for cis-*t*-BuNC), 30.14(*C*H$_3$ of trans-*t*-BuNC), 30.28, 34.75 (C(*C*H$_3$)$_3$ for dpa-NHCs), 56.48(*C*(CH$_3$)$_3$ for *trans*-*t*-BuNC), 57.02 (*C*(CH3)3 for *cis*-*t*-BuNC), 111.75 (C3) 119.69 (C5), 123.65 (q, $^3J_{CF}$ = 2 Hz, C9), 124.44 (q, $^1J_{CF}$ = 225 Hz, CF$_3$), 125.13(C2), 129.86(C8), 130.32 (q, $^2J_{CF}$ = 34 Hz, C10), 136.88 (C7), 139.10 (C6), 143.06 (C4), 148.45 (*C*N*t*-Bu of cis), Signals of the isocyanide sp carbon atoms (*C*N*t*Bu) and the carbene carbon atom were not observed.

^{19}F NMR (564 MHz, CD_2Cl_2)

δ = –62.50 (s, 6F)

ESI-HRMS (positive)

Calc. [$C_{48}H_{57}N_5F_6Ir$]$^+$ for 1010.41474, found for 1010.41418 as [M]$^+$

- *Synthesis of complex **23***

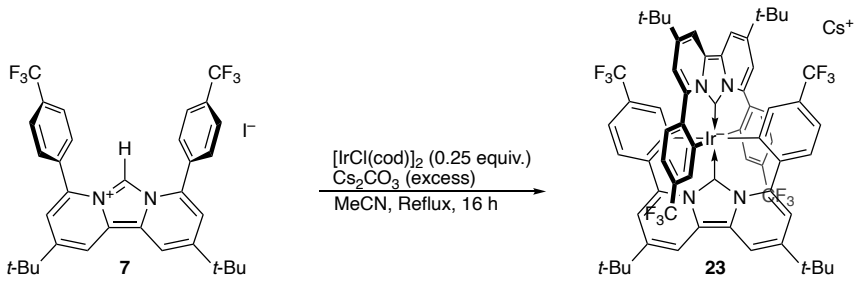

A solution of **7** (165 mg, 237 μmol), dry Cs_2CO_3 (370 mg, 1.10 mmol), and $[IrCl(cod)]_2$ (39.6 mg, 59.5 μmol) in dry MeCN (5 mL) was refluxed for 16 h. After cooling to room temperature, the inorganic salt was filtered through Celite and the collected filtrate was evaporated *in vacuo* to afford a dark purple solid. In a glovebox, further washing with Et_2O followed by hexane provided complex **23** as a wine-red solid (145 mg, 100 μmol) in 84 % yield (based on iridium). Single crystals suitable for X-ray diffraction were prepared by slow diffusion of pentane into THF solution of **23** at room temperature.

^{1}H NMR (600 MHz, CD_3CN)

δ = 1.51 (s, 36H, *t*-Bu), 6.16 (d, 4H, $^4J_{HH}$ = 2 Hz, He), 6.72 (dd, 4H, $^3J_{HH}$ = 8 Hz, $^4J_{HH}$ = 2 Hz, Hd) 7.72 (d, 4H, $^4J_{HH}$ = 2 Hz, Hb), 7.82 (d, 4H, $^3J_{HH}$ = 8 Hz, Hc), 8.17 (d, 4H, $^4J_{HH}$ = 2 Hz, Ha)

^{13}C{^{1}H} NMR (150 MHz, CD_3CN)

δ = 30.79 ($\underline{C}H_3$), 35.62 ($\underline{C}(CH_3)$), 111.58 (C5), 115.38 (C3), 116.36 (q, $^3J_{CF}$ = 6 Hz, C11), 124.98 (q, $^2J_{CF}$ = 28.5 Hz, C10), 125.09 (C7), 125.74 (C12), 125.89 (q, $^1J_{CF}$ = 225 Hz, $\underline{C}F_3$), 138.16(C6), 140.46(C2), 141.36 (q, $^3J_{CF}$ = 6 Hz, C9), 141.79 (C4), 152.43 (C1), 160.73 (C8),

^{19}F NMR (564 MHz, CD_3CN)

δ = –62.90 (s, 12F)

ESI-HRMS (Negative)

Calc. $[C_{66}H_{58}N_4F_{12}Ir]^-$ for 1325.39424 found for 1325.39428 as $[M]^-$

- *Preparation of **24***

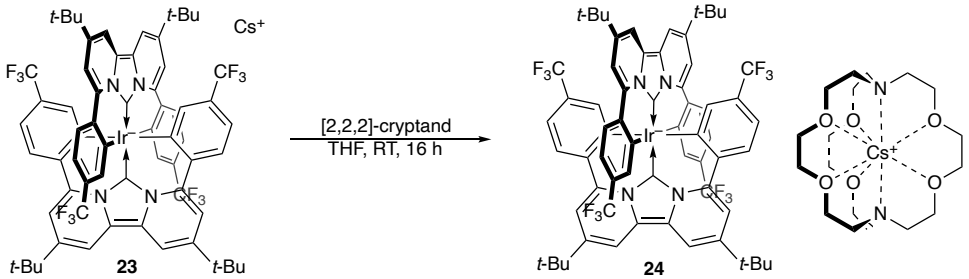

In a glovebox, a solution of iridium complex **23** (31.2 mg, 21.4 μmol) and (2,2,2)-cryptand (8.1 mg, 21.5 μmol) in THF (2 mL) was stirred for 1 h at room temperature. Hexane was added to the THF solution to precipitate **24** as a brownish red solid in 84% yield (33.6 mg,

17.8 µmol). X-ray-quality single crystals of **24** were obtained was obtained from recrystallization in CD_3CN at room temperature.

^{1}H NMR (600 MHz, CD_3CN)

δ: 1.50 (s, 36H, *t*-Bu), 2.48 (t, 9H, N–C$\underline{H_2}$CH$_2$–) 3.45 (*t*, 9H, N–CH$_2$C$\underline{H_2}$–), 3.53 (s, 18H, OC$\underline{H_2}$), 6.14 (d, 4H, $^4J_{HH}$ = 2 Hz, H_e), 6.69 (dd, 4H, $^3J_{HH}$ = 8 Hz, $^4J_{HH}$ = 2 Hz, H_d) 7.76 (d, 4H, $^4J_{HH}$ = 2 Hz, H_b), 7.78 (d, 4H, $^3J_{HH}$ = 8 Hz, H_c), 8.14 (d, 4H, $^4J_{HH}$ = 2 Hz, H_a)

^{13}C{^{1}H} NMR (150 MHz, CD_3CN)

δ = 29.84 ($\underline{C}$H$_3$), 34.67 (C($\underline{C}$H$_3$)), 111.58 (C5), 115.38 (C3), 116.36 (q, $^3J_{CF}$ = 6 Hz, C11), 124.52 (q, $^2J_{CF}$ = 28.5 Hz, C10), 125.09 (C7), 124.11 (C12), 124.76 (q, $^1J_{CF}$ = 225 Hz, CF$_3$), 137.2 (C6), 139.55 (C2), 140.43 (q, $^3J_{CF}$ = 6 Hz, C9), 140.83 (C4), 151.54 (C1), 159.81 (C8).

^{19}F NMR (564 MHz, CD_3CN)

δ = –62.96(s, 12F)

Elemental Analysis

Cal. for C, 54.99%; H, 5.05%; Cs, 7.24%; F, 12.43%; Ir, 10.48%; N, 4.58%; O, 5.23%
found for C, 55.08%; H: 5.06%; N: 4.33%

- *Generation of **25***

In a glovebox, NEt$_3$•HCl (3.5 mg, 24.7 µmol) was added to a solution of **23** (36.5 mg, 23.7 µmol) in MeCN (1 mL) and stirred for 24 h. After remove of the solvent, the resulting residue was extracted by Et$_2$O. The ether extract was then filtered. Further removal of the volatiles afforded **25** with a small amount of **7** Recrystallization of this crude product in CD_3CN (NMR sample) afforded single crystals of **25**, however, we were not able to remove **7** from the mixture.

^{1}H NMR (500 MHz, CD_3CN)

δ = 1.36 (s, 9H, *t*-Bu^3), 1.47 (s, 9H, *t*-Bu^2), 1.55 (s, 18H, *t*-Bu^1), 4.61 (d, 1H, $^4J_{HH}$ = 2 Hz H_E), 6.57 (d, 1H, $^3J_{HH}$ = 8 Hz, H_D), 6.61 (2H, $^3J_{HH}$ = 8 Hz, H_g), 6.71 (d, 2H, $^3J_{HH}$ = 8 Hz, H_d), 6.75 (d, 2H, $^4J_{HH}$ = 2 Hz, H_b), 6.92 (d, 2H, $^4J_{HH}$ = 2 Hz, H_e), 7.16 (d, 2H, $^3J_{HH}$ = 8 Hz, H_d), 7.59 (d, 2H, $^3J_{HH}$ = 8 Hz, H_C), 7.64 (d, 2H $^4J_{HH}$ = 2 Hz, H_B), 8.16 (d, 2H $^4J_{HH}$ = 2 Hz, overlapped with H_A and H_a), 8.17 (d, 2H $^4J_{HH}$ = 2 Hz, H_b), 8.37 (d, 2H, $^3J_{HH}$ = 2 Hz, H_c), 8.42 (d, 2H, $^4J_{HH}$ = 2 Hz, H_a)

$^{13}C\{^{1}H\}$ NMR (125 MHz, C_6D_6)

δ = 29.73, 29.84, 30.39, 34.22, 34.61, 34.77, 110.53, 110.97, 111.98, 114.81, 116.91, 117.52, 117.58, 118.88, 123.24, 123.55, 124.36, 124.64, 125.18, 125.37, 126.23, 126.51, 126.51, 127.06, 129.02, 130.09, 133.76, 135.68, 135.91, 137.11, 138.87, 138.91, 142.04, 142.09, 143.38, 144.10, 144.62, 153.45, 156.38. Some signals were overlapped with the residual C_6D_6 peak. Signals corresponding to *C*F_3 and *C*-CF_3 could not be observed due to coupling to fluorine.

^{19}F NMR (480 MHz, C_6D_6)

δ = –62.13 (s, 6F, CF_3), –63.36 (s, 3F, CF_3), –63.48 (s, 3F, CF_3)

ESI-HRMS (positive)

[$C_{66}H_{57}N_4F_{12}Ir$] Cal. for 1327.40992, found for 1327.40930 as $[M+H]^+$

- *Synthesis of 1,3-bis(N-methyl-imidazolium)-4,6-dimethylbenzene diiodide*

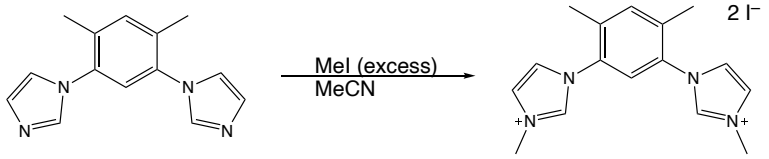

Methyl iodide (1.0 mL, 16.1 mmol) was added to a solution of 1,3-bis(imidazolyl)-4,6-dimethylbenzene (495 mg, 2.07 mmol) in MeCN (10 mL) and the reaction solution was stirred for 24 h at room temperature. Removal of volatiles followed by recrystallization from a MeCN/Et_2O two-layer system provided 1,3-bis(N-methyl-imidazolium)-4,6-dimethylbenzene diiodide (807 mg, 1.55 mmol) as a yellow solid in 75% yield.

^{1}H NMR (600 MHz, DMSO-*d*$_6$)

δ = 2.32 (s, 6H, Ar-C*H*$_3$), 3.97 (s, 6H, N- C*H*$_3$), 7.70 (s, 1H, Aryl), 7.83 (s, 1H Aryl), 8.00 (s, 2H, imidazolium), 8.05 (s, 2H, imidazolium), 9.49 (s, 2H, NC*H*N).

$^{13}C\{^{1}H\}$ NMR (150 MHz, DMSO-*d*$_6$)

δ = 16.96 (Ar-*C*H$_3$), 36.31 (N-*C*H$_3$), 123.52 (imidazolium), 124.19 (imidazolium), 124.67 (CH of aryl), 132.41 (C of Aryl), 134.41 (CH of aryl), 135.97 (C of aryl), 137.73 (N*C*HN).

ESI-HRMS (positive)

$[C_{16}H_{20}N_4]^{2+}$ Cal. 134.08434 found 134.08369 as $[M]^{2+}$

- Synthesis of reference complex **R**

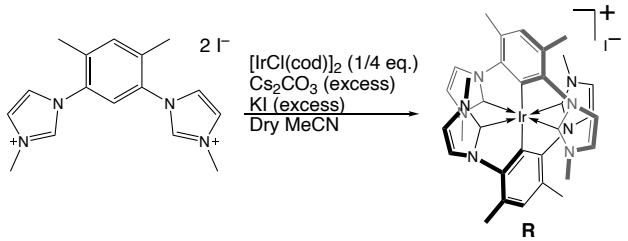

R

A suspension of 1,3-bis(N-methyl-imidazolium)-4,6-dimethylbenzene diiodide (110 mg, 213 µmol), dry Cs_2CO_3 (496 mg, 1.52 mmol), KI (108 mg, 650 µmol), and $[IrCl(cod)]_2$ (33.3 mg, 50.0 µmol) in MeCN (3 mL) was refluxed for 60 h. After cooling to room temperature, the inorganic salts were filtered off and the filtrate was evaporated in vacuo to afford an orange-yellow solid. Recrystallization from a MeCN/Et_2O two-layer system provided complex **R** as an off-white solid (42.0 mg, 49.4 µmol) in 48% yield.

^{1}H NMR (600 MHz, CD_3CN)

δ = 2.54 (s, 12H, Ar-C*H*$_3$), 2.71(s, 12H, N-C*H*$_3$), 6.80 (d, 4H, $^4J_{HH}$ = 2 Hz, NHC ring), 6.89 (s, 2H, trans to Ir) 7.90 (d, 4H, $^4J_{HH}$ = 2 Hz, NHC ring)

$^{13}C\{^1H\}$ NMR (150 MHz, CD_3CN)

δ = 19.53 (Ar-*C*H$_3$), 36.59 (N-*C*H$_3$), 119.51 (C of Aryl), 119.80 (C of NHC), 121.66 (C of NHC), 129.44 (Aryl), 143.75 (Ir–C_{Aryl}), 146.96 (C of Aryl), 162.05 (Ir–C_{car})

ESI-MS (positive)

$[C_{32}H_{34}IrN_8]^+$ Cal. 723.25384 and found 723.25336 as $[M]^+$

Chapter 3

- *Synthesis of* ***28***

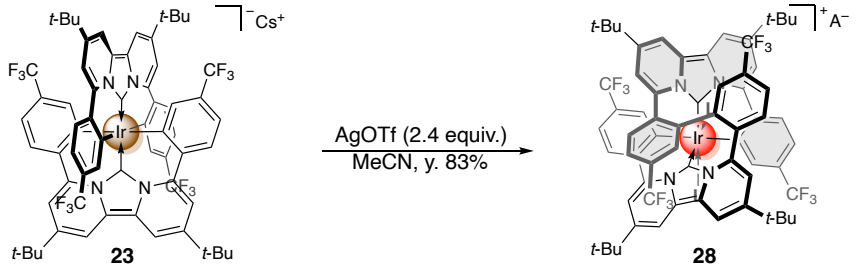

Cold MeCN (5 mL) was added to the pre-cold complex **23** (146 mg, 100 μmol) and AgOTf (58.0 mg, 220 μmol) in a brown vial, and the suspension was stirred for 1 hour at –30 °C. Afterward, the reaction mixture was allowed to warm up to room temperature. This suspension was filtered with a pad of Celite and MeCN was removed *in vacuo.* Extraction with toluene followed by washing with pentane provided complex **28** as a dark rad solid (133 mg, 83 μmol) in 83% yield.

^{1}H NMR (600 MHz, CD_3CN)

δ 1.32 (s, 18H, Hf), 1.50 (s, 18H, Hϕ), 5.73 (d, J = 2 Hz, He), 6.22 (d, J = 8 Hz, 2H, Hc), 6.53 (d, J = 2 Hz, 2H, Hε), 6.59 (d, J = 2 Hz, 2H, Hb), 6.87 (d, J = 8 Hz, 2H, Hd), 7.39 (d, J = 8 Hz, 2H, Hδ), 7.76 (d, J = 2 Hz, 2H, Hβ), 7.97 (d, J = 2 Hz, 2H, Hα), 8.04 (d, J = 2 Hz, 2H, Ha), 8.10 (d, J = 8 Hz, 2H, Hχ) Coordinated MeCN ligands were replaced by CD_3CN, and accordingly, a singlet signal of free CH_3CN was observed.

^{13}C{^{1}H} NMR (151 MHz, CD_3CN)

δ 29.77(overlapping both CH_3 of *t*-Bu group), 34.40(C14), 34.93(C14'), 112.15(C3'), 112.82(C3'), 114.69(Me*C*N), 120.16(q, $^{3}J_{CF}$ = 6 Hz, C9), 121.17(q, $^{3}J_{CF}$ = 6 Hz, C11'), 123.99(q, $^{3}J_{CF}$ = 6 Hz, C9'), 125.07(C5'), 125.54(C2), 124.94(q, $^{1}J_{CF}$ = 250 Hz, *C*F_3), 126.70(C2'), 126.90(C8) 127.62(q, $^{2}J_{CF}$ = 30 Hz C10/C10'), 130.39(C8'), 135.75(C7'), 135.94(q, $^{3}J_{CF}$ = 6 Hz, C11), 140.17(C7), 141.31(C6), 144.03(C4'), 145.20(C4), 153.75(C12), 161.37(C1).

^{19}F NMR (565 MHz, CD_3CN)

δ –79.28 (s, 3F, OTf), –63.78(s, 6F, CF_3 of biaryl linker), –62.49(s, 6F, CF_3 of cyclometallated aryl).

ESI-MS (Positive)

Calc. for 1325.39427, found for 1325.39478 as [M–2×MeCN]

- *Counter-anion Exchange from OTf^- to $BAr^F{}_4^-$*

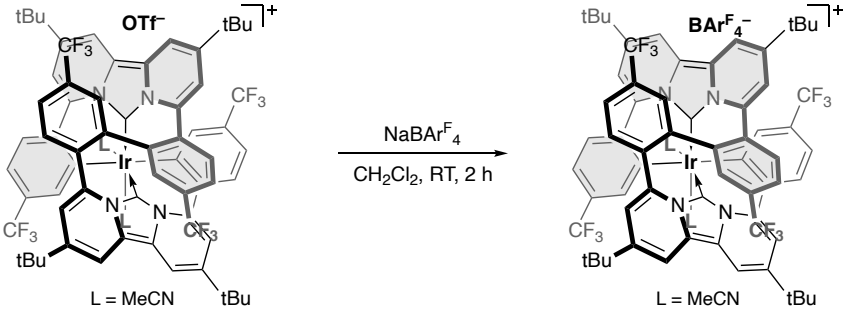

DCM (4 mL) was added to complex **28·OTf** (71.0 mg, 45.6 μmol) and $NaBAr^F{}_4$ (42.0 mg, 47.3 μmol) in a Schlenk flask, and the suspension was stirred for 2 hours at room temperature. The reaction mixture was filtered with a pad of Celite, and DCM was removed *in vacuo* followed by further washing with pentane provided complex **28·$BAr^F{}_4$** as dark red solid (91.8 mg, 40.4 μmol) in 89% yield. Single crystals suitable for X-ray diffraction were obtained from the slow evaporation of a mixture of DCM and hexane at room temperature.

^{1}H NMR (600 MHz, Acetonitrile-d_3)

δ 1.32 (s, 18H, Hf), 1.50 (s, 18H, Hϕ), 5.73 (d, J = 2 Hz, He), 6.22 (d, J = 8 Hz, 2H, Hc), 6.54 (d, J = 2 Hz, 2H, Hε), 6.59 (d, J = 2 Hz, 2H, Hb), 6.87 (d, J = 8 Hz, 2H, Hd), 7.39 (d, J = 8 Hz, 2H, Hδ), 7.64 (s, 8H, $BAr^F{}_4$), 7.68 (s, 12H, $BAr^F{}_4$), 7.76 (d, J = 2 Hz, 2H, Hβ), 7.97 (d, J = 2 Hz, 2H, Hα), 8.04 (d, J = 2 Hz, 2H, Ha), 8.10 (d, J = 8 Hz, 2H, Hχ). Coordinated MeCN ligands were replaced by CD_3CN, and accordingly, a singlet signal of free CH_3CN was observed.

^{13}C{^{1}H} NMR (151 MHz, Acetonitrile-d_3)

δ 29.77(overlapping both CH_3 of *t*-Bu group), 34.39(C14), 34.92(C14'), 112.15(C3'), 112.82(C3'), 114.69(Me*C*N), 117.75(*para*-$BAr^F{}_4$) 120.16(q, $^3J_{CF}$ = 6 Hz, C9), 121.17(q, $^3J_{CF}$ = 6 Hz, C11'), 123.99(q, $^3J_{CF}$ = 6 Hz, C9'), 125.07(C5'), 125.54(C2), 124.60(q, $^1J_{CF}$ = 285 Hz, *C*F_3-$BAr^F{}_4$), 124.94(q, $^1J_{CF}$ = 250 Hz, *C*F_3 on dpa-NHC tetradentate ligand), 126.70(C2'), 126.90(C8) 127.62(q, $^2J_{CF}$ = 30 Hz C10/C10'), 129.00(q, $^2J_{CF}$ = 32 Hz, *meta*-$BAr^F{}_4$), 130.39(C8'), 134.74(*ortho*-$BAr^F{}_4$), 135.75(C7'), 135.94(q, $^3J_{CF}$ = 6 Hz, C11), 140.17(C7), 141.31(C6), 144.03(C4'), 145.20(C4), 153.75(C12), 161.70(q, $^1J_{CB}$ = 50 Hz, *ipso*-$BAr^F{}_4$) The signal of C1 (bound to Ir center) was overlapping with the signal of *ipso*-C of $BAr^F{}_4$.

^{19}F NMR (565 MHz, Acetonitrile-d_3)

δ –63.81(s, 6F, CF_3 of biaryl linker), –63.15(s, 24F, $BAr^F{}_4$), –62.51 (s, 6F, CF_3 of cyclometallated aryl).

^{11}B{^{1}H} NMR (193 MHz, Acetonitrile-d_3)

δ –7.64 (s, 1B, $BAr^F{}_4^-$).

- *Detection of the transient iridium(IV) intermediate **26** by EPR Spectroscopy*

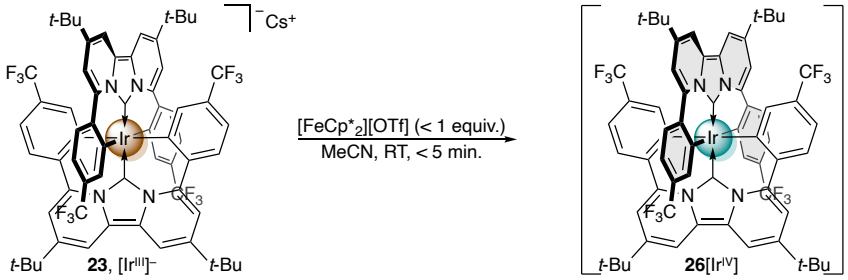

A vial was charged with complex **23** (2.4 mg, 1.64 µmol) and decamethylferrocenium triflate (0.5 mg, 0.8 µmol, ca. 0.5 equiv.). MeCN (0.15 mL) was added via a micropipette to the vial. After the reaction solution was shaken for 5 min, PrCN (0.85 mL) was added via a micropipette. A portion of this solution (0.3 mL) was transferred to an EPR tube. Then, the sample was frozen with liquid nitrogen until measurement.

- *Detection of the transient iridium(V) intermediate **29** by NMR spectroscopy*

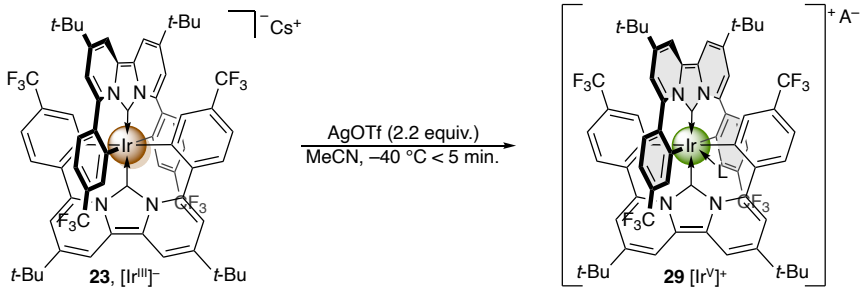

A J. Young tube was charged with complex **1** (13.2 mg, 9.04 µmol) and AgOTf (6.0 mg, 23.4 µmol, 2.6 equiv.). CD_3CN was added by vacuum transfer. This sample was then stored in an acetone bath, kept around –60 °C until the measurement. The pre-cooled sample was injected into the NMR machine, which was cooled at –20 °C beforehand.

- *Synthesis of **31***

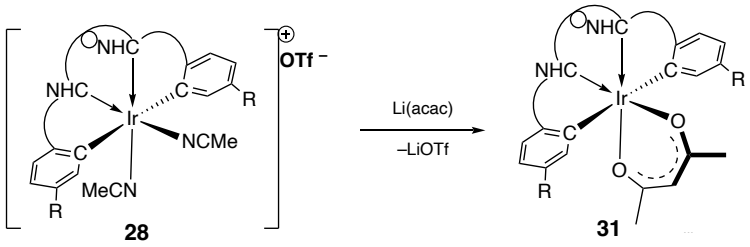

THF was added to complex **28** (47.1 mg, 30.3 μmol) and acac-Li (4.3 mg, 40.5 μmol) in a Schenk tube, and the suspension was stirred for 24 hours at room temperature. THF was evaporated *in vacuo*, then the residue was filtrated with hexane. After evaporation *in vacuo*, a dark pink solid of **31** (34.7 mg, 24.3 μmol) was obtained in 80% yield. Single crystals suitable for X-ray diffraction were obtained from the slow evaporation of MeCN at room temperature.

^{1}H NMR (500 MHz, Methylene Chloride-d_2)

δ 1.08 (s, 6H, CH_3 of acac), 1.31 (s, 18H, Hf), 1.46 (s, 18H, Hϕ), 4.48 (s, 1H, C*H* of acac), 5.84 (d, J = 2 Hz, He), 6.17 (d, J = 8 Hz, 2H, Hc), 6.32 (d, J = 2.0 Hz, 2H, Hε), 6.40 (d, J = 2 Hz, Hb), 6.81 (d, J = 8.0 Hz, 2H, Hd), 7.19 (d, J = 8 Hz, 2H, Hδ), 7.32 (d, J = 2 Hz, 2H, Hβ), 7.54 (d, J = 2 Hz, 2H, Hα), 7.67 (d, J = 2 Hz, 2H, Ha), 7.84 (d, J = 8 Hz, 2H, Hχ).

^{13}C{^{1}H} NMR (126 MHz, Methylene Chloride-d_2)

δ = 26.39(CH_3 of acac), 30.10, 30.18(both CH_3 of *t*-Bu group), 34.20, 34.73, 99.23 (*C*H of acac), 110.10(C3'), 111.95(C3), 112.94(C5), 118.66(C9), 121.26(C11'), 123.20(C9'), 123.52(C5'), 124.86(C8), 125.50(C2), 125.63(C2'), 127.59(C10/C10'), 129.70(C8'), 135.87(C12'), 136.05(overlapping both C6' and C7'), 137.62(C11), 139.42(C7), 141.83(C6), 142.82(C4'), 144.12(C4), 167.20(C12), 171.53(C1), 183.60 (*C*O of acac) The signal of CF_3 moieties were not observed.

^{19}F NMR (471 MHz, Methylene Chloride-d_2)

δ = –63.53(s, 6F, CF_3 of biaryl linker), –62.21(s, 6F, CF_3 of cyclometallated aryl).

APCI-MS (Positive)

Calc. for 1424.438879 as [$C_{71}H_{63}N_4O_2F_{12}Ir$], found for 1424.44153 as [M]

- *Synthesis of **32***

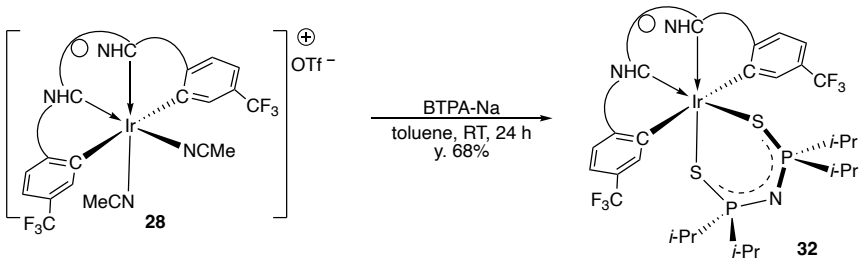

Toluene (3 mL) was added to complex **28** (47.0 mg, 30.2 μmol) and TBPA-Na (13.4 mg, 40.0 μmol) in a Schenk tube, and the suspension was stirred for 24 hours at room temperature. Toluene was evaporated *in vacuo*, then the residue was filtrated with hexane. After evaporation *in vacuo*, a dark pink solid of **32** (34.4 mg, 20.5 μmol) was obtained in 68% yield. Single crystals suitable for X-ray diffraction were obtained from the slow evaporation of MeCN at room temperature.

^{1}H NMR (500 MHz, Methylene Chloride-d_2)

δ 0.55 (m, 6H, C*H* of *i*-Pr), 1.30 (s, 18H, Hf), 1.32 (m, 12H, CH_3 of *i*-Pr) 1.50 (s, 18H, Hϕ), 1.52 (m, 12H, CH_3 of *i*-Pr), 5.55 (s, 2H, He), 6.30 (s, 2H, Hc), 6.40 (d, J = 8 Hz, 2H, Hc), 6.77 (d, J = 8 Hz, 2H, Hd), 7.18 (d, J = 8 Hz, 2H, Hδ), 7.42 (s, 2H, Hε), 7.53 (s, 2H, Hβ), 7.56 (s, 2H, Hα), 7.62 (s, 2H, Ha), 7.91 (d, J = 8 Hz, 2H, Hχ).

^{19}F NMR (471 MHz, Methylene Chloride-d_2)

δ –63.30 (s, 6F, CF_3 of biaryl linker), –61.51 (s, 6F, CF_3 of cyclometallated aryl).

^{31}P{^{1}H} NMR (243 MHz, Methylene Chloride-d_2)

δ 55.07 (s, 2P, BTPA).

- *Generations of **35***

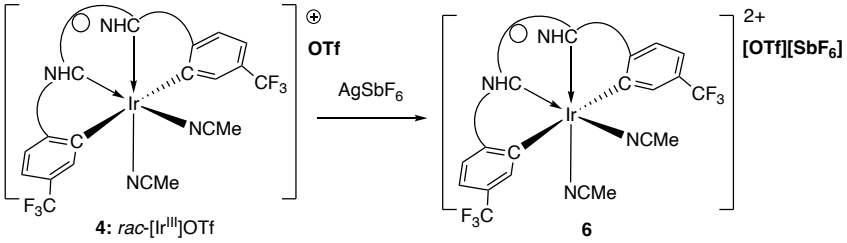

4: *rac*-[Ir^{III}]OTf **6**

Complex **28** (20.3 mg, 13.1 μmol) and $AgSbF_6$ (3.6 mg, 9.79 μmol) were charged in a Schleck tube, and fluorobenzene (1.5 mL) was added at room temperature. The reaction mixture immediately changed from dark red to dark brown. The suspension was filtrated with a pad of Celite. After removal of fluorobenzene, the crude product of **35** was used for its spectroscopic detection.

ESI-HRMS (positive)

Calc. for 703.72344, found for 703.72430 as $[M]^{2+}$

- *Generations of **36***

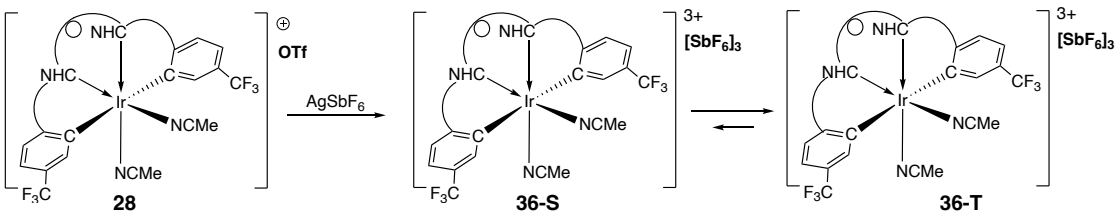

28 **36-S** **36-T**

Complex **28** (100 mg, 64.3 μmol) and $AgSbF_6$ (113 mg, 330 μmol) were charged in a Schleck tube, and fluorobenzene (7.5 mL) was added at room temperature. The suspension was stirred for 1 hour, and the solvent was removed via a pipette. The black sticky crude was extracted with DCM and filtrated with a pad of Celite. After concentrating DCM, a fluorobenzene solution of $TBASbF_6$ (75.1 mg, 157 μmol) was layered and stand it for 1 day, affording the black solid (96.4 mg, 45.6 μmol) in 71% yield based on the clean conversion to complex **36**. The solid-state structure of **36** was obtained in the same manner.

ESI-HRMS (positive)

Cal. for 469.14878, found for 469.14854 as $[M]^{3+}$

5.3. Computational methodology

- Chapter 2

Gas-phase theoretical calculations were performed using the Gaussian16 program[188]. Reaction mechanisms described herein were developed by exploring the potential energy surface through a combined semi-empirical-DFT approach (two-layered ONIOM scheme)[189–191]. Most of the dpa-NHC ligands and metal complex as well as other secondary fragments were considered as the high layer and treated with the hybrid, range-separated density-functional ω-B97XD[192], which considers dispersion interaction through a range separation (22% for short range and 100% Hartree-Fock for long range). The electronic configurations of this inner layer were described with a Pople's split-valence basis set of double-ζ quality with one polarization function (for atoms heavier than hydrogens), 6-31G(d) but for iridium the Couty-Hall modified LANL2DZ basis set was used[193–195] from the *basis set exchange* website[196]. For the outer part, we defined the *tert*-butyl ligands as the steric hindrance contributors described at the semi-empirical PM6 level[197], as it can give good weak interactions such as hydrogen bonds and has been shown to be significantly better for reproducing *ab initio* TS structures and barrier heights[198].

Geometry optimizations were carried out without symmetry constraints, and the stationary points were characterized by analytical frequency calculations, *i.e.* energy minima (reactants, intermediates and products) must exhibit only positive harmonic frequencies whereas each energy maximum (transition state) exhibits one and only one negative frequency. From these last calculations, zero-point energy (ZPE) and thermal and entropy corrections were obtained, which were added to the electronic energy to express the calculated values as Gibbs free energies.

Calculations were also performed to include the solvent effect through the PCM model using the SMD parameters according to Truhlar's model[199–203] with acetonitrile as solvent (ε = 35.688). We also took some experimental solvation free energies for naked Cs cation and anion chloride in acetonitrile from the literature considered for our calculations[204]. As a result, the composite level of theory can be expressed as follows: (SMD:acetonitrile)ONIOM[ω-B97XD/(6-31G(d),mod-LANL2DZ):PM6]. The optimized 3D structure was drawn by use of CYLview20.[205]

- Chapter 3

Density Functional Theory (DFT) calculations were performed using the quantum chemical software Gaussian 09 rev E.01.[206] Geometry optimizations were done employing a combined semi-empirical-DFT approach (two-layered ONIOM scheme[207], 1) the high-layer corresponds to the metal center and the central core of the bis-arylated dipyrido-annulated N-heterocyclic carbenes which was calculated using the range-separate hybrid density-functional ωB97X-D[192] in combination with a mixed Pople basis set: 6-31G(d) for C, N, F and H atoms and the relativistic

pseudopotential LANL2DZ[208] for Ir metal center. 2) The low-layer was set up for the *t*Bu groups which are described at the semi-empirical PM6 level. For the proposed reaction mechanism of **29** to **28**, the implicit inclusion of acetonitrile solvent was done using the SMD variant of the PCM model proposed by Truhlar in single-point calculations over the optimized geometries calculated at the same level of theory mentioned above. Furthermore, single point calculations were performed with a bigger basis set over the optimized structures to correct the electronic energy: a 6-311+G(d,p) for C, N, F and H atoms and LANL2TZ(f) [208] for Ir metal center.

Spin density populations for complexes **26**, **35** and **36** were obtained by integrating the electron spin density in the atomic space defined by Becke[209] (Becke spin population) and were calculated at the ONIOM(ωB97X-D/[6-31G(d),LANL2DZ]:PM6) level using the Multiwfn software version 3.8[210]. This level of theory was also used to calculate NBO charges (NBO software version 7.0.[211]) and to obtain the Charge Decomposition Analysis (CDA) diagrams. Intrinsic Bond Orbitals (IBO) were calculated over the optimized structure at the PBE0/def2-SVP level using the IBOView program.[212]

For the TD-DFT calculations, a single point calculation over the optimized geometries was carried out using the M06[213] functional in conjunction with the def2-SVP basis set[214] and fluorobenzene solvent was included implicitly with the aforementioned PCM(SMD) model[199–203].

The one-electron density matrix (required for the bond order and electron density of delocalized bonds (EDDB) analyses) was calculated at the wB97X/def2-SVPP level of the theory, as implemented in Gaussian G16 C.01, to reliably access the effect of exchange interactions at long distances. The previously obtained geometry was used, i.e. wB97X/def2-SVPP//ONIOM(wB97X-D/[6-31G(d),LANL2DZ]:PM6). The natural population analysis was used to perform the charge and bond order analyses. The RunEDDB program (ver. 2021-12-12)[215] was used to perform the Ir-atomic-block diagonalization and perform the EDDB analysis utilizing the global EDDB function, $EDDB_G(r)$, and the path-resolved EDDB function, $EDDB_P(r)$, to assess cyclic delocalization of electrons in the cycles including Ir atom. The optimized 3D structure was drawn by use of CYLview20.[205]

CHAPTER 6.
REFERENCES

[1] M. N. Hopkinson, C. Richter, M. Schedler, F. Glorius, *Nature* **2014**, *510*, 485–496.
[2] J. F. Hartwig, *Organotransition Metal Chemistry From Bonding to Catalysis*, New York, **2010**.
[3] E. O. Fischer, A. Maasböl, *Angew. Chemie Int. Ed. English* **1964**, *3*, 580–581.
[4] R. R. Schrock, *J. Am. Chem. Soc.* **1974**, *96*, 6796–6797.
[5] J. Santamaría, E. Aguilar, *Org. Chem. Front.* **2016**, *3*, 1561–1588.
[6] A. Igau, H. Grutzmacher, A. Baceiredo, G. Bertrand, *J. Am. Chem. Soc.* **1988**, *110*, 6463–6466.
[7] A. J. Arduengo, R. L. Harlow, M. Kline, *J. Am. Chem. Soc.* **1991**, *113*, 361–363.
[8] A. J. Arduengo, F. Davidson, H. V. R. Dias, J. R. Goerlich, D. Khasnis, W. J. Marshall, T. K. Prakasha, *J. Am. Chem. Soc.* **1997**, *119*, 12742–12749.
[9] R. W. Alder, P. R. Allen, M. Murray, A. G. Orpen, *Angew. Chemie Int. Ed. English* **1996**, *35*, 1121–1123.
[10] V. Lavallo, Y. Canac, C. Präsang, B. Donnadieu, G. Bertrand, *Angew. Chemie - Int. Ed.* **2005**, *44*, 5705–5709.
[11] F. Lavigne, E. Maerten, G. Alcaraz, N. Saffon-Merceron, C. Acosta-Silva, V. Branchadell, A. Baceiredo, *J. Am. Chem. Soc.* **2010**, *132*, 8864–8865.
[12] H. J. Barnett, A. F. Hill, *Angew. Chemie - Int. Ed.* **2020**, *59*, 4274–4277.
[13] C. Hu, X. F. Wang, R. Wei, C. Hu, D. A. Ruiz, X. Y. Chang, L. L. Liu, *Chem* **2022**, *8*, 2278–2289.
[14] F. E. Hahn, L. Wittenbecher, R. Boese, D. Bläser, *Chem. - A Eur. J.* **1999**, *5*, 1931–1935.
[15] T. W. Hudnall, J. P. Moerdyk, C. W. Bielawski, *Chem. Commun.* **2010**, *46*, 4288–4290.
[16] D. Enders, K. Breuer, G. Raabe, J. Runsink, J. H. Teles, J. -P Melder, K. Ebel, S. Brode, *Angew. Chemie Int. Ed. English* **1995**, *34*, 1021–1023.
[17] M. Nonnenmacher, D. Kunz, F. Rominger, T. Oeser, *Chem. Commun.* **2006**, *386*, 1378.
[18] D. Martin, N. Lassauque, B. Donnadieu, G. Bertrand, *Angew. Chemie - Int. Ed.* **2012**, *51*, 6172–6175.
[19] V. Lavallo, J. Mafhouz, Y. Canac, B. Donnadieu, W. W. Schoeller, G. Bertrand, *J. Am. Chem. Soc.* **2004**, *126*, 8670–8671.
[20] E. Aldeco-Perez, A. J. Rosenthal, B. Donnadieu, P. Parameswaran, G. Frenking, G. Bertrand, *Science (80-.).* **2009**, *326*, 556–559.
[21] S. Solé, H. Gornitzka, W. W. Schoeller, D. Bourissou, G. Bertrand, *Science (80-.).* **2001**, *292*, 1901–1903.
[22] R. Nakano, R. Jazzar, G. Bertrand, *Nat. Chem.* **2018**, *10*, 1196–1200.
[23] V. Lavallo, Y. Canac, B. Donnadieu, W. W. Schoeller, G. Bertrand, *Science (80-.).* **2006**, *312*, 722–724.
[24] T. Kato, H. Gornitzka, A. Baceiredo, A. Savin, G. Bertrand, V. Uni, D. Paris, F.- Paris, V. Recei, V. No, *Jounal Am. Chem. Soc.* **2000**, *173*, 998–999.
[25] Y. Ishida, B. Donnadieu, G. Bertrand, *Proc. Natl. Acad. Sci. U. S. A.* **2006**, *103*, 13585–13588.
[26] E. Despagnet-ayoub, R. H. Grubbs, **2004**, *21*, 10198–10199.
[27] D. Martin, A. Baceiredo, H. Gornitzka, W. W. Schoeller, G. Bertrand, *Angew. Chemie - Int. Ed.* **2005**, *44*, 1700–1703.
[28] K. E. Krahulic, G. D. Enright, M. Parvez, R. Roesler, *J. Am. Chem. Soc.* **2005**, *127*, 4142–4143.
[29] A. J. Arduengo, J. R. Goerlich, W. J. Marshall, *Liebigs Ann-Recl.* **1997**, 365–374.
[30] R. W. Alder, C. P. Butts, A. G. Orpen, *J. Am. Chem. Soc.* **1998**, *120*, 11526–11527.
[31] E. P. Beaumier, C. P. Gordon, R. P. Harkins, M. E. Mcgreal, X. Wen, C. Copéret, J. D. Goodpaster, I. A. Tonks, *J. Am. Chem. Soc.* **2020**, *142*, 8006–8018.
[32] J. Böhnke, H. Braunschweig, W. C. Ewing, C. Hörl, T. Kramer, I. Krummenacher, J. Mies, A. Vargas, *Angew. Chemie - Int. Ed.* **2014**, *53*, 9082–9085.
[33] T. Tsushima, H. Tanaka, K. Nakanishi, M. Nakamoto, H. Yoshida, *ACS Catal.* **2021**, *11*, 14381–14387.
[34] H. Clavier, S. P. Nolan, *Chem. Commun.* **2010**, *46*, 841–861.
[35] D. Di, A. S. Romanov, L. Yang, J. M. Richter, J. P. H. Rivett, S. Jones, T. H. Thomas, M. A. Jalebi, R. H. Friend, M. Linnolahti, M. Bochmann, D. Credgington, *Science (80-.).* **2017**, *356*, 159–163.

[36] R. Hamze, S. Shi, S. C. Kapper, D. S. M. Ravinson, L. Estergreen, M. C. Jung, A. C. Tadle, R. Haiges, P. I. Djurovich, J. L. Peltier, R. Jazzar, G. Bertrand, S. E. Bradforth, M. E. Thompson, *J. Am. Chem. Soc.* **2019**, *141*, 8616–8626.
[37] A. S. Romanov, L. Yang, S. T. E. Jones, D. Di, O. J. Morley, B. H. Drummond, A. P. M. Reponen, M. Linnolahti, D. Credgington, M. Bochmann, *Chem. Mater.* **2019**, *31*, 3613–3623.
[38] A. S. Romanov, S. T. E. Jones, Q. Gu, P. J. Conaghan, B. H. Drummond, J. Feng, F. Chotard, L. Buizza, M. Foley, M. Linnolahti, D. Credgington, M. Bochmann, *Chem. Sci.* **2020**, *11*, 435–446.
[39] P. J. Conaghan, C. S. B. Matthews, F. Chotard, S. T. E. Jones, N. C. Greenham, M. Bochmann, D. Credgington, A. S. Romanov, *Nat. Commun.* **2020**, *11*, 1–8.
[40] V. Nesterov, D. Reiter, P. Bag, P. Frisch, R. Holzner, A. Porzelt, S. Inoue, *Chem. Rev.* **2018**, *118*, 9678–9842.
[41] R. Yadav, S. Sinhababu, R. Yadav, S. Kundu, *Dalt. Trans.* **2022**, *51*, 2170–2202.
[42] G. Frenking, *Angew. Chemie - Int. Ed.* **2014**, *53*, 6040–6046.
[43] Y. Wang, G. H. Robinson, *J. Am. Chem. Soc.* **2023**, *145*, 5592–5612.
[44] J. Cheng, L. Wang, P. Wang, L. Deng, *Chem. Rev.* **2018**, *118*, 9930–9987.
[45] C. F. Harris, M. B. Bayless, N. P. Van Leest, Q. J. Bruch, B. N. Livesay, J. Bacsa, K. I. Hardcastle, M. P. Shores, B. De Bruin, J. D. Soper, *Inorg. Chem.* **2017**, *56*, 12421–12435.
[46] G. E. Martinez, C. Ocampo, Y. J. Park, A. R. Fout, *J. Am. Chem. Soc.* **2016**, *138*, 4290–4293.
[47] J. L. Martinez, S. A. Lutz, H. Yang, J. Xie, J. Telser, B. M. Hoffman, V. Carta, M. Pink, Y. Losovyj, J. M. Smith, *Science (80-.).* **2020**, *370*, 356–359.
[48] M. Ding, G. E. Cutsail III, D. Aravena, M. Amoza, M. Rouzi`eres, P. Dechambenoit, Y. Losovyj, M. Pink, E. Ruiz, R. Cl´erac, J. M. Smith, *Chem. Sci.* **2016**, *7*, 6132–6140.
[49] J. J. Scepaniak, J. A. Young, R. P. Bontchev, J. M. Smith, *Angew. Chemie - Int. Ed.* **2009**, *48*, 3158–3160.
[50] A. S. Mccall, H. Wang, J. M. Desper, S. Kraft, *J. Am. Chem. Soc.* **2011**, *133*, 1832–1848.
[51] M. Baltrun, F. A. Watt, R. Schoch, S. Hohloch, *Organometallics* **2019**, *38*, 3719–3729.
[52] M. C. Lehman, D. R. Pahls, J. M. Meredith, R. D. Sommer, D. M. Heinekey, T. R. Cundari, E. A. Ison, *J. Am. Chem. Soc.* **2015**, *137*, 3574–3584.
[53] M. Bouché, G. Dahm, M. Wantz, S. Fournel, T. Achard, *Dalt. Trans.* **2016**, *45*, 11362–11368.
[54] Á. Vivancos, D. Bautista, P. González-Herrero, *Chem. – A Eur. J.* **2019**, *25*, 6014–6025.
[55] B. L. Lin, P. Kang, T. D. P. Stack, *Organometallics* **2010**, *29*, 3683–3685.
[56] E. M. Zolnhofer, M. Käß, M. M. Khusniyarov, F. W. Heinemann, L. Maron, M. Van Gastel, E. Bill, K. Meyer, *J. Am. Chem. Soc.* **2014**, *136*, 15072–15078.
[57] M. Keilwerth, J. Hohenberger, F. W. Heinemann, J. Sutter, A. Scheurer, H. Fang, E. Bill, F. Neese, S. Ye, K. Meyer, *J. Am. Chem. Soc.* **2019**, *141*, 17217–17235.
[58] G. Bertrand, G. Junor, J. Lorkowski, C. Weinstein, R. Jazzar, C. Pietraszuk, *Angew. Chemie Int. Ed.* **2020**, *5*, 1–7.
[59] P. De Fre, N. M. Scott, E. D. Stevens, S. P. Nolan, **2005**, 2411–2418.
[60] R. Shang, S. Saito, J. O. C. Jimenez-Halla, Y. Yamamoto, *Dalt. Trans.* **2018**, *47*, 5181–5188.
[61] Y. Kimura, L. I. Lugo-Fuentes, S. Saito, J. O. C. Jimenez-Halla, J. Barroso-Flores, Y. Yamamoto, M. Nakamoto, R. Shang, *Dalt. Trans.* **2022**, *51*, 7899–7906.
[62] A. K. Guha, A. K. Phukan, *Chem. - A Eur. J.* **2012**, *18*, 4419–4425.
[63] M. Gruber, W. Bauer, H. Maid, K. Schöll, R. R. Tykwinski, *Inorganica Chim. Acta* **2017**, *468*, 152–158.
[64] C. A. Dyker, V. Lavallo, B. Donnadieu, G. Bertrand, *Angew. Chemie - Int. Ed.* **2008**, *47*, 3206–3209.
[65] R. Weiss, S. Reichel, M. Handke, F. Hampel, *Angew. Chemie Int. Ed.* **1998**, *37*, 344–347.
[66] R. Weiss, S. Reichel, *Eur. J. Inorg. Chem.* **2000**, 1935–1939.
[67] M. Nonnenmacher, D. Kunz, F. Rominger, T. Oeser, *J. Organomet. Chem.* **2005**, *690*, 5647–5653.
[68] M. Nonnenmacher, D. Kunz, F. Rominger, *Organometallics* **2008**, *27*, 1561–1568.
[69] M. Nonnenmacher, D. M. Buck, D. Kunz, *Beilstein J. Org. Chem.* **2016**, *12*, 1884–1896.
[70] V. Gierz, A. Seyboldt, C. Maichle-Mössmer, R. Fröhlich, F. Rominger, D. Kunz, *Eur. J. Inorg. Chem.* **2012**, 1423–1429.
[71] G. De Ruiter, S. Garhwal, A. Kaushansky, N. Fridman, L. J. W. Shimon, *J. Am. Chem. Soc.* **2020**, *142*, 17131–17139.
[72] S. Garhwal, A. Kaushansky, N. Fridman, G. de Ruiter, *Chem Catal.* **2021**, *1*, 631–647.
[73] S. Garhwal, J. Panda, N. Fridman, A. Karton, G. de Ruiter, *Chem. Commun.* **2023**, *59*, 426–429.
[74] S. Garhwal, N. Fridman, G. De Ruiter, *Inorg. Chem.* **2020**, *59*, 13817–13821.
[75] S. I. Fuku-En, J. Yamamoto, S. Kojima, Y. Yamamoto, *Chem. Lett.* **2014**, *43*, 468–470.

[76] S. I. Fuku-En, J. Yamamoto, M. Minoura, S. Kojima, Y. Yamamoto, *Inorg. Chem.* **2013**, *52*, 11700–11702.
[77] N. Maeta, J. Yamamoto, S. Fuku-en, R. Shang, Y. Yamamoto, *Zeitschrift für Anorg. und Allg. Chemie* **2015**, *641*, 2199–2203.
[78] S. Zhang, R. Shang, M. Nakamoto, Y. Yamamoto, Y. Adachi, J. Ohshita, *Inorg. Chem.* **2019**, *58*, 6328–6335.
[79] S. Zhang, R. Shang, M. Nakamoto, Y. Yamamoto, Y. Adachi, J. Ohshita, *Dalt. Trans.* **2019**, *48*, 12250–12256.
[80] D. Kunz, C. Deißler, V. Gierz, F. Rominger, T. Oeser, *Zeitschrift fur Naturforsch. - Sect. B J. Chem. Sci.* **2010**, *65*, 861–872.
[81] G. van Koten, *Pure Appl. Chem* **1989**, *61*, 1681–1694.
[82] C. J. Moulton, B. L. Shaw, *J. Chem. Soc. Dalt. Trans* **1976**, 1020–1024.
[83] G. Van Koten, K. Timmer, J. G. Nolte, A. L. Spek, *J. Chem. Soc., Chem. Commun.* **1978**, 250–252.
[84] A. F. Hill, G. R. Owen, A. J. P. White, D. J. Williams, *Angew. Chemie Int. Ed.* **1999**, *38*, 2759–2761.
[85] S. Bontemps, H. Gornitzka, G. Bouhadir, K. Miqueu, D. Bourissou, *Angew. Chemie - Int. Ed.* **2006**, *45*, 1611–1614.
[86] D. You, F. P. Gabbaï, *Trends Chem.* **2019**, *1*, 485–496.
[87] L. Rubio-Pérez, M. Iglesias, J. Munárriz, V. Polo, V. Passarelli, J. J. Pérez-Torrente, L. A. Oro, *Chem. Sci.* **2017**, *8*, 4811–4822.
[88] M. Iglesias, L. A. Oro, *Chem. Soc. Rev.* **2018**, *47*, 2772–2808.
[89] A. R. Chianese, M. J. Drance, K. H. Jensen, S. P. McCollom, N. Yusufova, S. E. Shaner, D. Y. Shopov, J. A. Tendler, *Organometallics* **2014**, *33*, 457–464.
[90] C. Cebrián, M. Mauro, *Beilstein J. Org. Chem.* **2018**, *14*, 1459–1481.
[91] T. Y. Li, X. Liang, L. Zhou, C. Wu, S. Zhang, X. Liu, G. Z. Lu, L. S. Xue, Y. X. Zheng, J. L. Zuo, *Inorg. Chem.* **2015**, *54*, 161–173.
[92] M. Albrecht, G. Van Koten, *Angew. Chemie - Int. Ed.* **2001**, *40*, 3750–3781.
[93] A. J. Arduengo, R. L. Harlow, M. Kline, *J. Am. Chem. Soc.* **1991**, *113*, 361–363.
[94] W. Wang, L. Cui, P. Sun, L. Shi, C. Yue, F. Li, *Chem. Rev.* **2018**, *118*, 9843–9929.
[95] R. Visbal, M. C. Gimeno, *Chem. Soc. Rev.* **2014**, *43*, 3551–3574.
[96] M. L. H. Green, *J. Organomet. Chem.* **1995**, *500*, 127–148.
[97] R. Taakili, Y. Canac, *Molecules* **2020**, *25*, 2231.
[98] E. Borré, G. Dahm, A. Aliprandi, M. Mauro, S. Dagorne, S. Bellemin-Laponnaz, *Organometallics* **2014**, *33*, 4374–4384.
[99] J. Navarro, O. Torres, M. Martín, E. Sola, *J. Am. Chem. Soc.* **2011**, *133*, 9738–9740.
[100] C. Y. Tang, N. Phillips, M. J. Kelly, S. Aldridge, *Chem. Commun.* **2012**, *48*, 11999.
[101] H. J. Liu, M. S. Ziegler, T. D. Tilley, *Dalt. Trans.* **2018**, *47*, 12138–12146.
[102] R. Taakili, C. Barthes, A. Goëffon, C. Lepetit, C. Duhayon, D. A. Valyaev, Y. Canac, *Inorg. Chem.* **2020**, *59*, 7082–7096.
[103] M. Raynal, R. Pattacini, C. S. J. Cazin, C. Vallée, H. Olivier-Bourbigou, P. Braunstein, *Organometallics* **2009**, *28*, 4028–4047.
[104] L. González-Sebastián, A. B. Chaplin, *Inorganica Chim. Acta* **2017**, *460*, 22–28.
[105] K. Kubo, N. D. Jones, M. J. Ferguson, R. McDonald, R. G. Cavell, *J. Am. Chem. Soc.* **2005**, *127*, 5314–5315.
[106] B. Eguillor, M. A. Esteruelas, V. Lezáun, M. Oliván, E. Oñate, J.-Y. Tsai, C. Xia, *Chem. - A Eur. J.* **2016**, *22*, 9106–9110.
[107] Z.-B. Yan, K.-L. Dai, B.-M. Yang, Z.-H. Li, Y.-Q. Tu, F.-M. Zhang, X.-M. Zhang, M. Peng, Q.-L. Chen, Z.-R. Jing, *Sci. China Chem.* **2020**, *63*, 1761–1766.
[108] N. Stylianides, A. A. Danopoulos, D. Pugh, F. Hancock, A. Zanotti-Gerosa, *Organometallics* **2007**, *26*, 5627–5635.
[109] N. Phillips, C. Y. Tang, R. Tirfoin, M. J. Kelly, A. L. Thompson, J. Gutmann, S. Aldridge, *Dalt. Trans.* **2014**, *43*, 12288–12298.
[110] M. Viciano, M. Poyatos, M. Sanaú, E. Peris, A. Rossin, G. Ujaque, A. Lledós, *Organometallics* **2006**, *25*, 1120–1134.
[111] M. Xue, D.-L. Zhuang, H. Li, P. He, C. Liu, J. Zhu, X.-Y. Yi, *Inorg. Chem.* **2020**, *59*, 960–963.
[112] M. Raynal, C. S. J. Cazin, C. Vallée, H. Olivier-Bourbigou, P. Braunstein, *Organometallics* **2009**, *28*, 2460–2470.
[113] J. Campos, M. F. Espada, J. López-Serrano, E. Carmona, *Inorg. Chem.* **2013**, *52*, 6694–6704.
[114] J. A. Cabeza, P. García-Álvarez, L. González-Álvarez, *Chem. Commun.* **2017**, *53*, 10275–10278.

[115] A. J. Wilkinson, H. Puschmann, J. A. K. Howard, C. E. Foster, J. A. G. Williams, *Inorg. Chem.* **2006**, *45*, 8685–8699.
[116] R. A. Kelly III, H. Clavier, S. Giudice, N. M. Scott, E. D. Stevens, J. Bordner, I. Samardjiev, C. D. Hoff, L. Cavallo, S. P. Nolan, *Organometallics* **2008**, *27*, 202–210.
[117] S. Fuku-en, J. Yamamoto, S. Kojima, Y. Yamamoto, *Chem. Lett.* **2013**, *43*, 468–470.
[118] W. Zuo, P. Braunstein, *Organometallics* **2012**, *31*, 2606–2615.
[119] N. Darmawan, C.-H. Yang, M. Mauro, M. Raynal, S. Heun, J. Pan, H. Buchholz, P. Braunstein, L. De Cola, *Inorg. Chem.* **2013**, *52*, 10756–10765.
[120] M. Jagenbrein, A. A. Danopoulos, P. Braunstein, *J. Organomet. Chem.* **2015**, *775*, 169–172.
[121] D. García-Cuadrado, A. A. C. Braga, F. Maseras, A. M. Echavarren, *J. Am. Chem. Soc.* **2006**, *128*, 1066–1067.
[122] D. Lapointe, K. Fagnou, *Chem. Lett.* **2010**, *39*, 1118–1126.
[123] J. E. Wheatley, C. A. Ohlin, A. B. Chaplin, *Chem. Commun.* **2014**, *50*, 685–687.
[124] J.-U. Rohde, W.-T. Lee, *J. Am. Chem. Soc.* **2009**, *131*, 9162–9163.
[125] D. Y. Shopov, B. Rudshteyn, J. Campos, D. J. Vinyard, V. S. Batista, G. W. Brudvig, R. H. Crabtree, *Chem. Sci.* **2017**, *8*, 1642–1652.
[126] D. Y. Shopov, L. S. Sharninghausen, S. B. Sinha, B. Q. Mercado, D. Balcells, G. W. Brudvig, R. H. Crabtree, *Inorg. Chem.* **2018**, *57*, 5684–5691.
[127] J.-H. Shon, S. Sittel, T. S. Teets, *ACS Catal.* **2019**, *9*, 8646–8658.
[128] G. Wang, M. Zhou, J. T. Goettel, G. J. Schrobilgen, J. Su, J. Li, T. Schlöder, S. Riedel, *Nature* **2014**, *514*, 475–477.
[129] P. Pyykkö, W. H. Xu, *Angew. Chemie - Int. Ed.* **2015**, *54*, 1080–1081.
[130] L. A. Oro, C. Claver, Eds. , *Iridium Complexes in Organic Synthesis*, Wiley-VCH, **2008**.
[131] J. M. Thomsen, D. L. Huang, R. H. Crabtree, G. W. Brudvig, *Dalt. Trans.* **2015**, *44*, 12452–12472.
[132] M. H. Shaw, J. Twilton, D. W. C. MacMillan, *J. Org. Chem.* **2016**, *81*, 6898–6926.
[133] T. M. Boller, J. M. Murphy, M. Hapke, T. Ishiyama, N. Miyaura, J. F. Hartwig, *J. Am. Chem. Soc.* **2005**, *127*, 14263–14278.
[134] H. Tamura, H. Yamazaki, H. Sato, S. Sakaki, *J. Am. Chem. Soc.* **2003**, *125*, 16114–16126.
[135] C. Karmel, C. Z. Rubel, E. V. Kharitonova, J. F. Hartwig, *Angew. Chemie - Int. Ed.* **2020**, *59*, 6074–6081.
[136] C. Karmel, Z. Chen, J. F. Hartwig, *J. Am. Chem. Soc.* **2019**, *141*, 7063–7072.
[137] P. Gao, W. Guo, J. Xue, Y. Zhao, Y. Yuan, Y. Xia, Z. Shi, *J. Am. Chem. Soc.* **2015**, *137*, 12231–12240.
[138] M. R. Ringenberg, S. L. Kokatam, Z. M. Heiden, T. B. Rauchfuss, *J. Am. Chem. Soc.* **2008**, *130*, 788–789.
[139] S. Morisako, S. Watanabe, S. Ikemoto, S. Muratsugu, M. Tada, M. Yamashita, *Angew. Chemie Int. Ed.* **2019**, *58*, 15031–15035.
[140] E. Gutiérrez-Puebla, A. Monge, M. Paneque, M. L. Poveda, S. Taboada, M. Trujillo, E. Carmona, *J. Am. Chem. Soc.* **1999**, *121*, 346–354.
[141] C. I. Lee, J. Zhou, O. V. Ozerov, *J. Am. Chem. Soc.* **2013**, *135*, 3560–3566.
[142] J. L. McBee, J. Escalada, T. D. Tilley, *J. Am. Chem. Soc.* **2009**, *131*, 12703–12713.
[143] T. Komuro, K. Furuyama, T. Kitano, H. Tobita, *J. Organomet. Chem.* **2014**, *751*, 686–694.
[144] J. A. Cabeza, P. García-Álvarez, L. González-Álvarez, *Chem. Commun.* **2017**, *53*, 10275–10278.
[145] A. Caise, J. A. B. Abdalla, R. Tirfoin, A. J. Edwards, S. Aldridge, *Chem. - A Eur. J.* **2017**, *23*, 16906–16913.
[146] R. A. Cipriano, W. Levason, D. Pletcher, N. A. Powell, M. Webster, *J. Chem. Soc. Dalt. Trans.* **1987**, 1901–1901.
[147] R. A. Cipriano, L. R. Hanton, W. Levason, D. Pletcher, N. A. Powell, M. Webster, *J. Chem. Soc. Dalt. Trans.* **1988**, 2483–2490.
[148] Z. Lu, C.-H. Jun, S. R. de Gala, M. P. Sigalas, O. Eisenstein, R. H. Crabtree, *Organometallics* **1995**, *14*, 1168–1175.
[149] K. Shin, Y. Park, M.-H. Baik, S. Chang, *Nat. Chem.* **2018**, *10*, 218–224.
[150] R. Fu, J. E. Bercaw, J. A. Labinger, **2011**.
[151] S. Frieß, A. Benyak, A. Herrera, A. M. Escalona, F. W. Heinemann, J. Langer, D. Fehn, D. Pividori, A. Grasruck, D. Munz, K. Meyer, R. Dorta, *Inorg. Chem.* **2022**, *61*, 1236–1248.
[152] D. Y. Shopov, B. Rudshteyn, J. Campos, V. S. Batista, R. H. Crabtree, G. W. Brudvig, *J. Am. Chem. Soc.* **2015**, *137*, 7243–7250.
[153] S. B. Sinha, D. Y. Shopov, L. S. Sharninghausen, C. J. Stein, B. Q. Mercado, D. Balcells, T. B. Pedersen, M. Reiher, G. W. Brudvig, R. H. Crabtree, *Jounal Am. Chem. Soc.* **2017**, *139*, 9672–9683.

[154] L. S. Sharninghausen, S. B. Sinha, D. Y. Shopov, B. Q. Mercado, D. Balcells, G. W. Brudvig, R. H. Crabtree, *Angew. Chemie Int. Ed.* **2017**, *56*, 13047–13051.
[155] D. Y. Shopov, L. S. Sharninghausen, S. B. Sinha, J. E. Borowski, B. Q. Mercado, G. W. Brudvig, R. H. Crabtree, *New J. Chem.* **2017**, *41*, 6709–6719.
[156] M. G. Scheibel, B. Askevold, F. W. Heinemann, E. J. Reijerse, B. de Bruin, S. Schneider, *Nat. Chem.* **2012**, *4*, 552–558.
[157] J. Abbenseth, M. Finger, C. Würtele, M. Kasanmascheff, S. Schneider, *Inorg. Chem. Front.* **2016**, *3*, 469–477.
[158] M. Kinauer, M. Diefenbach, H. Bamberger, S. Demeshko, E. J. Reijerse, C. Volkmann, C. Würtele, J. van Slageren, B. de Bruin, M. C. Holthausen, S. Schneider, *Chem. Sci.* **2018**, *9*, 4325–4332.
[159] D. Delony, M. Kinauer, M. Diefenbach, S. Demeshko, C. Würtele, M. C. Holthausen, S. Schneider, *Angew. Chemie - Int. Ed.* **2019**, *58*, 10971–10974.
[160] C. L. Lee, L. Wu, J.-S. Huang, C.-M. Che, *Chem. Commun.* **2019**, *55*, 3606–3609.
[161] H. F. Ip, Y. M. So, H. K. Lee, I. D. Williams, W. H. Leung, *Eur. J. Inorg. Chem.* **2012**, 3289–3295.
[162] T. Harimoto, Y. Ishigaki, *Chempluschem* **2022**, *87*, 1–14.
[163] B. J. Frogley, L. J. Wright, *Chem. - A Eur. J.* **2018**, *24*, 2025–2038.
[164] J. R. Bleeke, Y. Xie, L. Bass, M. Y. Chiang, *J. Am. Chem. Soc.* **1991**, 4703–4704.
[165] J. Chen, R. J. Angelici, *Coord. Chem. Rev.* **2000**, *206–207*, 63–99.
[166] K. Nakanishi, J. O. C. Jimenez-Halla, S. Yamazoe, M. Nakamoto, R. Shang, Y. Yamamoto, *Inorg. Chem.* **2021**, *60*, 9970–9976.
[167] A. Paul, R. Borrelli, H. Bouyanfif, S. Gottis, F. Sauvage, *ACS Omega* **2019**, *4*, 14780–14789.
[168] B. J. Zhao, D. H. Evans, N. A. Macías-Ruvalcaba, H. J. Shine, *J. Org. Chem.* **2006**, *71*, 3737–3742.
[169] T. Sajoto, P. I. Djurovich, A. Tamayo, M. Yousufuddin, R. Bau, M. E. Thompson, R. J. Holmes, S. R. Forrest, *Inorg. Chem.* **2005**, *44*, 7992–8003.
[170] B. Bleaney, K. D. Bowers, *Proc. R. Soc. Lond. A* **1952**, *214*, 451–465.
[171] A. E. Thorarinsdottir, A. I. Gaudette, T. D. Harris, *Chem. Sci.* **2017**, *8*, 2448–2456.
[172] D. W. Szczepanik, M. Andrzejak, K. Dyduch, E. Żak, M. Makowski, G. Mazur, J. Mrozek, *Phys. Chem. Chem. Phys.* **2014**, *16*, 20514–20523.
[173] D. W. Szczepanik, M. Solà, in *Aromaticity* (Ed.: Israel Fernandez), Elsevier, **2021**, pp. 259–284.
[174] D. W. Szczepanik, M. Andrzejak, J. Dominikowska, B. Pawełek, T. M. Krygowski, H. Szatylowicz, M. Solà, *Phys. Chem. Chem. Phys.* **2017**, *19*, 28970–28981.
[175] S. C. Chan, P. Gupta, X. Engelmann, Z. Z. Ang, R. Ganguly, E. Bill, K. Ray, S. Ye, J. England, *Angew. Chemie - Int. Ed.* **2018**, *57*, 15717–15722.
[176] S. C. Chan, Z. Z. Ang, P. Gupta, R. Ganguly, Y. Li, S. Ye, J. England, *Inorg. Chem.* **2020**, *59*, 4118–4128.
[177] P. Ghosh, R. Naastepad, C. F. Riemersma, M. Lutz, M. E. Moret, R. J. M. Klein Gebbink, *Chem. - A Eur. J.* **2017**, *23*, 10732–10737.
[178] C. J. Curtis, A. V. Astashkin, J. Conradie, A. Ghosh, E. Tomat, *Inorg. Chem.* **2021**, *60*, 12457–12466.
[179] A. Kawamura, J. Xie, J. N. Boyn, K. A. Jesse, A. J. McNeece, E. A. Hill, K. A. Collins, J. A. Valdez-Moreira, A. S. Filatov, J. W. Kurutz, D. A. Mazziotti, J. S. Anderson, *J. Am. Chem. Soc.* **2020**, *142*, 17670–17680.
[180] D. L. J. Broere, R. Plessius, J. Tory, S. Demeshko, B. de Bruin, M. A. Siegler, F. Hartl, J. I. van der Vlugt, *Chem. - A Eur. J.* **2016**, *22*, 13965–13975.
[181] B. Hirani, J. Li, P. I. Djurovich, M. Yousufuddin, J. Oxgaard, P. Persson, S. R. Wilson, R. Bau, W. A. Goddard, M. E. Thompson, *Inorg. Chem.* **2007**, *46*, 3865–3875.
[182] C. D. Morris, M. Spulber, M. Neuburger, C. G. Palivan, E. C. Constable, C. E. Housecroft, *Polyhedron* **2016**, *106*, 51–57.
[183] T. Steinke, B. K. Shaw, H. Jong, B. O. Patrick, M. D. Fryzuk, J. C. Green, *J. Am. Chem. Soc.* **2009**, *131*, 10461–10466.
[184] G. M. Sheldrick, *Acta Crystallogr. Sect. A Found. Crystallogr.* **2015**, *71*, 3–8.
[185] G. M. Sheldrick, *Acta Crystallogr. Sect. A Found. Crystallogr.* **2008**, *64*, 112–122.
[186] C. B. Hübschle, G. M. Sheldrick, B. Dittrich, *J. Appl. Crystallogr.* **2011**, *44*, 1281–1284.
[187] C. Cason, **2009**.
[188] M. J. Frisch, G. W. Trucks, H. B. Schlegel, G. E. Scuseria, M. A. Robb, J. R. Cheeseman, G. Scalmani, V. Barone, G. A. Petersson, H. Nakatsuji, X. Li, M. Caricato, A. V. Marenich, J. Bloino, B. G. Janesko, R. Gomperts, B. Mennucci, H. P. Hratchian, J. V. Ortiz, A. F. Izmaylov, J. L. Sonnenberg, Williams, F. Ding, F. Lipparini, F. Egidi, J. Goings, B. Peng, A. Petrone, T. Henderson, D. Ranasinghe, V. G. Zakrzewski, J. Gao, N. Rega, G. Zheng, W. Liang, M. Hada, M. Ehara, K.

Toyota, R. Fukuda, J. Hasegawa, M. Ishida, T. Nakajima, Y. Honda, O. Kitao, H. Nakai, T. Vreven, K. Throssell, J. A. Montgomery Jr., J. E. Peralta, F. Ogliaro, M. J. Bearpark, J. J. Heyd, E. N. Brothers, K. N. Kudin, V. N. Staroverov, T. A. Keith, R. Kobayashi, J. Normand, K. Raghavachari, A. P. Rendell, J. C. Burant, S. S. Iyengar, J. Tomasi, M. Cossi, J. M. Millam, M. Klene, C. Adamo, R. Cammi, J. W. Ochterski, R. L. Martin, K. Morokuma, O. Farkas, J. B. Foresman, D. J. Fox, **2009**.
[189] S. Dapprich, I. Komáromi, K. S. Byun, K. Morokuma, M. J. Frisch, *J. Mol. Struct. THEOCHEM* **1999**, *461–462*, 1–21.
[190] T. Vreven, K. Morokuma, *Annu. Rep. Comput. Chem.* **2006**, *2*, 35–51.
[191] M. Svensson, S. Humbel, R. D. J. Froese, T. Matsubara, S. Sieber, K. Morokuma, *J. Phys. Chem.* **1996**, *100*, 19357–19363.
[192] J. Da Chai, M. Head-Gordon, *Phys. Chem. Chem. Phys.* **2008**, *10*, 6615–6620.
[193] W. R. Wadt, P. J. Hay, *J. Chem. Phys.* **1985**, *82*, 284–298.
[194] P. J. Hay, W. R. Wadt, *J. Chem. Phys.* **1985**, *82*, 299–310.
[195] M. Couty, M. B. Hall, *J. Comput. Chem.* **1996**, *17*, 1359–1370.
[196] B. P. Pritchard, D. Altarawy, B. Didier, T. D. Gibson, T. L. Windus, *J. Chem. Inf. Model.* **2019**, *59*, 4814–4820.
[197] J. J. P. Stewart, *J. Mol. Model.* **2007**, *13*, 1173–1213.
[198] S. Schenker, C. Schneider, S. B. Tsogoeva, T. Clark, *J. Chem. Theory Comput.* **2011**, *7*, 3586–3595.
[199] A. V. Marenich, C. J. Cramer, D. G. Truhlar, *J. Phys. Chem. B* **2009**, *113*, 6378–6396.
[200] V. Barone, M. Cossi, *J. Phys. Chem. A* **1998**, *102*, 1995–2001.
[201] M. Cossi, V. Barone, B. Mennucci, J. Tomasi, *Chem. Phys. Lett.* **1998**, *286*, 253–260.
[202] V. Barone, M. Cossi, J. Tomasi, *J. Comput. Chem.* **1998**, *19*, 404–417.
[203] J. Tomasi, B. Mennucci, R. Cammi, *Chem. Rev.* **2005**, *105*, 2999–3093.
[204] B. Case, R. Parsons, *Trans. Faraday Soc.* **1967**, *63*, 1224–1239.
[205] C. Y. Legault, **2020**.
[206] M. J. Frisch, G. W. Trucks, H. B. Schlegel, G. E. Scuseria, M. A. Robb, J. R. Cheeseman, G. Scalmani, V. Barone, G. A. Petersson, H. Nakatsuji, X. Li, M. Caricato, A. V. Marenich, J. Bloino, B. G. Janesko, R. Gomperts, B. Mennucci, H. P. Hratchian, J. V. Ortiz, A. F. Izmaylov, J. L. Sonnenberg, Williams, F. Ding, F. Lipparini, F. Egidi, J. Goings, B. Peng, A. Petrone, T. Henderson, D. Ranasinghe, V. G. Zakrzewski, J. Gao, N. Rega, G. Zheng, W. Liang, M. Hada, M. Ehara, K. Toyota, R. Fukuda, J. Hasegawa, M. Ishida, T. Nakajima, Y. Honda, O. Kitao, H. Nakai, T. Vreven, K. Throssell, J. A. Montgomery Jr., J. E. Peralta, F. Ogliaro, M. J. Bearpark, J. J. Heyd, E. N. Brothers, K. N. Kudin, V. N. Staroverov, T. A. Keith, R. Kobayashi, J. Normand, K. Raghavachari, A. P. Rendell, J. C. Burant, S. S. Iyengar, J. Tomasi, M. Cossi, J. M. Millam, M. Klene, C. Adamo, R. Cammi, J. W. Ochterski, R. L. Martin, K. Morokuma, O. Farkas, J. B. Foresman, D. J. Fox, **2016**.
[207] Q. Cui, H. Guo, M. Karplus, *J. Chem. Phys.* **2002**, *117*, 5617–5631.
[208] L. E. Roy, P. J. Hay, R. L. Martin, *J. Chem. Theory Comput.* **2008**, *4*, 1029–1031.
[209] A. D. Becke, *J. Chem. Phys.* **1988**, *88*, 2547–2553.
[210] T. Lu, F. Chen, *J. Comput. Chem.* **2012**, *33*, 580–592.
[211] E. D. Glendening, J. K. Badenhoop, A. E. Reed, J. E. Carpenter, J. A. Bohmann, C. M. Morales, P. Karafiloglou, C. R. Landis, F. Weinhold, **2018**.
[212] G. Knizia, *J. Chem. Theory Comput.* **2013**, *9*, 4834–4843.
[213] Y. Zhao, D. G. Truhlar, *Theor. Chem. Acc.* **2008**, *120*, 215–241.
[214] F. Weigend, R. Ahlrichs, *Phys. Chem. Chem. Phys.* **2005**, *7*, 3297–3305.
[215] D. W. Szczepanik, **2021**.

CHAPTER 7.
APPENDIX

7.1. NMR data

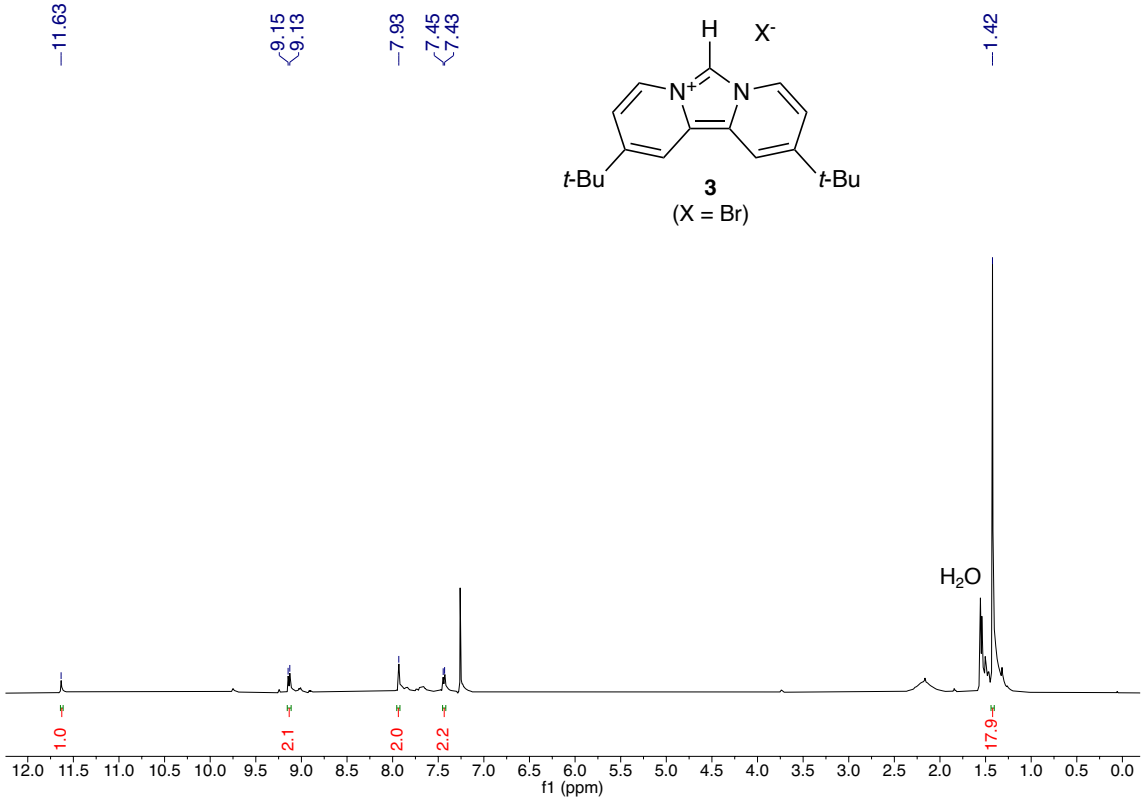

Figure.7.1. ^{1}H NMR chart of compound **3** (400 MHz) in $CDCl_3$

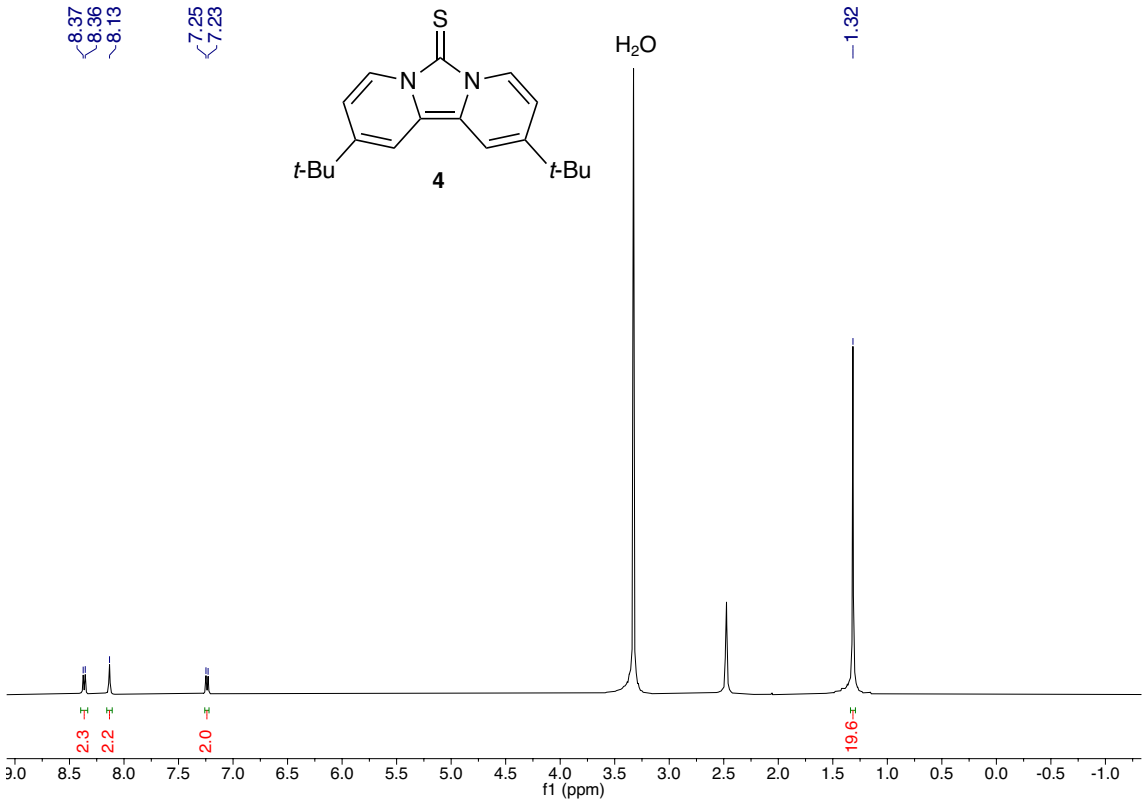

Figure.7.2 ^{1}H NMR chart of compound **4** (400 MHz) in $CDCl_3$

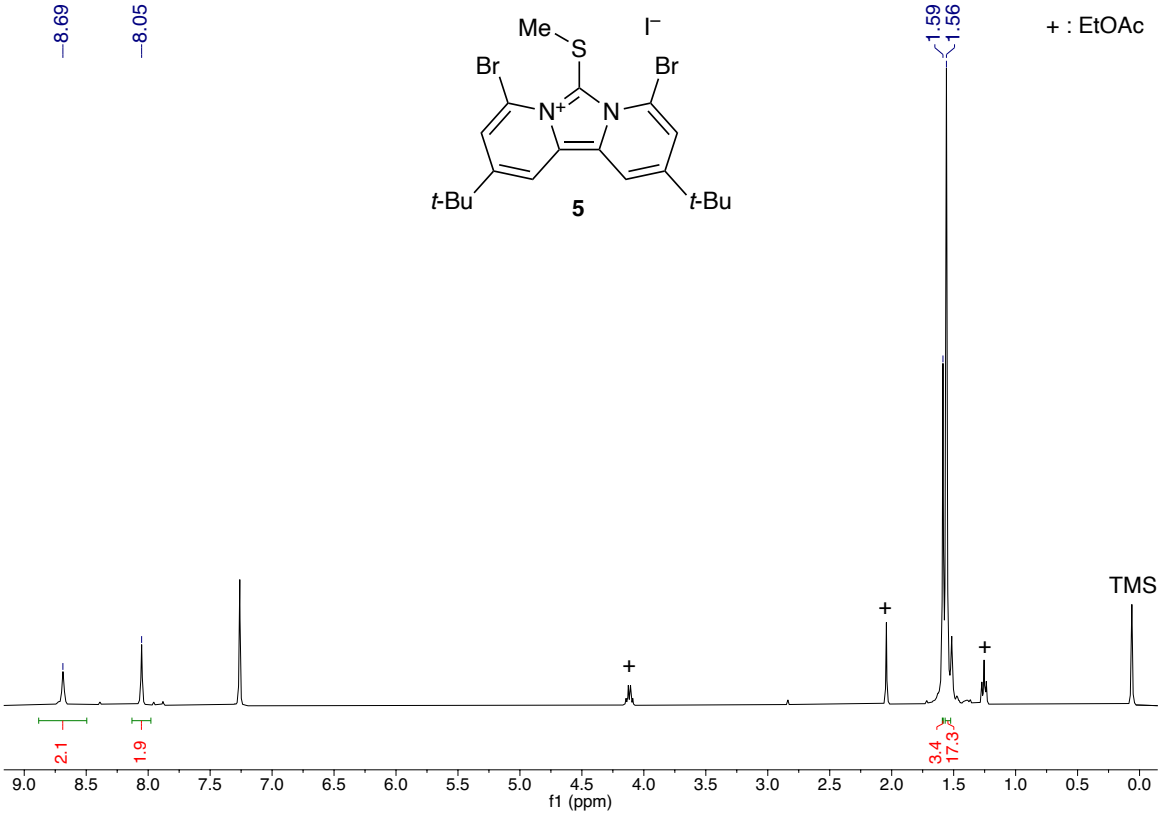

Figure.7.3. ^{1}H NMR chart of compound **5** (400 MHz) in $CDCl_3$

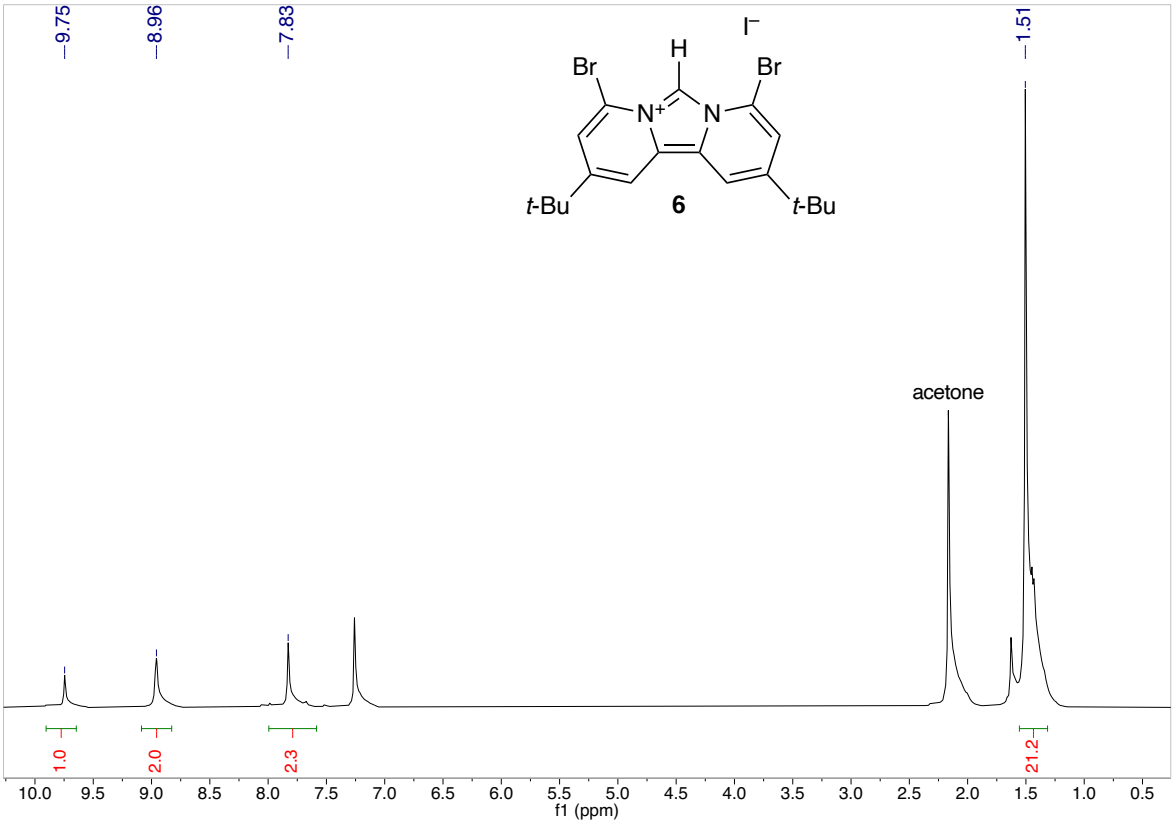

Figure.7.4. ^{1}H NMR chart of compound **6** (400 MHz) in $CDCl_3$

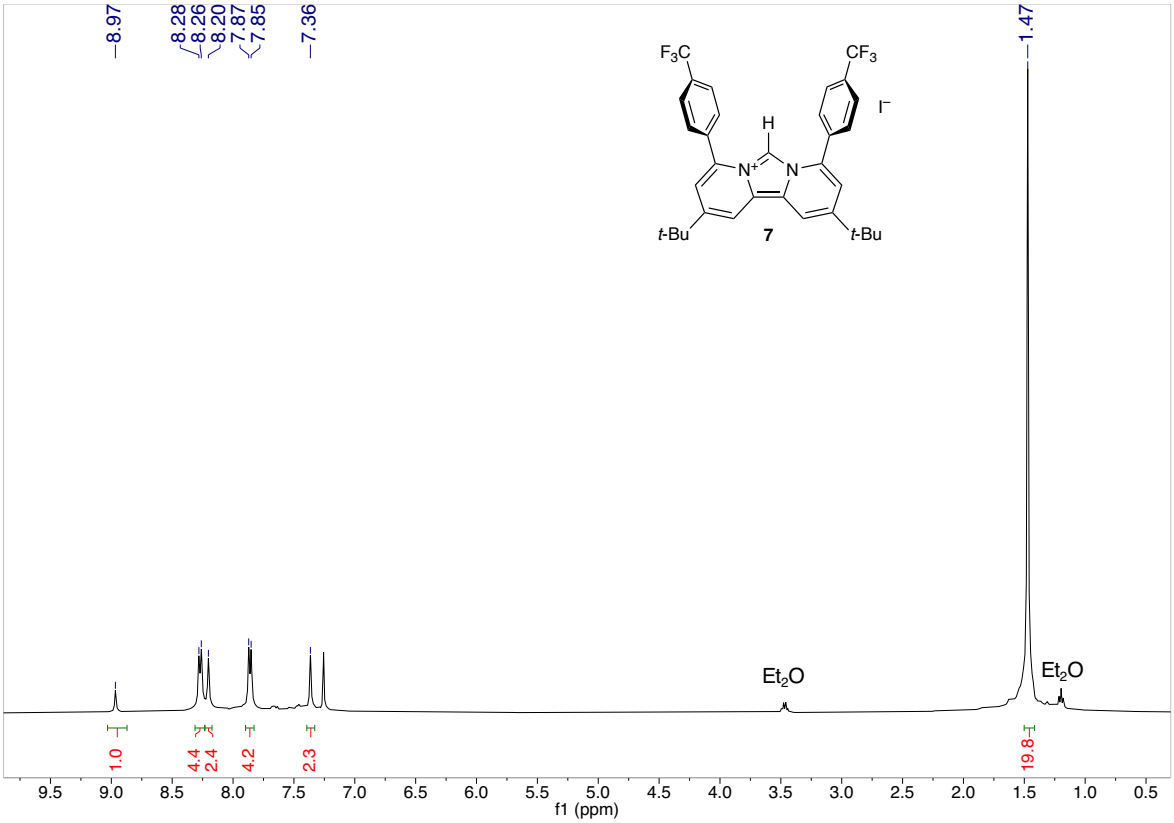

Figure.7.5. ^{1}H NMR chart of compound **7** (400 MHz) in $CDCl_3$

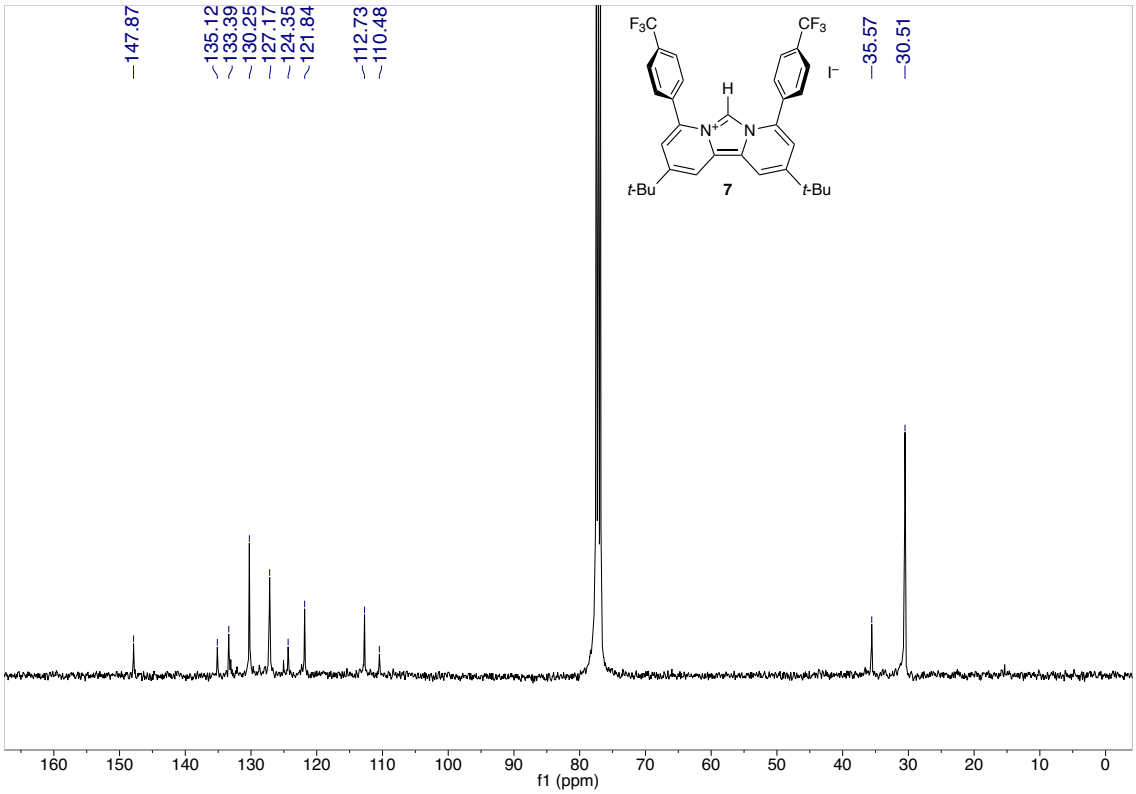

Figure.7.6. ^{13}C {^{1}H} NMR chart of compound **7** (100 MHz) in $CDCl_3$

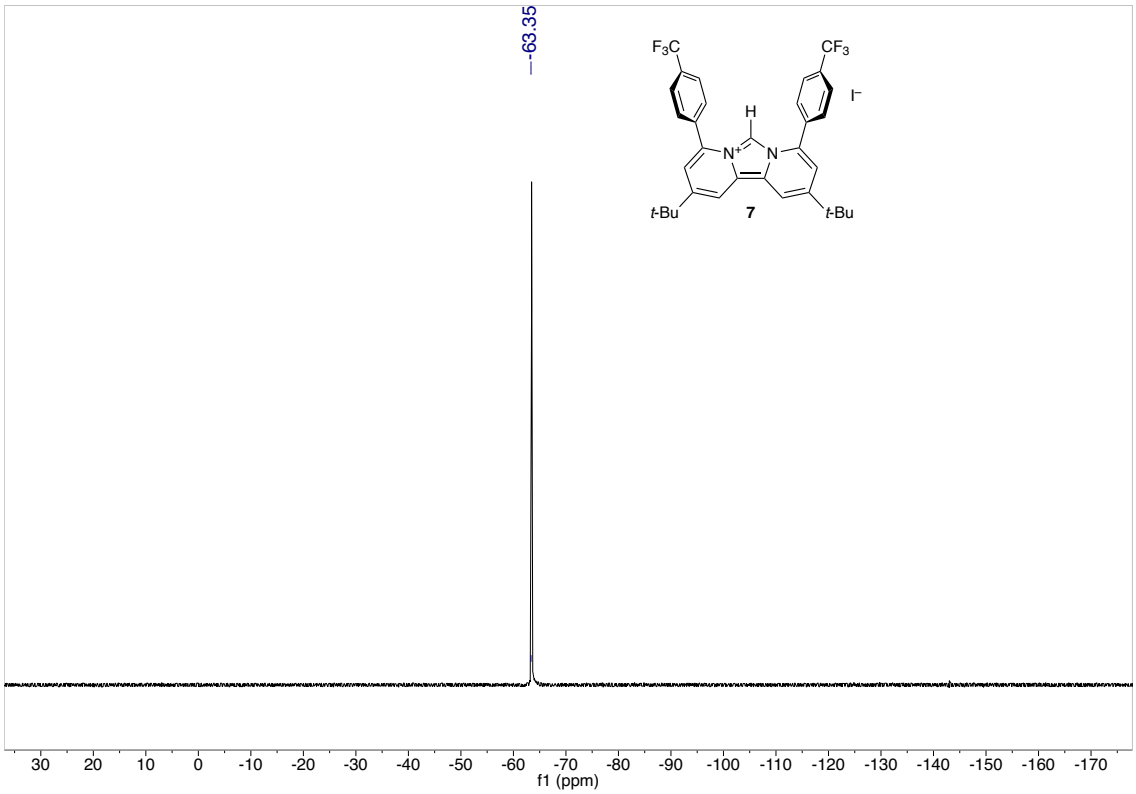

Figure.7.7 ^{19}F NMR chart of compound **7** (376 MHz) in $CDCl_3$

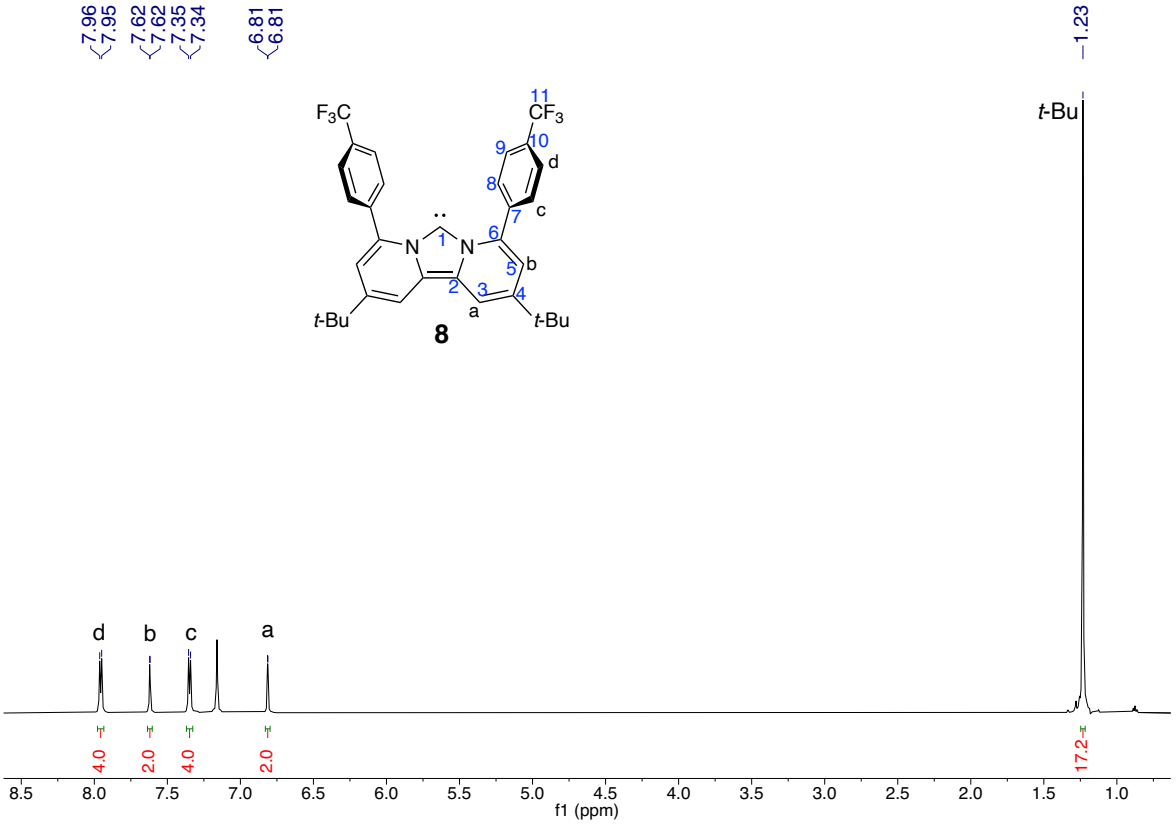

Figure.7.8 ^{1}H NMR chart of free carbene **8** (600 MHz, C_6D_6)

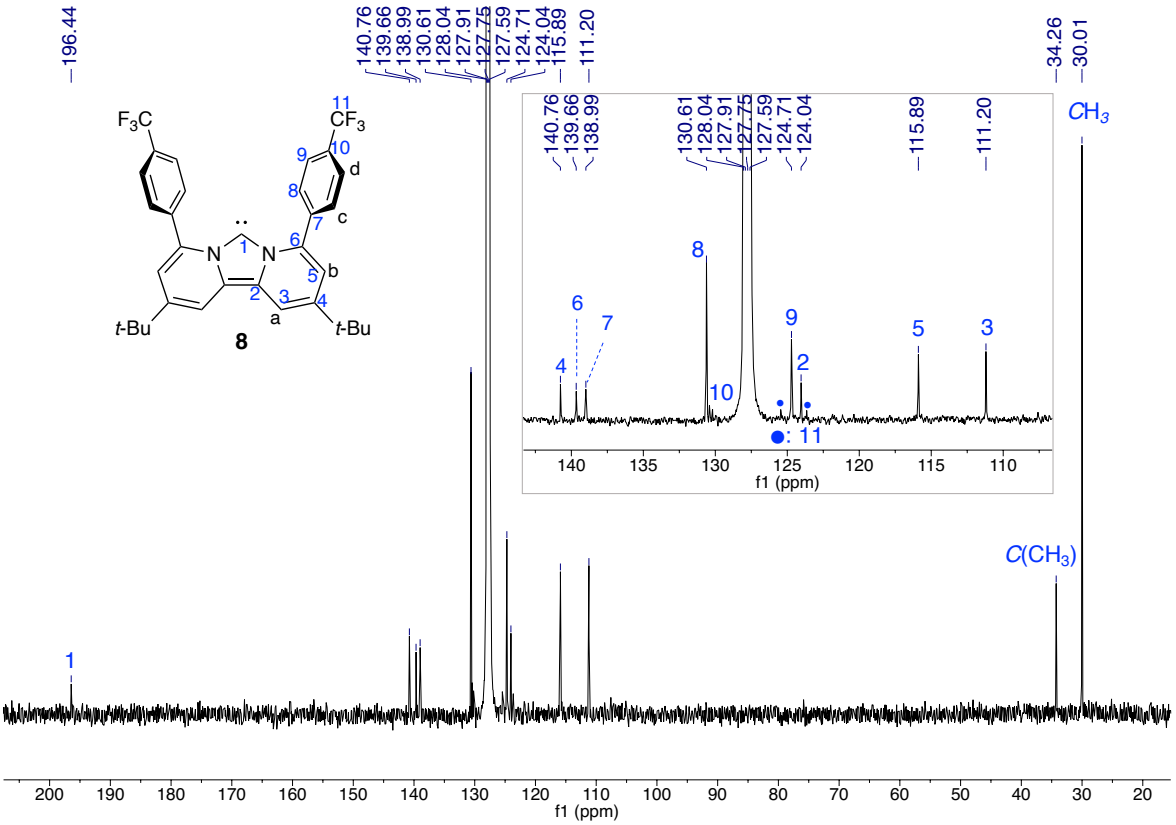

Figure.7.9 ^{13}C{^{1}H} NMR chart of **8** (150 MHz, C_6D_6)

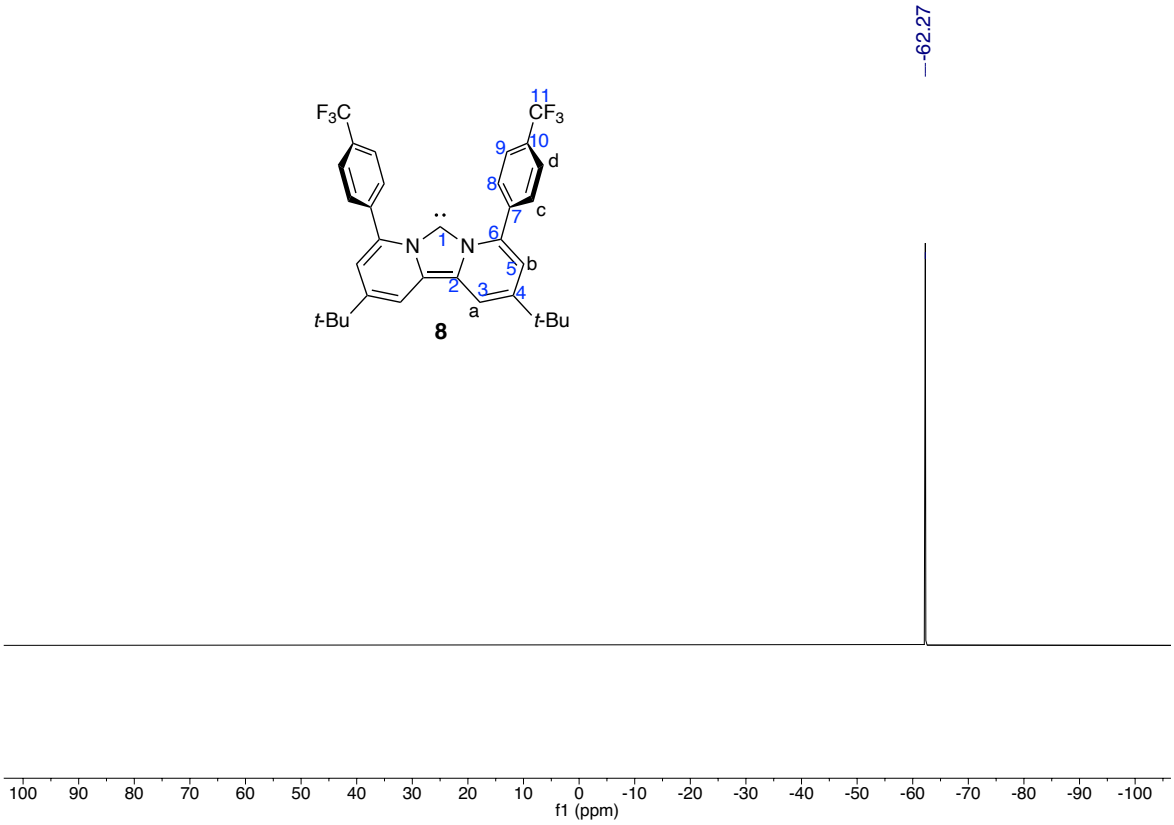

Figure 7.10 ^{19}F NMR chart of free carbene **8** (576 MHz, C_6D_6)

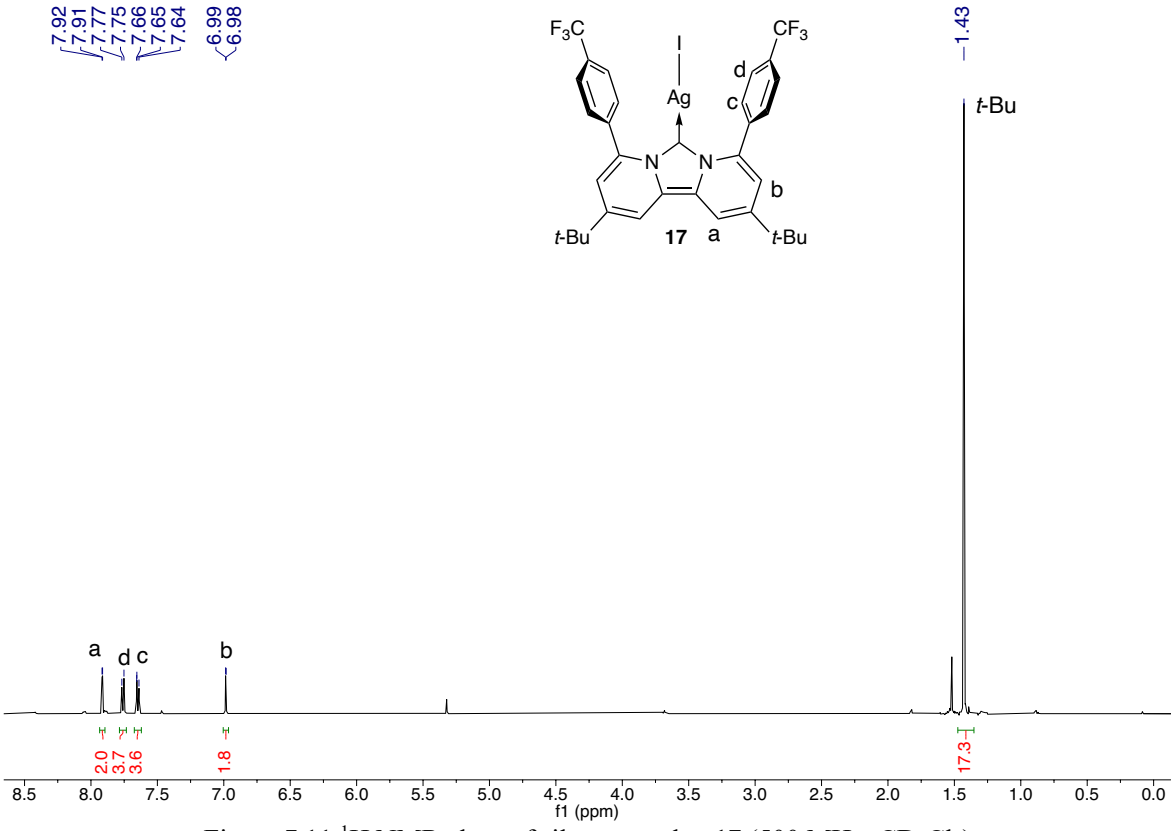

Figure.7.11 ^{1}H NMR chart of silver complex **17** (500 MHz, CD_2Cl_2)

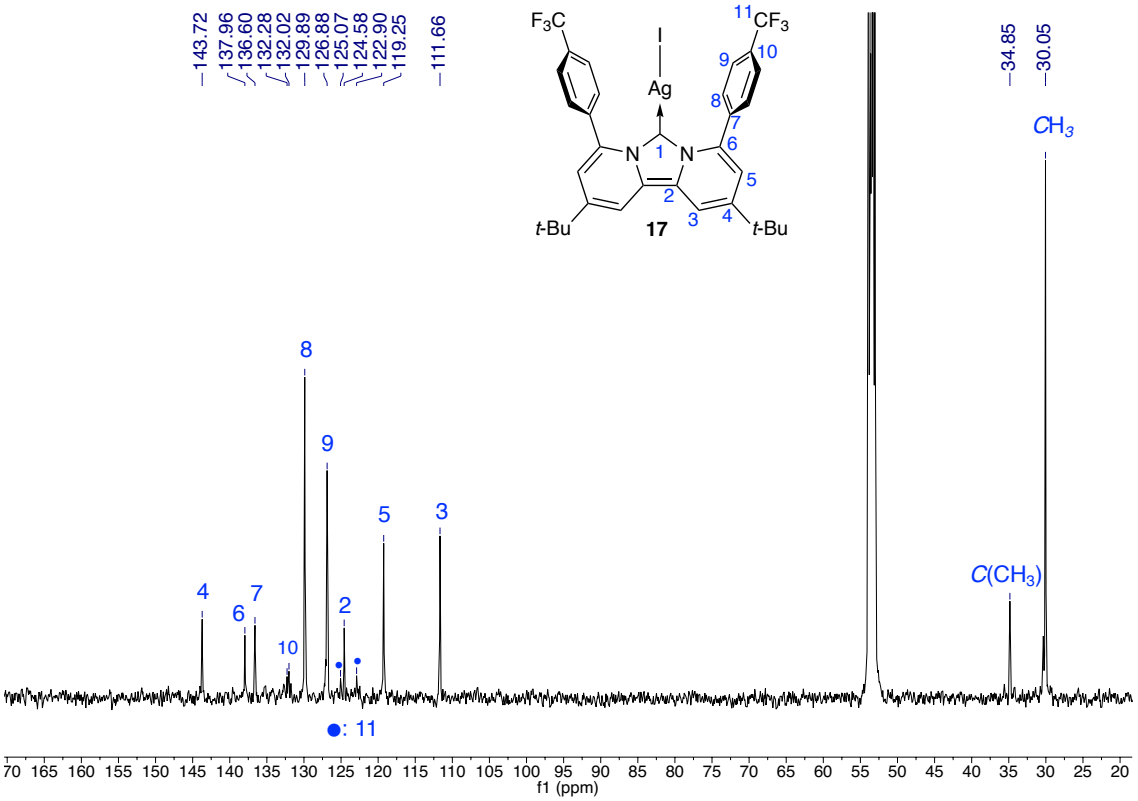

Figure.7.12 $^{13}C\{^{1}H\}$ NMR chart of **17** (125 MHz, CD_2Cl_2)

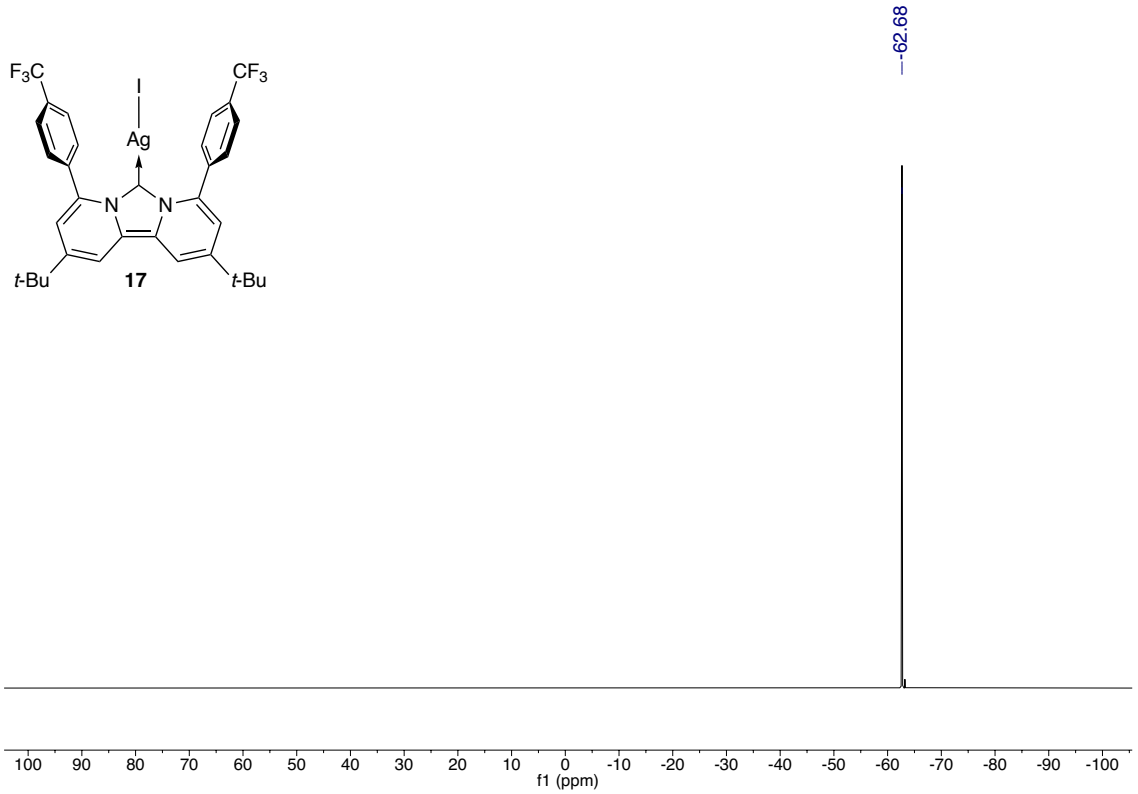

Figure.7.13 ^{19}F NMR chart of silver complex **17** (470 MHz, CD_3CN)

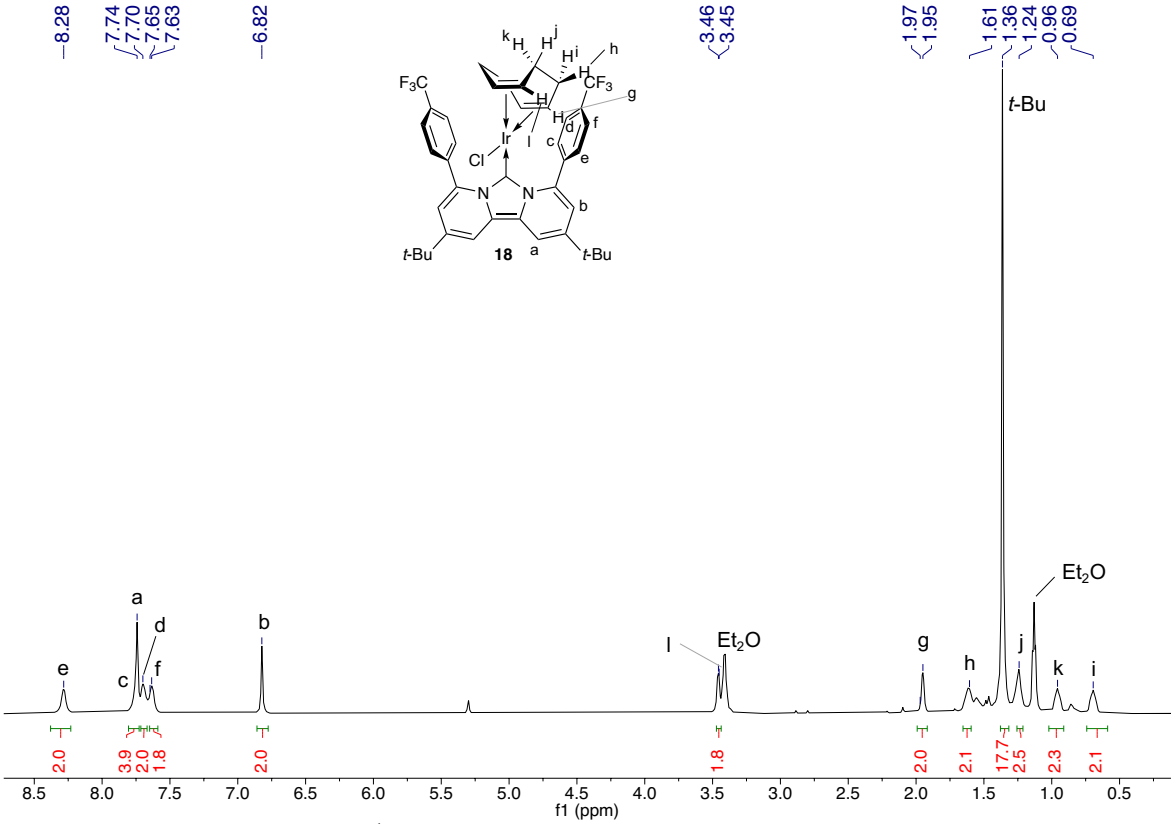

Figure.7.14 ^{1}H NMR chart of complex **18** (600 MHz, CD_2Cl_2)

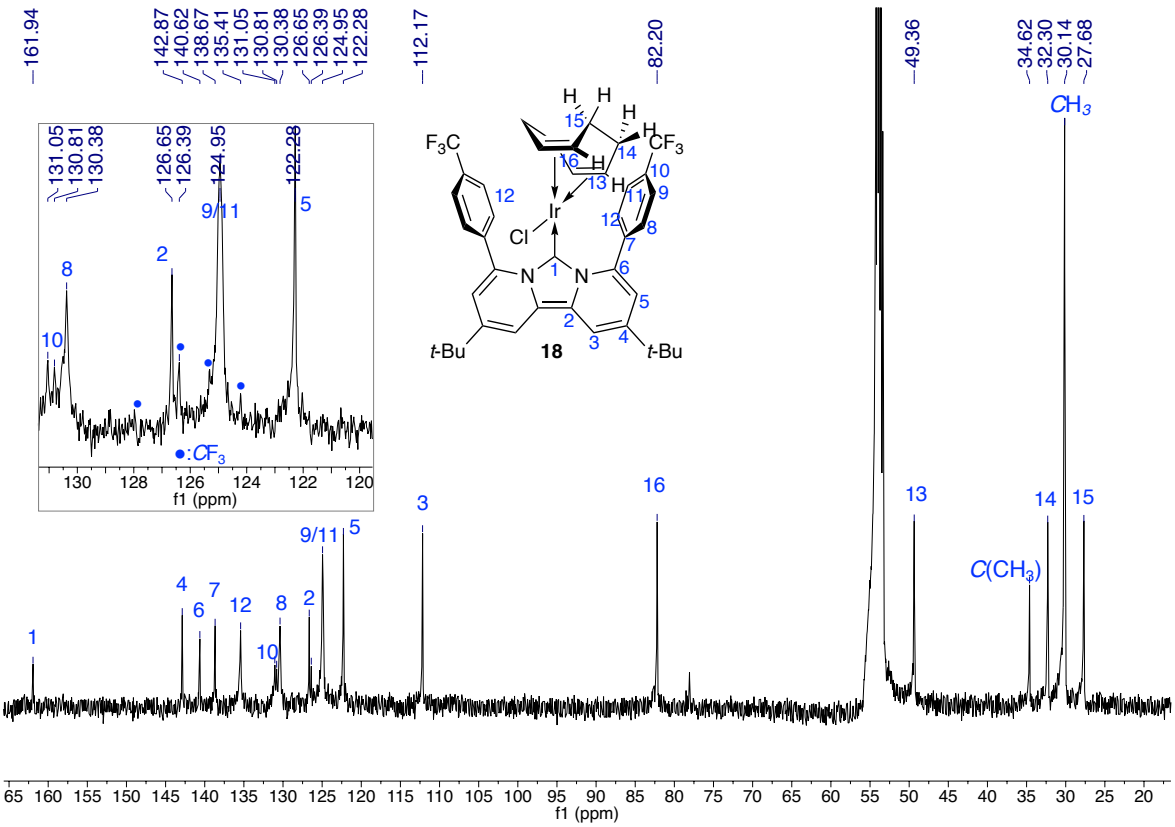

Figure.7.15 ^{13}C{^{1}H} NMR chart of complex **18** (150 MHz, CD_2Cl_2)

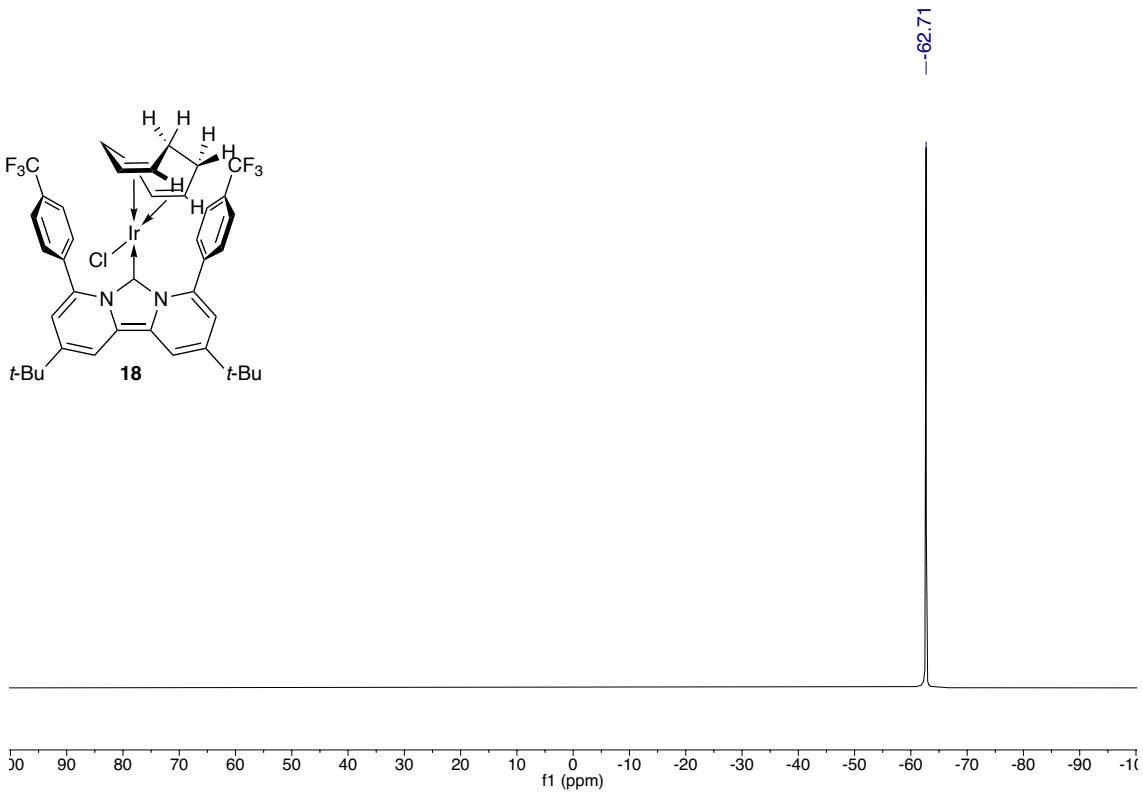

Figure 7.16 ^{19}F NMR chart of complex **18** (576 MHz, CD_2Cl_2)

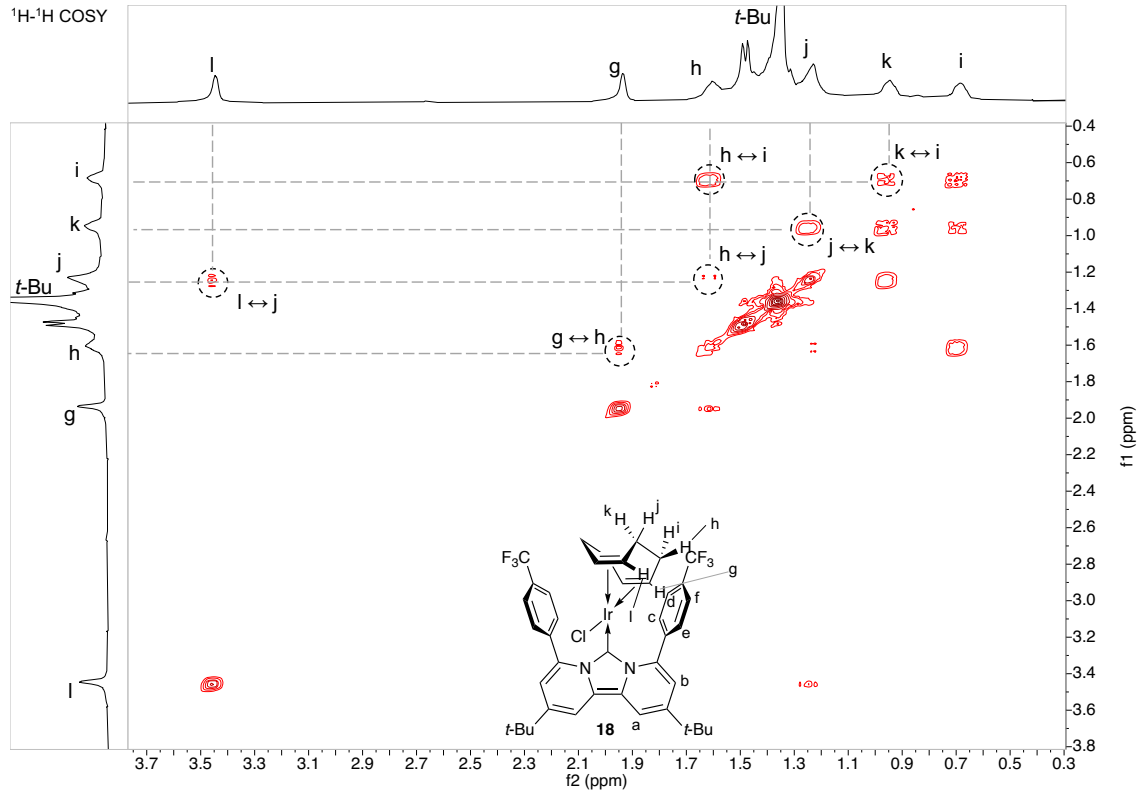

Figure 7.17 ^{1}H-^{1}H COSY chart of complex **18**

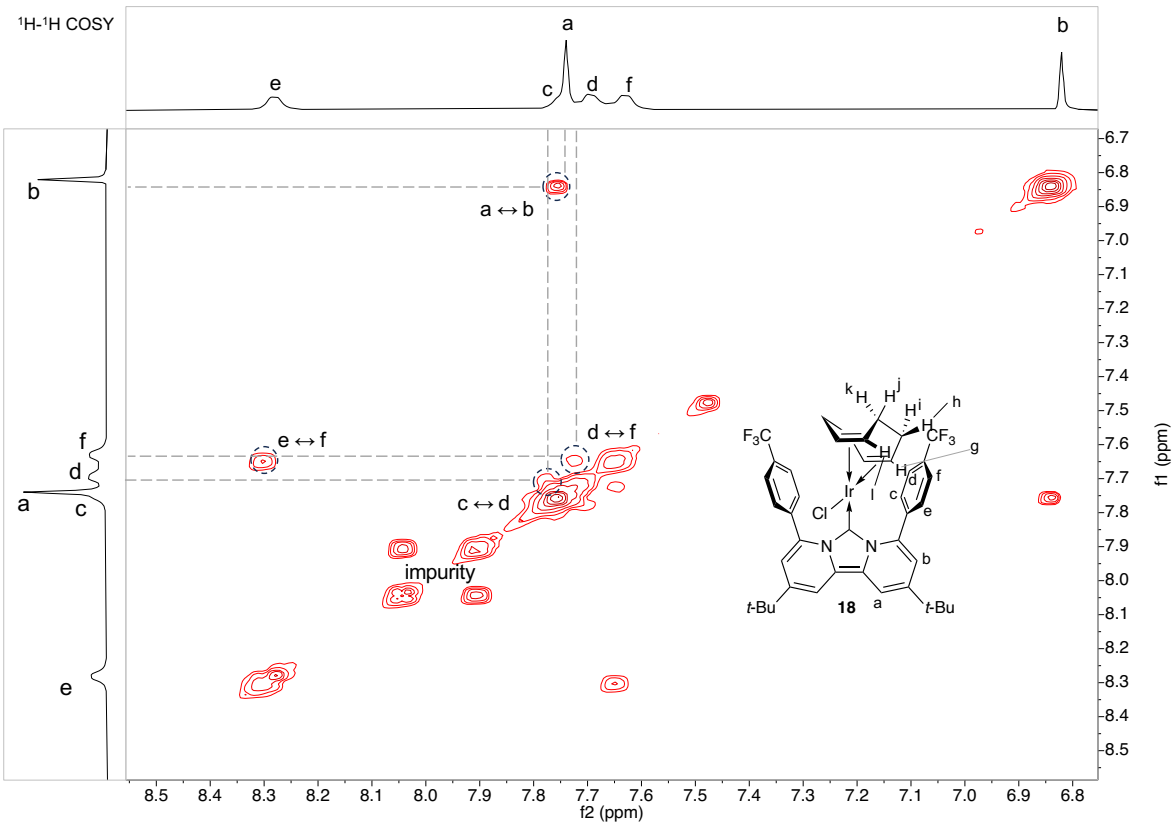

Figure.7.18 ^{1}H-^{1}H COSY chart of complex **18**

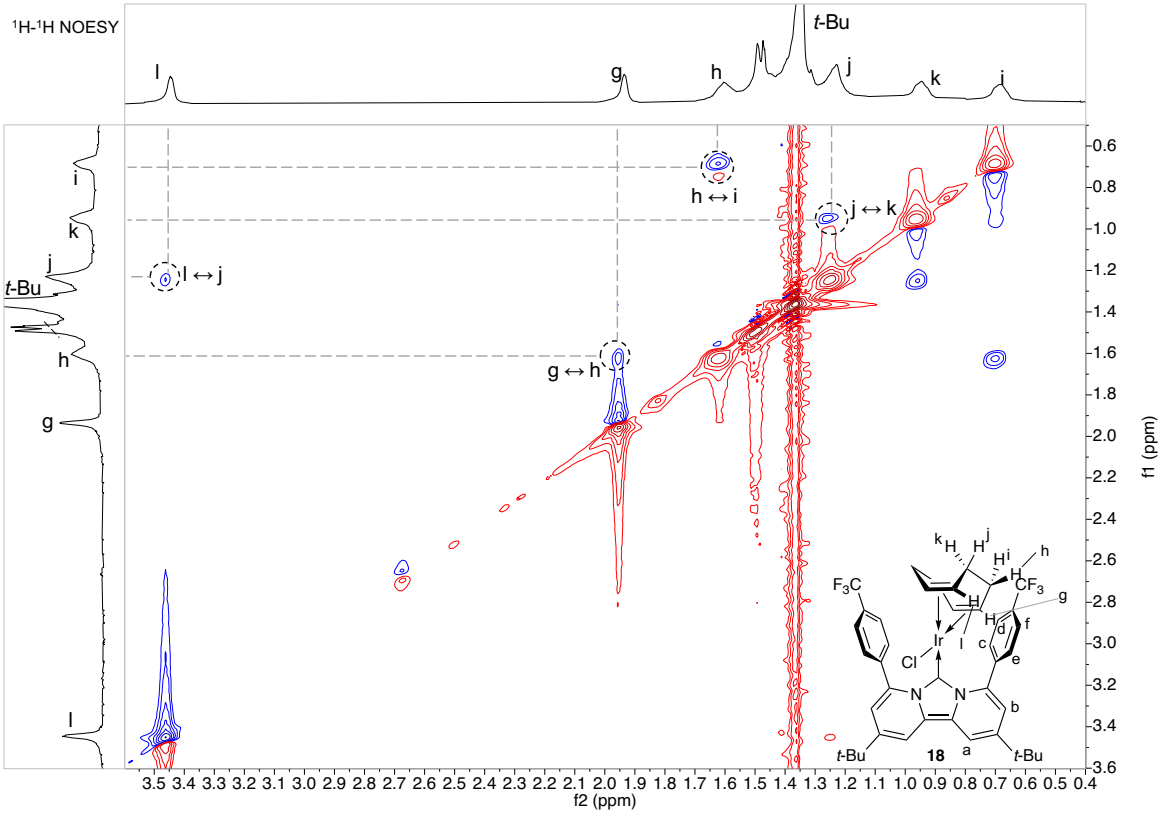

Figure.7.19 ^{1}H-^{1}H NOESY chart of complex **18**

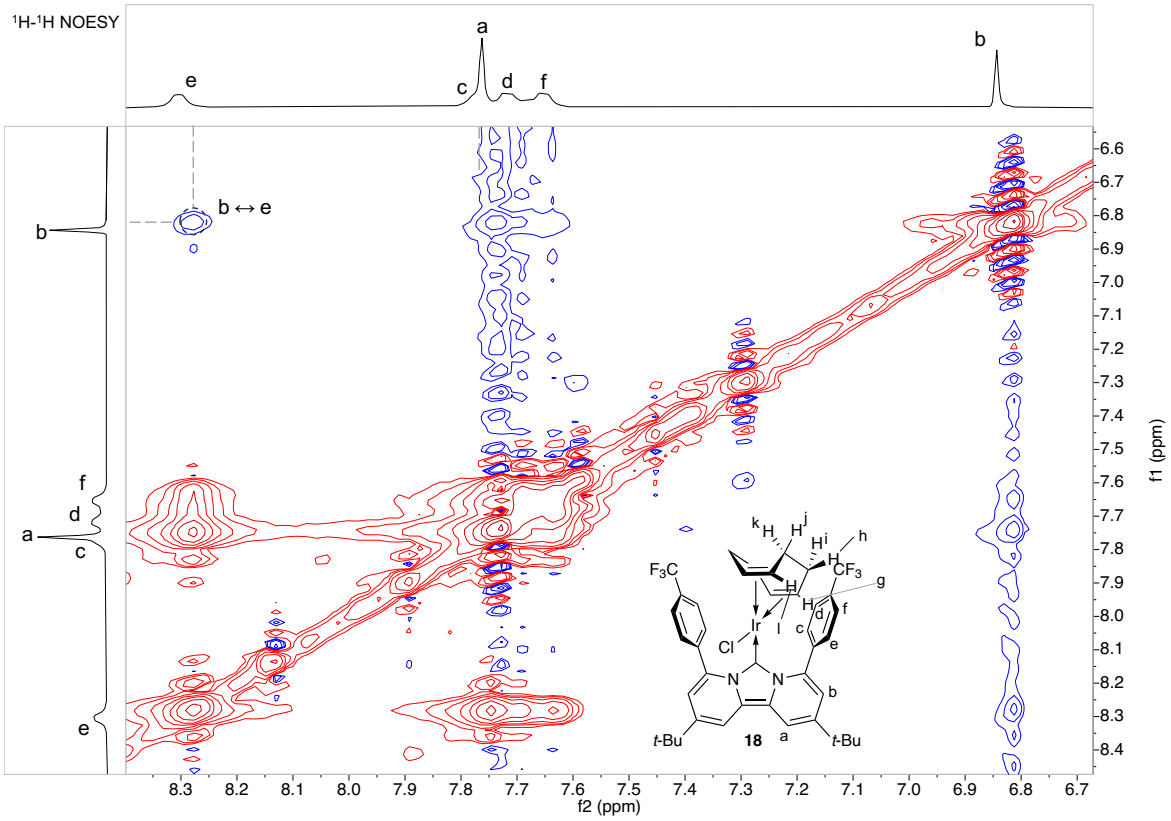

Figure.7.20 ^{1}H-^{1}H NOESY chart of complex **18**

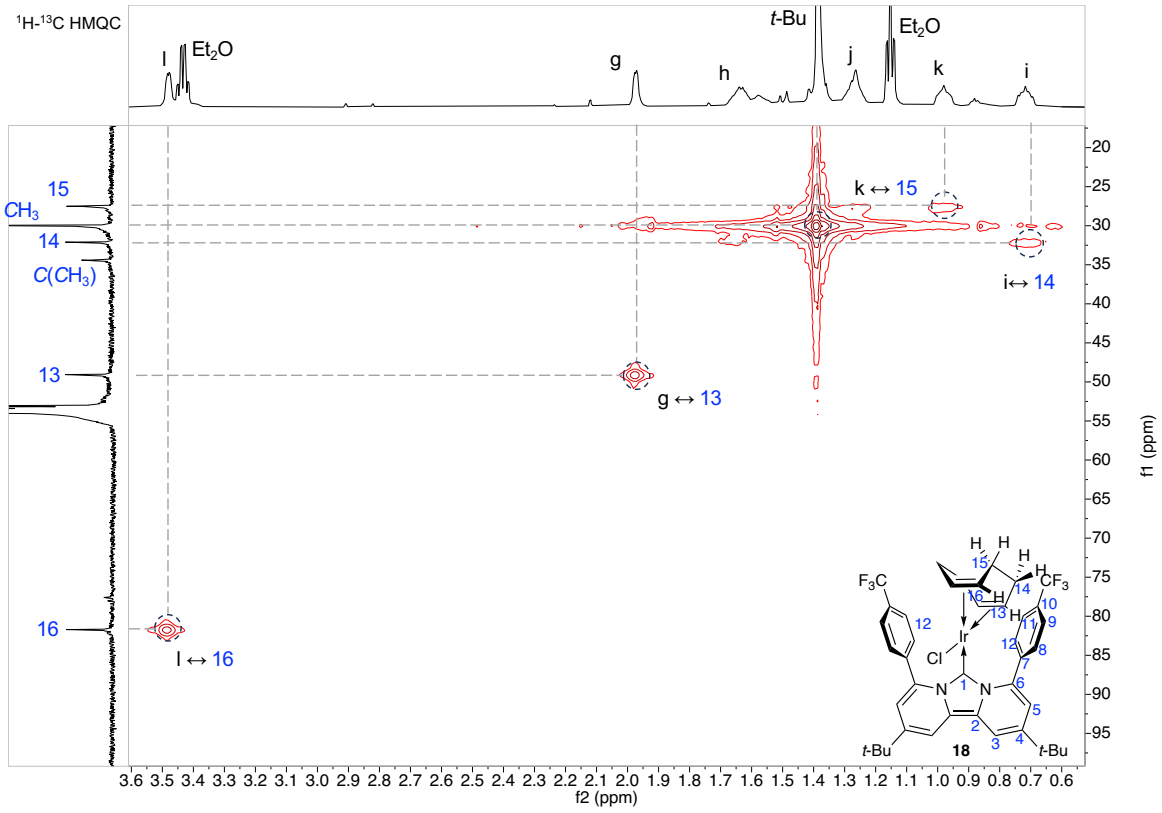

Figure.7.21 ^{1}H-^{13}C HMQC chart of complex **18**

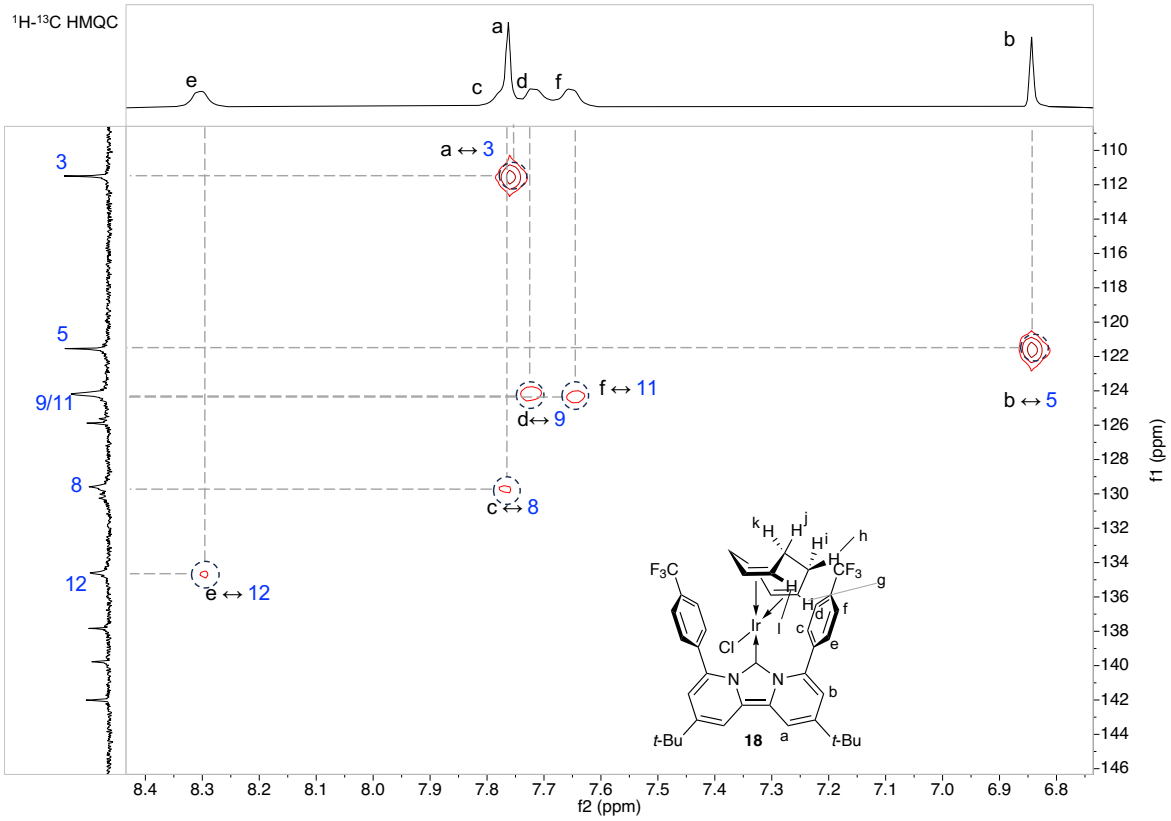

Figure.7.22 ^{1}H-^{13}C HMQC chart of complex **18**

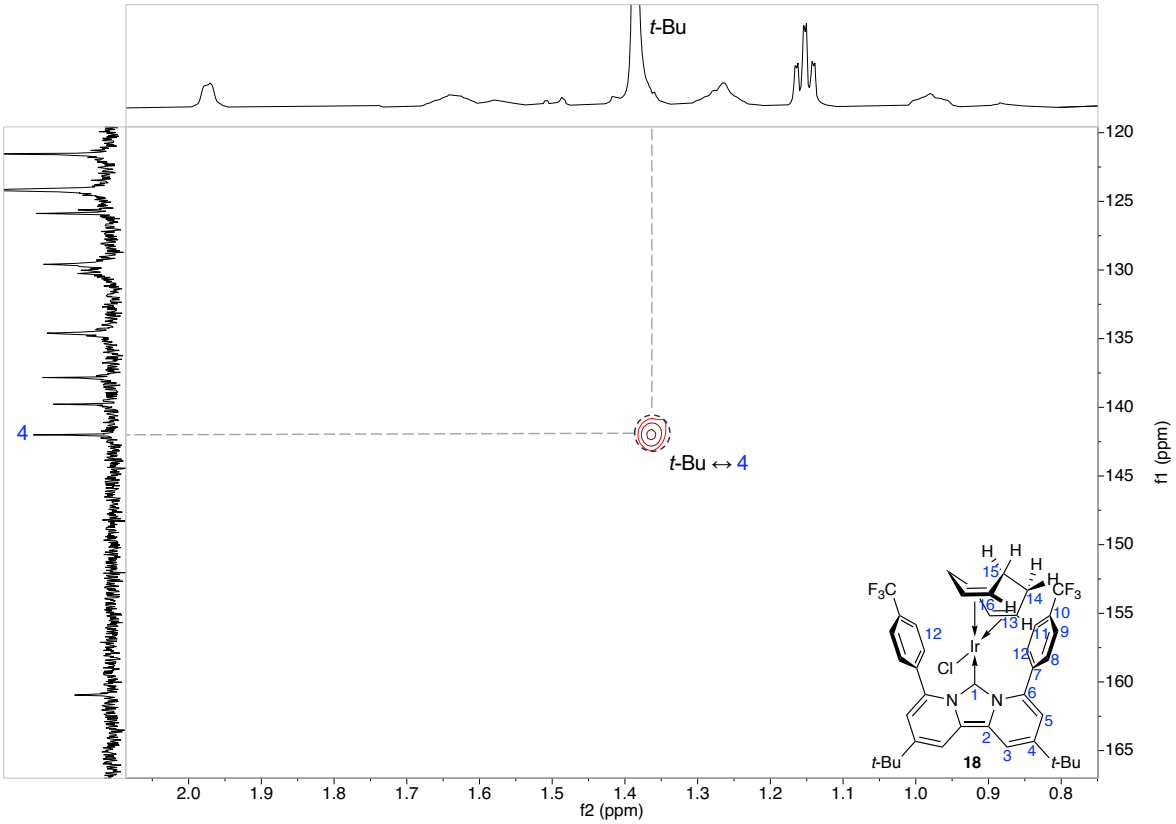

Figure.7.23 ^{1}H-^{13}C HMBC chart of complex **18**

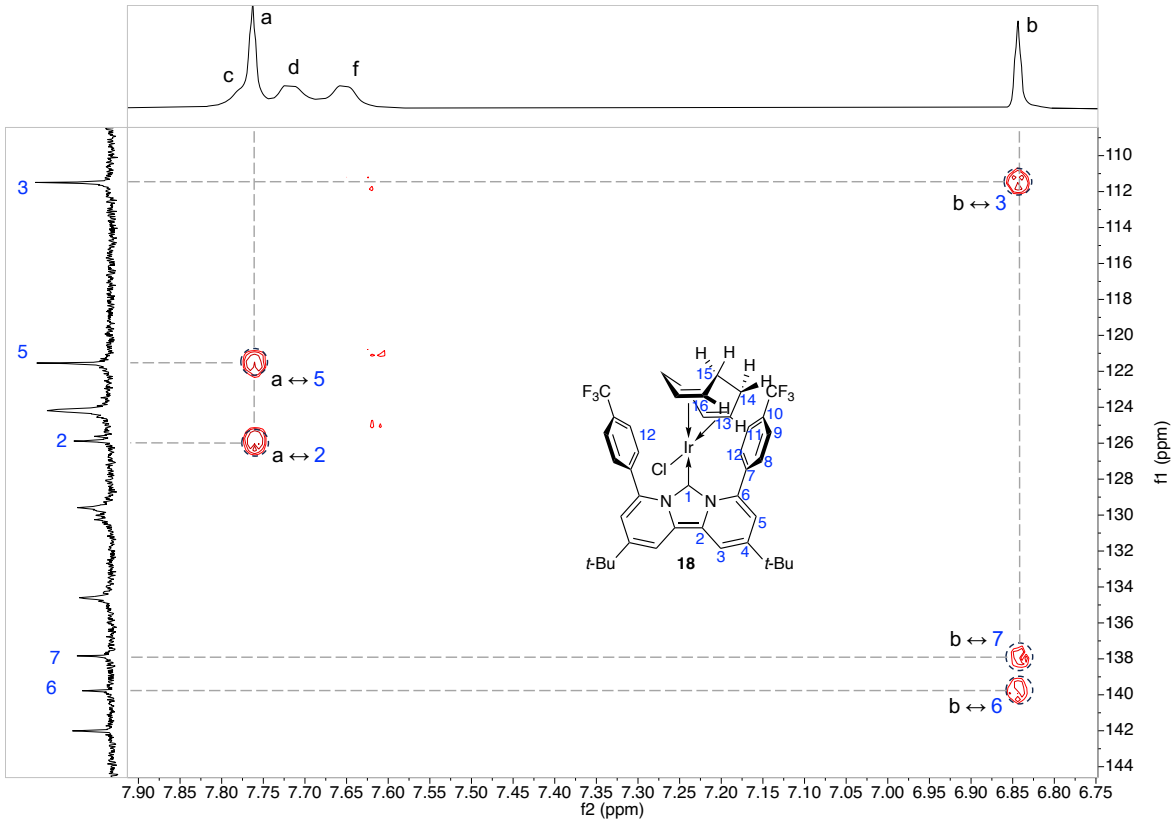

Figure.7.24 ^{1}H-^{13}C HMBC chart of complex **18**

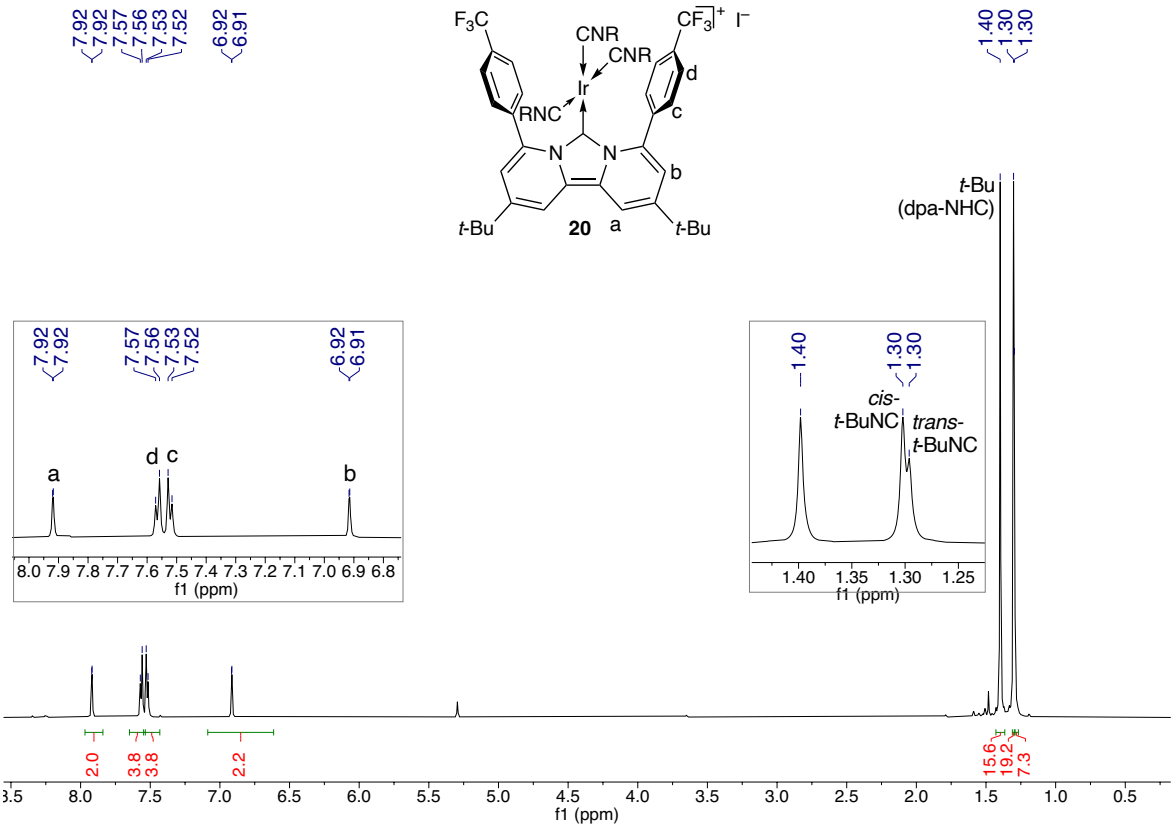

Figure.7.25 ^{1}H NMR chart of complex **20** (600 MHz, CD_2Cl_2).

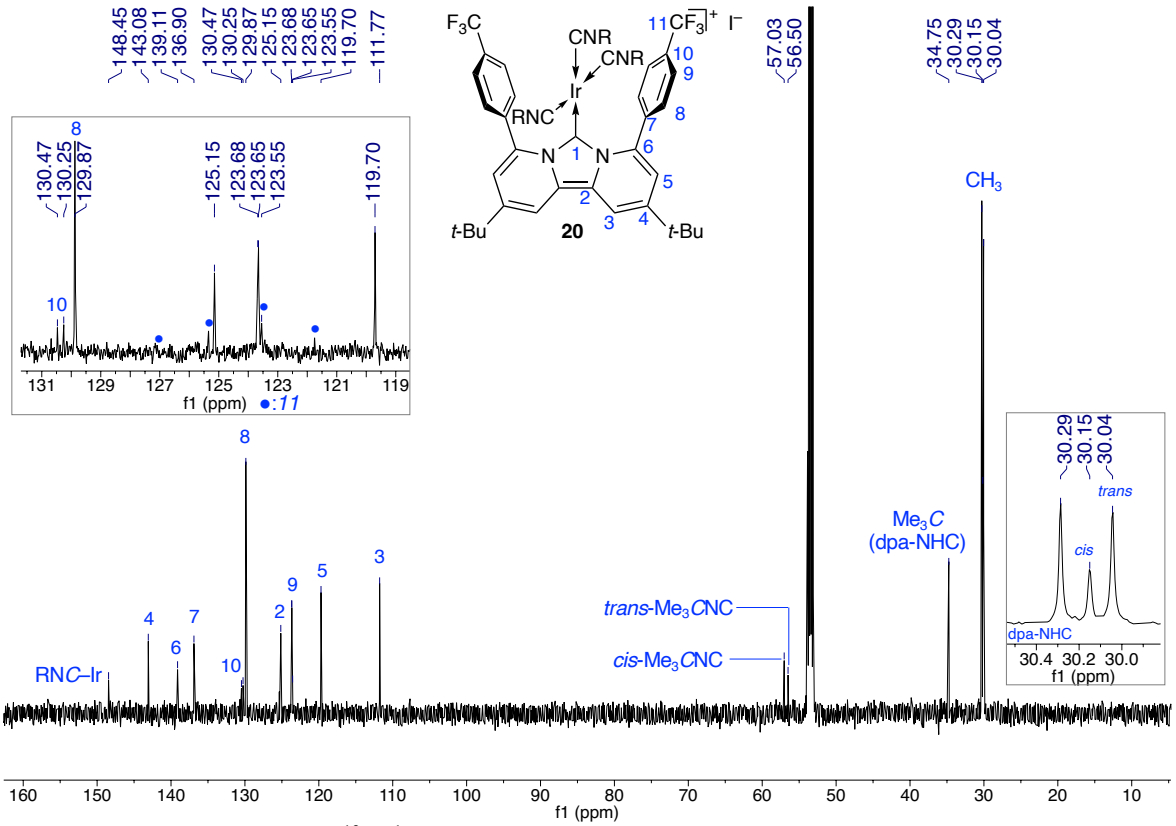

Figure.7.26 $^{13}C\{^{1}H\}$ NMR chart of complex **20** (150 MHz, CD_2Cl_2)

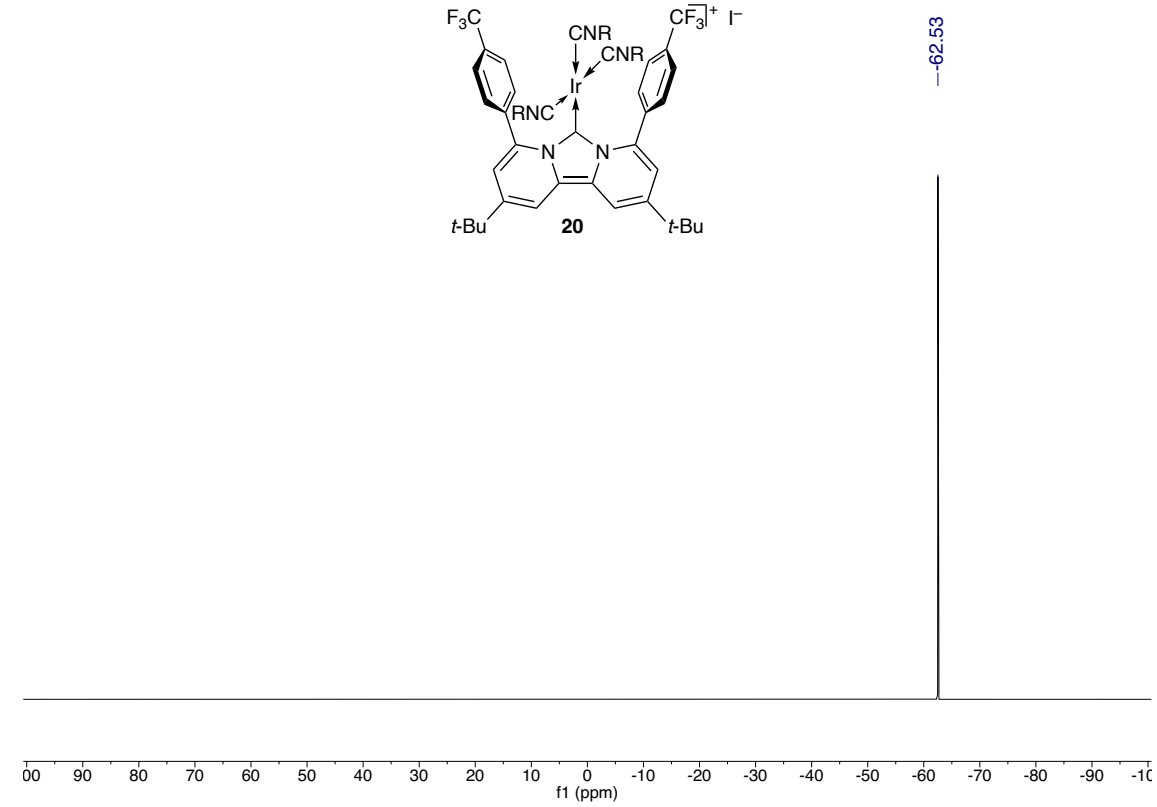

Figure.7.27 ^{19}F NMR chart of complex **20** (564 MHz, CD_2Cl_2)

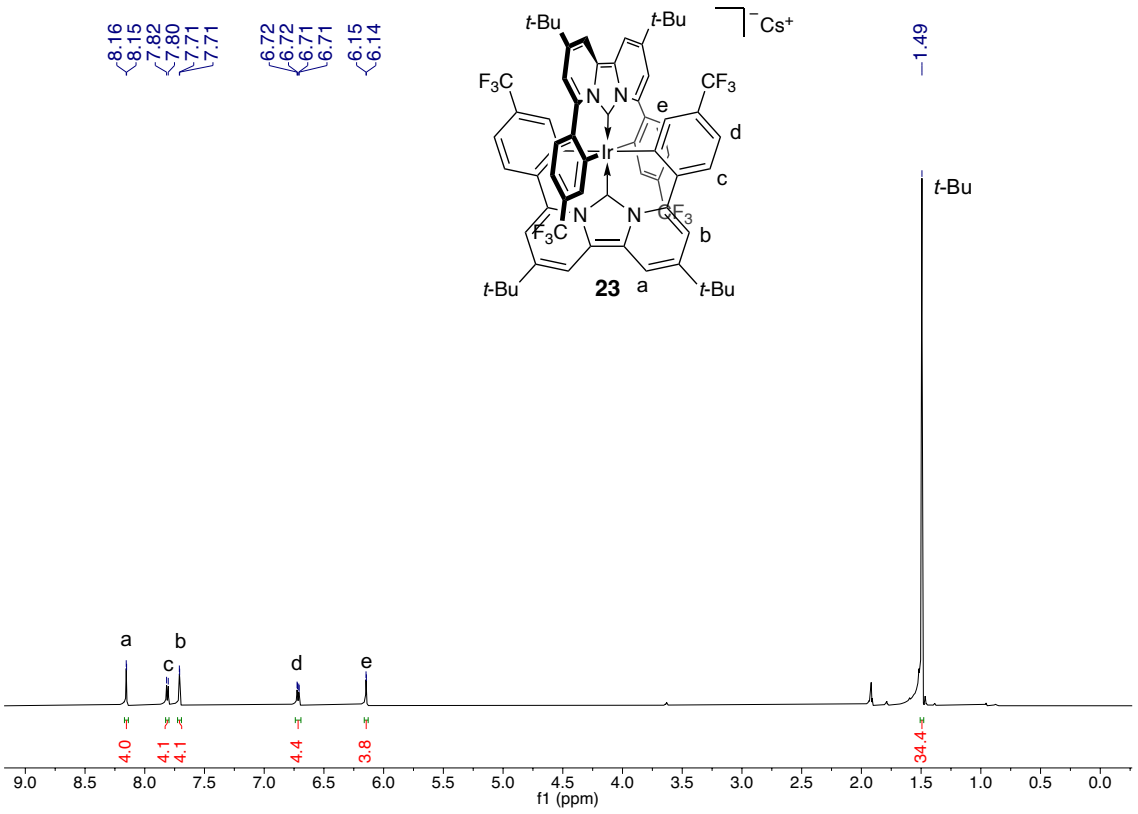

Figure.7.28 ^{1}H NMR chart of complex **23** (600 MHz, CD_3CN)

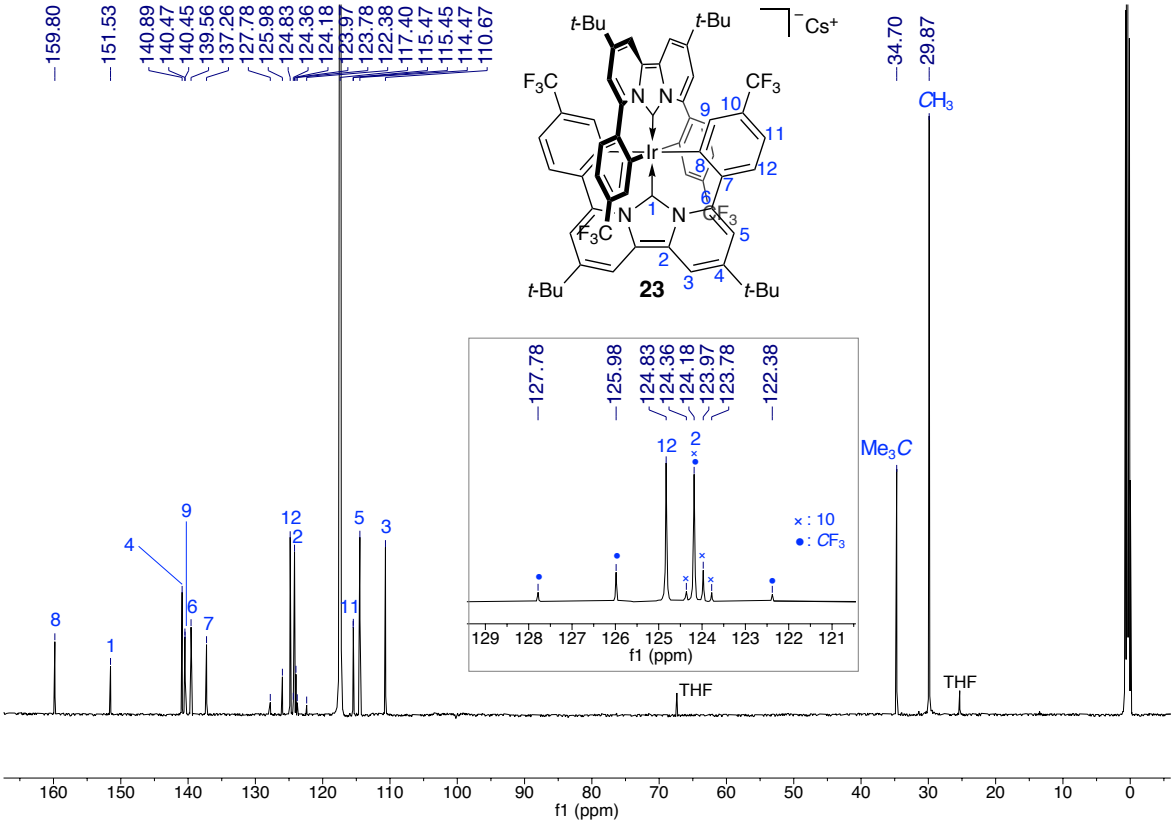

Figure 7.29^{13}C{^{1}H} NMR chart of complex **23** (150 MHz, CD_3CN)

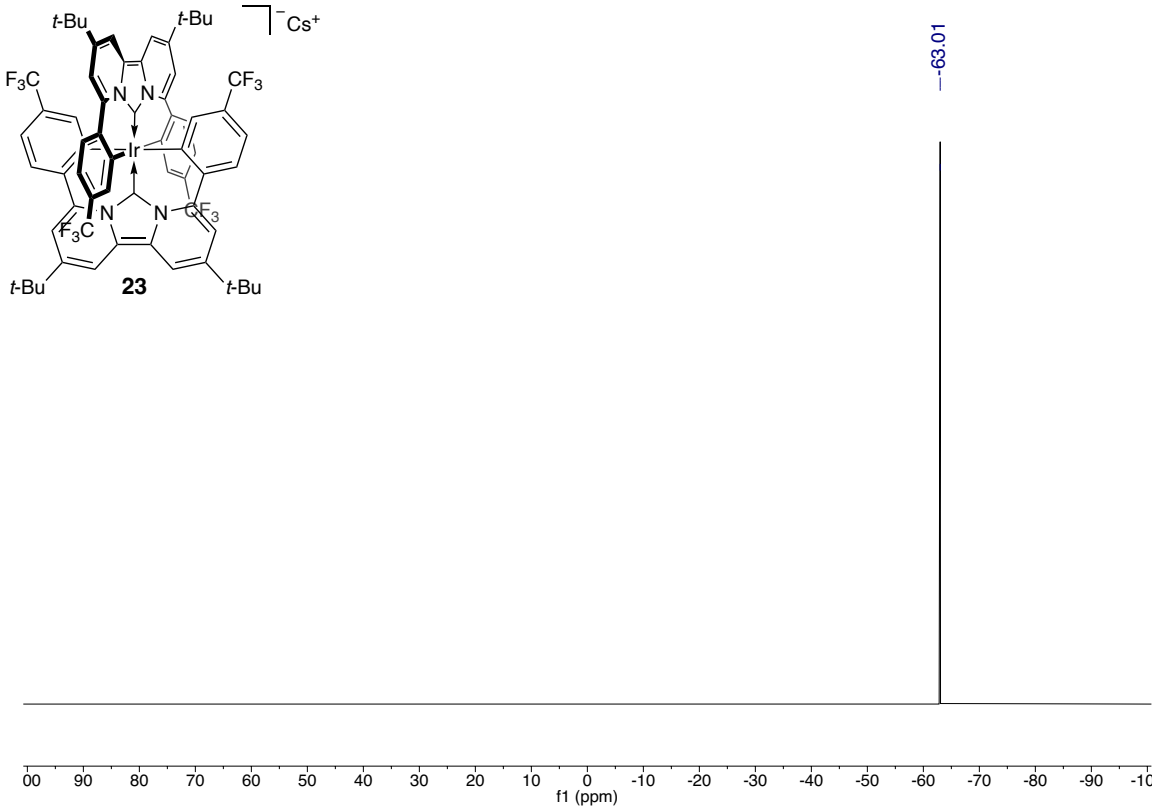

Figure.7.30 ^{19}F NMR chart of complex **23** (564 MHz, CD_3CN)

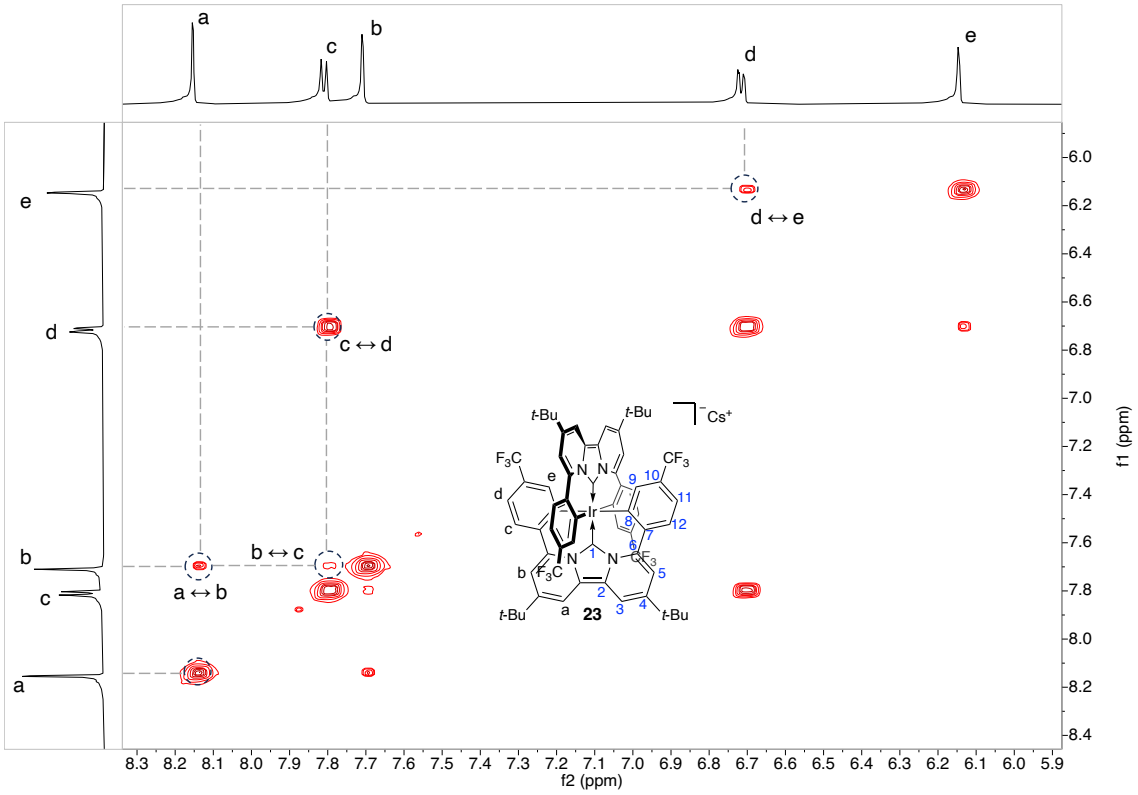

Figure.7.31 ^{1}H-^{1}H COSY chart of complex **23**

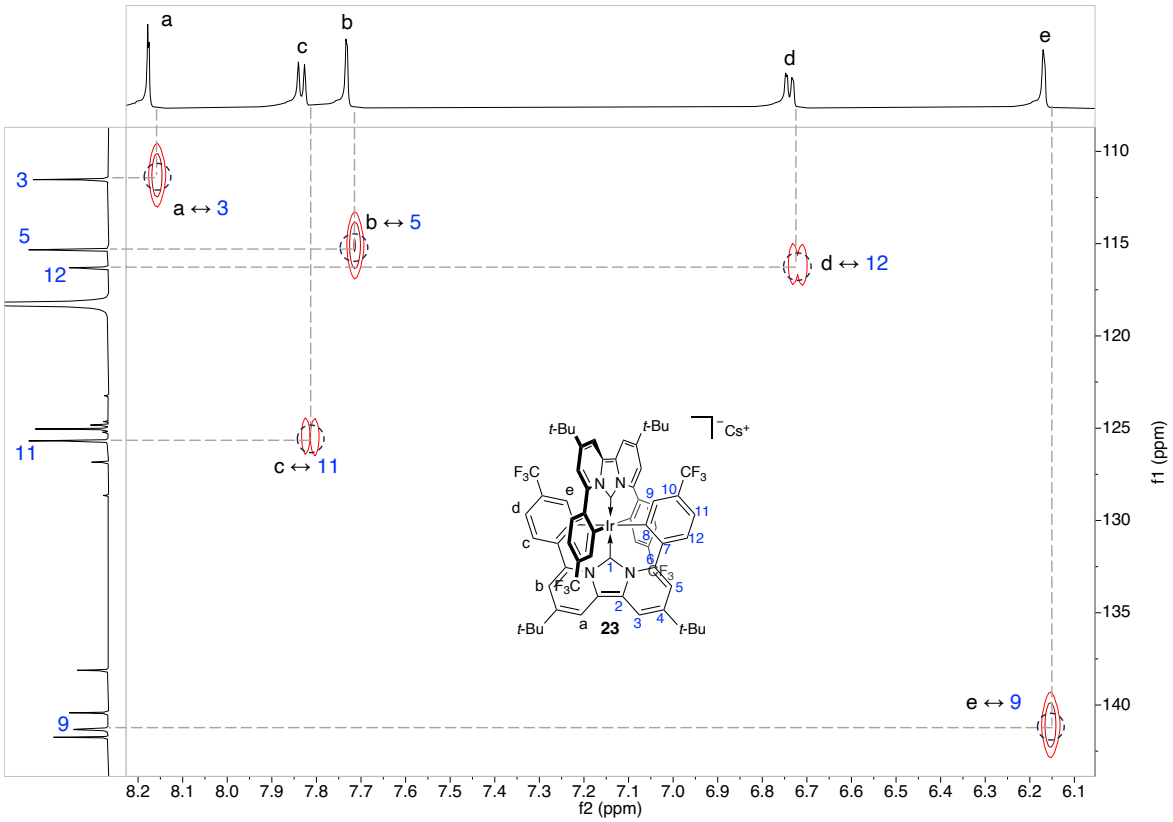

Figure.7.32 ^{1}H-^{13}C HMQC chart of complex **23**

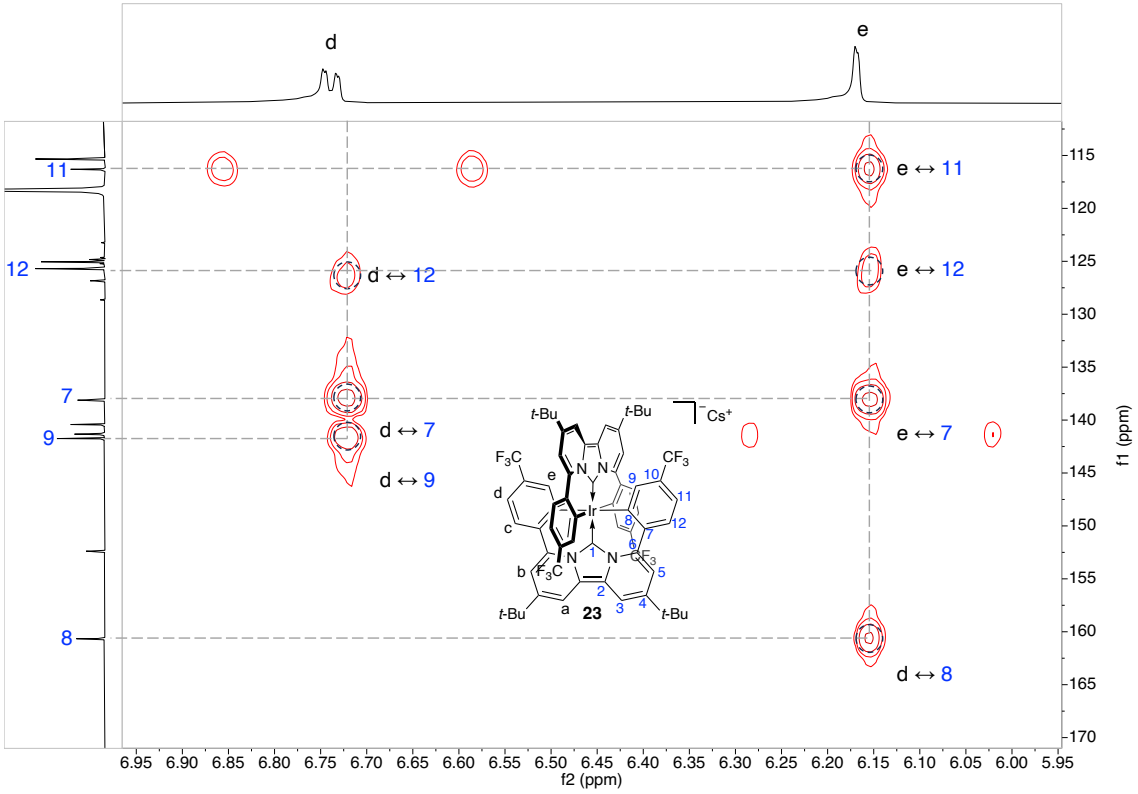

Figure.7.33 ^{1}H-^{13}C HMBC chart of complex **23**

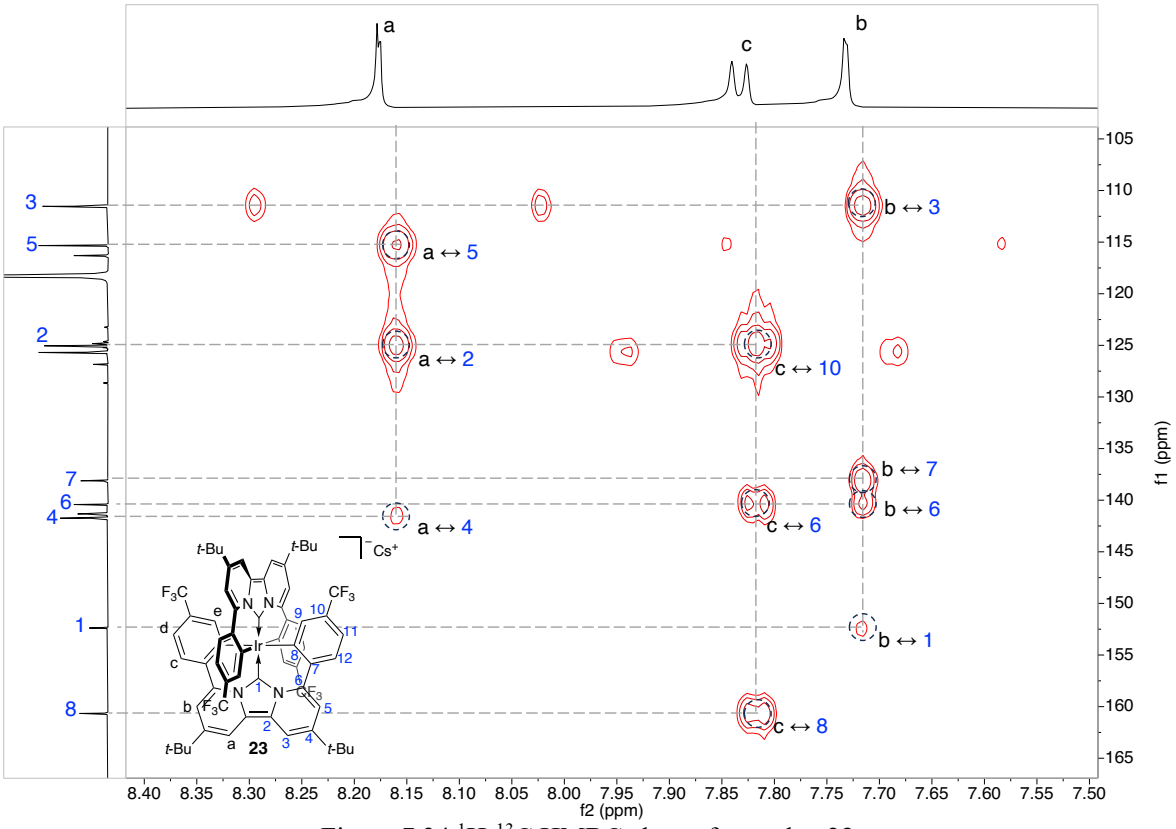

Figure.7.34 ^{1}H-^{13}C HMBC chart of complex **23**

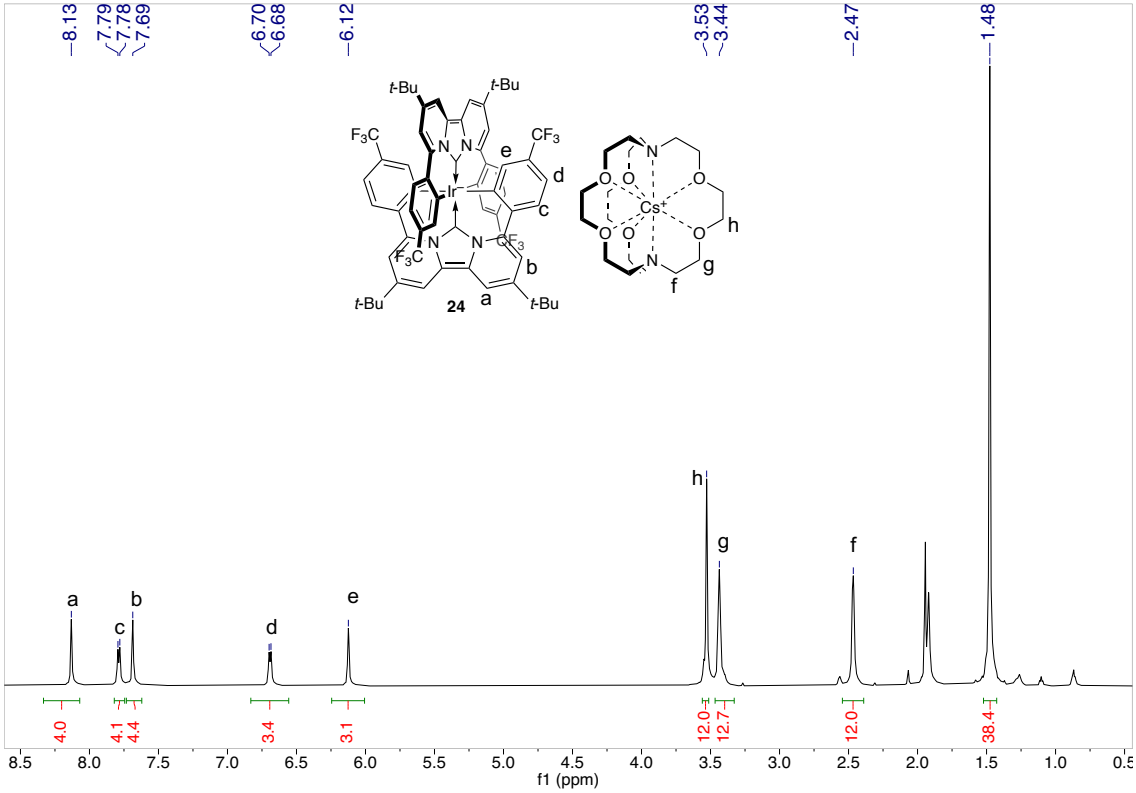

Figure.7.35 ^{1}H NMR chart of complex **24** (600 MHz, CD_3CN)

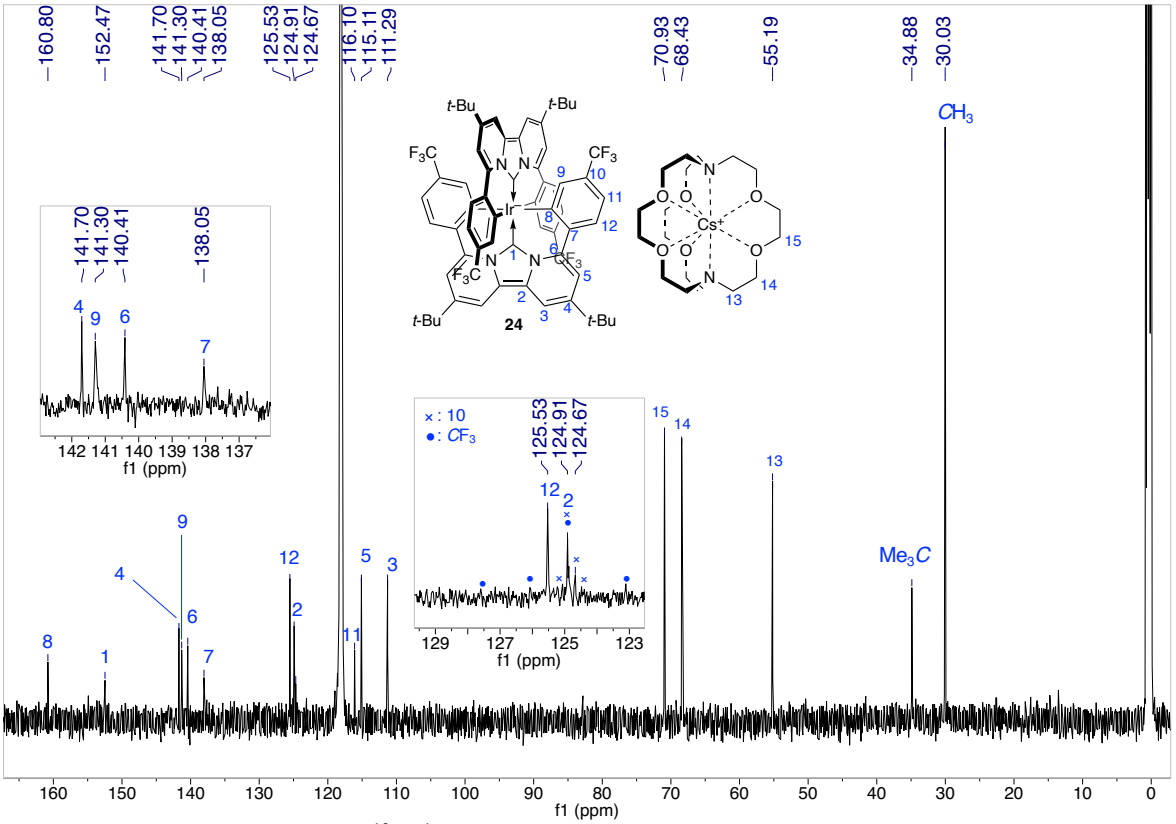

Figure.7.36 $^{13}C\{^{1}H\}$ NMR of complex **24** (150 MHz, CD_3CN)

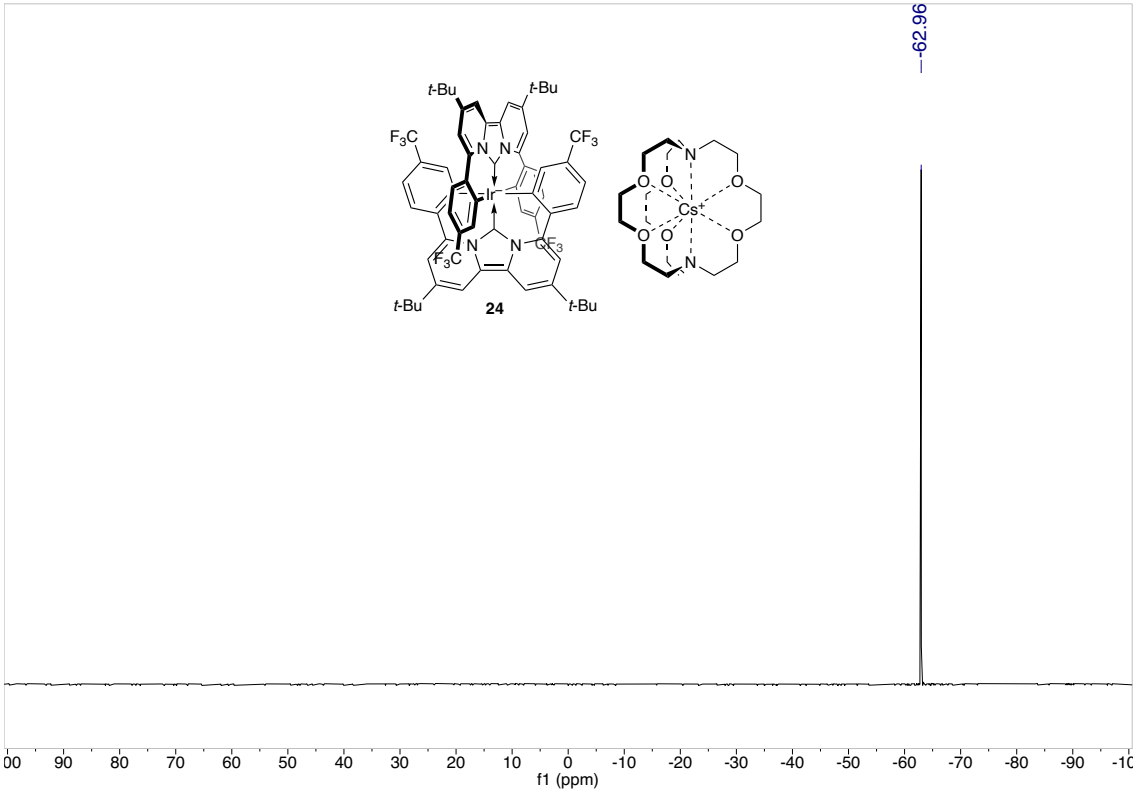

Figure.7.37 ^{19}F NMR of complex **24** (576 MHz, CD_3CN)

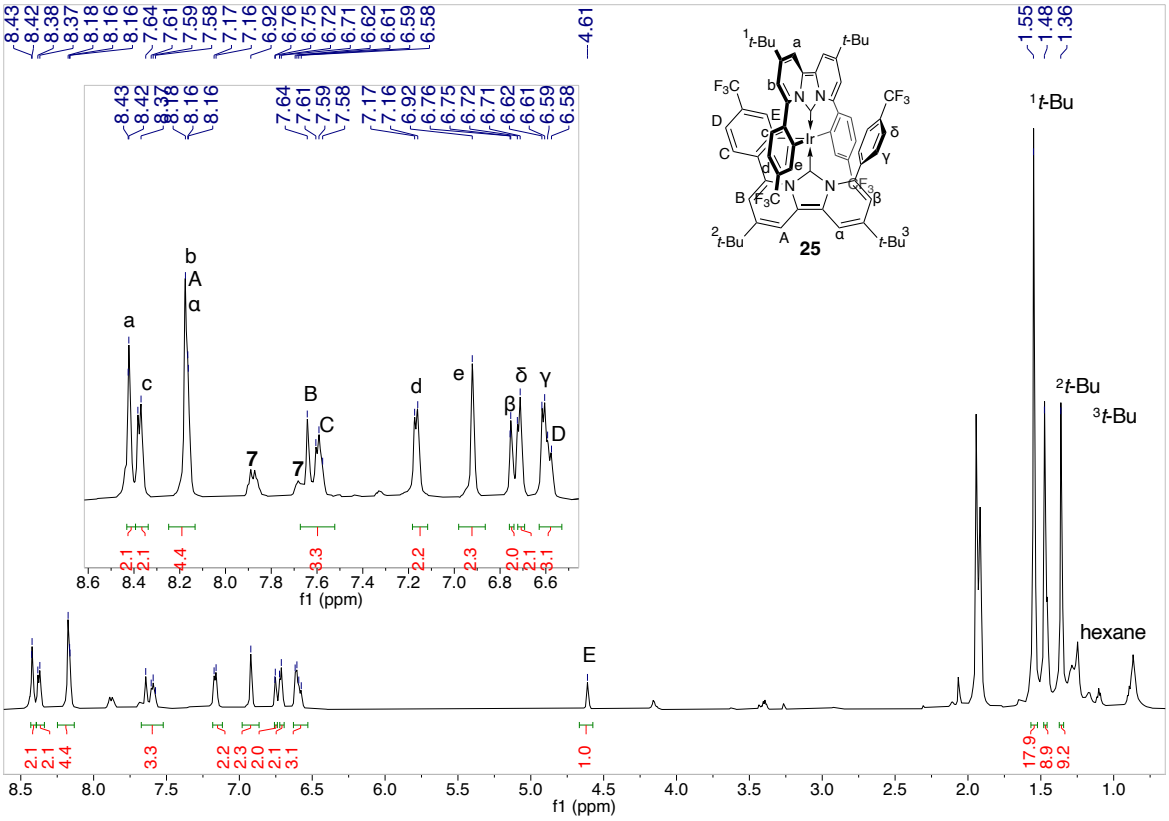

Figure.7.38 ^{1}H NMR chart of complex **25** (500 MHz, CD_3CN)

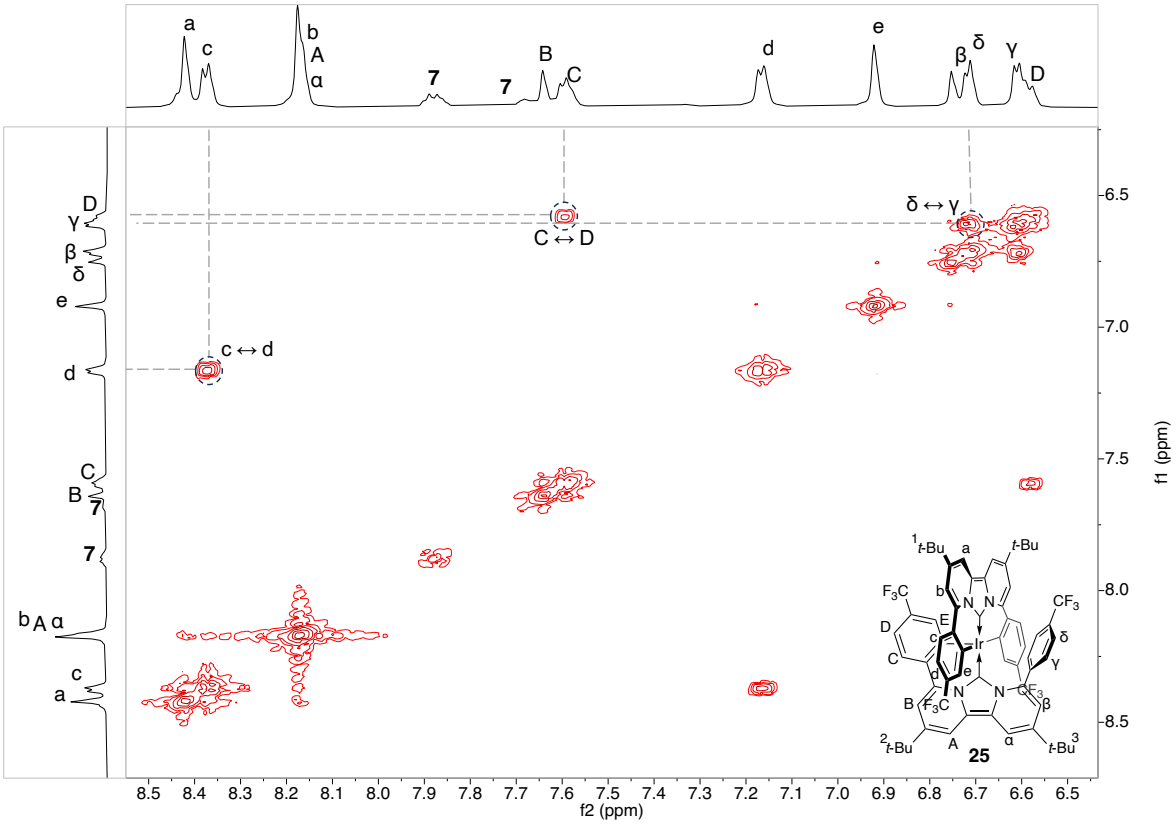

Figure.7.39 ^{1}H-^{1}H COSY chart of complex **25** in CD_3CN

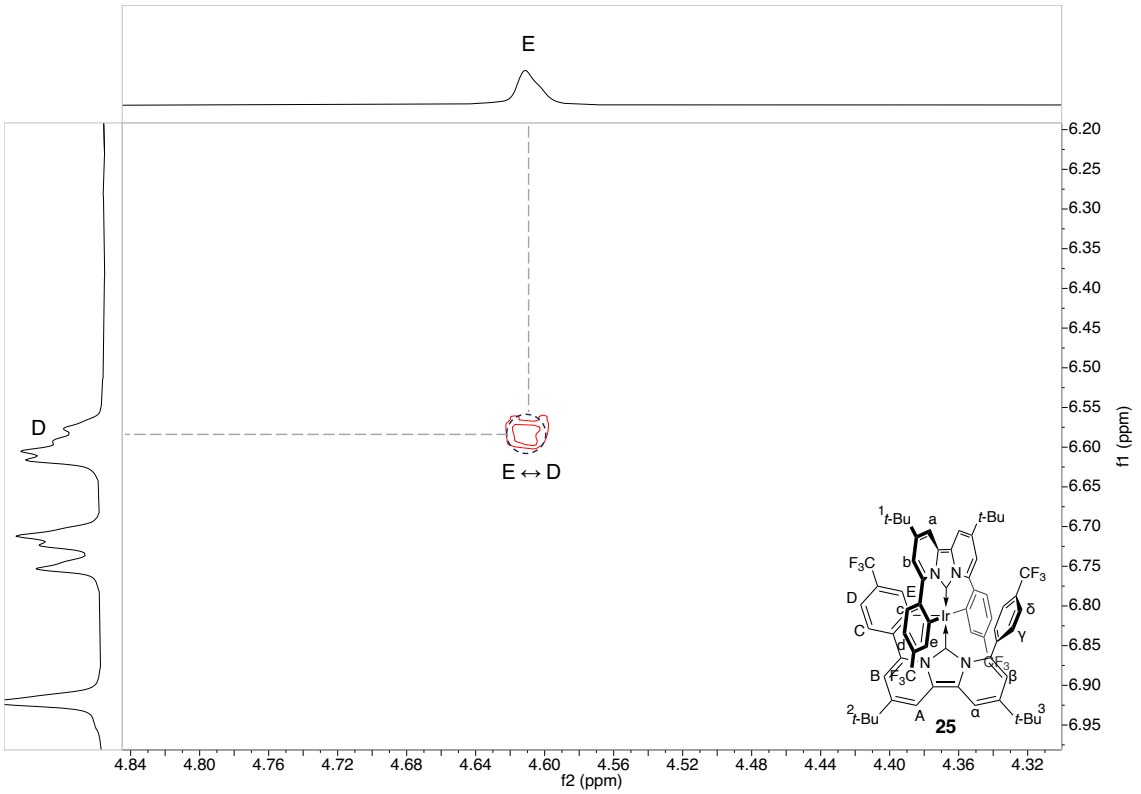

Figure 7.40^{1}H-^{1}H COSY chart of complex **25** in CD_3CN

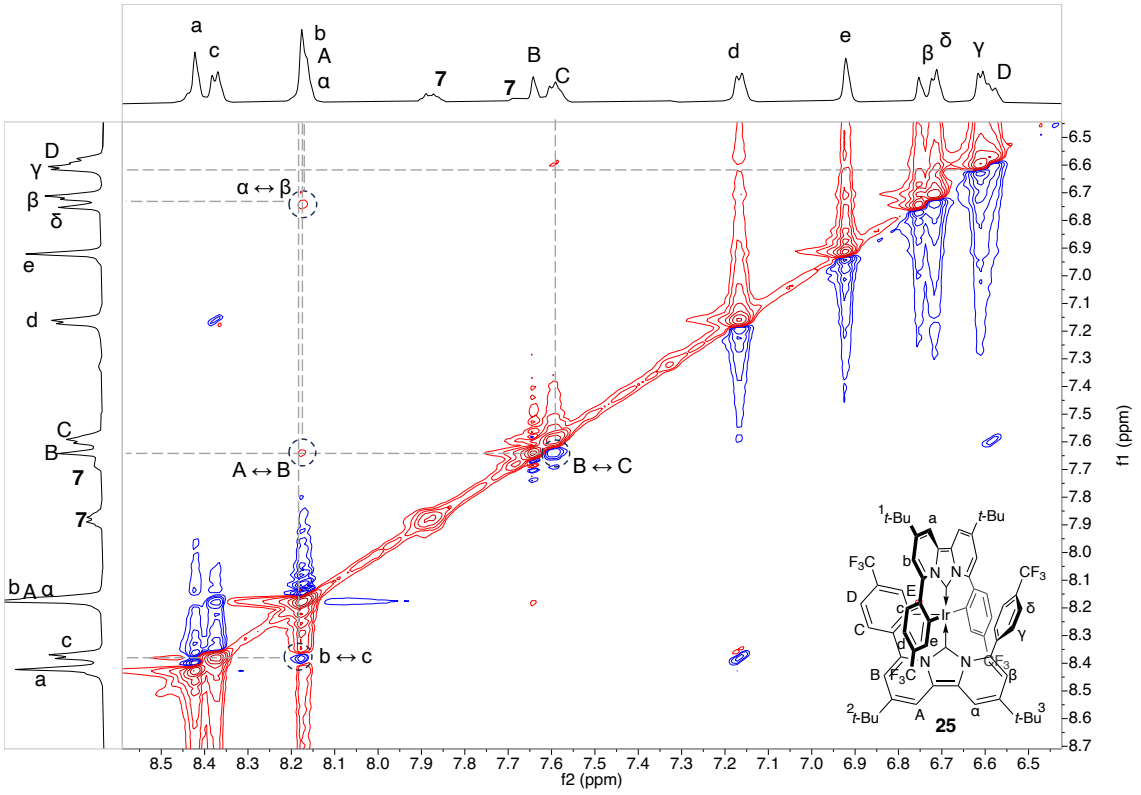

Figure.7.41 ^{1}H-^{1}H NOESY chart of complex **25** in CD_3CN

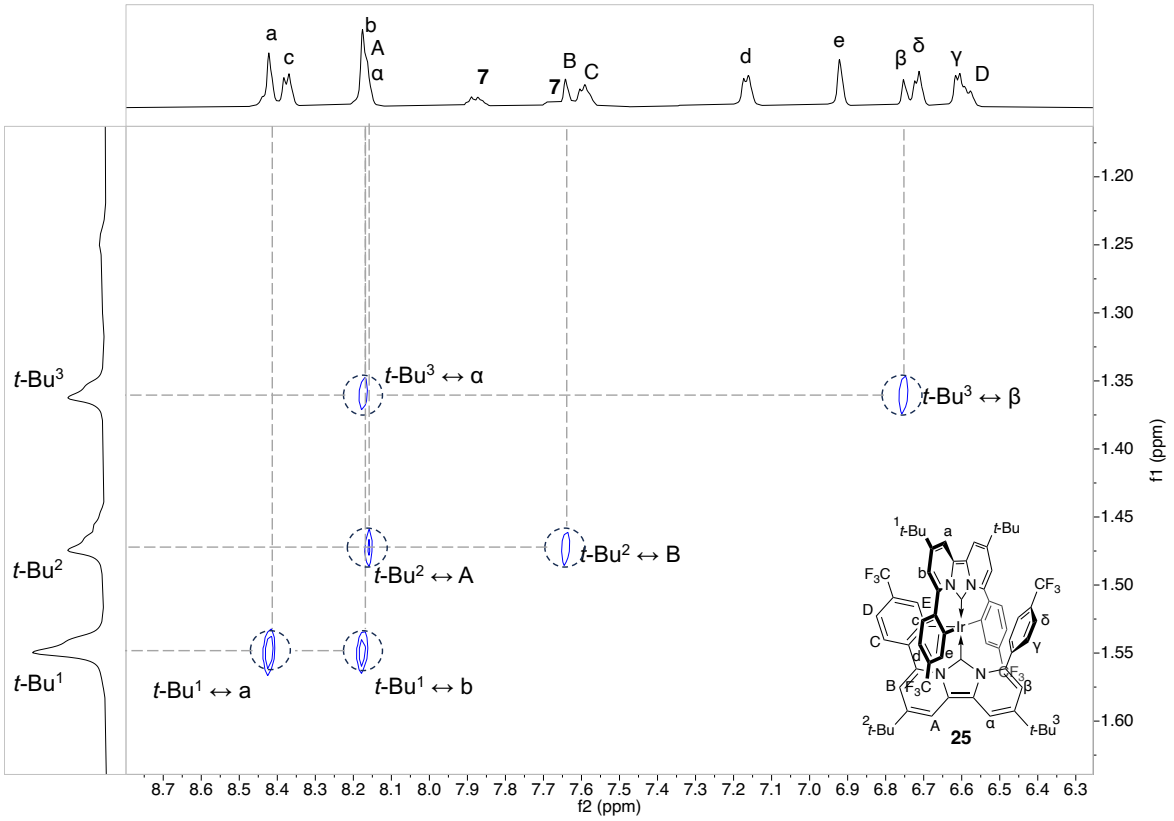

Figure 7.42 ^{1}H-^{1}H NOESY chart of complex **25** in CD_3CN

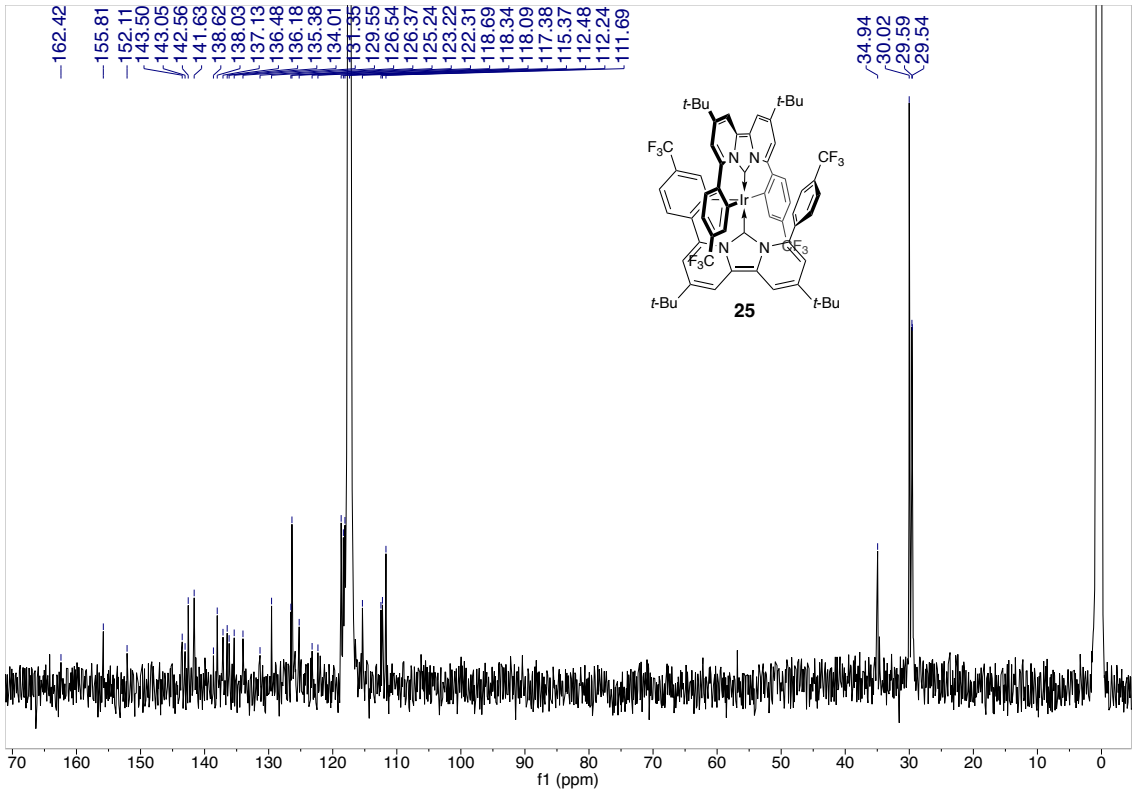

Figure.7.43 ^{13}C{^{1}H} NMR of complex **25** (125 MHz, CD_3CN)

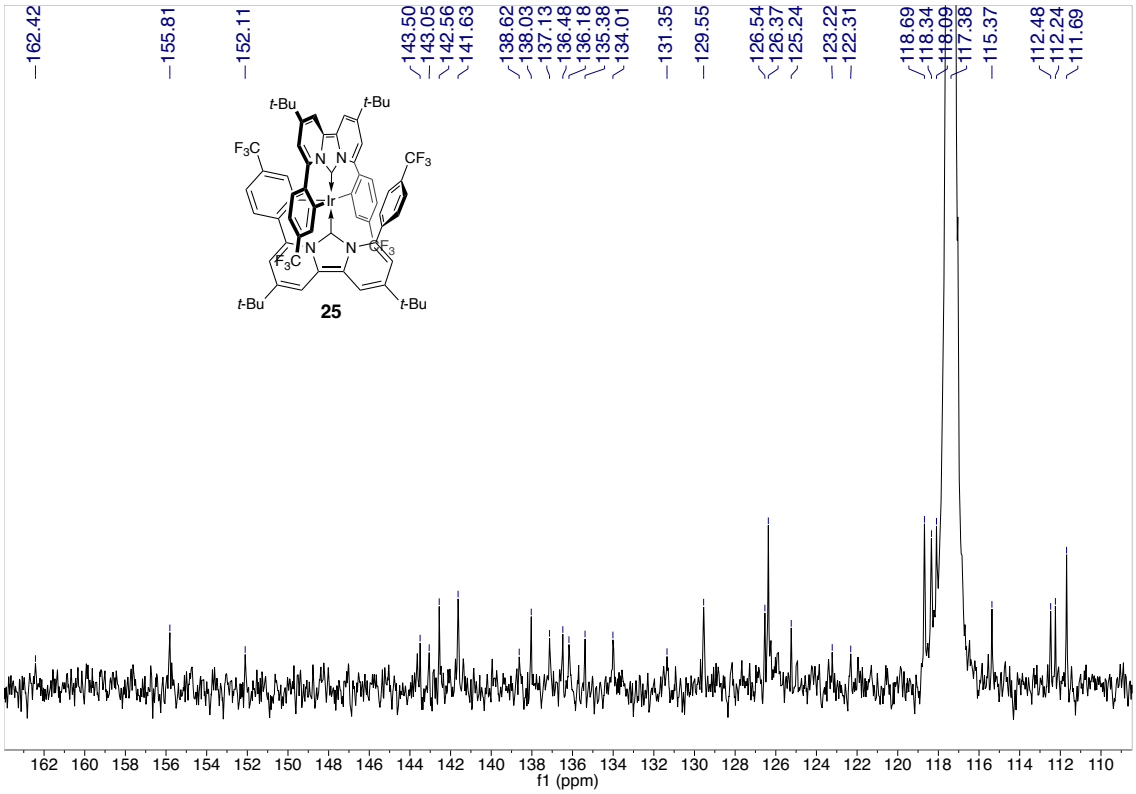

Figure.7.44 Zoomed $^{13}C\{^{1}H\}$ NMR chart of complex **25** (125 MHz, CD_3CN) from 110 to 165 ppm

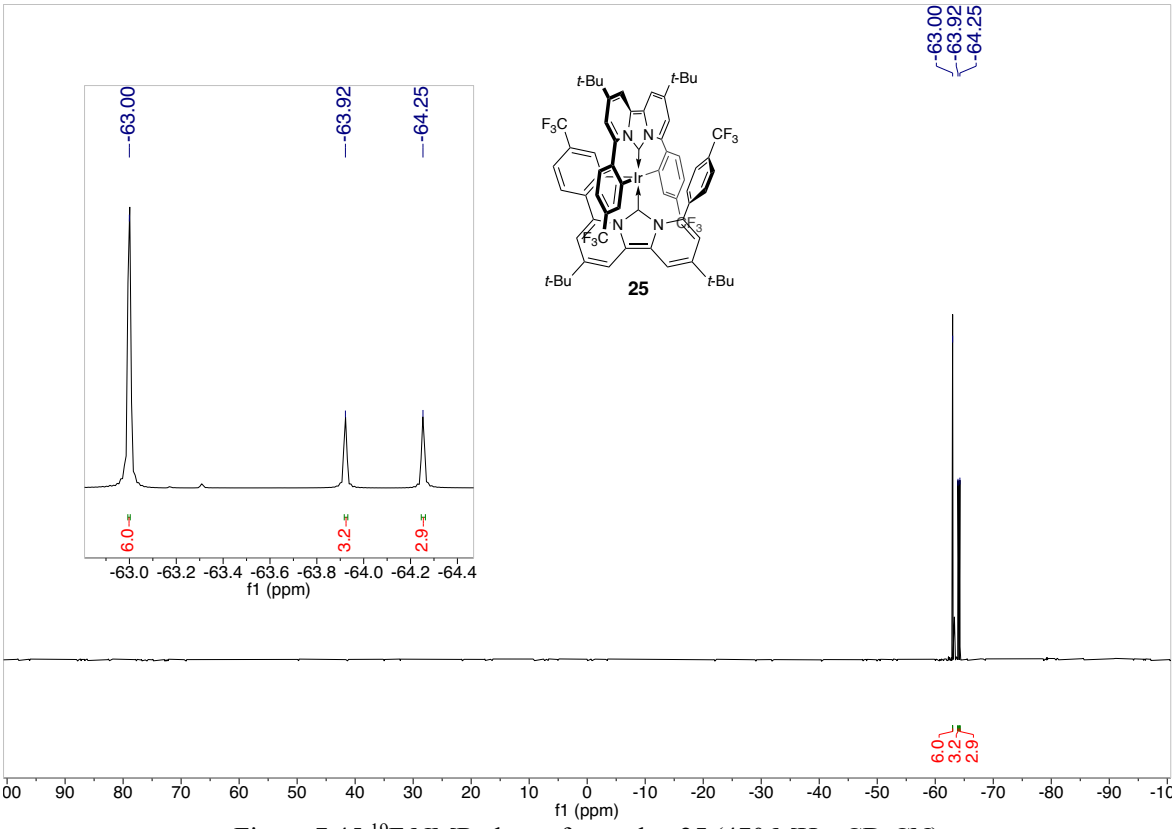

Figure.7.45 ^{19}F NMR chart of complex **25** (470 MHz, CD_3CN)

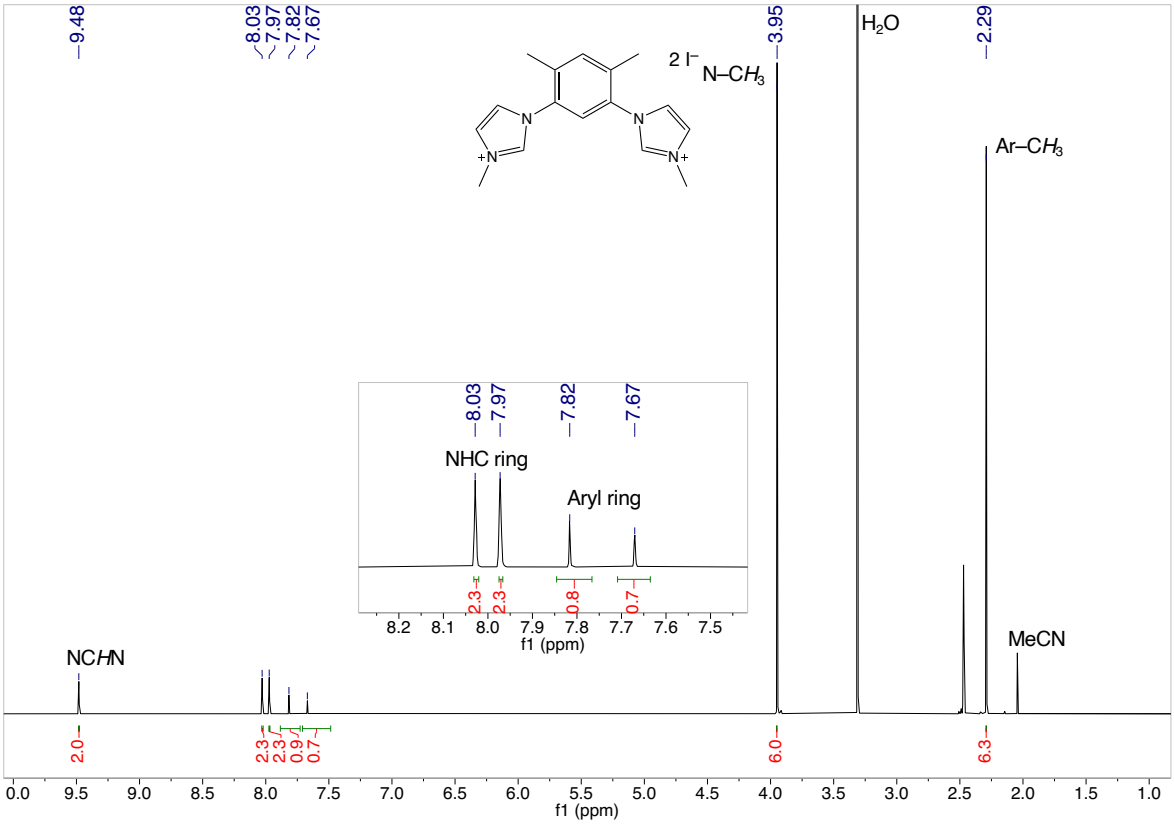

Figure.7.46 ^{1}H NMR chart of 1,3-bis(N-methyl-imidazolium)-4,6-dimethylbenzene diiodide (600 MHz, CD_3CN)

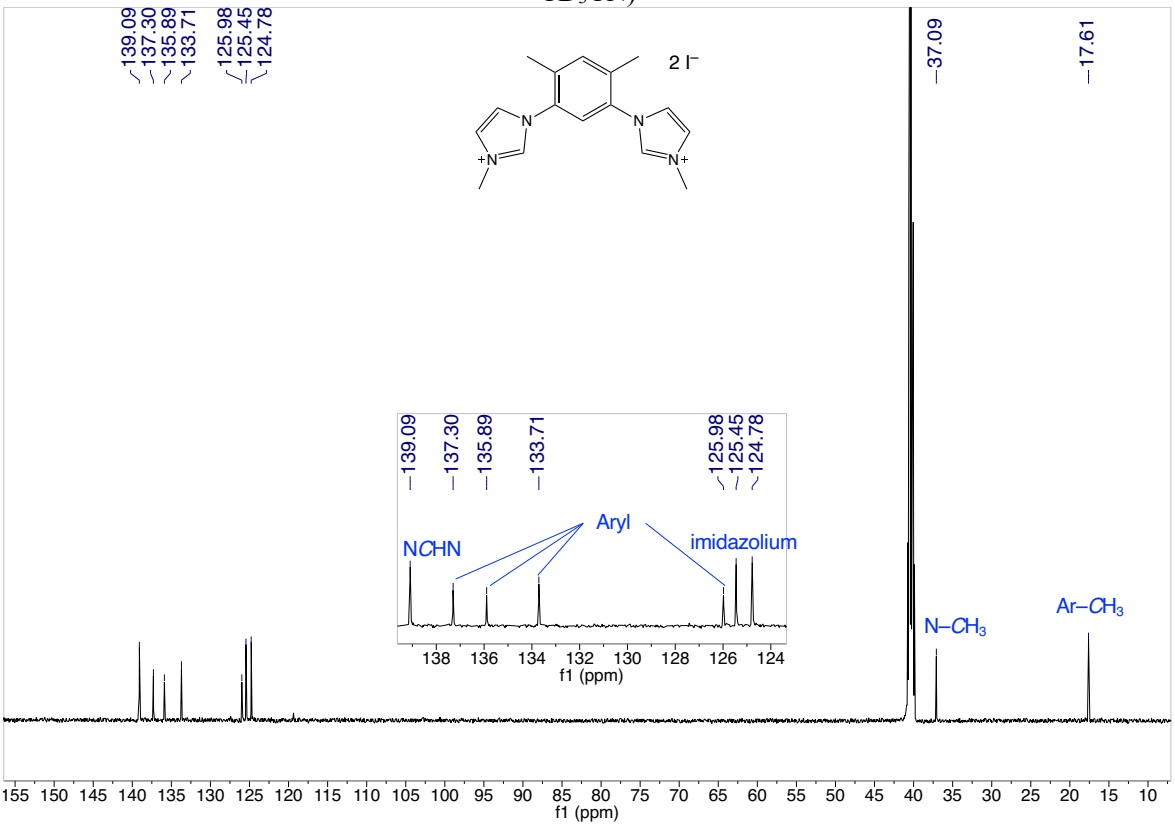

Figure.7.47 ^{13}C{^{1}H} NMR chart of 1,3-bis(N-methyl-imidazolium)-4,6-dimethylbenzene diiodide (150 MHz, DMSO-d_6)

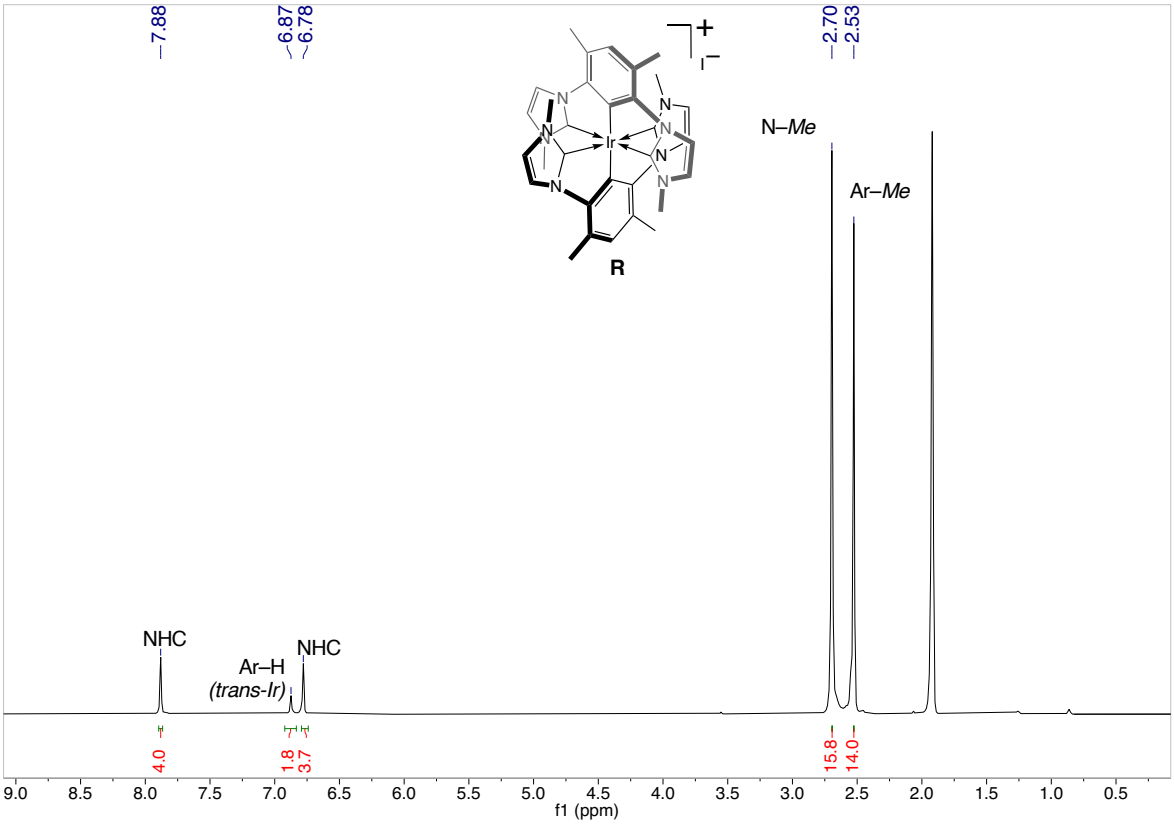

Figure.7.48 ^{1}H NMR chart of complex **R** (600 MHz, CD_3CN)

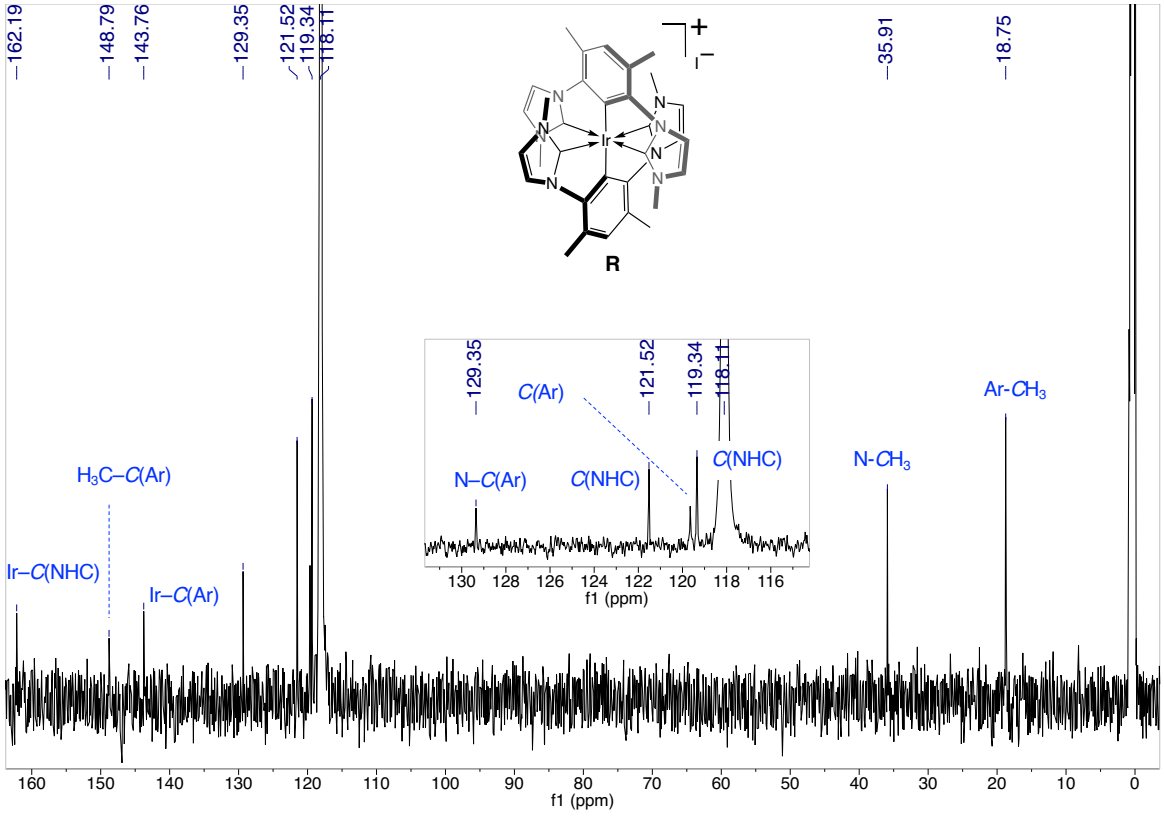

Figure.7.49 $^{13}C\{^{1}H\}$ NMR chart of complex **R** (150 MHz, CD_3CN)

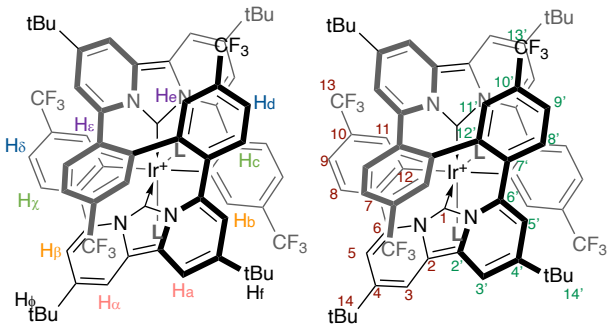

Chart 7.1 numbering schemes of the tetradentate ligand on the iridium

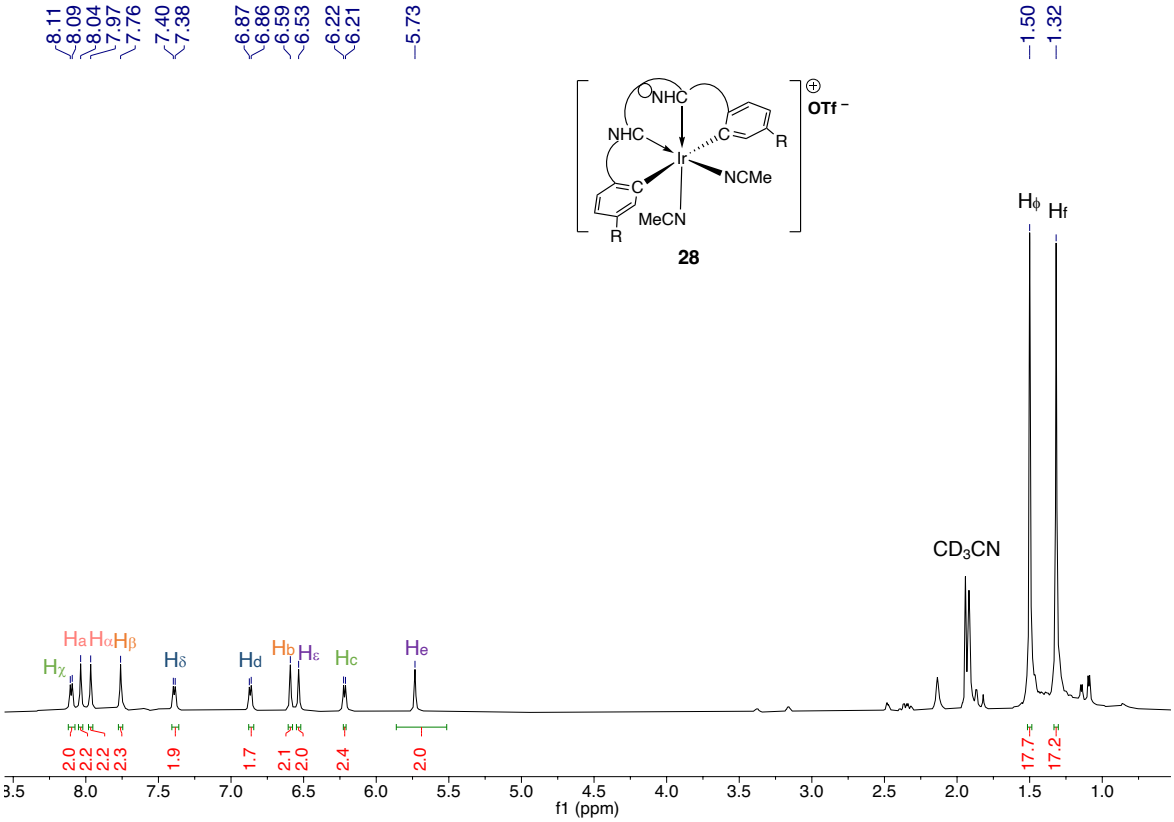

Figure 7.50 ^{1}H NMR chart of complex **28** (X^{-} = OTf) (600 MHz, acetonitrile-d_3)

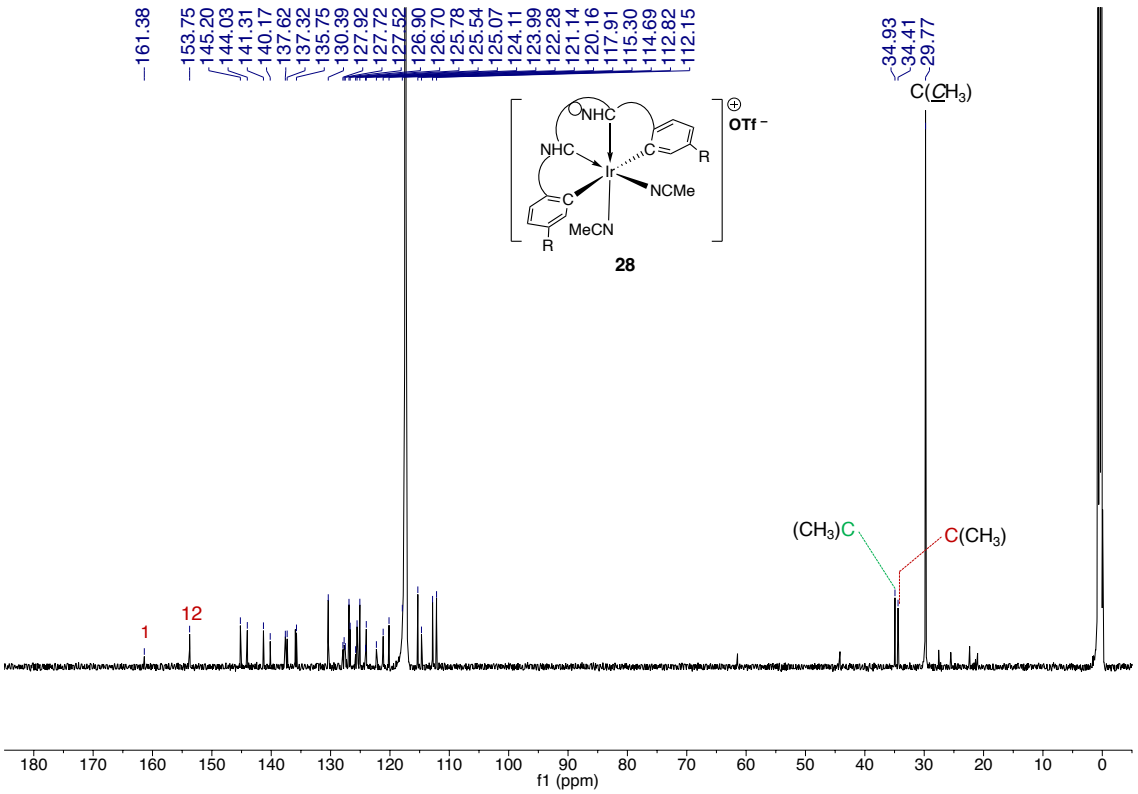

Figure 7.51 $^{13}C\{^{1}H\}$ NMR chart of complex **28** (X^- = OTf) (151 MHz, Acetonitrile-d3)

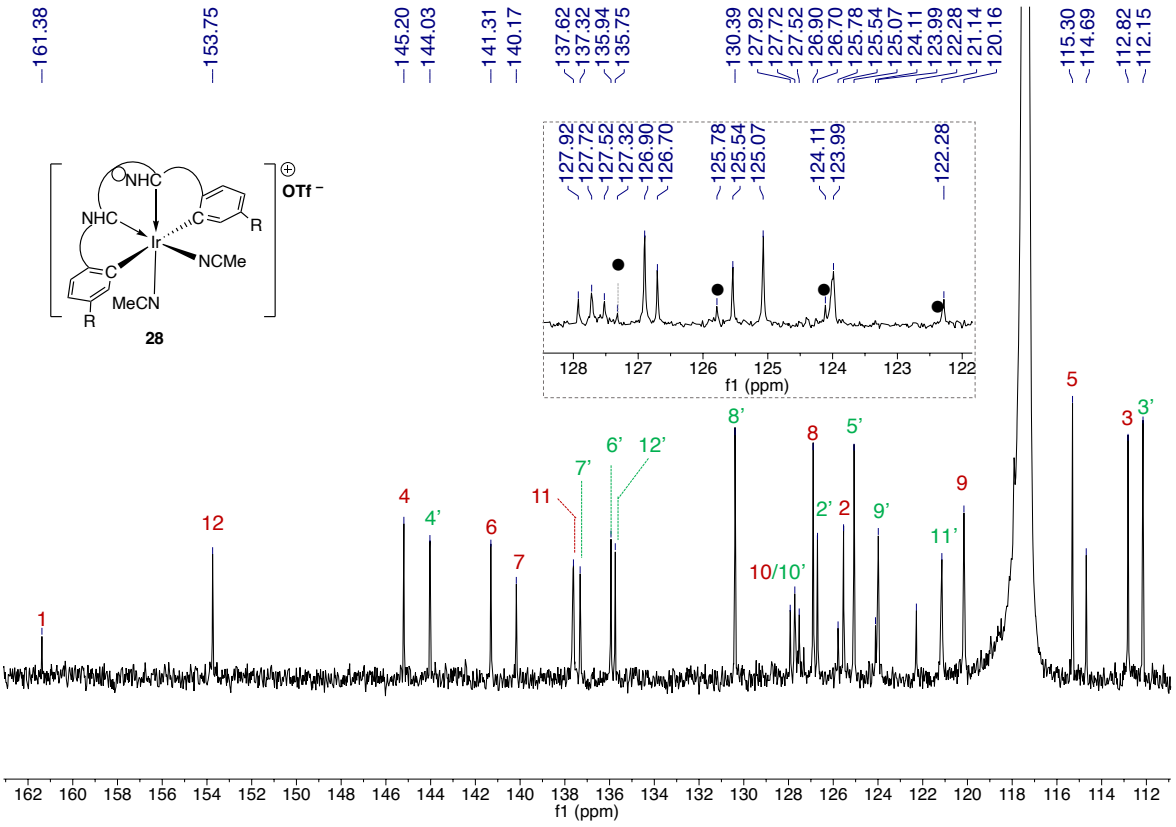

Figure 7.52 $^{13}C\{^{1}H\}$ NMR chart of complex **28** (X^- = OTf) (151 MHz, Acetonitrile-d3), ● = CF_3

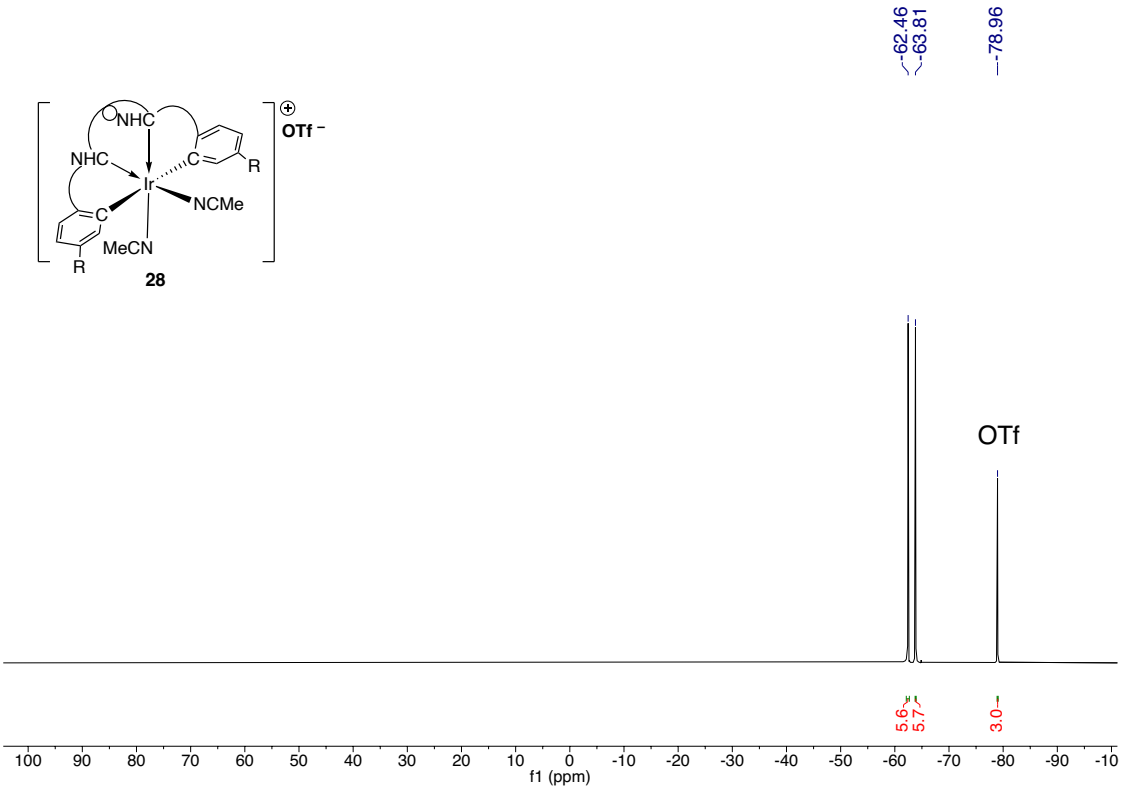

Figure 7.53 ^{19}F NMR chart of complex **28** (A^- = OTf) (565 MHz, acetonitrile-d_3)

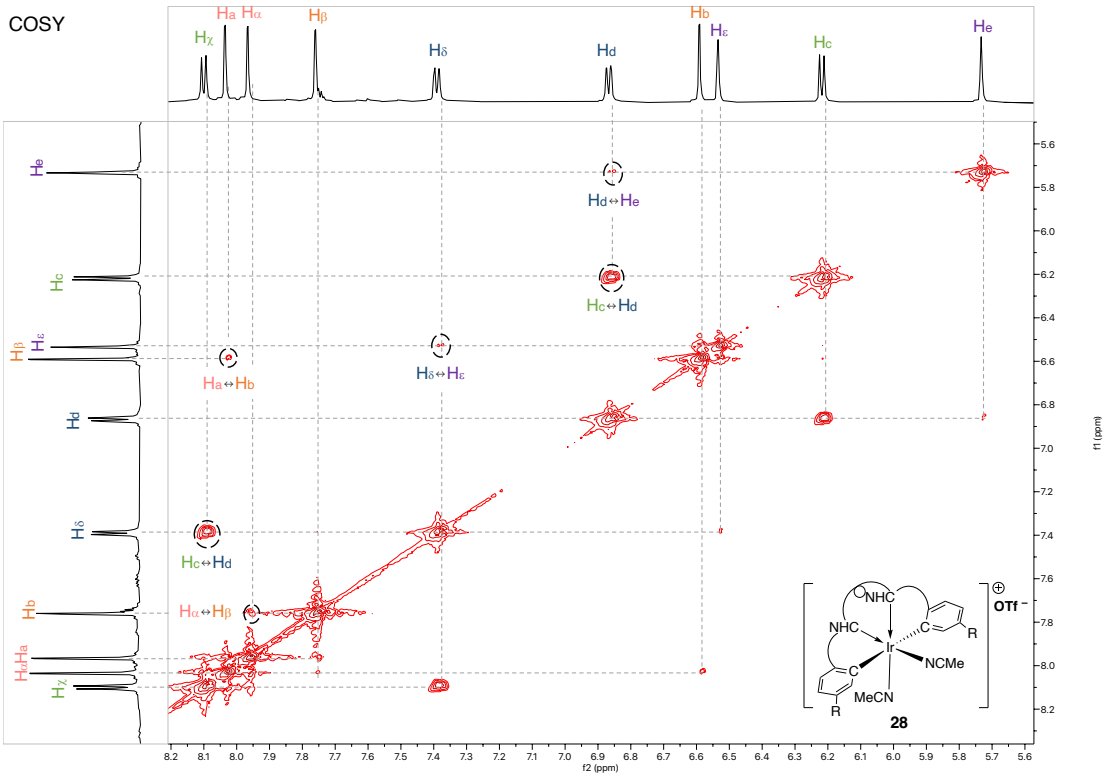

Figure 7.54 COSY chart of complex **28**

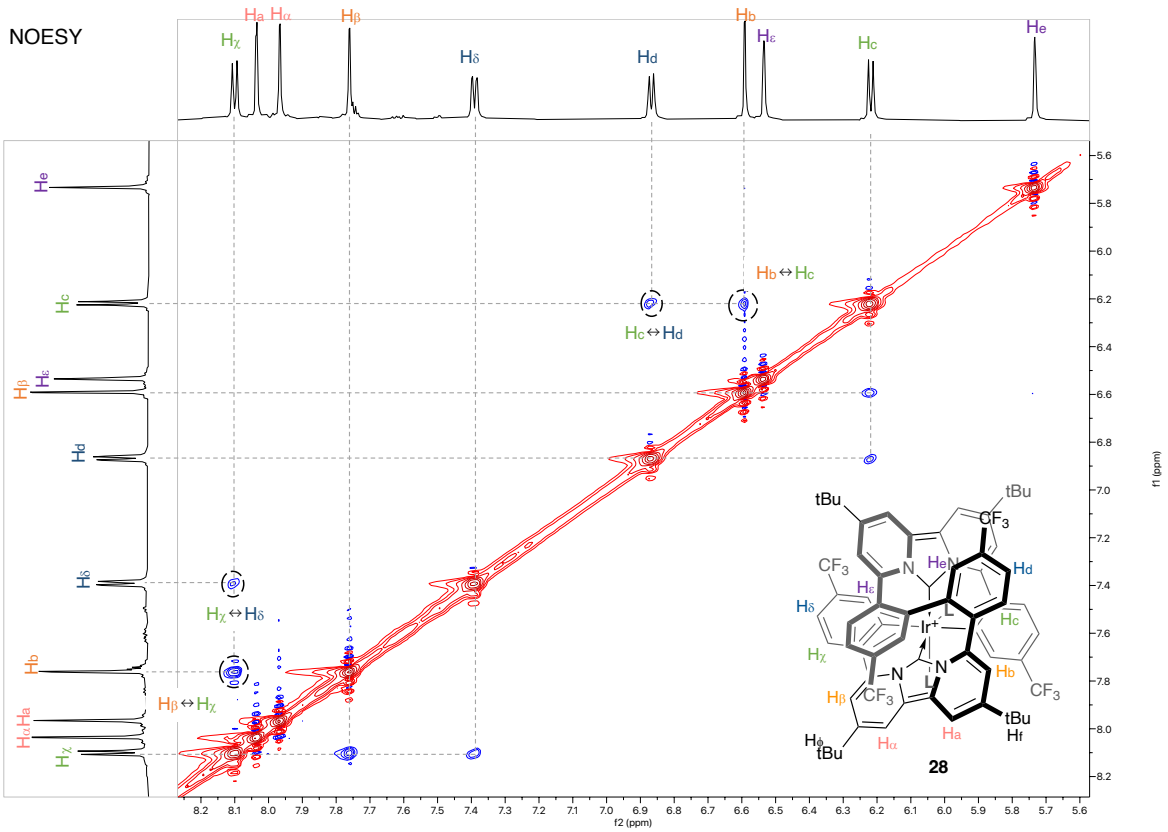

Figure 7.55 NOESY chart of complex **28**

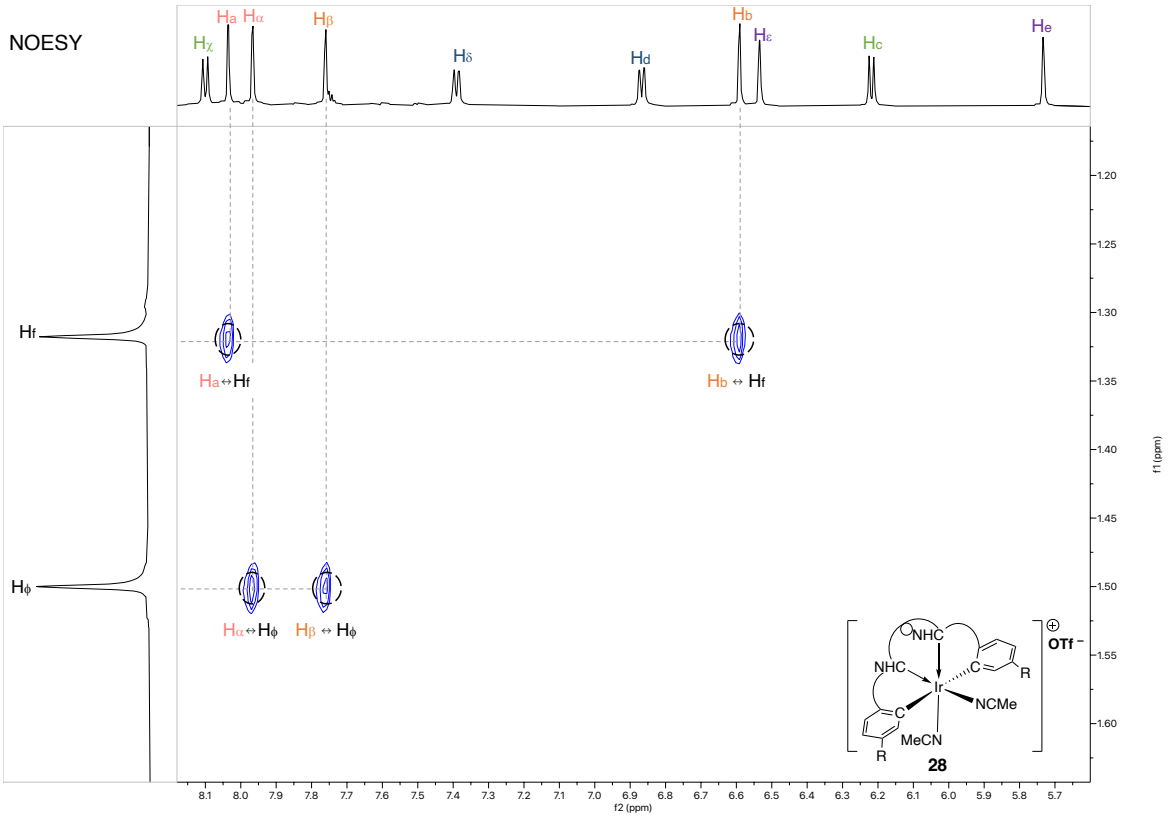

Figure 7.56 NOESY chart of complex **28**

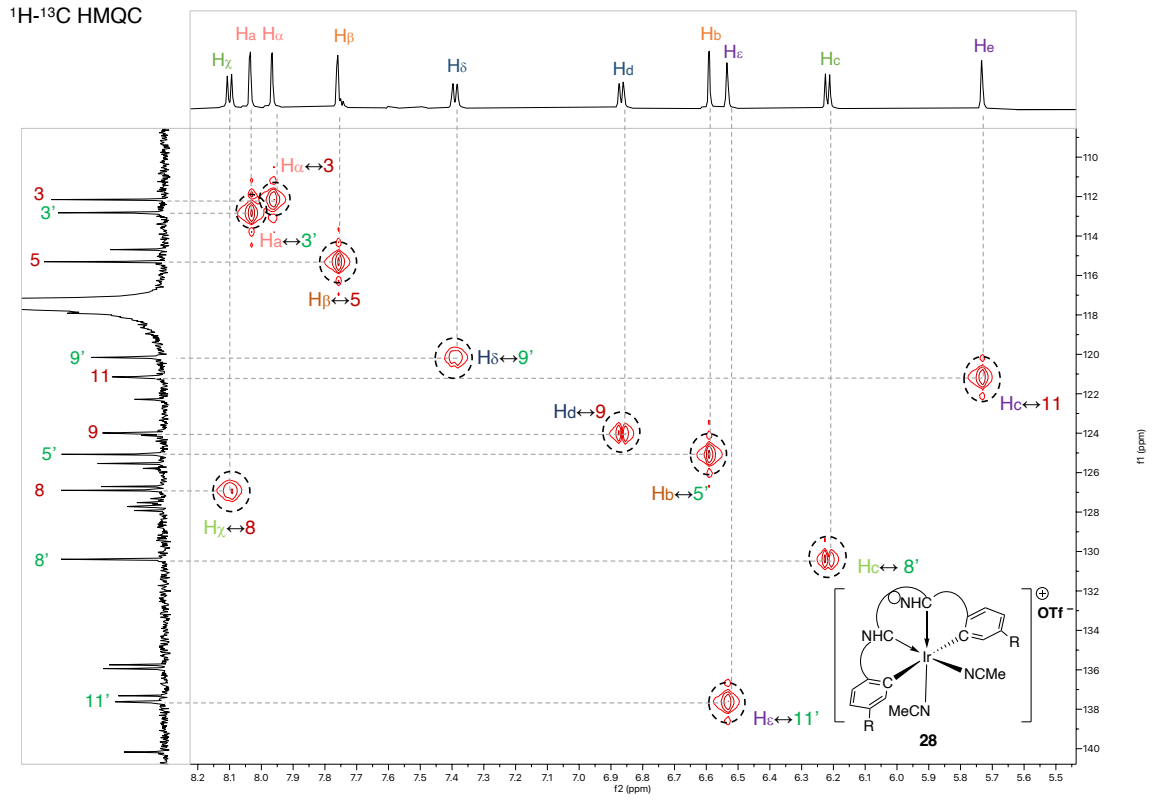

Figure 7.57 ^{1}H–^{13}C HMQC chart of complex **28**

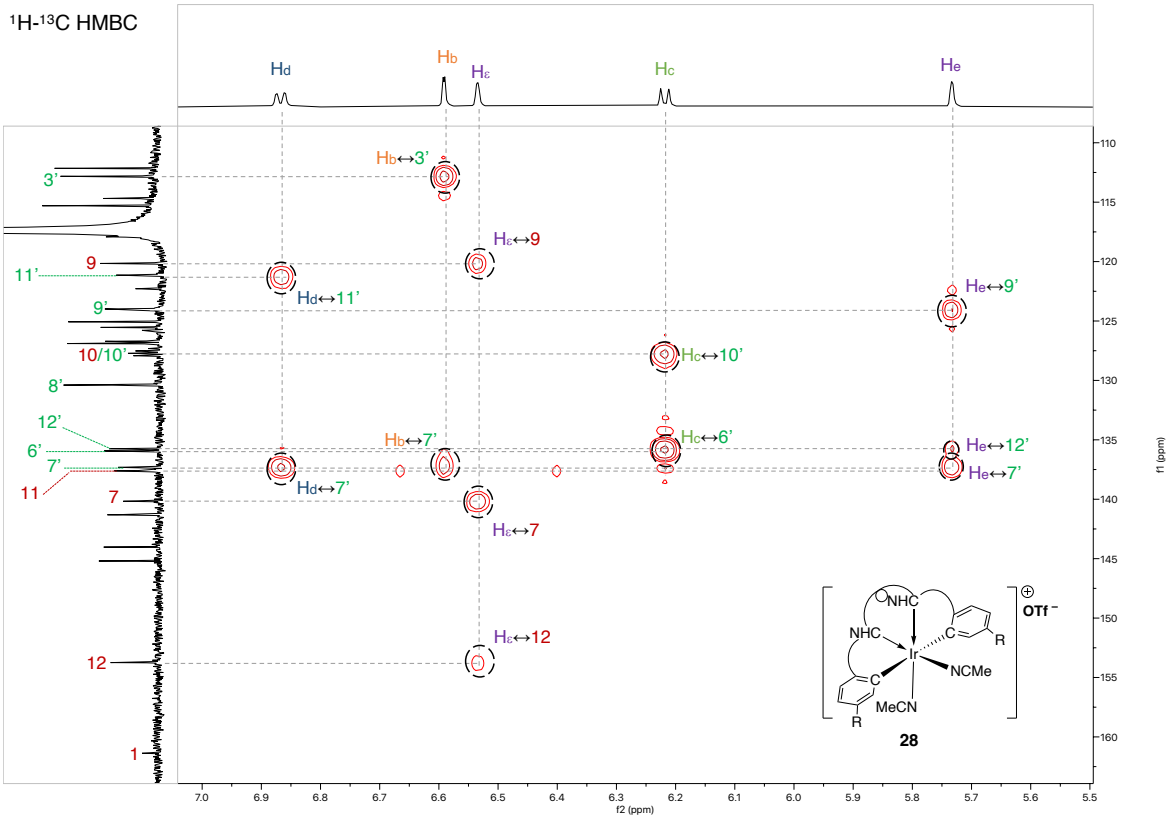

Figure 7.58 ^{1}H–^{13}C HMBC chart of complex **28**

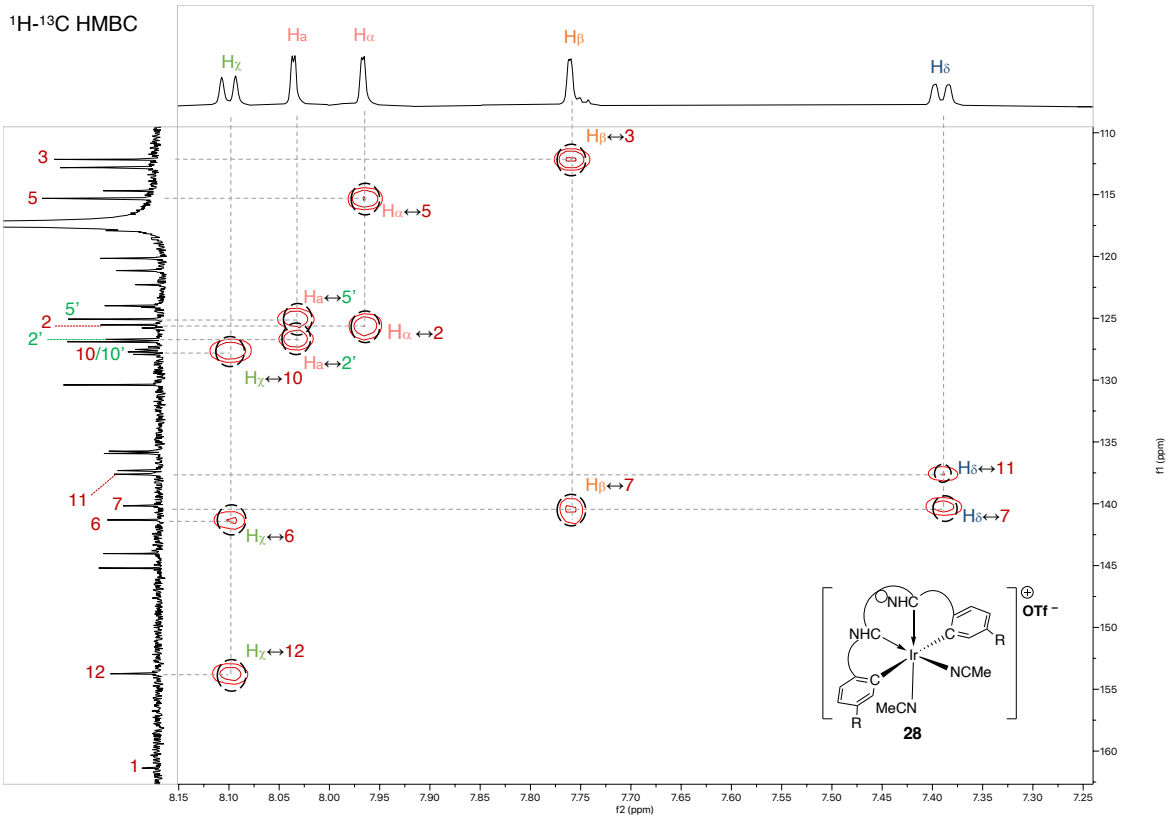

Figure 7.59 ^{1}H–^{13}C HMBC chart of **28**

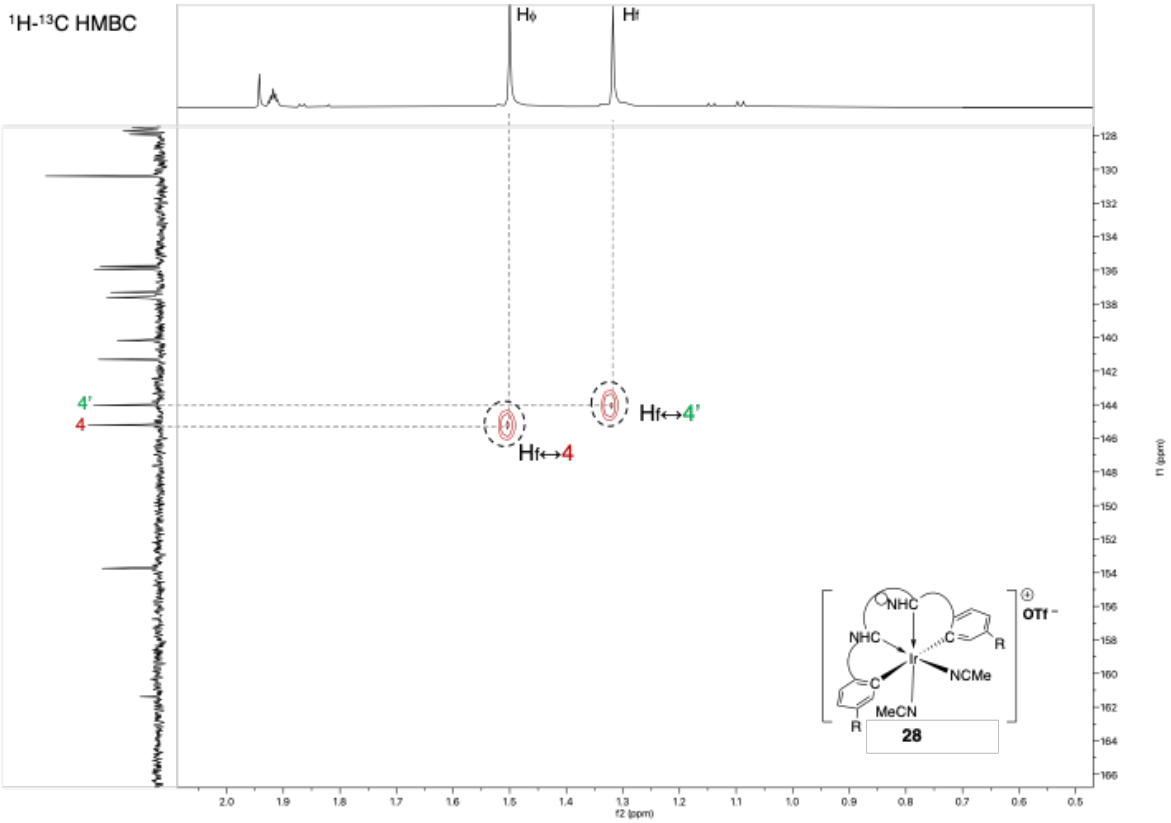

Figure 7.60 ^{1}H–^{13}C HMBC chart of complex **28**

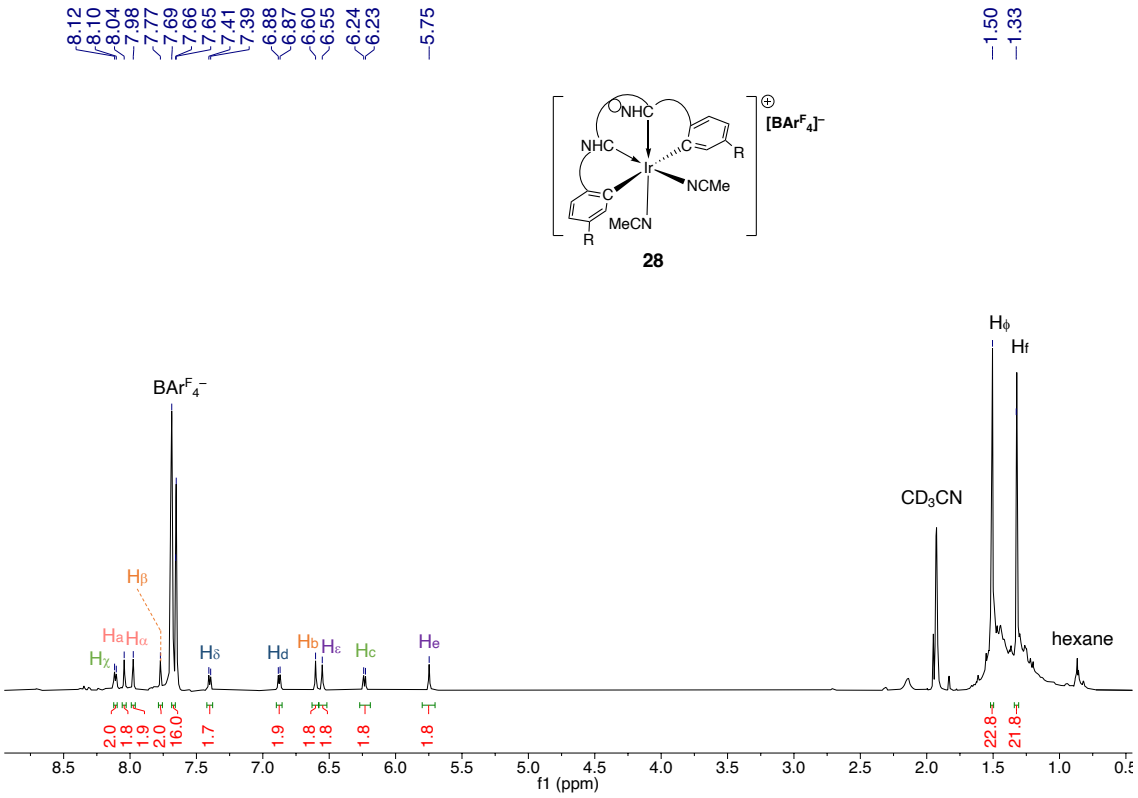

Figure 7.61 ^{1}H NMR chart of complex **28** (X$^-$ = BAr$^F_4$) (600 MHz, acetonitrile-d_3)

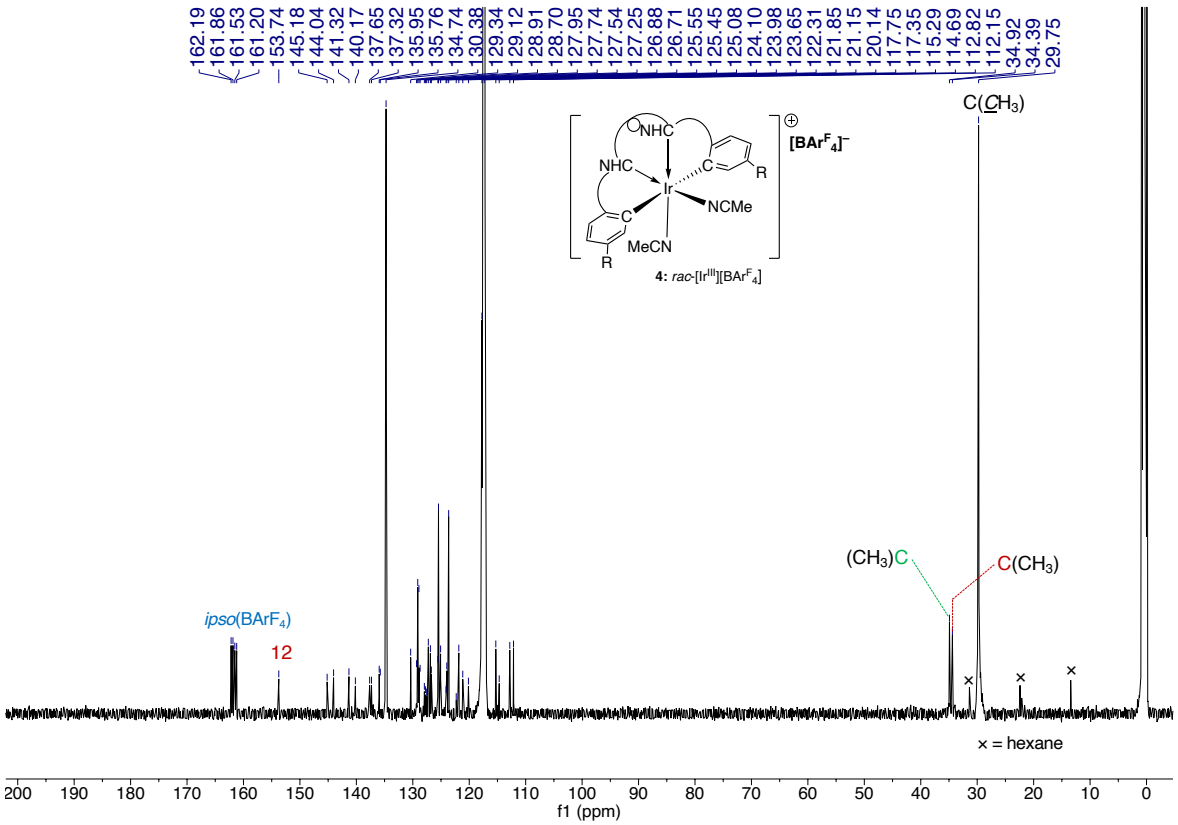

Figure SA1 ^{13}C{^{1}H} NMR chart of complex **28** (X$^-$ = BAr$^F_4$) (151 MHz, Acetonitrile-d3)

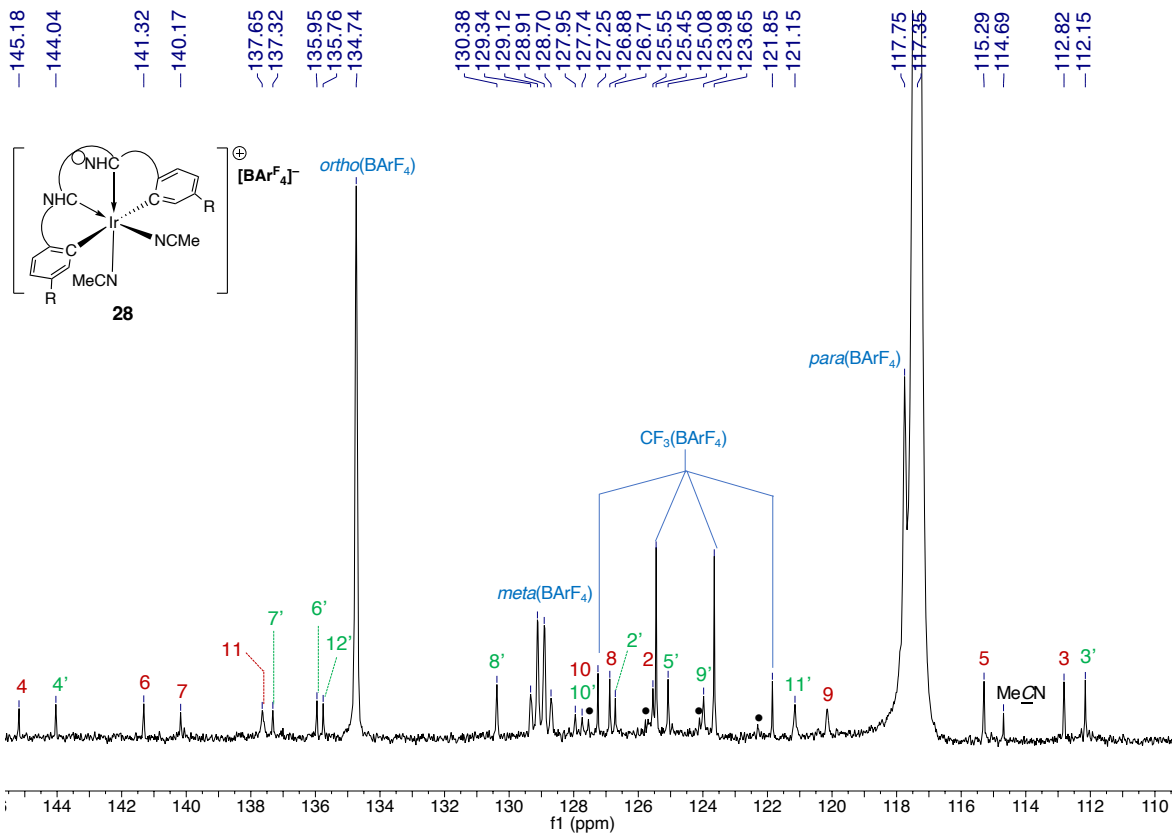

Figure 7.62 $^{13}C\{^1H\}$ NMR chart of complex **28** (X^- = BAr^F_4) (151 MHz, Acetonitrile-d3) ● = CF_3

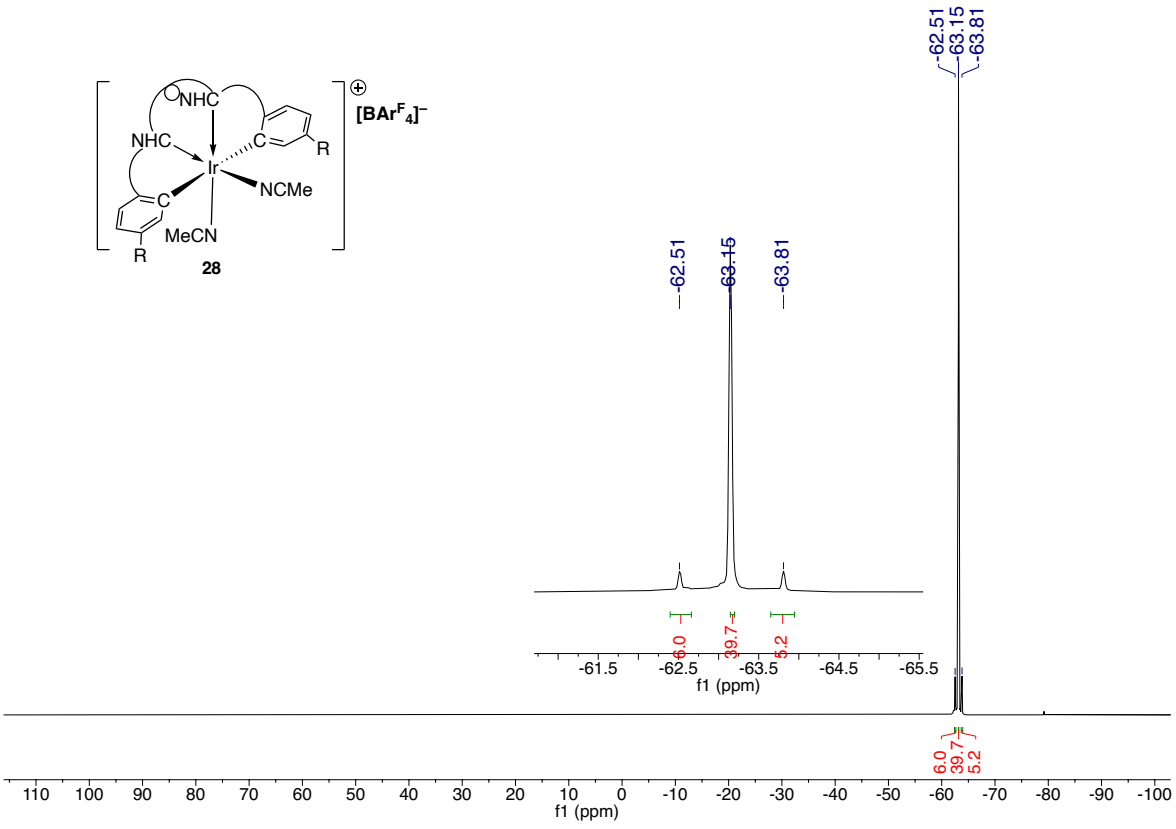

Figure.7.63 ^{19}F NMR chart of complex **28** (X^- = BAr^F_4) (565 MHz, acetonitrile-d_3)

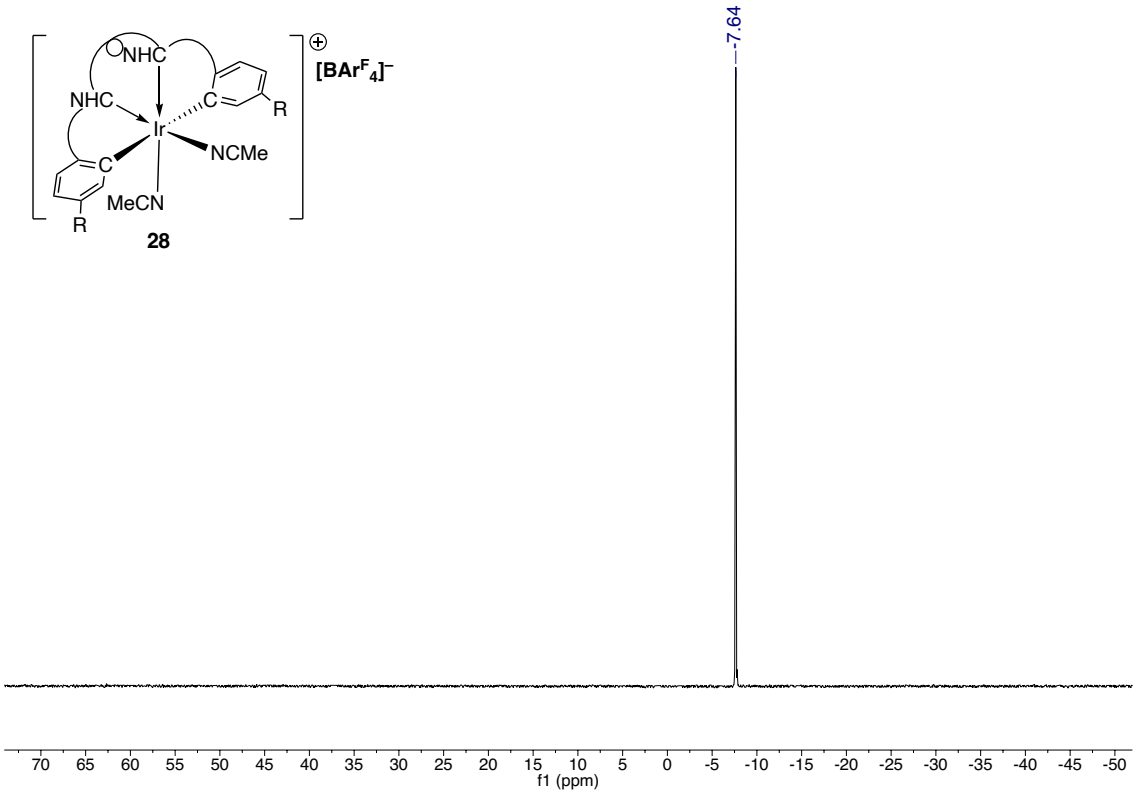

Figure SA2 $^{11}B\{^1H\}$ NMR chart of complex **28** ($X^- = BAr^F_4$) (193 MHz, Acetonitrile-*d3*)

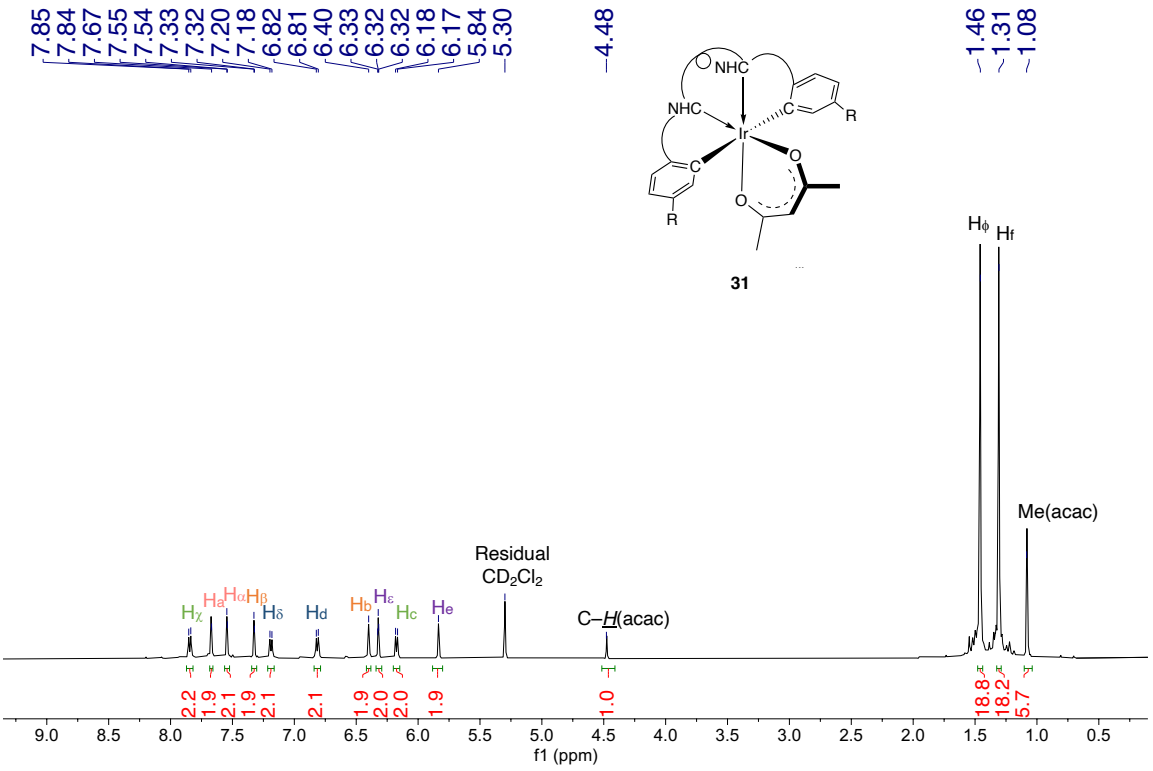

Figure 7.64 ^1H NMR chart of complex **31** (500 MHz, dichloromethane-d_2)

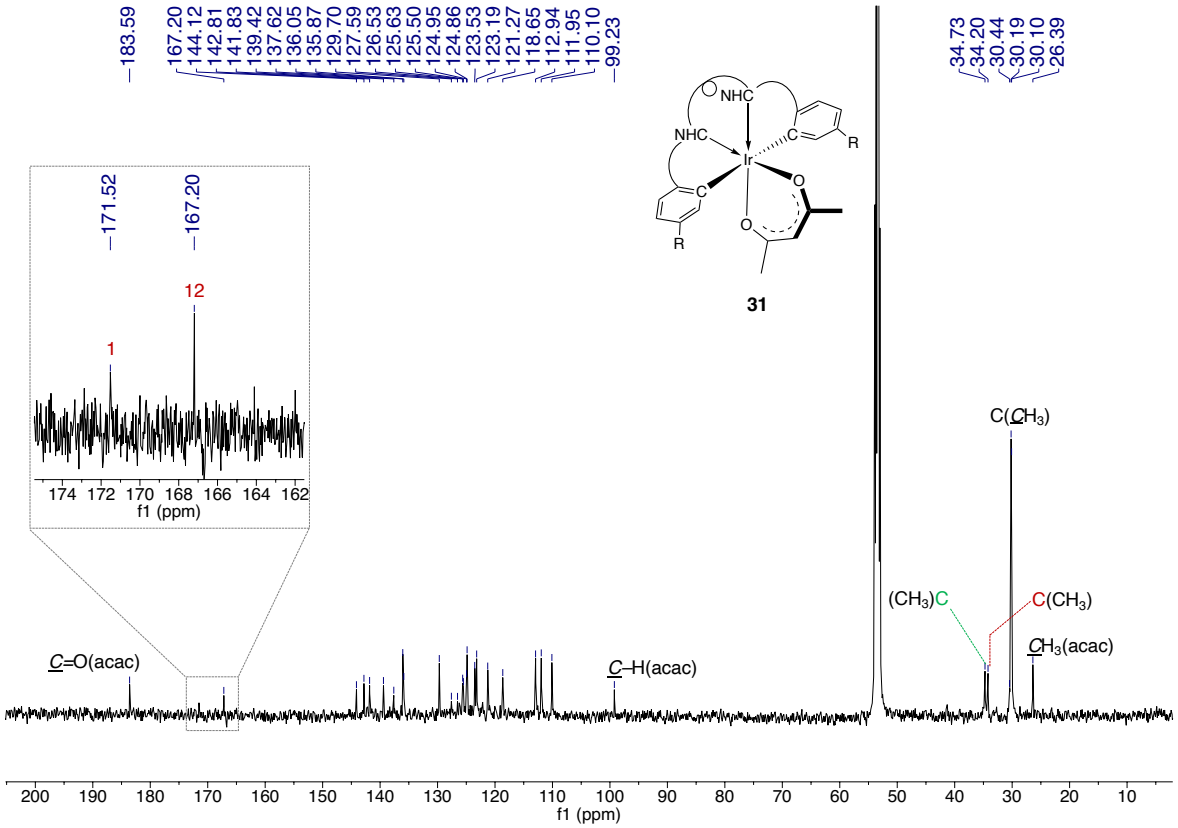

Figure 7.65 $^{13}C\{^{1}H\}$ NMR chart of complex **31** (125 MHz, dichloromethane-d_2)

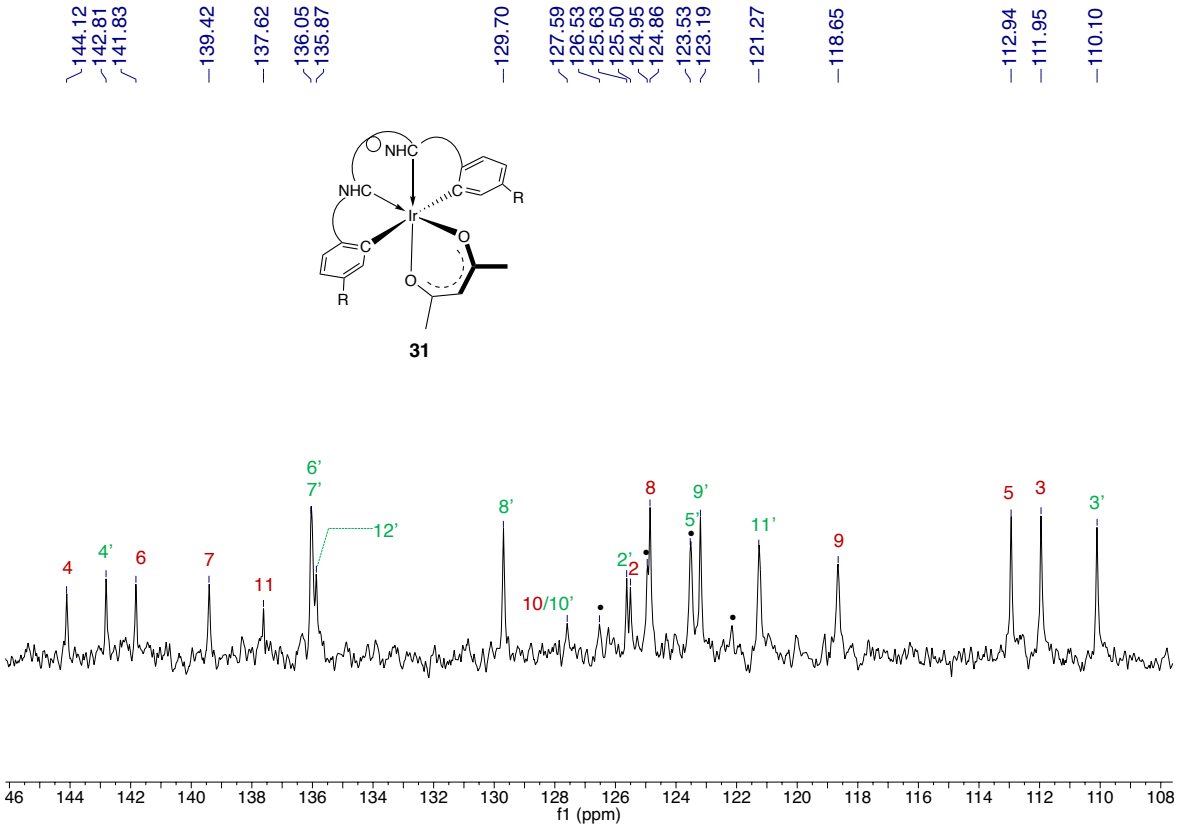

Figure 7.66 $^{13}C\{^{1}H\}$ NMR chart of complex **31** (125 MHz, dichloromethane-d_2)

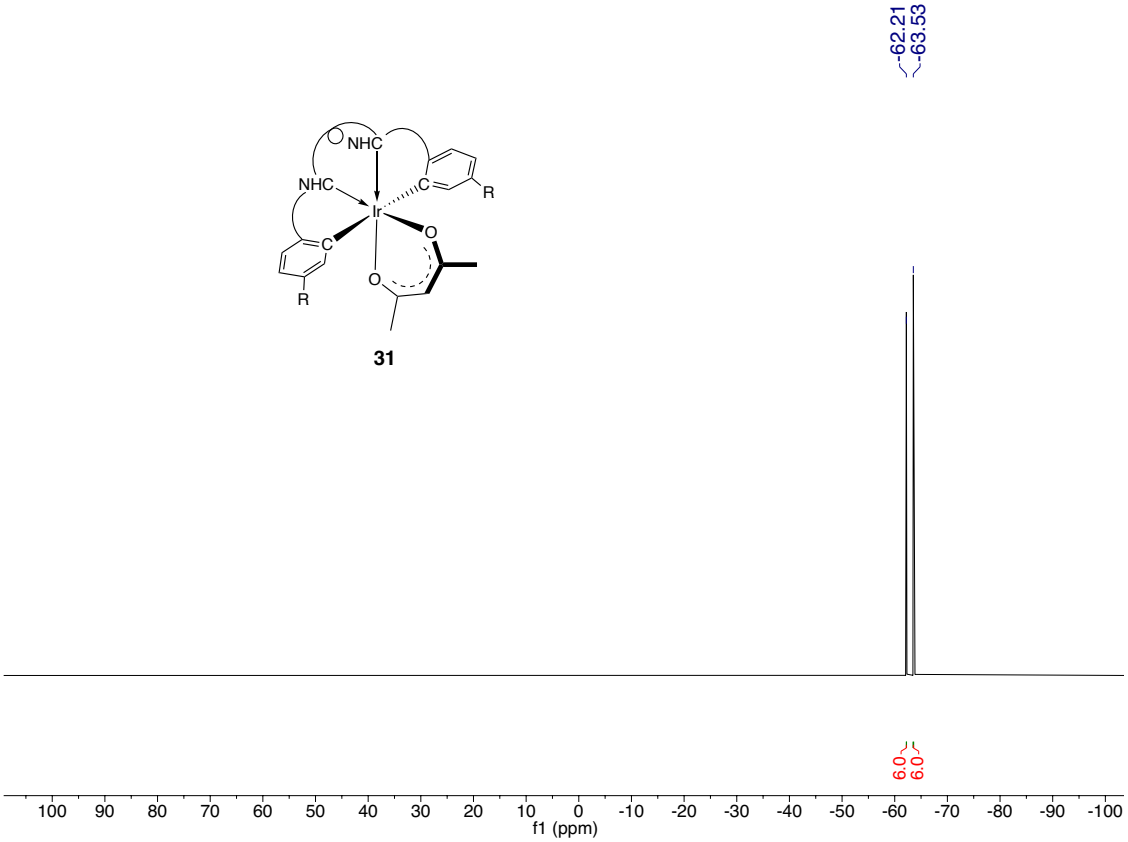

Figure 7.67 ^{19}F NMR chart of complex **31** (470 MHz, dichloromethane-d_2)

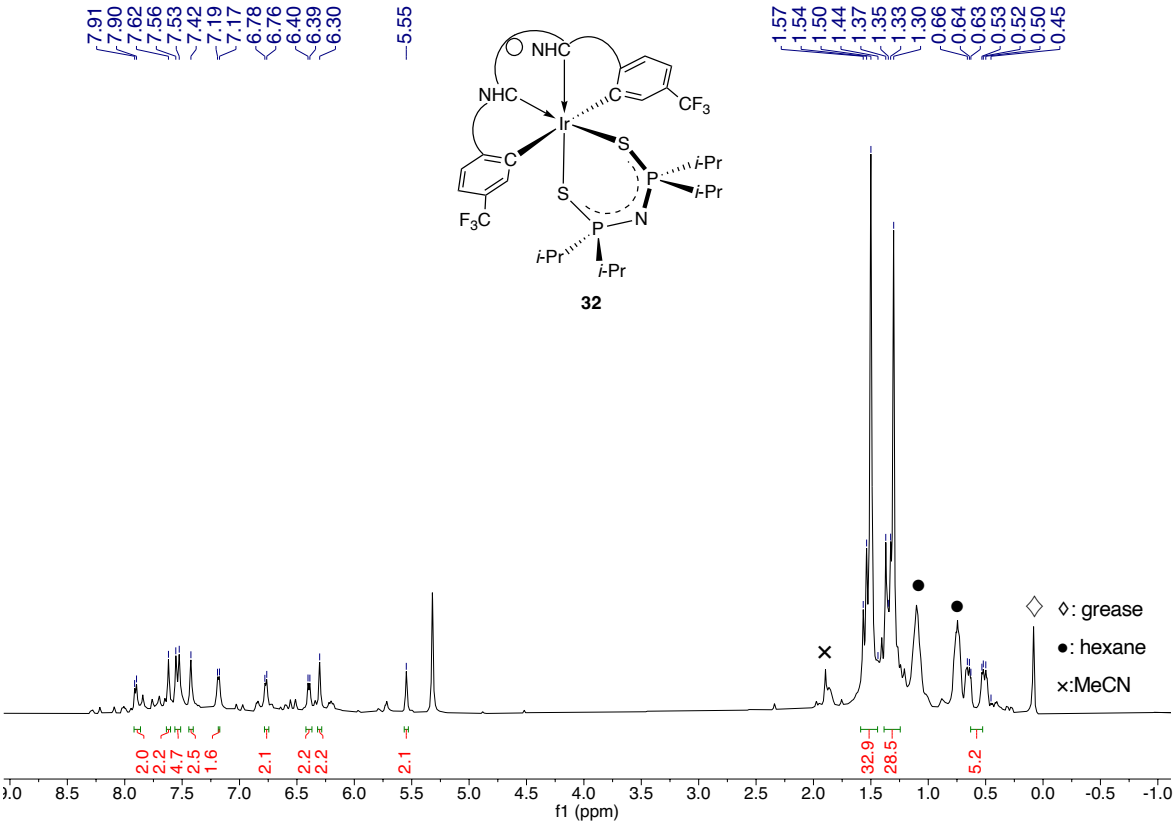

Figure 7.68 ^{1}H NMR chart of complex **32** (500 MHz, dichloromethane-d_2)

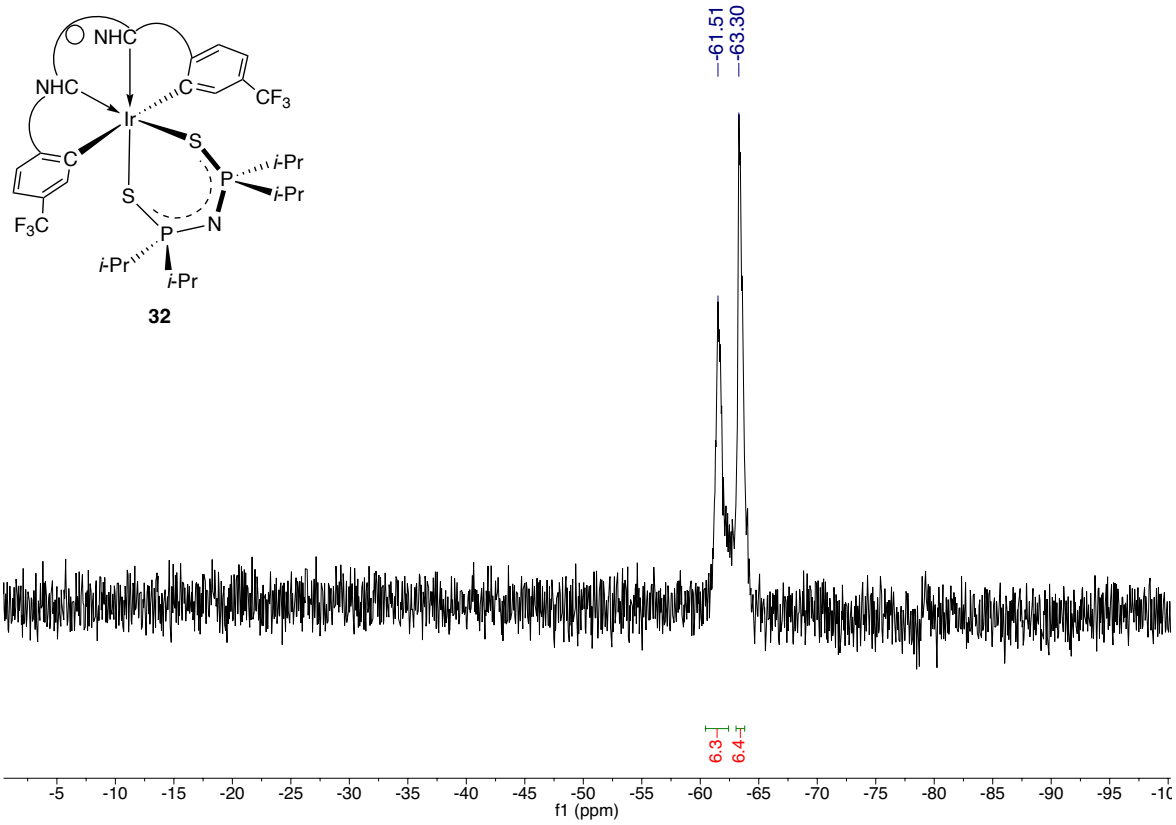

Figure 7.69 ^{19}F NMR chart of complex **32** (470 MHz, dichloromethane-d_2)

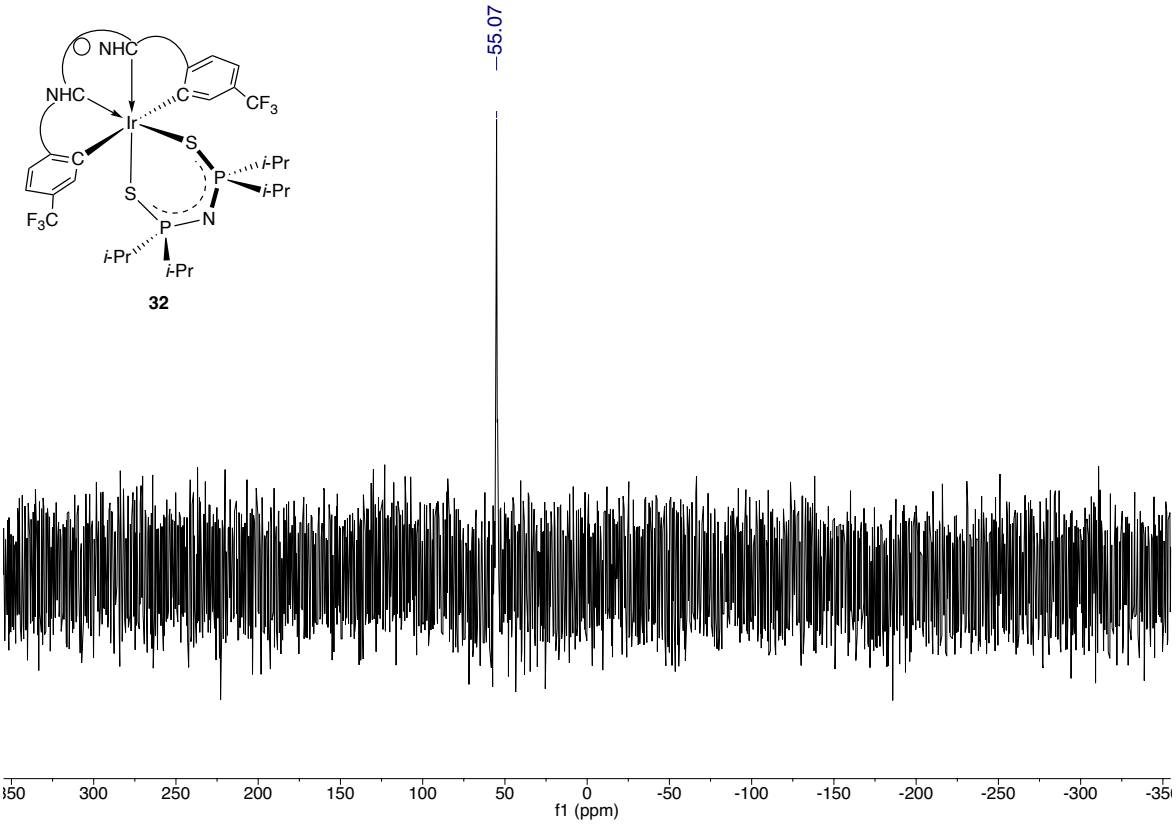

Figure 7.70 ^{31}P{^{1}H} NMR chart of complex **32** (243 MHz, dichloromethane-d_2).

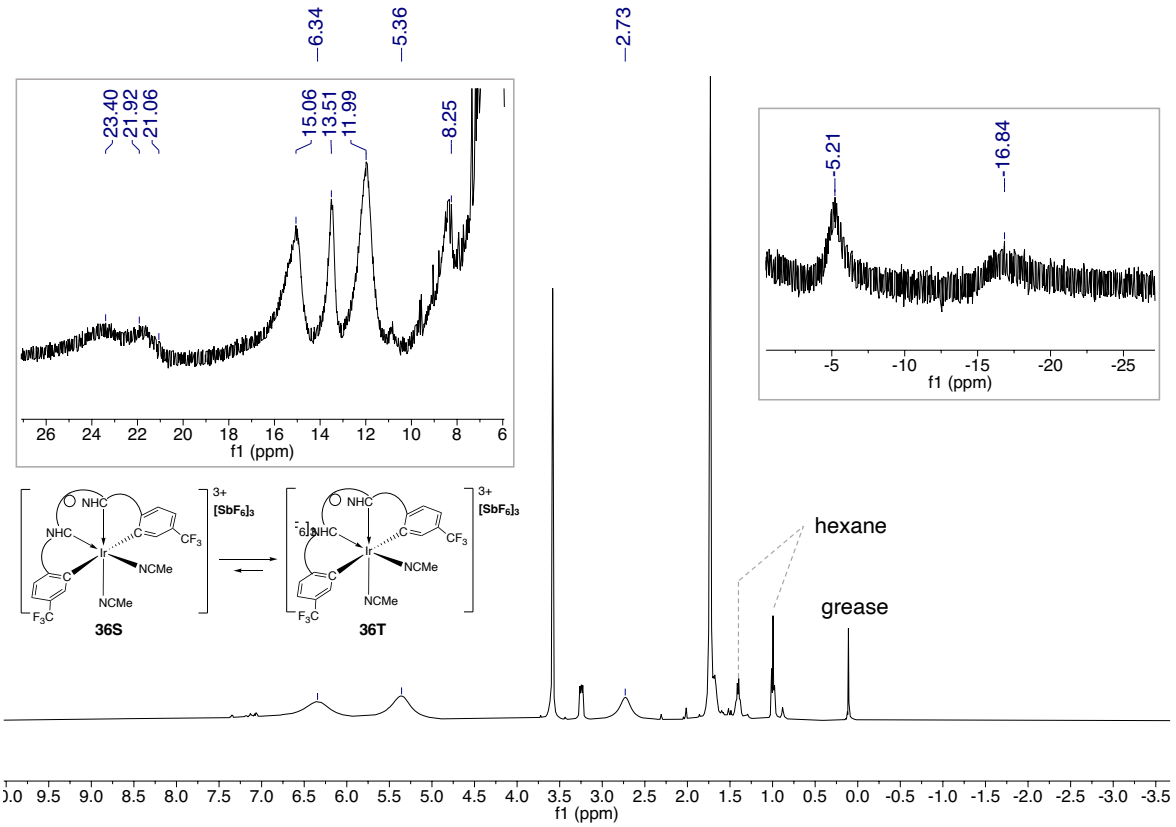

Figure 7.71 ^{1}H NMR chart of complex **36** (500 MHz, THF-d_8) at 20 °C

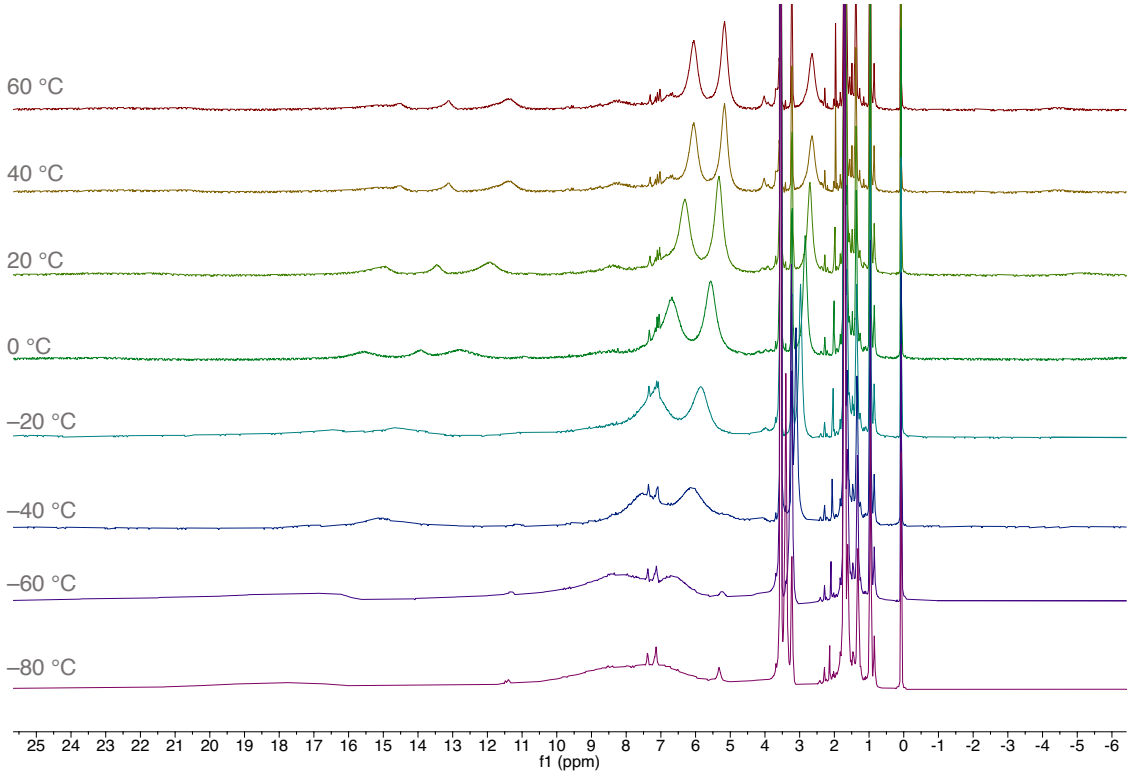

Figure 7.72 VT-^{1}H NMR chart of complex **36** (500 MHz, THF-d_8)

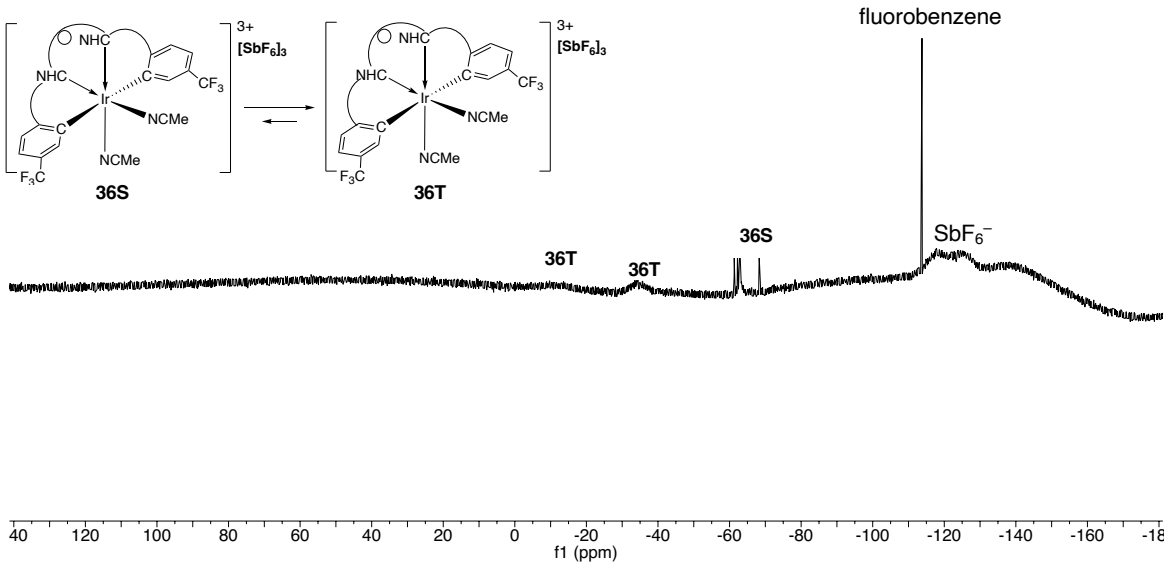

Figure 7.73 ^{19}F NMR chart of complex **36** (470 MHz, THF-d_8) at 20 °C

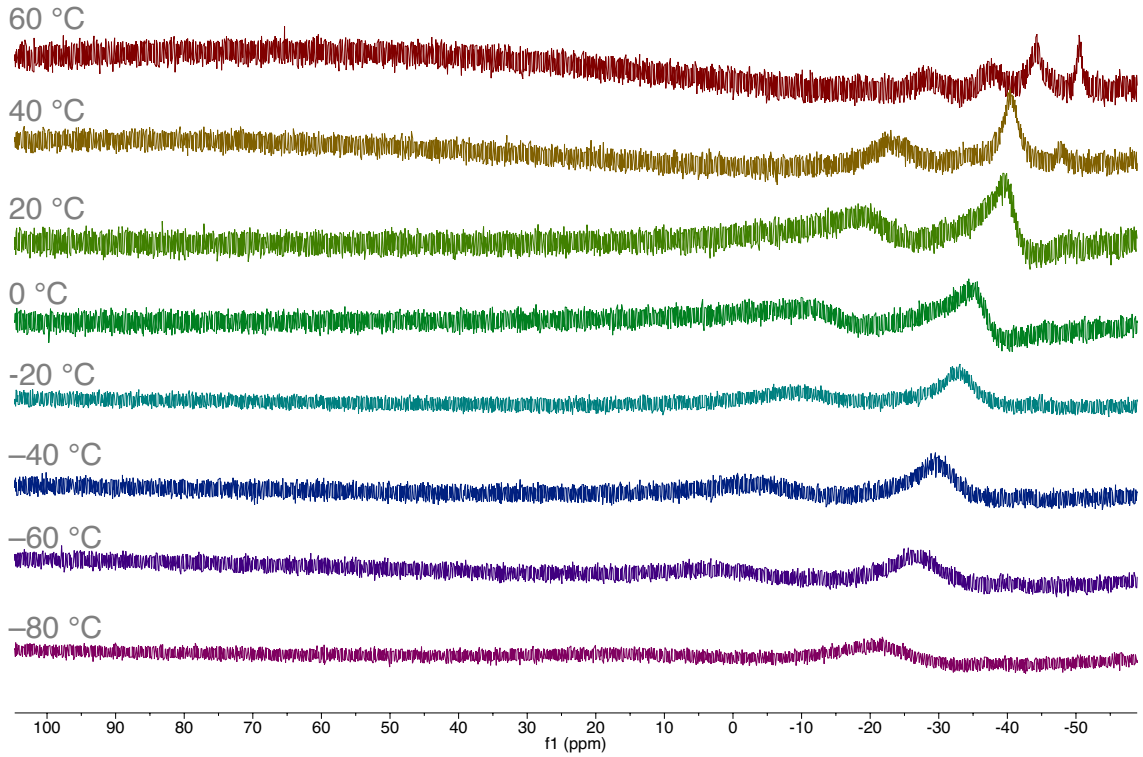

Figure 7.74 VT-^{19}F NMR chart of complex **36** (470 MHz, THF-d_8)

7.2. Crystallographic Data

Table 7.1 Crystal data and structure refinement for compound **8** (CCDC No. 2077110)

Identification code	compound **8**	
Empirical formula	$C_{20}H_{19}F_3N$	
Formula weight	330.36	
Temperature	173(2) K	
Wavelength	0.71073 Å	
Crystal system	Triclinic	
Space group	P-1	
Unit cell dimensions	a = 10.7247(18) Å	a= 103.741(2)°.
	b = 13.137(2) Å	b= 107.370(2)°.
	c = 13.304(2) Å	g = 93.611(2)°.
Volume	1719.5(5) $Å^3$	
Z	4	
Density (calculated)	1.276 Mg/m^3	
Absorption coefficient	0.097 mm^{-1}	
F(000)	692	
Crystal size	0.381 x 0.363 x 0.241 mm^3	
Theta range for data collection	1.982 to 27.185°.	
Index ranges	-13<=h<=13, -16<=k<=16, -17<=l<=17	
Reflections collected	19488	
Independent reflections	7570 [R(int) = 0.0219]	
Completeness to theta = 26.000°	99.40%	
Refinement method	Full-matrix least-squares on F^2	
Data / restraints / parameters	7570 / 261 / 505	
Goodness-of-fit on F^2	1.03	
Final R indices [I>2sigma(I)]	R1 = 0.0542, wR2 = 0.1343	
R indices (all data)	R1 = 0.0681, wR2 = 0.1430	
Extinction coefficient	n/a	
Largest diff. peak and hole	0.550 and -0.444 $e.Å^{-3}$	

Table 7.2 Crystal data and structure refinement for compound **18** (CCDC No. 2077111)

Identification code	compound **18**	
Empirical formula	$C_{41.06}\ H_{42.13}\ Cl_{1.13}\ F_6\ Ir\ N_2$	
Formula weight	909.87	
Temperature	173(2) K	
Wavelength	0.71073 Å	
Crystal system	Triclinic	
Space group	P-1	
Unit cell dimensions	a = 12.0016(10) Å	α= 90.6300(10)°.
	b = 17.2729(14) Å	β= 106.1580(10)°.
	c = 18.7698(15) Å	γ = 91.5680(10)°.
Volume	3735.2(5) $Å^3$	
Z	4	
Density (calculated)	1.618 Mg/m^3	
Absorption coefficient	3.717 mm^{-1}	
F(000)	1811	
Crystal size	0.128 x 0.100 x 0.060 mm^3	
Theta range for data collection	1.767 to 29.221°.	
Index ranges	-16<=h<=16, -23<=k<=22, -25<=l<=24	
Reflections collected	45541	
Independent reflections	18471 [R(int) = 0.0188]	
Completeness to theta = 26.000°	99.20%	
Refinement method	Full-matrix least-squares on F^2	
Data / restraints / parameters	18471 / 126 / 1051	
Goodness-of-fit on F^2	1.019	
Final R indices [I>2sigma(I)]	R1 = 0.0227, wR2 = 0.0508	
R indices (all data)	R1 = 0.0303, wR2 = 0.0534	
Extinction coefficient	n/a	
Largest diff. peak and hole	1.065 and -0.712 $e.Å^{-3}$	

Table 7.3.Crystal data and structure refinement for compound **20** (CCDC No. 2077113)

Identification code	compound **20**
Empirical formula	C_{49} H_{59} Cl_2 F_6 I Ir N_5
Formula weight	1222.01
Temperature	173(2) K
Wavelength	0.71073 Å
Crystal system	Monoclinic
Space group	$P2_1/c$
Unit cell dimensions	a = 15.226(12) Å α= 90°.
	b = 10.859(8) Å β= 94.107(15)°.
	c = 34.39(3) Å γ = 90°.
Volume	5672(8) $Å^3$
Z	4
Density (calculated)	1.431 Mg/m^3
Absorption coefficient	3.046 mm^{-1}
F(000)	2424
Crystal size	0.325 x 0.307 x 0.250 mm^3
Theta range for data collection	1.187 to 28.036°.
Index ranges	-15<=h<=20, -14<=k<=11, -43<=l<=45
Reflections collected	33358
Independent reflections	13602 [R(int) = 0.0280]
Completeness to theta = 26.000°	100.00%
Refinement method	Full-matrix least-squares on F^2
Data / restraints / parameters	13602 / 180 / 688
Goodness-of-fit on F^2	1.11
Final R indices [I>2sigma(I)]	R1 = 0.0482, wR2 = 0.1325
R indices (all data)	R1 = 0.0629, wR2 = 0.1400
Extinction coefficient	n/a
Largest diff. peak and hole	2.359 and -1.410 e.Å-3

Table 7.4.Crystal data and structure refinement for compound **23** (CCDC No. 2077112)

Identification code	compound **23**	
Empirical formula	C_{74} H_{72} Cs F_{12} Ir N_4 O_2	
Formula weight	1602.46	
Temperature	123(2) K	
Wavelength	0.71073 Å	
Crystal system	Monoclinic	
Space group	C2/c	
Unit cell dimensions	a = 32.535(11) Å	a= 90°.
	b = 9.541(3) Å	b= 118.673(3)°.
	c = 24.126(8) Å	g = 90°.
Volume	6571(4) $Å^3$	
Z	4	
Density (calculated)	1.620 Mg/m^3	
Absorption coefficient	2.662 mm^{-1}	
F(000)	3200	
Crystal size	0.280 x 0.270 x 0.230 mm^3	
Theta range for data collection	1.762 to 28.056°.	
Index ranges	-42<=h<=42, -12<=k<=12, -31<=l<=31	
Reflections collected	38041	
Independent reflections	7956 [R(int) = 0.0192]	
Completeness to theta = 25.242°	100.00%	
Refinement method	Full-matrix least-squares on F^2	
Data / restraints / parameters	7956 / 294 / 537	
Goodness-of-fit on F2	1.067	
Final R indices [I>2sigma(I)]	R1 = 0.0157, wR2 = 0.0395	
R indices (all data)	R1 = 0.0164, wR2 = 0.0399	
Extinction coefficient	n/a	
Largest diff. peak and hole	0.734 and -0.452 $e.Å^{-3}$	

Table 7.5.Crystal data and structure refinement for compound **24** (CCDC No. 2077115)

Identification code	compound **24**
Empirical formula	$C_{86.67}\ H_{93.34}\ Cs\ F_{12}\ Ir\ N_{7.33}\ O_6$
Formula weight	1886.83
Temperature	123(2) K
Wavelength	0.71073 Å
Crystal system	Triclinic
Space group	P-1
Unit cell dimensions	a = 15.575(13) Å α= 80.132(19)°.
	b = 25.32(2) Å β= 84.508(8)°.
	c = 33.43(3) Å γ = 85.925(13)°.
Volume	12907(18) Å3
Z	6
Density (calculated)	1.456 Mg/m^3
Absorption coefficient	2.050 mm^{-1}
F(000)	5716
Crystal size	0.152 x 0.084 x 0.042 mm^3
Theta range for data collection	1.696 to 27.974°.
Index ranges	-20<=h<=20, -33<=k<=33, -44<=l<=44
Reflections collected	155152
Independent reflections	61174 [R(int) = 0.0478]
Completeness to theta = 26.000°	99.50%
Refinement method	Full-matrix least-squares on F^2
Data / restraints / parameters	61174 / 1380 / 3261
Goodness-of-fit on F^2	1.037
Final R indices [I>2sigma(I)]	R1 = 0.0494, wR2 = 0.1035
R indices (all data)	R1 = 0.0788, wR2 = 0.1137
Extinction coefficient	n/a
Largest diff. peak and hole	2.378 and -1.695 $e.Å^{-3}$

Table 7.6 Crystal data and structure refinement for Compound **25** (CCDC No. 2077114)

Identification code	Compound **25**	
Empirical formula	C_{66} H_{57} F_{12} Ir N_4	
Formula weight	1326.35	
Temperature	123(2) K	
Wavelength	0.71073 Å	
Crystal system	Monoclinic	
Space group	$P2_1/n$	
Unit cell dimensions	a = 16.568(16) Å	α= 90°.
	b = 19.859(19) Å	β= 92.76(3)°.
	c = 17.670(17) Å	γ = 90°.
Volume	5807(10) $Å^3$	
Z	4	
Density (calculated)	1.517 Mg/m^3	
Absorption coefficient	2.383 mm^{-1}	
F(000)	2664	
Crystal size	0.146 x 0.112 x 0.013 mm3	
Theta range for data collection	1.544 to 25.116°.	
Index ranges	-19<=h<=19, -23<=k<=23, -21<=l<=21	
Reflections collected	56056	
Independent reflections	10338 [R(int) = 0.1252]	
Completeness to theta = 25.116°	99.90%	
Refinement method	Full-matrix least-squares on F^2	
Data / restraints / parameters	10338 / 272 / 830	
Goodness-of-fit on F^2	0.884	
Final R indices [I>2sigma(I)]	R1 = 0.0366, wR2 = 0.0664	
R indices (all data)	R1 = 0.0597, wR2 = 0.0712	
Extinction coefficient	n/a	
Largest diff. peak and hole	1.818 and -1.256 $e.Å^{-3}$	

Table 7.7 Crystal data, Data collection, and structure refinement of **28**

Identification code	Compound **28**
CCDC number	2257592
Chemical formula	$C_{102}H_{74}BF_{36}IrN_6$
Formula weight	2270.68
Crystal system	Triclinic
Space group	P-1
Temperature / K	123
a, b, c / Å	a = 15.042 (14)
	b = 18.150 (17)
	c = 18.576 (18)
α, β, γ / °	α = 84.525 (14)
	β = 76.023 (13)
	γ = 84.449 (12)
Volume /Å^3	4885 (8)
Z	2
μ (mm^{-1})	1.49
Crystal size (mm)	0.12 × 0.06 × 0.04
T_{min}	0.836
T_{max}	0.944
No. of measured	35653
No. of independent	17149
No. of observed [I > 2σ(I)] reflections	12589
R_{int}	0.069
$(\sin\theta/\lambda)_{max}$ (Å^{-1})	0.595
R [$F^2 > 2\sigma(F^2)$]	0.052
$wR(F^2)$	0.105
Goodness-of-fit on F^2	1.01
No. of reflections	17149
No. of parameters	1509
No. of restraints	330
$\Delta\rho_{max}$ (e Å^{-3})	0.77
$\Delta\rho_{min}$ (e Å^{-3})	−1.08

Table 7.8 Crystal data, Data collection, and structure refinement of **31**

Identification code	Compound **31**
CCDC number	2257593
Chemical formula	$C_{77}H_{72}F_{12}IrN_7O_2$
Formula weight	1547.61
Crystal system	Triclinic
Space group	P-1
Temperature / K	123
a, b, c / Å	a = 13.835 (11)
	b = 14.886 (11)
	c = 17.538 (15)
α, β, γ / °	α = 97.034 (7)
	β = 99.75 (3)
	γ = 91.746(14)
Volume /Å^3	3528 (5)
Z	2
μ (mm^{-1})	1.97
Crystal size (mm)	0.21 × 0.09 × 0.05
T_{min}	0.757
T_{max}	0.913
No. of measured	37918
No. of independent	14347
No. of observed [I > 2σ(I)] reflections	13074
R_{int}	0.033
$(\sin\theta/\lambda)_{max}$ (Å^{-1})	0.625
R [$F^2 > 2\sigma(F^2)$]	0.025
$wR(F^2)$	0.061
Goodness-of-fit on F^2	1.04
No. of reflections	14347
No. of parameters	1083
No. of restraints	199
$\Delta\rho_{max}$ (e Å^{-3})	1.07
$\Delta\rho_{min}$ (e Å^{-3})	−0.64

Table 7.9 Crystal data and structure refinement for Compound **32**

Identification code	Compound **32**	
Empirical formula	$C_{78}\ H_{87}\ F_{12}\ Ir\ N_6\ P_2\ S_2$	
Formula weight	1678.84	
Temperature	100(2) K	
Wavelength	0.71073 Å	
Crystal system	Monoclinic	
Space group	P-1	
Unit cell dimensions	a = 15.2806(3)Å	α= 90°.
	b = 19.859(19) Å	β= 92.76(3)°.
	c = 17.670(17) Å	γ = 90°.
Volume	5807(10) $Å^3$	
Z	4	
Density (calculated)	1.517 Mg/m^3	
Absorption coefficient	2.383 mm^{-1}	
F(000)	2664	
Crystal size	0.146 x 0.112 x 0.013 mm3	
Theta range for data collection	1.544 to 25.116°.	
Index ranges	-19<=h<=19, -23<=k<=23, -21<=l<=21	
Reflections collected	56056	
Independent reflections	10338 [R(int) = 0.1252]	
Completeness to theta = 25.116°	99.90%	
Refinement method	Full-matrix least-squares on F^2	
Data / restraints / parameters	10338 / 272 / 830	
Goodness-of-fit on F^2	0.884	
Final R indices [I>2sigma(I)]	R1 = 0.0366, wR2 = 0.0664	
R indices (all data)	R1 = 0.0597, wR2 = 0.0712	
Extinction coefficient	n/a	
Largest diff. peak and hole	1.818 and -1.256 $e.Å^{-3}$	

Table 7.10 Crystal data and structure refinement for Compound **33**

Identification code	Compound **33**	
Empirical formula	$C_{120}\ H_{101}\ F_{36}\ Ir\ N_6\ O$	
Formula weight	2530.07	
Temperature	123(2) K	
Wavelength	0.71073 Å	
Crystal system	Monoclinic	
Space group	P-1	
Unit cell dimensions	a = 14.863(14)Å	α= 79.550(19)°.
	b = 19.605(18) Å	β= 87.872(10)°.
	c = 21.470(15) Å	γ = 81.217(15)°.
Volume	6080(10) $Å^3$	
Z	2	
Density (calculated)	1.382 Mg/m^3	
Absorption coefficient	1.202 mm^{-1}	
F(000)	2554	
Crystal size	0.222 x 0.216 x 0.061 mm^3	
Theta range for data collection	1.544 to 25.116°.	
Index ranges	-17<=h<=17, -22<=k<=22, -25<=l<=25	
Reflections collected	20108	
Independent reflections	14305 [R(int) = 0.1252]	
Completeness to theta = 25.116°	99.50%	
Refinement method	Full-matrix least-squares on F^2	
Data / restraints / parameters		
Goodness-of-fit on F^2	1.043	
Final R indices [I>2sigma(I)]	R1 = 0.0592, wR2 = 0.01493	
R indices (all data)	R1 = 0.0954, wR2 = 01672	
Extinction coefficient	n/a	
Largest diff. peak and hole		

Table 7.11 Crystal data, Data collection, and structure refinement of **36**

Identification code	Compound **36**
CCDC number	2257594
Chemical formula	$C_{82}H_{72}F_{32}IrN_6Sb_3$
Formula weight	2306.9
Crystal system	Triclinic
Space group	P-1
Temperature / K	100
a, b, c / Å	a = 13.6795 (3)
	b = 18.2795 (4)
	c = 18.8256 (4)
α, β, γ / °	α =111.009 (2)
	β = 103.697 (2)
	γ = 95.981 (2)
Volume /Å^3	4175.70 (17)
Z	2
μ (mm^{-1})	2.67
Crystal size (mm)	0.08 × 0.05 × 0.04
T_{min}	0.872
T_{max}	1.000
No. of measured	54102
No. of independent	16368
No. of observed [I > 2σ(I)] reflections	12296
R_{int}	0.05
$(\sin\theta/\lambda)_{max}$ (Å^{-1})	0.617
R [$F^2 > 2\sigma(F^2)$]	0.053
$wR(F^2)$	0.144
Goodness-of-fit on F^2	1.02
No. of reflections	16368
No. of parameters	1307
No. of restraints	762
$\Delta\rho_{max}$ (e Å^{-3})	2.13,
$\Delta\rho_{min}$ (e Å^{-3})	−2.00

7.3. Optimized Structure

Table 7.12 Relationship between color and corresponding elements in optimized structures

Color	White	Gray	Blue	Red	Green	Orange	Dark-yellow
Element	H	C	N	O	F	Cl	Ir

- Chapter 2

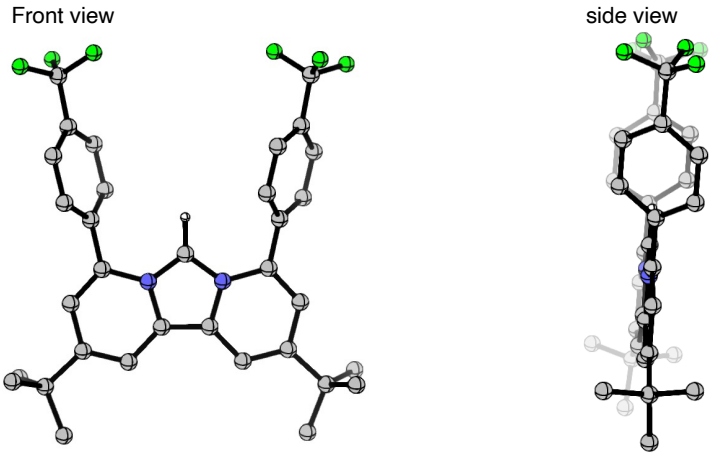

Figure 7.75 Optimized structure of **7** (cation moiety only)

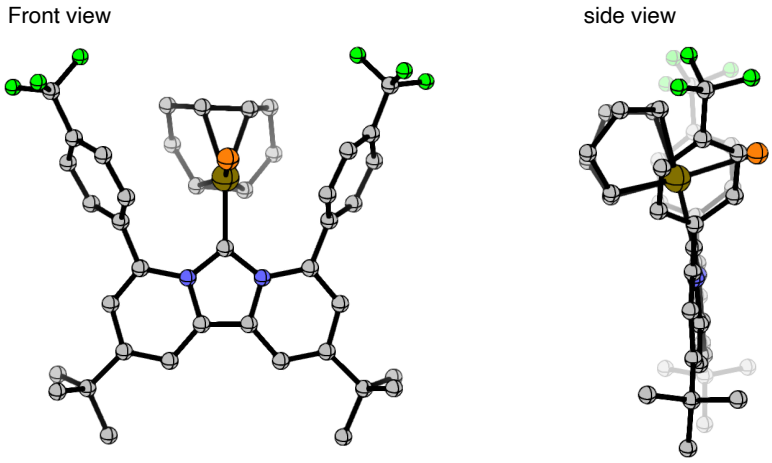

Figure 7.76 Optimized structure of **18**

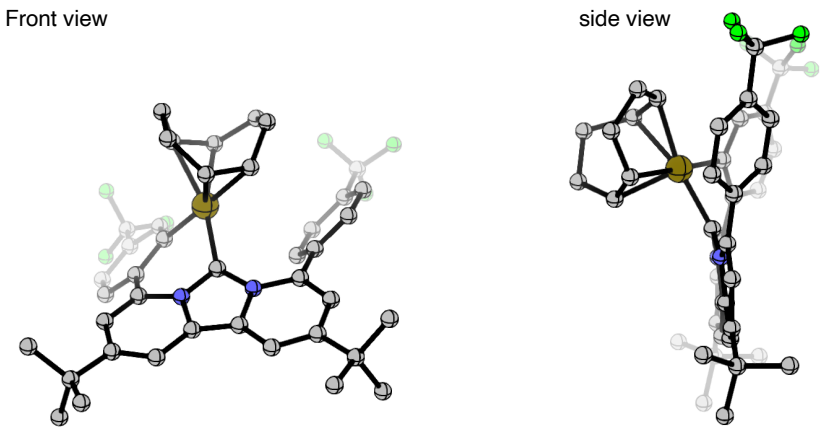

Figure 7.77 Optimized structure of **INT1**

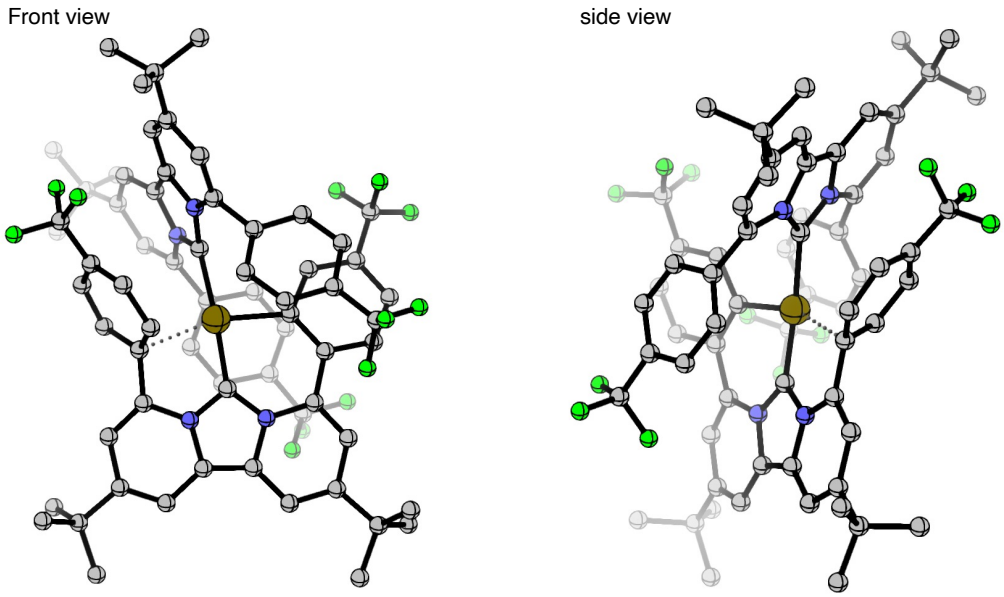

Figure 7.78 Optimized structure of **INT2**

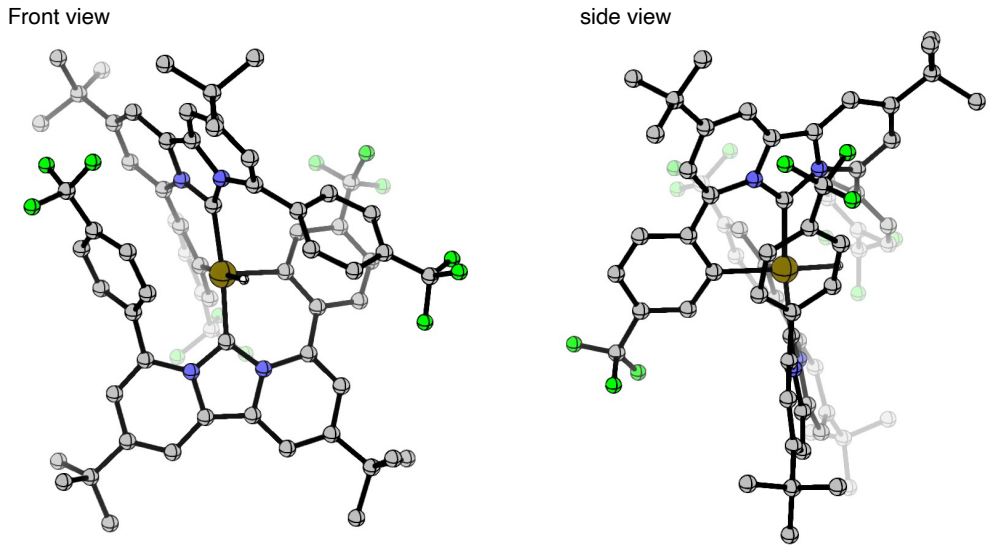

Figure 7.79 Optimized structure of **INT3**

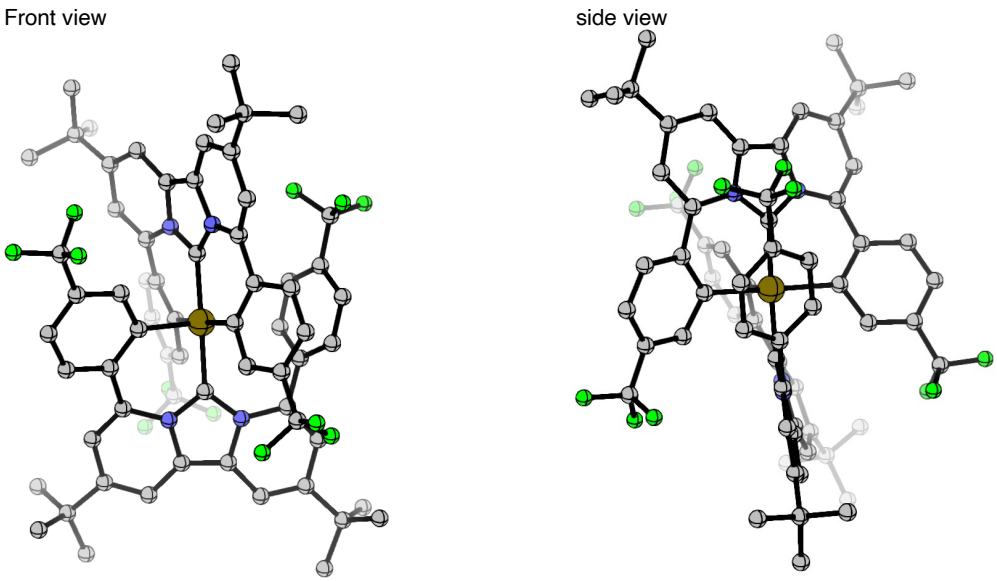

Figure 7.80 Optimized structure of **INT4**

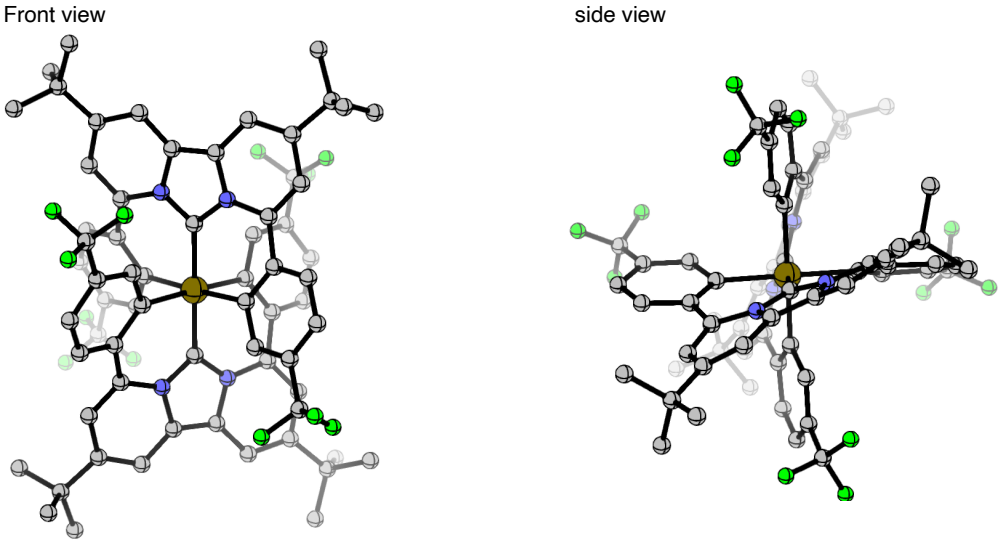

Figure 7.81 Optimized structure of **23**

- Chapter 3

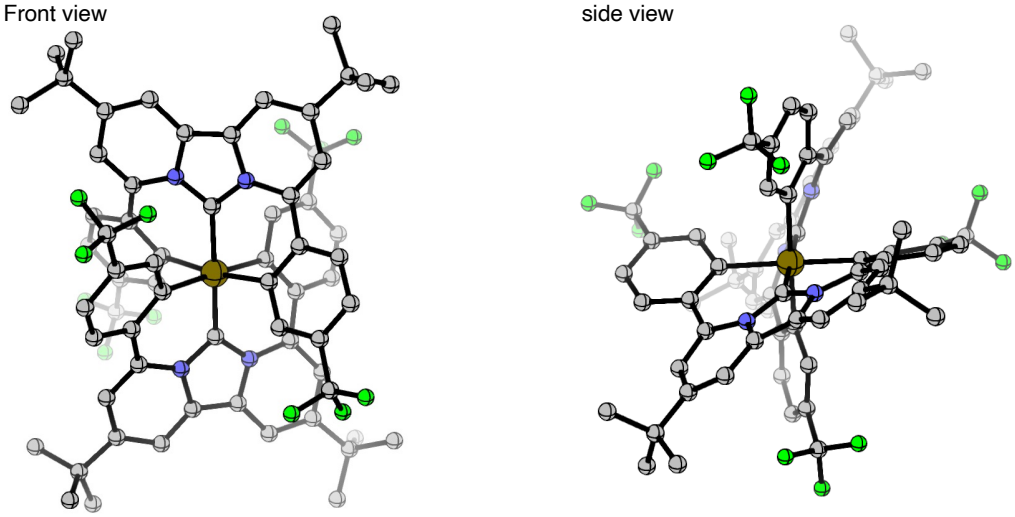

Figure 7.82 Optimized structure of **26**

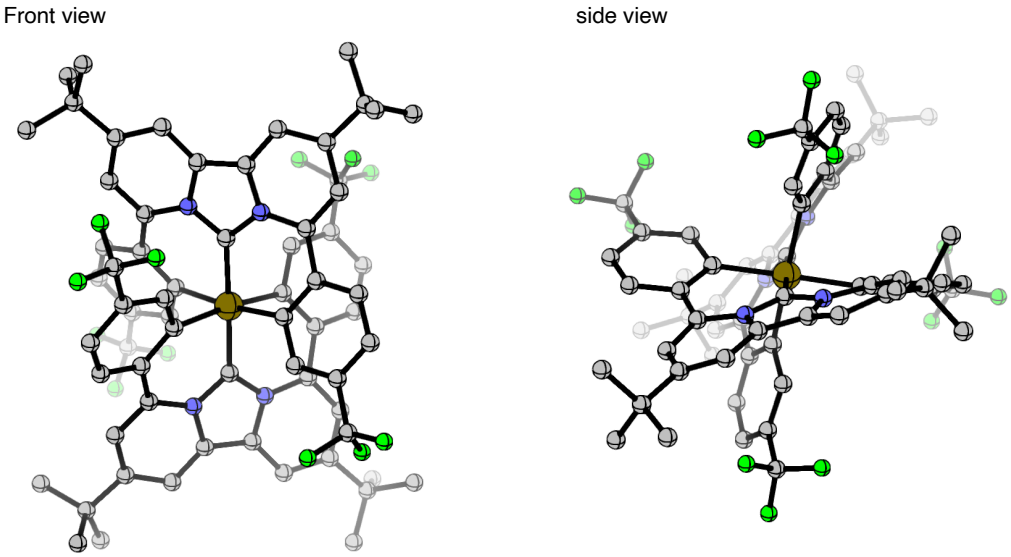

Figure 7.83 Optimized structure of **27**

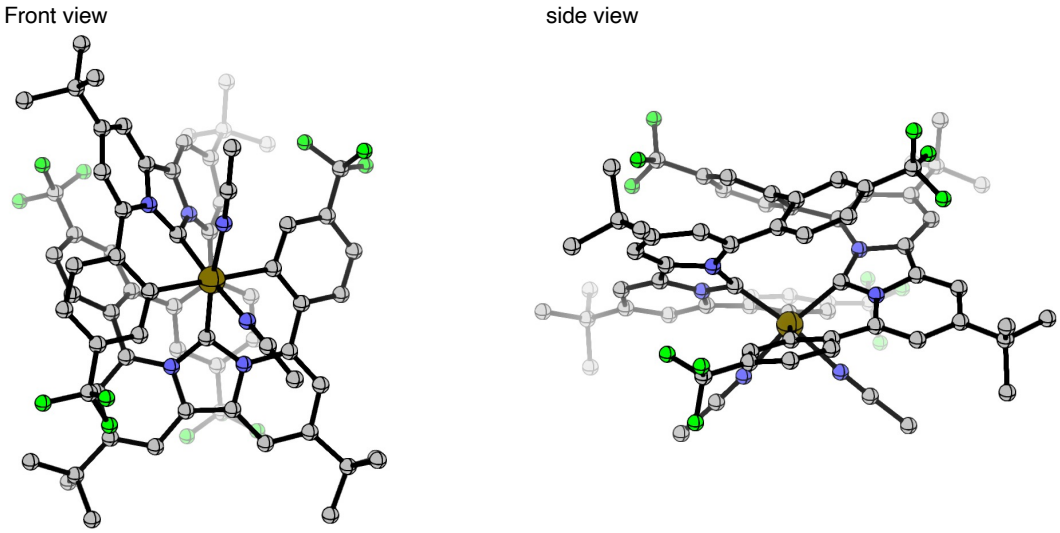

Figure 7.84 Optimized structure of **28**

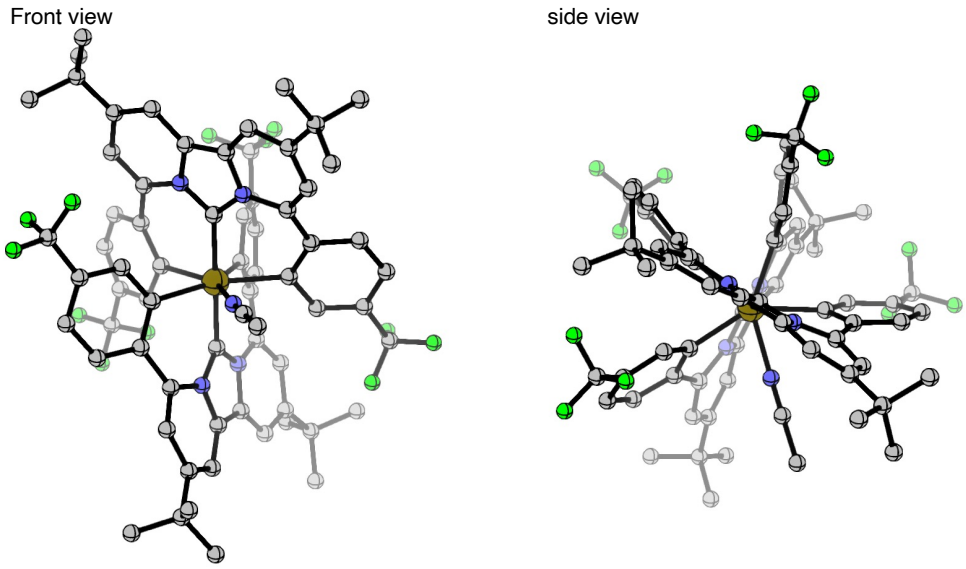

Figure 7.85 Optimized structure of **29**

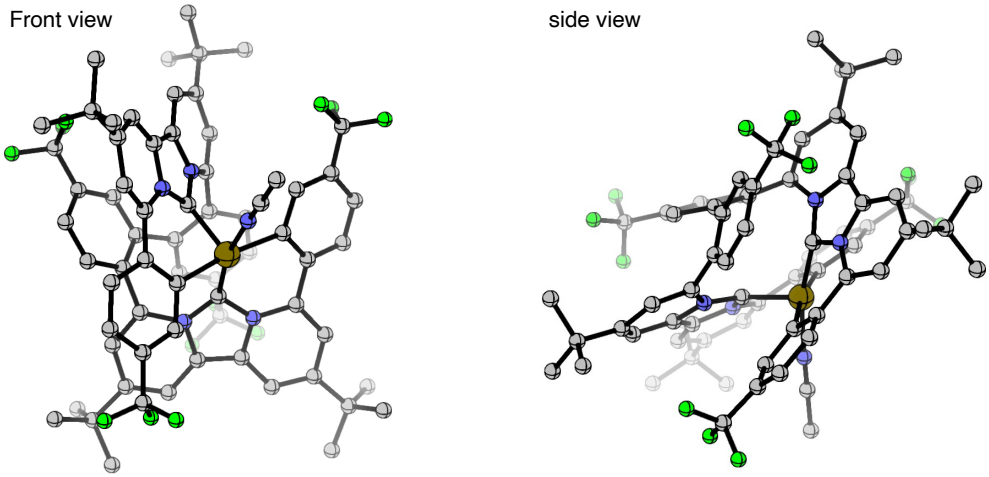

Figure 7.86 Optimized structure of **30**

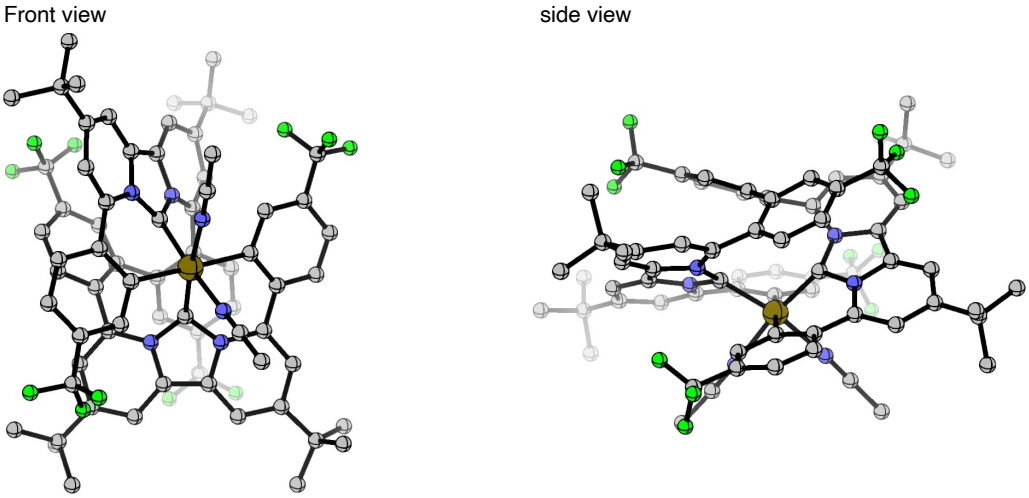

Figure 7.87 Optimized structure of **35**

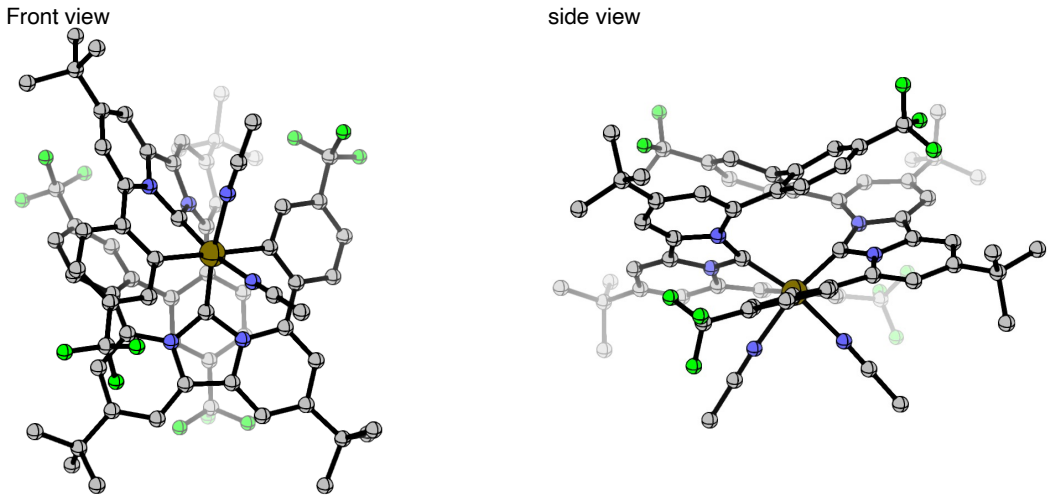

Figure 7.88 Optimized structure of **36-S**

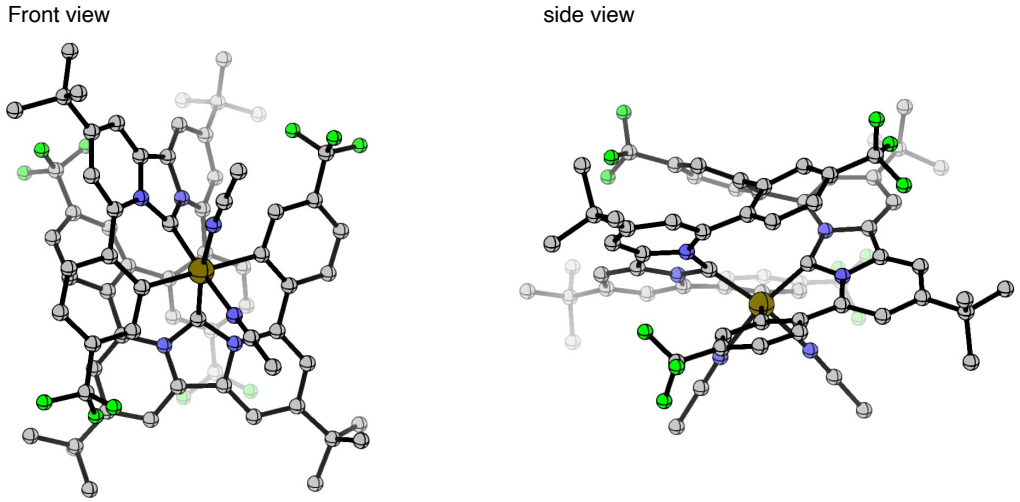

Figure 7.89 Optimized structure of **36-T**

7.4. Cyclic Voltammetry

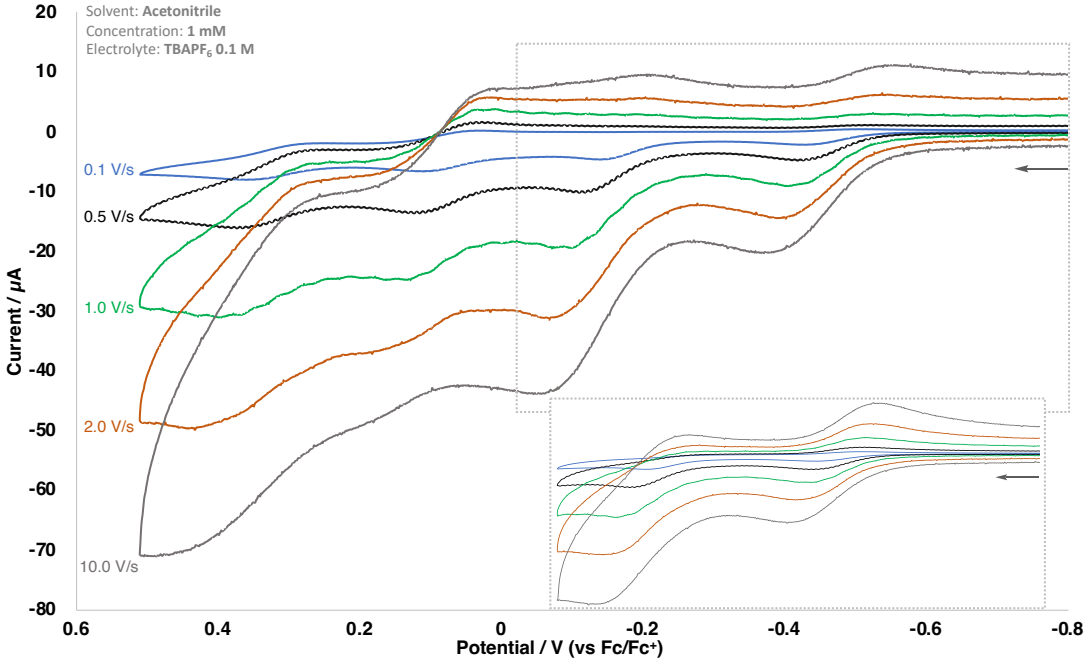

Figure 7.90 Cyclic voltammetry of complex **23** at room temperature

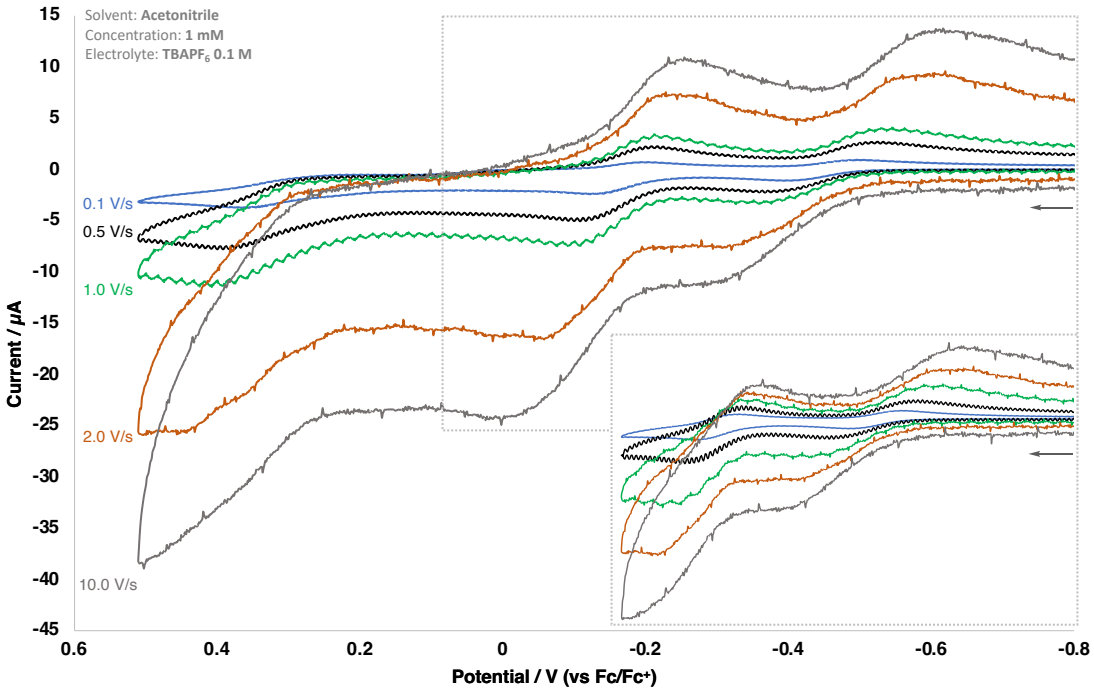

Figure 7.91 Cyclic voltammetry of complex **23** at –45 °C.

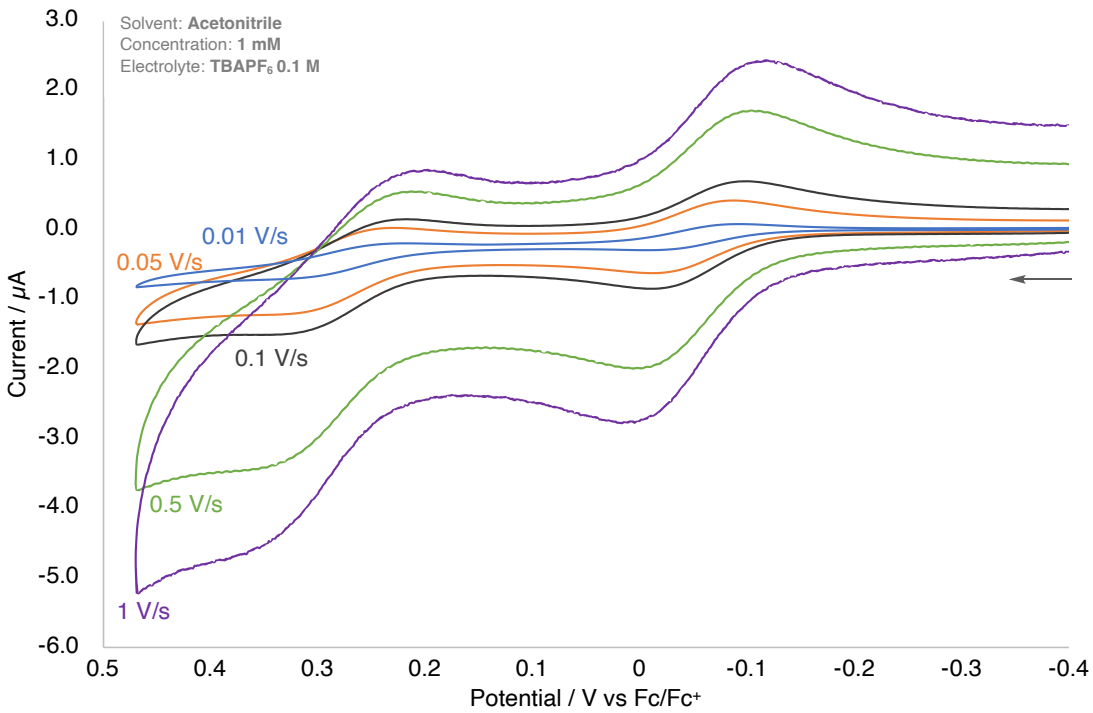

Figure7.92 Cyclic voltammetry of complex **28** at room temperature.

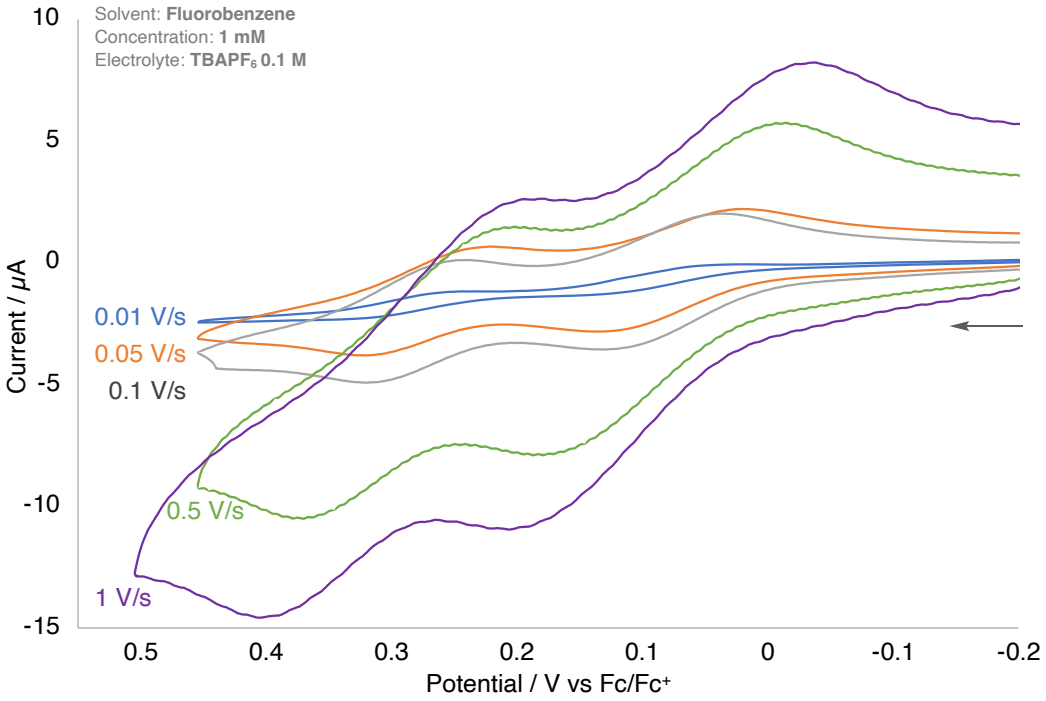

Figure 7.93 Cyclic voltammetry of complex **28** at room temperature.

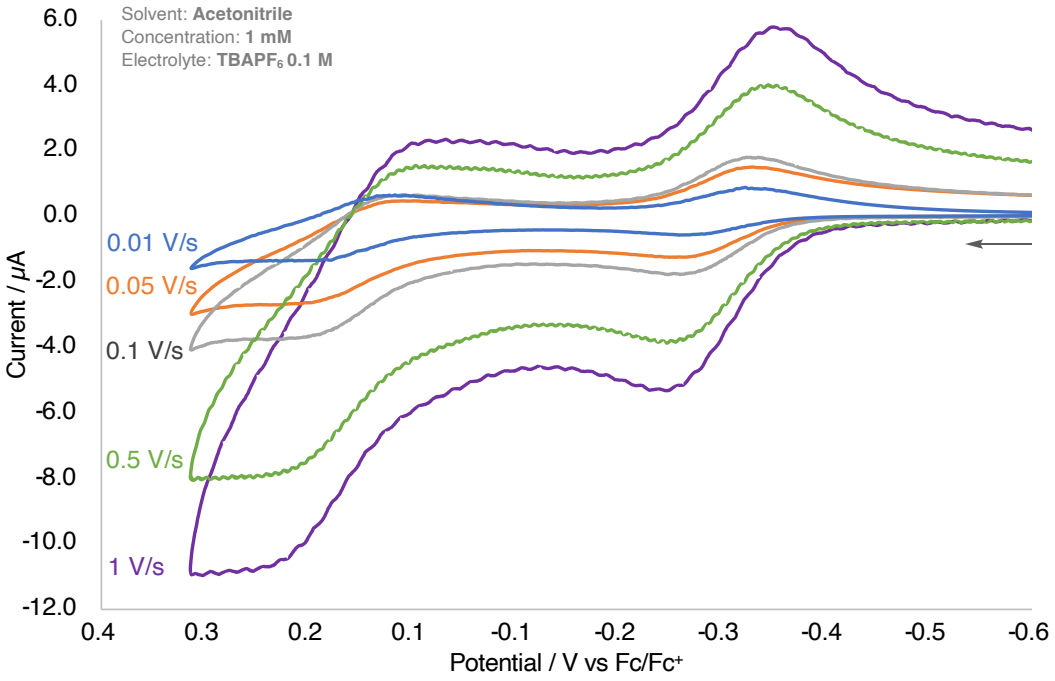

Figure 7.94 Cyclic voltammetry of complex **31** at room temperature.

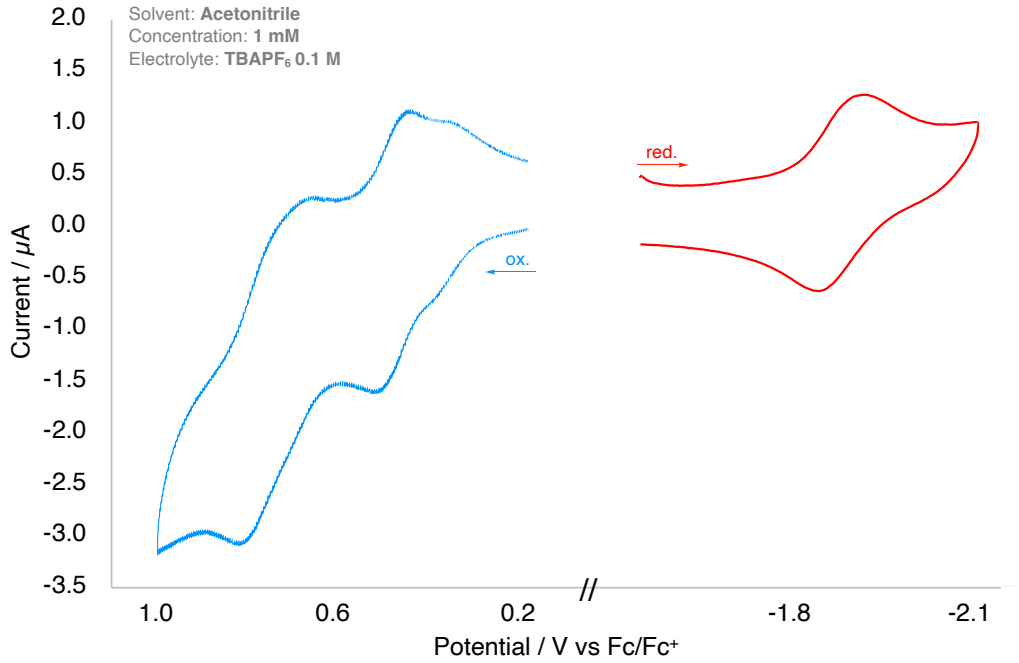

Figure 7.95 Cyclic voltammetry of complex **33** at room temperature

7.5. EPR Data

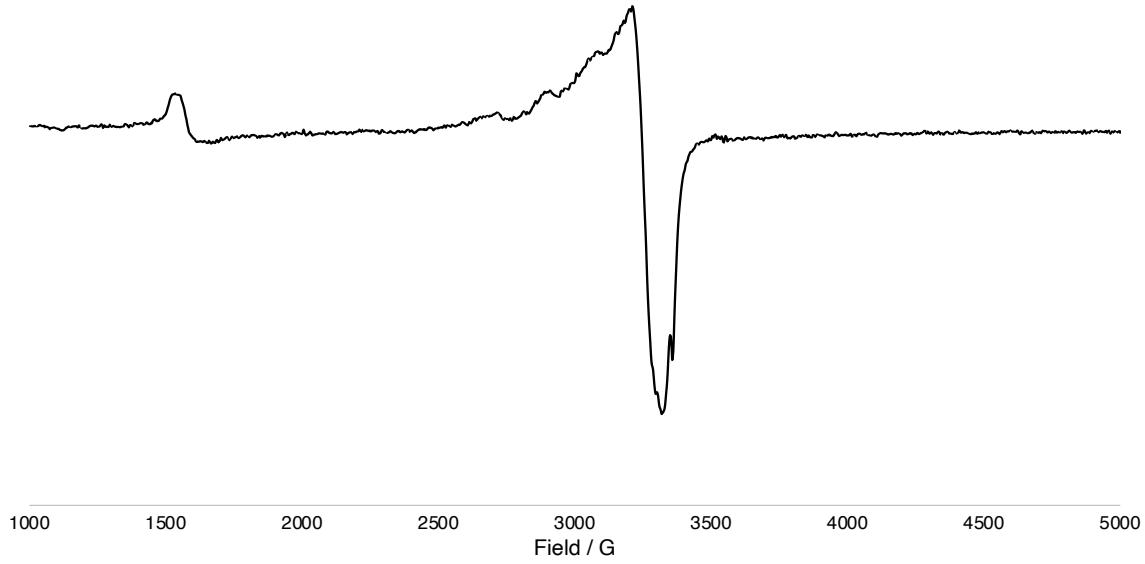

Figure 7.96 EPR chart of decamethylferrocenium triflate [Cp*$_2$Fe][OTf] at 4.2 K

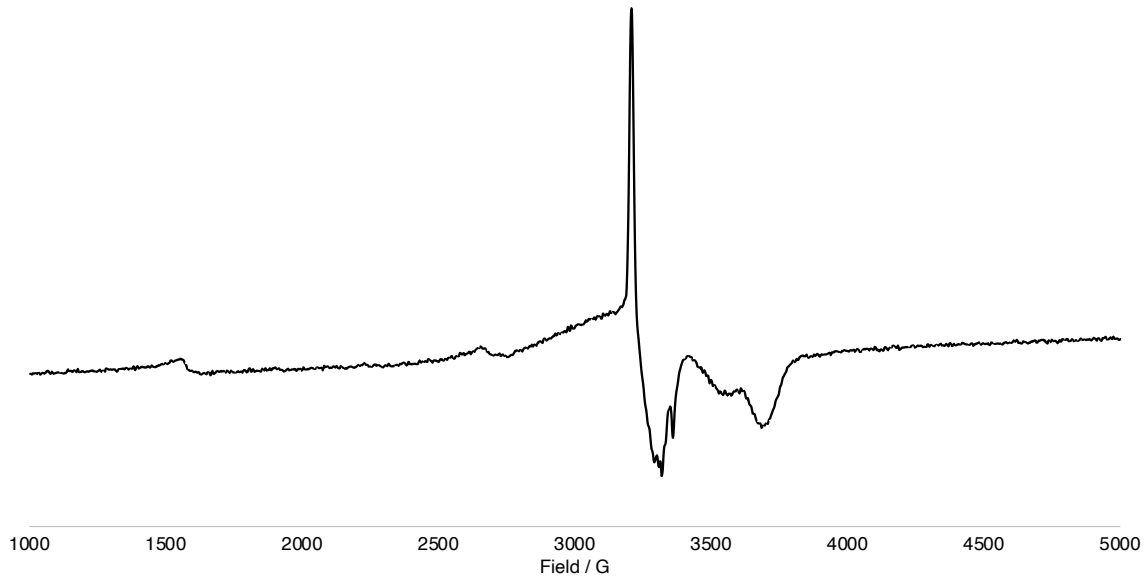

Figure 7.97 EPR chart of *in situ RT* oxidation of **23** by [Cp*$_2$Fe][OTf] measured at 4.2 K

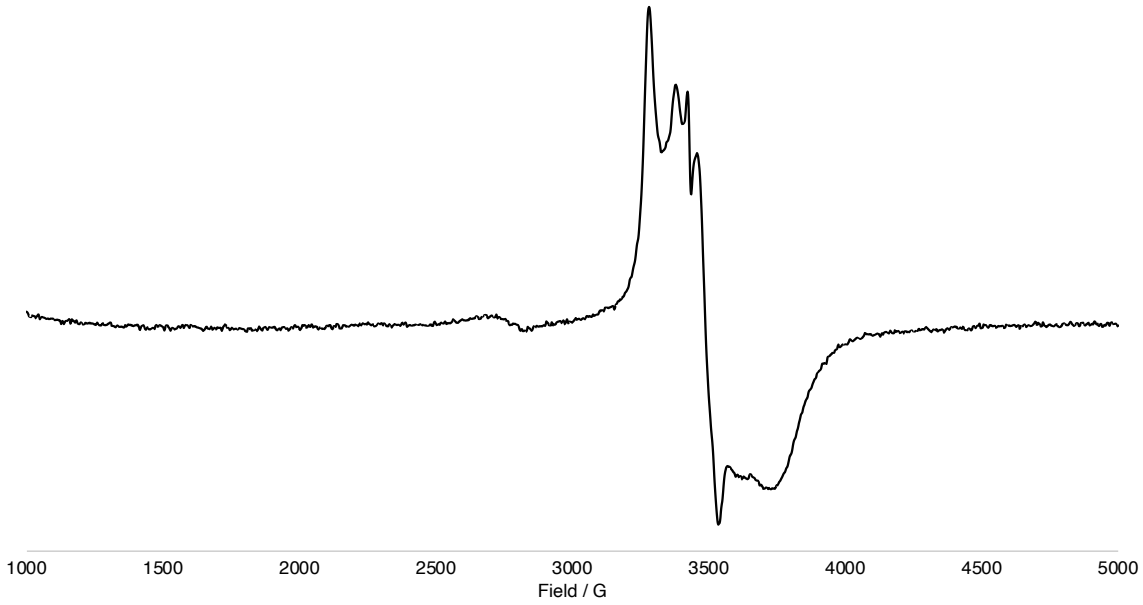

Figure 7.98 EPR chart of *in situ RT* oxidation of **23** by AgOTf measured at 77 K

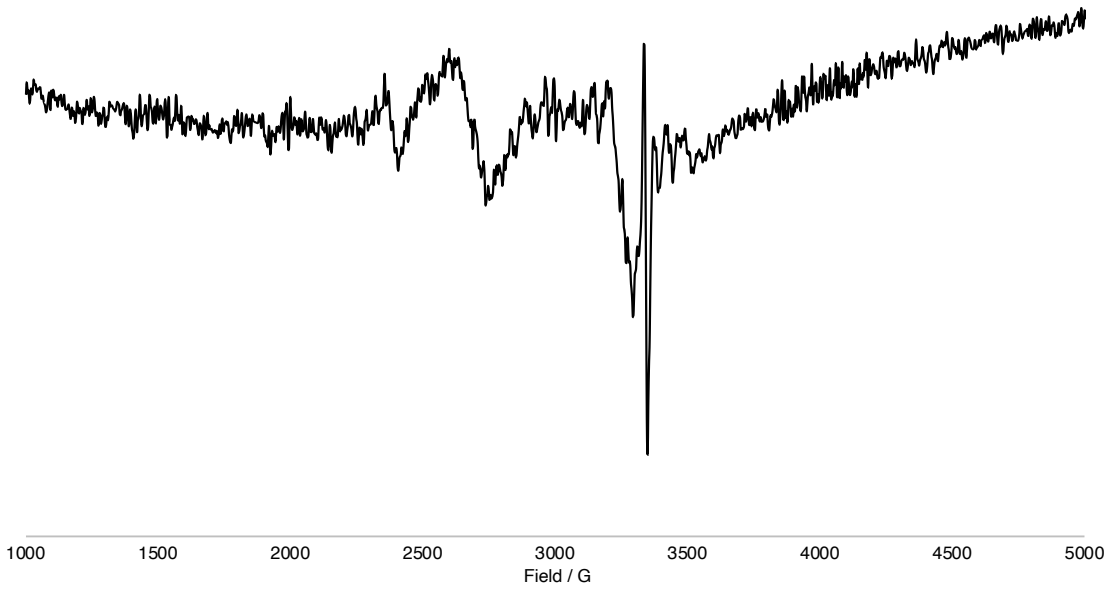

Figure 7.99 EPR chart of thianthrenium hexafluoroantimonate at 60 K

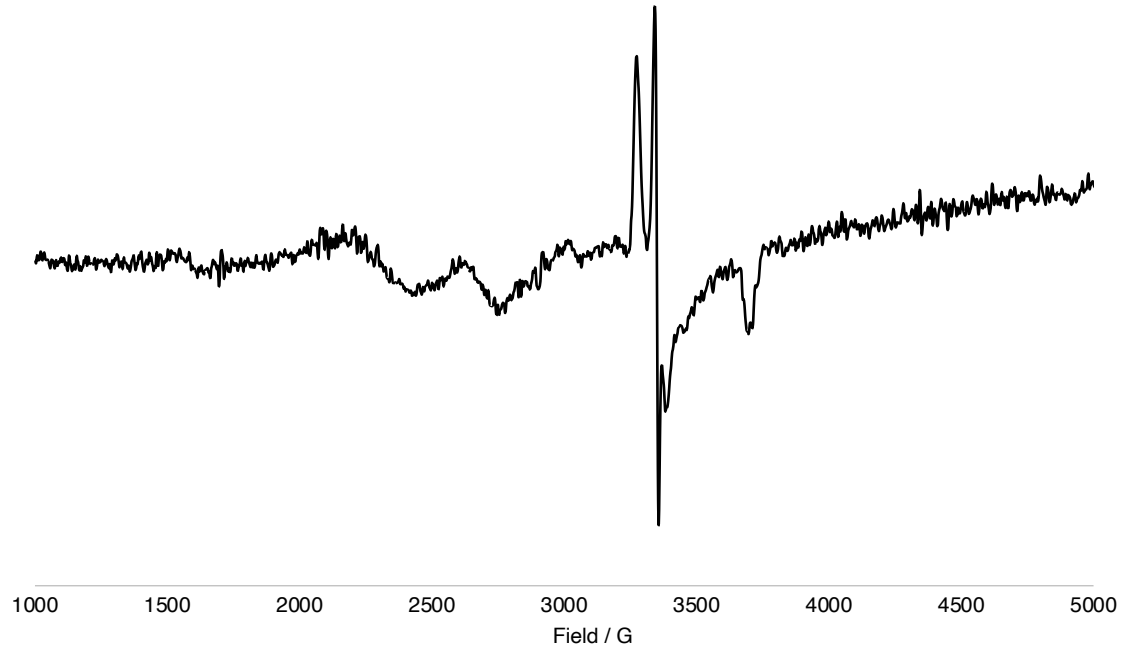

Figure 7.100 EPR chart of *in situ RT* oxidation of **23** by thianthrenium radical cation measured at 60 K

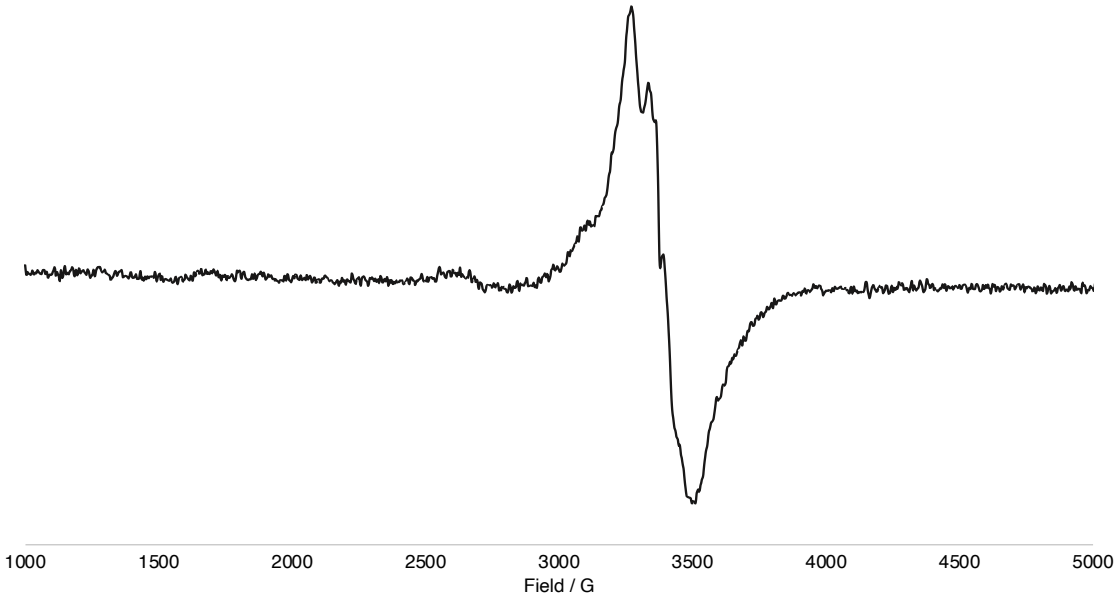

Figure 7.101 EPR chart of **35** at 200 K

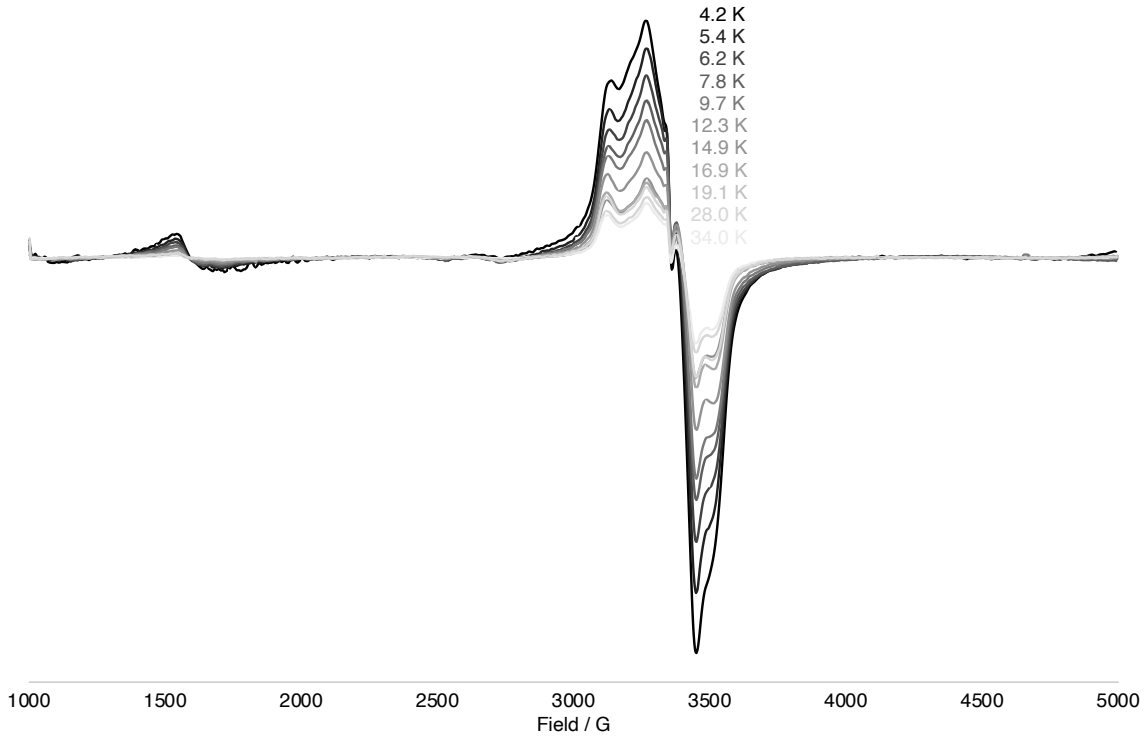

Figure 7.102 VT-EPR chart of **36**

7.6. XPS Data

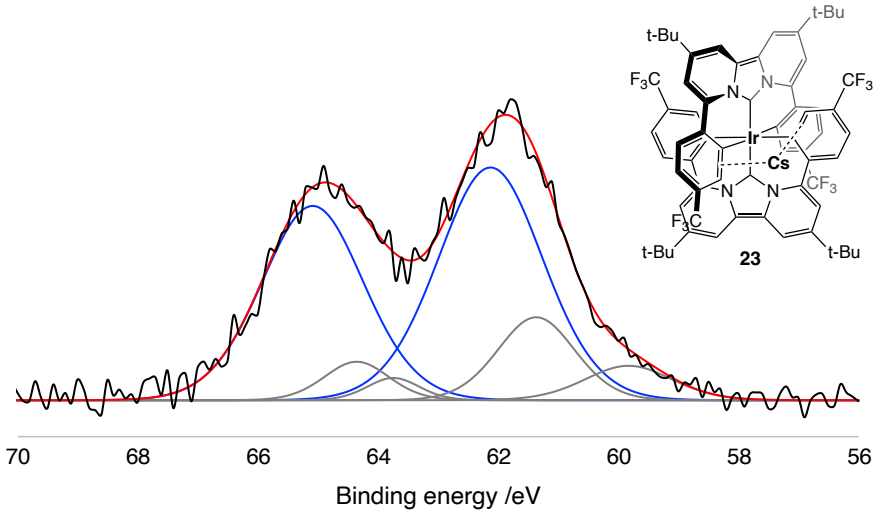

Figure 7.103 XPS spectra of complex **23** in Ir 4f region. Black line: experimental, Red line: cumulation, Blue line: Ir 4f spectra, Gray line: decomposition.

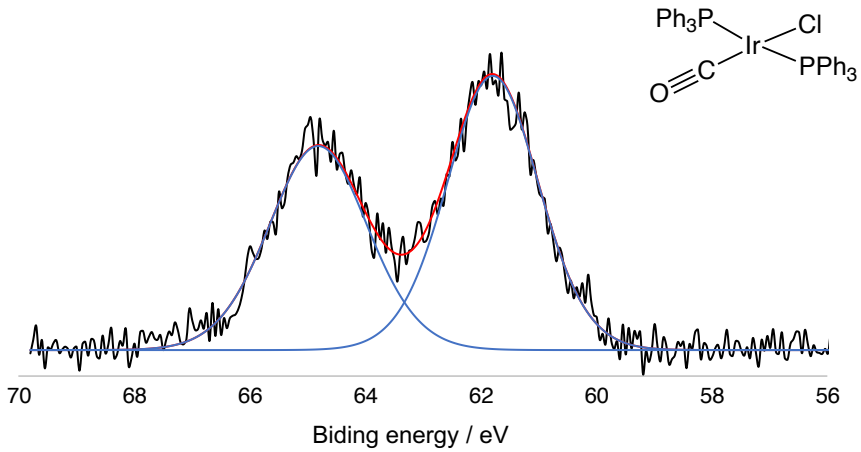

Figure7.104 XPS spectra of *trans*-IrCl(CO)(PPh_3)$_2$ in Ir 4f region. Black line: experimental, Red line: cumulation, Blue line: Ir 4f spectra.

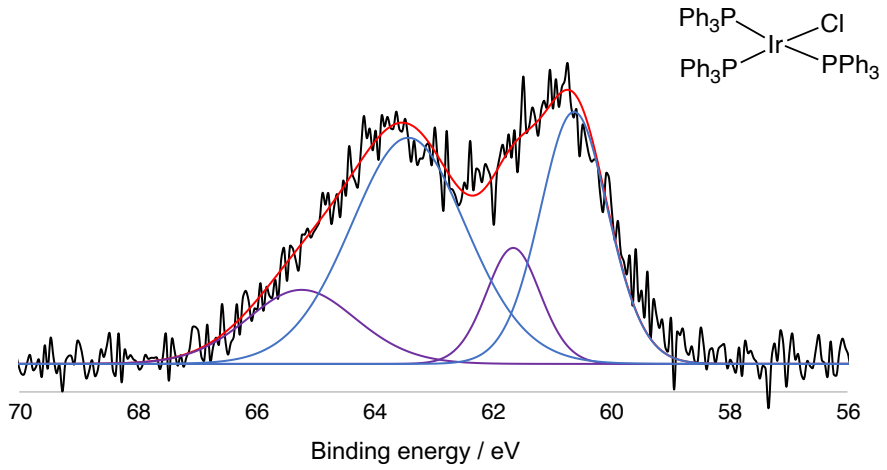

Figure7.105 XPS spectra of $IrCl(CO)(PPh_3)_3$ in Ir 4f region. Black line: experimental, Red line: cumulation, Blue line: Ir 4f spectra, Purple line: decomposition

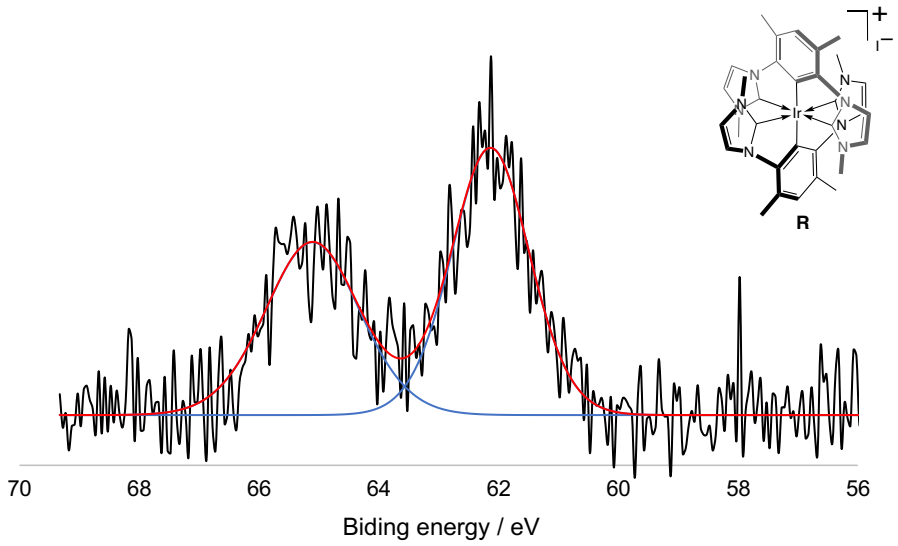

Figure7.106 XPS spectra of complex R in Ir 4f region. Black line: experimental, Red line: cumulation, Blue line: Ir 4f spectra,

Table 7.13 summarized XPS chemical shifts of 4 organoiridium complexes

Complexes	**23**	*trans*-$IrCl(CO)(PPh_3)_2$	$IrCl(PPh_3)_3$	**R**
Ir $4f_{5/2}$ /eV	62.0	61.6	60.8	62.0
Ir $4f_{7/2}$ /eV	65.0	64.6	63.8	65.0